GAS FOIL BEARINGS INTEGRATED WITH ACTIVE MAGNETIC BEARINGS: NUMERICAL MODELLING AND ANALYSIS

A thesis submitted in partial fulfilment of the requirements

for the degree of Doctor of Philosophy

by

Kamal Kumar Basumatary

DEPARTMENT OF MECHANICAL ENGINEERING
INDIAN INSTITUTE OF TECHNOLOGY GUWAHATI,
GUWAHATI - 781 039

August 2020

GAS FOIL BEARINGS INTEGRATED WITH ACTIVE MAGNETIC BEARINGS: NUMERICAL MODELLING AND ANALYSIS

A thesis submitted in partial fulfilment of the requirements
for the degree of Doctor of Philosophy

by

Kamal Kumar Basumatary

DEPARTMENT OF MECHANICAL ENGINEERING
INDIAN INSTITUTE OF TECHNOLOGY GUWAHATI,
GUWAHATI - 781 039
March 2020

CERTIFICATE

This is to certify that the thesis entitled **"Gas Foil Bearings integrated with Active Magnetic Bearing: Numerical Modelling and Analysis"**, submitted by **Kamal Kumar Basumatary (136103031)**, a research scholar in the *Department of Mechanical Engineering, Indian Institute of Technology Guwahati*, for the award of **Doctor of Philosophy** is a record of an original research work carried out by him under our supervision and guidance. The results embodied in this thesis have not been submitted to any other University or Institute for the award of any degree or diploma.

Prof. S. K. Kakoty

Professor
Dept. of Mechanical Engineering
IIT Guwahati

Prof. K. Kalita

Professor
Dept. of Mechanical Engineering
IIT Guwahati

Date:
Guwahati

Dedicated

To

My Parents

and

Wife

Acknowledgement

This thesis would not have been possible without the immense help, support and guidance of several people in various measures. I would like to convey my acknowledgment to all of them. I would like to express my special thanks of sincere gratitude to my supervisors Prof. Sashindra K Kakoty and Prof. Karuna Kalita who gave me the opportunity to work on this interesting project on the topic "Gas Foil Bearing integrated with Active Magnetic Bearings: Numerical Modelling and Analysis". Without them, it would have not been possible for me to give a structured and concrete form to my research study. Their encouragement helped in boosting my confidence level. My supervisors ensured that the best in me was brought out by ensuring that my commitment and dedication towards my research work was not compromised at any point of time. I could not have achieved the desired outcome if they had not given me the full freedom to use the laboratory and its valuable instruments during the research study.

I sincerely thank Prof. Seamus D. Garvey, Professor of Dynamics, Faculty of Engineering, Nottingham University, and Director of the Rolls-Royce UTC in Gas Turbine Transmission Systems, for his valuable suggestions on my research work.

I extend my gratitude to my doctoral committee members Prof. S. K. Diwedy, Prof. S Senthivelan and Prof. S. Talukdar for their valuable feedback and suggestions on my work. I want to thank faculty members and the office staffs of the Department of Mechanical Engineering, IIT Guwahati, for their assistance in carrying out this research work.

I am thankful to my fellow Ph.D. student Mrs. Firdausa Ahmed for her constant help and support in my Ph.D. journey. I would like to thank my past Lab mates Madhurjya Dev Choudhury, Dr. Gaurav Kumar, Dr. Shivarama Krishnan Natesan, Juan Choudhury, Syed Nayab Rasool and Ashutosh Kumar for having good technical discussion and help during my Ph.D. I would also like to thank Devarshi Kashyap, Dudul Das, Samar Das, Hirakjyoti Basumatary, Tapashi Kalita, Bhaben Kalita, Dr. Anupam Alok, Dr. Soumya Nanda, Masruddin Shaik and Saurav Dutta for accompanying me in this journey at IIT Guwahati. I would also like to thank Shahnawaz Ahmed, Dr. Debabrata Gayen and Sibananda Mohanty for their valuable support during my stay at IIT Guwahati.

I would also like thank Dr. Rosang Pongen, HOD Mechanical, NIT Nagaland, Dr. Thingujam Jackson Singh, Michael, Mahesh, Satya, Manikanta and the authorities of NIT Nagaland for their support in completing my thesis.

I have no words to acknowledge my wife, Mrs. Sanjita Basumatary who took it on her stride to manage all the domestic problems on her own for most of the period and

gave me all sorts of support without any complaints.

Kamal Kumar Basumatary

Abstract

Gas foil bearings (GFBs) has been considered as an alternative to traditional bearings in recent turbomachinery industries. However, the applications of Gas Foil Bearings have been narrowed due to low damping and nonlinear characteristics. Moreover, the presence of sub-synchronous and super synchronous frequencies introduces undesirable nonlinear effects to the system. This necessitates a non-conventional bearing system, which can overcome all these shortcomings. The current trend is to develop hybrid bearings which combines conventional bearing (GFB) along with active magnetic bearing as an electromagnetic actuator (EMA). The GFBs are used for normal operation and the magnetic actuator can be used for the improvement of the stability and the load capacity of the bearing. In the present study, a coupled dynamic model combining the dynamics of GFB and EMA has been developed. The fluid film forces from the GFBs and the electromagnetic forces from the EMAs are integrated into the equations of motion of the rotor. The developed model has been used to investigate the stability and unbalance response of the rotor supported on GFB. It has also been observed that the sub synchronous vibration which is dominating in conventional GFB, is eliminated using the hybrid GFB. Moreover, the hybrid GFB is capable of adapting to the sudden unbalance. It has also been observed that a high magnetic force is required to control the rotor for a set reference value other than the natural steady-state value of the response of the rotor supported by GFB without the effect of EMA.

Further, the cost of the combined bearing system will be much higher compared to its individual bearing. Therefore, in this work, a new electrical winding scheme for the electromagnetic actuators of the hybrid Gas Foil Bearing has been proposed. The new arrangement requires only two drives per bearing and the bias current has been provided (in the same set of windings) through a simple rectifier with small series choke and shunt capacitor. As the number of drives required is less, the proposed bearing will have low cost. Implementing the new approach, the force vectors are achieved using only two current-source drives whereas the usual conventional arrangement requires four such drives. The new control approach removes the usual constraint of bias current. With the knowledge of the state of the currents in the bearing and the bearing rotor position, the forces present in the bearing are calculated at any one instant, and the controller is updated at high rates.

Contents

List of Figures

List of Tables

List of Nomenclature

a_{cond} . . . . . Cross section area of the wire (m^2)

A_c . . . . . Required Coil Area (m^2)

A_p . . . . . Area of pole (m^2)

A_{slot} . . . . . Area of the slot m^2

A_v . . . . . Available Coil Area (m^2)

A_w . . . . . Coil Winding Area (m^2)

B_j . . . . . Magnetic Flux Density (T)

B_{sat} . . . . . Saturation flux (Wb)

C . . . . . Clearance (m)

e . . . . . Eccentricity (m)

$e_{x,y}$, $\bar{e}_{x,y}$ . . . . . Displacement of the rotor at the bearing location (m)

e_μ . . . . . Unbalance eccentricity (m)

E_{mag} . . . . . Magnetic energy stored

f_i . . . . . Iron ratio

F_{AB}, $\bar{F}_{AB}$ . . . . . Hydrodynamic force at the bearing locations A and B (N), $\bar{F}_{AB}=\frac{F_{AB}}{P_a r^2}$

F_{mag-AB}, $\bar{F}_{mag-AB}$ Magnetic force at the bearing locations A and B (N), $\bar{F}_{mag-AB}=\frac{F_{mag-AB}}{P_a r^2}$

F_{mag-x}, $\bar{F}_{mag-x}$. Magnetic force along X axis (N), $\bar{F}_{mag-x} = \frac{F_{mag-x}}{P_a r^2}$

F_{mag-y}, $\bar{F}_{mag-y}$. Magnetic force along Y axis (N), $\bar{F}_{mag-y} = \frac{F_{mag-y}}{P_a r^2}$

F_x, $\bar{F}_x$ . . . . . Hydrodynamic force along X axis (N), $\bar{F}_x = \frac{F_x}{P_a r^2}$

F_y, $\bar{F}_y$ . . . . . Hydrodynamic force along Y axis (N), $\bar{F}_y = \frac{F_y}{P_a r^2}$

G_{AB}, $\bar{G}_{AB}$ . . . . Gyroscopic matrix $(\text{Kg m}^2/\text{s}^2)$, $\bar{G}_{AB} = \frac{C\omega^2}{P_a r^2} G_{AB}$

$h, \bar{H}$ . . . . . Film thickness (m), $\bar{H} = h/C$

H_b . . . . . Height of the bobin (m)

H_{mag} . . . . . Magnetic field (A/m)

h_p . . . . . Height of the pole (m)

h_{s1} . . . . . Smaller distance between the two poles (m)

h_{s2} . . . . . Larger distance between the two poles (m)

i_0 . . . . . Bias Current (A)

I . . . . . Instantaneous current (A)

I_A . . . . . Current vector of half coil currents

I_B . . . . . Current vector of conventional AMB

I_C . . . . . Current vector of bridge configured AMB

I_M . . . . . Current vector of nine independent currents

K_d . . . . . Derivative gain (A s/m)

K_f . . . . . Bump foil stiffness $(\mathrm{N/m^3})$

K_p . . . . . Proportional gain (A/m)

l_{fp} . . . . . Flux path length (m)

L . . . . . Length of the bearing (m)

L_{AMB} . . . . . Axial length of the actuator (m)

L_C . . . . . Inductance

m . . . . . Number of nodes along θ direction

M_{AB}, $\bar{M}_{AB}$ . . . . Mass matrix (Kg), $\bar{M}_{AB} = \frac{C\omega^2}{P_a r^2} M_{AB}$

n . . . . . Number of nodes along Z direction

n_p . . . . . Number of poles

N . . . . . Number of turns

p,$\bar{P}$ . . . . . Pressure across the bearing, $(\mathrm{N/m^2})$, $\bar{P} = p/P_a$

P_a . . . . . Ambient pressure $(\mathrm{N/m^2})$

P_{cu} . . . . . Copper loss

P_m . . . . . Permeance (Wb/A-turn)

r . . . . . Radius of the bearing (m)

r_c . . . . . Radius of the back of the core (m)

r_j . . . . . Radius of the journal (m)

r_p . . . . . Radius of the pole (m)

r_r . . . . . Radius of the rotor (m)

r_s . . . . . Outer radius of the stator (m)

r_w . . . . . Radius of the wire (m)

R_c . . . . . Reluctance of the magnetic core (A-turn/Wb)

R_{coil} . . . . . Resistance of the coil

R_{HCP} . . . . . Resistance of single half coil

R_j . . . . . Reluctance of the rotor (A-turn/Wb)

R_m . . . . . Reluctance of the magnetic circuit (A-turn/Wb)

R_{NET} . . . . . Reluctance matrix

R_p . . . . . Reluctance of the poles

R_s . . . . . Reluctance of the core of the bearing

R_{S_0} . . . . . Reluctance of the air gap (A-turn/Wb)

S_0 . . . . . Air gap (m)

t,τ . . . . . Time (s), $\tau = \omega t$

t_b . . . . . Thickness of the coil casing (m)

t_{ins} . . . . . Thickness of the insulation on the coil (m)

t_p . . . . . Thickness of the top foil (m)

T . . . . . Temperature (K)

V_B . . . . . Voltage vector of conventional AMB

w_p . . . . . Width of the pole (m)

$W_{AB}, \bar{W}_{AB}$ . . . . Rotor weight at bearing locations A and B (N), $\bar{W}_{AB}$=$\frac{1}{P_a r^2} W_{AB}$

W_r . . . . . Winding resistance

W_w . . . . . Winding width (m)

x, θ . . . . . Circumferential co-ordinates of the bearing, θ=x/r

z, Z . . . . . Axial co-ordinates of the bearing, $Z = \frac{z}{L/2}$

Greek Symbols

α . . . . . Biasing ratio

β . . . . . Flux spliting

γ . . . . . Gas expansion exponent

δ . . . . . Pole angle

Λ . . . . . Bearing number, $\Lambda = \left(6\mu\omega/P_a\right)\left(r/C\right)^2$

μ . . . . . Dynamic Viscosity $(\mathrm{Ns/m^2})$

μ_0 . . . . . Permeability of free space (H/m) or $(\mathrm{N/A^2})$

μ_m . . . . . Permeability of the material (H/m) or $(\mathrm{N/A^2})$

μ_r . . . . . Relative permeability

ω . . . . . Angular Velocity $(\mathrm{rad/s})$

ϕ . . . . . Magnetic flux (Wb)

Φ . . . . . Flux vector

ψ . . . . . Fluid Film State Variable $\psi = \bar{P}\bar{H}$

Ψ . . . . . Flux Linkage

ρ . . . . . Density $(\mathrm{kg/m^3})$

List of Abbreviations

AMB . . . . . Active Magnetic Bearing

BCW . . . . . Bridge Configured Winding

EMA . . . . . Electro-Magnetic Actuator

GFB . . . . . Gas Foil Bearing

HCP . . . . . Half Coil Pair

PD . . . . . Proportional Derivative

PID . . . . . Proportional Integral Derivative

1

Introduction and Literature Review

Contents

1.1 Introduction

The development of rotating machinery has been an influential factor in the modern industrial revolution. This modern-day rotating machinery is exposed to severe kinds of mechanical and environmental conditions. Even with best design practices and most effective control methods, rotor vibration effects are so discreet and prevalent that occurrences of excessive vibration require attention. In this regard, bearings are recognized as one of the significant components of the rotor-bearing system and one of the influencing factors governing the vibration characteristics of rotating machinery. Modification of bearings is also one of the economical and efficient means for improving the dynamic performance of a rotating machine. Furthermore, an unconventional bearing is necessary for high performance rotating machines system for stable and reliable operation.

Gas Foil Bearings (GFBs) has made a remarkable influence on the modern oil-free turbomachinery propulsion and energy systems by increasing the reliability and mechanical efficiency. GFBs are currently employed in air cycle machines and auxiliary power units of aircraft. Few applications in which GFB has proven to be a potential alternative are the high-speed dental drills, fuel cell compressors, microturbines and pumps, cryogenic turboexpanders and turbochargers, single-use turbojet engines for missiles, reusable target drones and unmanned vehicles. Computer peripherals, like, read and write heads, high packing density magnetic memory devices, including tapes, disks, and drums, are practically possible due to the implementation of gas lubrication. Although the working fluid is generally the air, inert gas like helium and xenon also commonly used. Moreover, the use of refrigerants, liquid oxygen, and liquid nitrogen are also been reported [1]. Therefore, the use of different process fluid makes the application of GFBs over a wide range of temperatures. As the oil lubricating system is removed, The overall weight of the system gets reduced due to the removal of oil lubricating system. This in turn improves the performance and also reduces the maintenance cost.

Magnetic Bearings are also an oil-free technology, have the advantage of operating at both zero and even at high speed. The contactless operation and absence of mechanical wear make it suitable for vacuum, clean operation with lower maintenance cost and longer lifetime. The absence of lubrication seals allows the larger and stiffer rotor shafts. Magnetic bearings are currently employed in flywheels of space applications for energy storage, watthour meters, high-speed centrifuges, blood pumps, microelectronics [2].

It has been observed that AMBs and GFBs share many common characteristics, and hence a combination of this two oil-free technology has been popular among the

researchers. Therefore, a hybrid bearing that synergy the advantages of the two oil-free bearings is a decent possibility. Rotors supported on these hybrid bearing will have enhanced performance over a wide range of operating conditions. The capability of AMBs to apply controllable forces will help to reduce the hitches arising out of unbalancing and loading conditions and thereby increase the performance of the machine.

1.2 Basics of Gas Foil Bearing

Gas foil bearings are different from the rigid surface gas bearing since it consists of a top foil and an underlying flexible foil structure beneath it [3]. The top foil is a thin plane surface held over a series of underlying substructure acting as flexible support. The flexible foil structure supports the top foil, which in turn supports the rotor. The substructure is also helpful in providing the necessary passage for the flow of the cooling air. However, sliding friction occurs between the top foil and the underlying sub-structure and generates coulomb damping between the bump foil and sleeve, which can cause instability in the system [4].

1.2.1 Working Principle

The working principle of the GFB is the same as the principle of air or gas bearing, where the hydrodynamic pressure is the primary load-carrying function. The physics of the generation of hydrodynamic pressure can be understood from the hydrodynamic theory of lubrication as shown in Fig. 1.1(a). Considering two inclined surfaces separated by a lubricating film and one of the surface moves relative to the other surface, a different type of the velocity distribution can be observed. It can be clearly observed that there is a discontinuity in the flow continuity. Since the flow has both pressure induced and velocity induced component, and the continuity of the flow has to be satisfied. Therefore, the discontinuity in the velocity leads to the generation of pressure between the two surfaces. In any of the journal bearing, an eccentric condition is observed between the bearing center and the journal center due to the weight of the rotor or external load forming a wedge. As a result, a hydrodynamic pressure generated, as shown in Fig. 1.1(b). As the speed increases, the pressure increases, and when the lift-off speed is reached, the journal becomes completely airborne supported on the hydrodynamic air film pressure.

In bump-type foil bearings, the top foil is supported on a flexible substructure called the bump foil, which deforms elastically under the hydrodynamic air film pressure

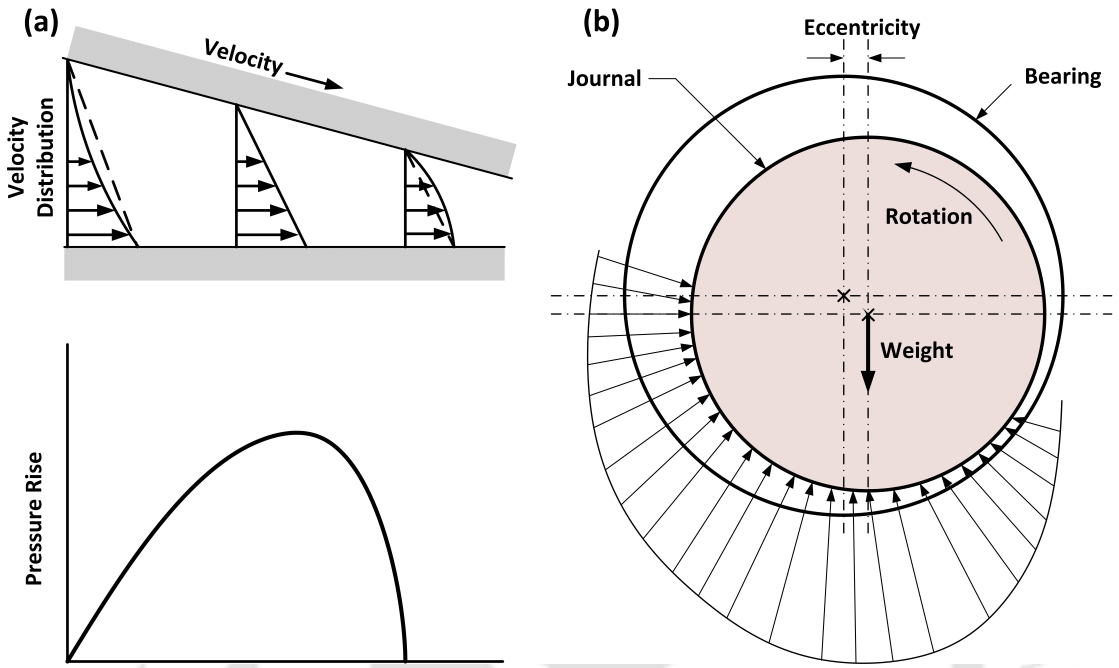

Figure 1.1: Generation of Hydrodynamic Pressure [1]

generated due to the rotation of the journal (Fig. 1.2). The deformation of the foils drags the air between the top foil and the journal creating a film thickness larger than the film thickness in the rigid gas bearing. Moreover, the underlying sub-structure has the capability of accommodating the shaft run-out, misalignment, minor thermal growth, and centrifugal growth of the journal.

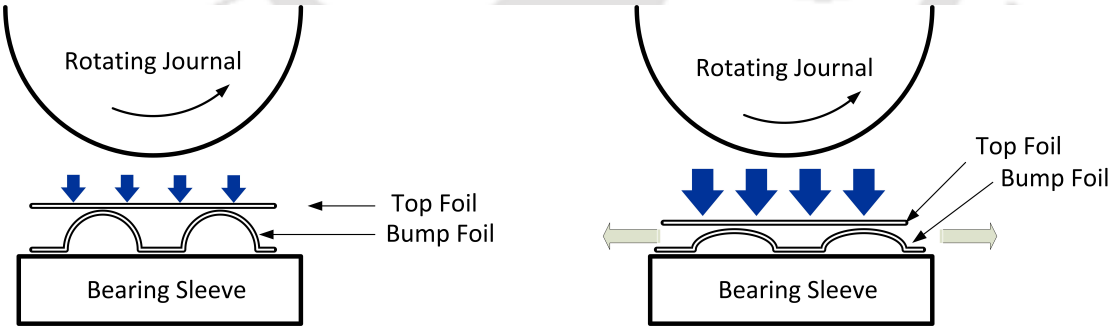

Figure 1.2: Foil deflection due to Hydrodynamic Pressure [5]

1.2.2 Manufacturing Aspects of GFB

There has been a limited number of literature available on the manufacturing know-how of the GFB. The GFBs are mainly the assembly of the three components which are the top foil, the bump foil, and the bearing sleeve. The essential elements in the manufacturing

process of GFBs consist mainly of the four steps [6].

1. **Material Selection**

   The performance of the GFBs is greatly affected by the compliance of the underlying bump foil and the top foil, which in turn is dependent on the material and geometry of the foils [7]. The limitations of the material will affect the overall performance of the bearing. Therefore, choosing the proper foil material is essential in the design and application of the GFBs. The foils should necessarily be able to offer compliance, endure the temperature difference, and provide the required damping at the supports. In general, Inconel has been used because of its satisfactory modulus of elasticity and its ability to withstand elevated temperature [8–10]. On the other hand, for low temperature operation, a cheaper alternative could be stainless steel. However, they are sensitive to certain coatings [6]. Further, the top foil and bump foil made from chromium molybdenum steel have also been reported which could operate at 157°C-188°C [11, 12]. The Beryllium-Copper alloy exhibits self lubricating properties and better metal working properties, which was exploited to manufacture the bump foils by Xu et al. [13] and Kulkarni et al. [14]. However, the exposure to Beryllium could lead to health issues limiting its use in specific foil bearing applications. The estimation of load-carrying capacity with different top foil materials of GFBs has revealed that carbon fiber reinforced composite material as a promising material compared to structural steel and copper [15].

2. **Shaping of Foils**

   The annealed foils first have to be cut into the required dimensions. In order to cut the foils, simple shearing processes are not recommended as it results in edge distortion in the foils. Therefore, using the wire electrode discharge machining (EDM) technique, the foils are cut in the required shape [16]. The cutting operation is followed by a pressing operation. The bumps foils of desired pitch and variations are pressed inside a corrugated die with the necessary foil geometry. Thus the contour of the bump die is impressed on the bump foil, irrespective of the thickness of the bump foil used. Therefore, the die has to be manufactured from a heat resistant alloy usually, Inconel steel, which allows the die to resist thermal fatigue. The foils are then rolled around a mandrel to get the required curvature and diameter. One of the significant problems with the cold forming of the foils is the spring back effect, which can produce inaccuracy in the foil geometry. Therefore, the die has to be manufactured with perfection to provide an excellent surface finish, which in turn is reflected on the foils.

3. **Heat Treatment**

   The heat treatment process is significantly dependent on the foil material and the state of the shaped material. Nevertheless, several heat treatment processes are available for any material. However, for foil bearings, the heat treatment process should result in high spring properties and fatigue resistance. These properties are required for the foils to function as a compliant structure. In this regard, DellaCorte et al. [17] described a few of the possible heat treatment processes for Inconel X-750 foils. Further, in the case of Stainless Steel, the heat treatment of the shaped foils reduces the residual stress after the cold working. The main difference between the heat treatment process of the Stainless Steel and the Inconel is the fact that the heat treatment of Stainless Steel is done inside the pressed die, because the Stainless Steel available in the market is partially hardened, while the annealed Stainless Steels are not heat treatable for hardening purposes [6].

4. **Coating**

   At low speed i.e., before the formation of the hydrodynamic pressure film and during start-up and shut down, GFBs encounter wear and generate a high amount of heat due to friction in the top foil [18]. Moreover, during bearing overloads, the hydrodynamic film fails, and the top foil suffers wear and tear. Therefore, an advanced coating system has to be implemented for compliant foil bearings for higher operating speeds and temperatures [19, 20]. In this regard, DellaCorte et al. [21] suggested a coating of PS304 with a sacrificial layer of MoS_2 to the shaft and Al-Cu coating to the top foils to increase the load-carrying capacity and minimise wear during repeated high temperature start/stop operation. Heshmat et al. [20] demonstrated the efficiency of Korolon^{TM}coating. The top foil was coated with a combination of Korolon^{TM}1350A and Korolon^{TM}800. Moreover, a thick coating of chrome was applied to the journal surface, which reduced the friction coefficient and wear during start up and shut down [20, 22]. Lubell et al. [23] improved the coating process and optimised the composition of PS304 for better characteristics of the foil bearing. Heshmat et al. [22] further suggested a nickel chrome based coating as an alternative of PS3O4 for the operation of foil bearings up to 820°C.

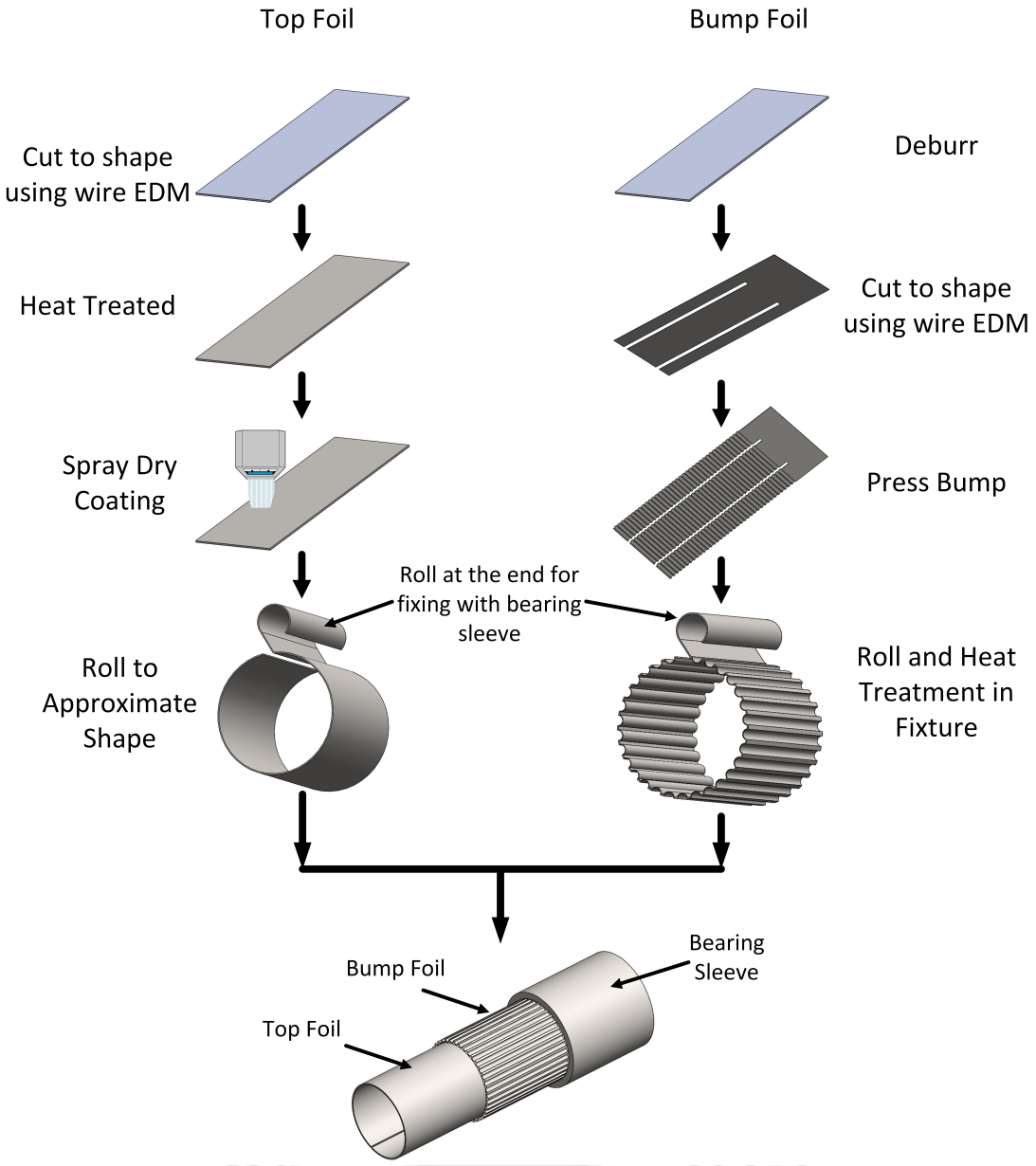

Figure 1.3: Foil bearing fabrication procedure [16]

1.3 Basics of Active Magnetic Bearing

Magnetic Bearings are the bearings that use magnetic forces to provide support (levitate) to any ferromagnetic object without any mechanical contact. Based on the physical cause of the magnetic field involved, the magnetic bearings are classified as reluctance force bearings and Lorentz force bearings [2]. The reluctance force is the force produced due to the difference in magnetic permeability of the two materials in the presence of a magnetic field while the Lorentz force is produced due to the movement of charges in a

magnetic field. As the name suggests, Lorentz force bearings operate on the principle of Lorentz force. Due to the ability to produce both rotary torque and levitation torque using the Lorentz principle, the Lorentz force magnetic bearings are commonly employed in self bearing motors.

Further, based on the control method applied, the magnetic bearings are classified into the active magnetic bearing (AMBs) and passive magnetic bearings (PMBs) [24]. In AMB, the reluctance force is produced with the help of an electromagnetic stator, which controls the ferromagnetic rotor. Power amplifiers are required to supply the necessary currents to the electromagnets for controlling the rotor. In addition to these, displacement sensors are required to provide feedback of the rotor position. On the other hand, in the case of passive magnetic bearings, the magnetic forces produced by the interaction of permanent magnets. Although passive magnetic bearings are relatively cheap and lightweight, it has lower load capacity and poor dynamic properties. Moreover, using an AMB one can have active control over the dynamics of the rotor-bearing system which can be used in vibration isolation and passing critical speeds. However, the saturation properties of the electromagnet core material limit the static and dynamic load capacity of the AMBs. To generate an equivalent load-capacity compared to conventional hydrodynamic bearing, the size has to be very large. The windage from the rotor is also a limitation to the high speed of rotation.

1.3.1 Working Principle

In general, the reluctance force is generally employed in AMBs. In Fig. 1.4(a), the working principle of the AMBs is shown. When the electrical coil wound around a ferrous core (electromagnet) is energised with a current, the ferrous object is attracted towards the electromagnet [25]. The reluctance force is generated due to the magnetic flux in the air gap while the currents in the coils regulate the flux. The attractive force exerted on the rotor mainly depends on the current in the electromagnet and the air gap between the electromagnet and the rotor. The attractive magnetic force, increases as the air gap decreases. However, the weight of the rotor, does not change with the increase or decrease of the air gap. Therefore, if the rotor gets close enough to the electromagnet, the attractive magnetic force overcomes the weight of the rotor, and the rotor will stick to the electromagnet. Conversely, if the air gap is large, the weight of the rotor becomes more significant than the magnetic force, F_{mag} produced by the electromagnet and the rotor falls to the ground.

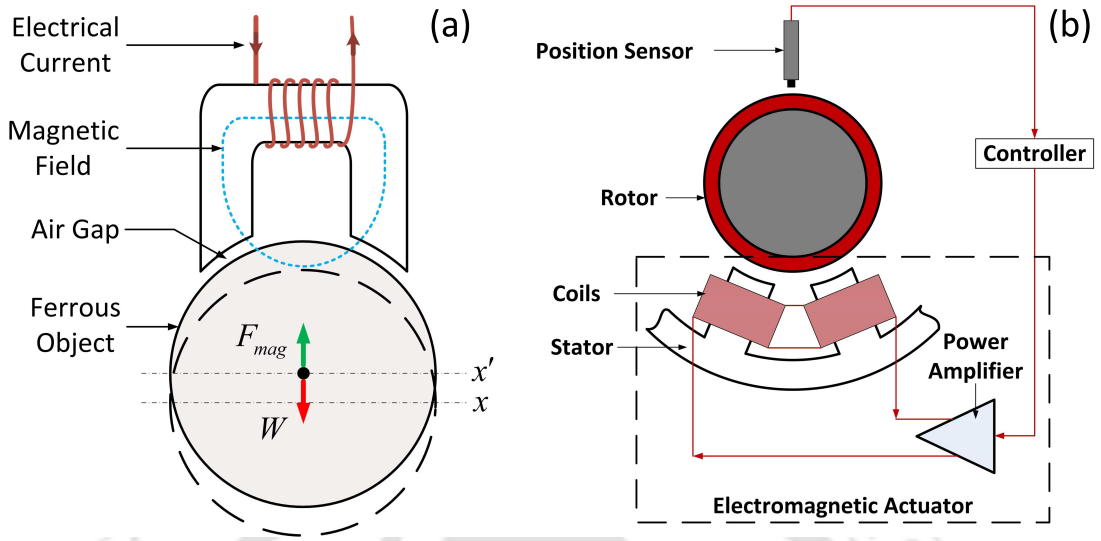

Figure 1.4: Working principle and Components of AMB

Therefore, active control over the rotor position is necessary in the case of magnetic bearings. At any instant, the position of the rotor is measured using a position sensor. The signal from the position sensor is then fed into the controller, which controls the rotor in the desired position. The controller then directs the signal to a power amplifier, which transforms the signal into the electric current in the electromagnet, thus generating the desired magnet force F_{mag}. Figure 1.4 shows the basic components of an active magnetic bearing. The components are briefly described below [26]:

1. **Sensors**

   One of the essential components of the magnetic bearing is the position sensor. The characteristics of the position sensors have a significant effect on the performance of the magnetic bearings. The sensors must be contact-free and able to measure the position of a rotating body. Hence, the geometry of the rotor at the sensor location significantly affects the accuracy of the signal. Therefore, noise and disturbances will be produced from a bad surface. In addition to it, the rotational frequency or the multiples of its frequency may also get affected due to the errors in the geometry. Moreover, depending on the application, different sensors are used to measure the rotor speeds, currents, flux densities, and temperatures of the magnetic bearing systems. Therefore, while selecting the sensors, factors such as measuring range, sensitivity, resolution, and frequency range of the sensors have to be taken into account depending on the application.

2. **Controller**

   Active magnetic bearings are a mechatronic product, and for a mechatronic system,

the controller is an indispensable part. In order to apply the desired force to the shaft accurately, the controller has to be designed appropriately. The main aim of the controller is to coordinate the transformation of sensor signals required by the control algorithm and generate control current according to the control algorithm. A control algorithm can be implemented using either analog, digital, or hybrid controller. Although the Proportional Integral Differential (PID) controllers are most commonly used in the industries, different control algorithms are also being experimented on rotors equipped with active magnetic bearings [27].

3. **Power Amplifiers**

   The control signals are converted to the control currents using the power amplifiers. The power amplifiers are the primary source of losses in the AMB, other than the bearing magnets. Therefore, these losses must be kept low for obvious reasons. There are two main types of power amplifiers, namely, analog amplifier and switching amplifier. The analog amplifiers are simple in structure and are generally used for sensitive applications or where the low power is required. On the other hand, switching amplifiers are used in high power applications. Although a high remagnetization loss is induced due to the eddy currents from the switching, it is significantly more efficient than an analog amplifier. Thus the switching amplifiers are most extensively used for industrial applications because of their low losses. The switching amplifier switches the fixed voltage very fast so that the average current of output and input voltage remains proportional. The output transistors are either "on" or "off". In general, four transistors are employed in one amplifier channel to form an H-bridge, as shown in Fig. 1.5 [28].

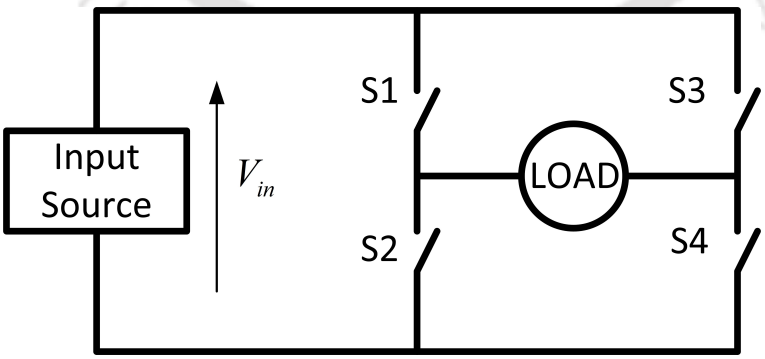

Figure 1.5: H-Bridge [28]

4. **Rotor**

   In general, the rotor is constructed with electrical steel lamination on a non-magnetic shaft. They laminations improve the generation and maintaining the magnetic fields

while reducing the hysteresis loss. Tight manufacturing tolerances are required to avoid unbalances. Moreover, to prevent centrifugal stress due to high speed rotation, the rotor lamination is required to have good mechanical properties.

5. **Stator**

   The stator is the non-rotating part of the magnetic bearing mounted on the machine housing. The stator consists of the iron core and generates the magnetic field. The material of the iron core conducts the magnetic field to the air gap. The magnetic permeability, as well as the magnetic saturation of the iron core, has to be high with minimal eddy current losses [26]. Therefore, to minimize the Eddy current loss, the core is usually made of insulated lamination sheets.

6. **Winding**

   The current passing through the coils wrapped around the iron core is the source of the magnetic field. The current determines the amount of magnetic force generated. Therefore, the coils which have a good electrical property, reliable electrical insulation, and high heat transfer capabilities are choosen to improve the efficiency of the AMB [26]. The number of turns in the winding is in general, dependent on the amount of magnetomotive force required. The winding scheme describes in what way the coils are wounded around the poles while the connection scheme describes in what way the single coils are connected to each other. The winding schemes are dependent on the type of magnetic bearing and the selected driving mode. The winding arrangement is made to reduce the remagnetization of the rotor upon rotation [2].

1.3.2 Structural Configurations of AMBs

Based on the magnetic polarities observed as the rotor rotates, there are two primary configurations of radial AMBs, namely heteropolar and homopolar [2]. In heteropolar AMBs, all the magnetic flux is restricted to a plane perpendicular to the axis of rotor rotation. Thus having alternate polarity in magnetic poles around the rotor, as shown in Fig. 1.6(a). Heteropolar AMBs are commonly used because of its simplicity and low cost. On the other hand, in the case of homopolar AMBs, some portion of the magnetic flux is allowed to pass axially along with the rotor and stator. Thus it is possible for all of the poles in a given plane to have the same polarity as shown in Fig. 1.6(b). The alternation of polarity occurs along the axial of the rotor. Homopolar AMBs experiences less variation of the field around the circumference, which in turn reduces the Eddy

current loss occurring due to the rotation of the rotor.

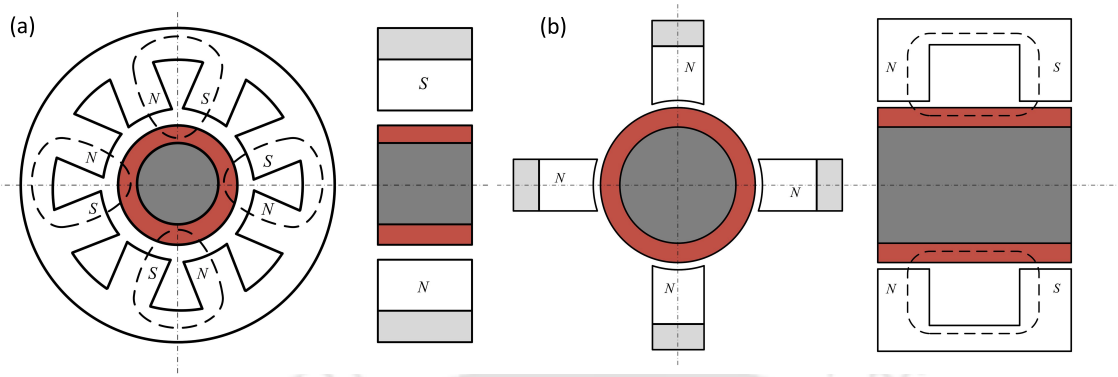

Figure 1.6: Configuration of radial AMBs [2]

1.4 Literature Review

The literature gives a brief description of the historical developments on the GFBs. The numerical models used in the modelling of GFBs have also been discussed. The literature also discusses the combination of gas bearings with other types of bearings. Therefore, the literature review is divided into the following sections and are discussed individually:

1. History of Foil Bearings
2. Types of Foil Bearings
3. Numerical Prediction Methods of Foil Bearings
4. Hybrid Gas Foil Bearings

1.4.1 History of Foil Bearing

In 1953, the phenomenon of hydrodynamic air film pressure was first observed in the tape recording industry. It was observed that at high rotating speed, the magnetic tape which passed over the recording heads lost its contact with the recording surface. The loss of contact resulted in poor recording quality. Therefore, a year later, Baumeister of IBM patented a device that reduced the tape float [29]. Further, Gross developed a mathematical model of the tape float and suggested the use of gas film pressure in the hydrodynamic bearings [30]. This concept fascinated NASA and the Office of Naval Research. Thus, encouraging Gross to develop a foil bearing for reliable high speed and high-temperature applications. Gross demonstrated the use of gas-foil bearing into the high-speed turbomachinery, such as high-speed gas circulators and compressor-turbines

for cooling gas-filled nuclear reactors. NASA's Brayton cycle turbo-alternator-compressor was the first to employ tension-type gas foil bearings which previously employed pivoted-shoe gas bearings. In the foil bearing, thin metal foil under tension was used to create the hydrodynamic wedge and support the rotor. The pivoted-shoe gas bearings were prone to instabilities because of its low damping, but due to the implementation of the gas foil bearing many of the rotordynamic issues in NASA's Brayton was fixed. Thereafter, in all of the subsequent units of the Brayton cycle of NASA, gas foil bearings were used [31].

In 1969, Garrett AiResearch obtained a breakthrough in utilizing the foil bearings in the air cycle machines. GFBs was first implemented in the environmental control system of McDonnell Douglas DC-10. Thus, due to the development and implementation of gas foil bearings, the Garrett AiResearch took the market of manufacturing the air cycle machine in aircraft applications. In the early 1970s, Hamilton Standard partnered with Mechanical Technologies Incorporated (MTI) entered the gas-foil bearing market with their patented bump-type gas foil bearing design called the "Hydresil" [1, 18, 32]. The Hydresil bearing had a similar load carrying capacity as that of the AiResearch's bearings. However, the damping capacity was low. During the test flights, the Hydresil bearings used in ACMs survived between 4 and 50 hrs., before failure. In later years, Hamilton designed its foil bearings and succeeded in taking the market of ACMs in fighter and commercial aircraft as well as in military tanks [1, 18, 33]. In a parallel development, the foil bearings were tested for high speed and temperature in automotive gas turbines in order to replace the internal combustion engine in passenger vehicles. Therefore, it was found that the gas foil bearings could replace the oil-lubricated bearing in the power generation. Further, in the 1980s, Capstone Turbines, a branch of Garrett AiResearch, became the lead manufacturer of the oil-free microturbines [18, 33].

Following this, from the year 1995, NASA's Oil-Free turbomachinery team, MTI, Mohawk Innovative Technology Incorporated, Schwitzer Corporation, and Caterpillar began developing a completely oil-free turbocharge. Thus, the revolution of oil-free turbomachinery started, and the gas foil bearings expanded its application in new industries. The tested foil bearing could be operated at speeds up to 120,000 rpm and also functioned at 650°C (12000°F). NASA's Oil-free turbocharger introduced its bump-type foil bearings in 1999 [33, 34]. Thus, in the last five decades, the foil bearing technology has almost reached the matured state in various oil-free turbomachinery applications. It became the critical component in air cycle machines, auxiliary power unit, closed Brayton cycle, cryogenic turboexpanders and compressors as well as automotive turbochargers.

1.4.2 Types of Foil Bearings

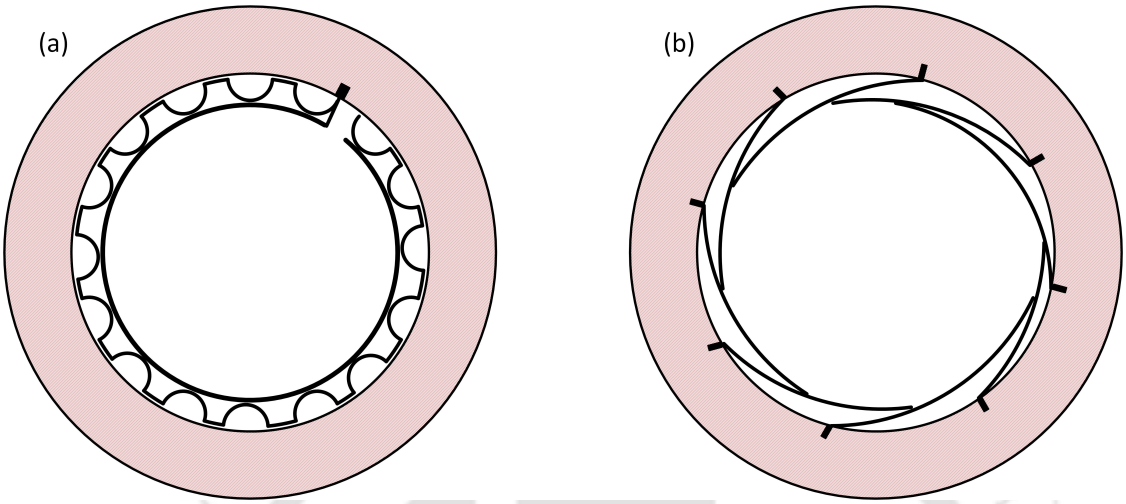

Figure 1.7: Foil Bearing Configurations

Due to the increasing demand for high speed and reliability, the gas foil bearing had to undergo tremendous design modification over the years. The tension-type of foil bearing was the first type of gas foil bearing. In tension-type gas bearing, the hydrodynamic pressure is formed in between the shaft and a thin metal foil forming three arcs. The tension-type bearing could accommodate misalignment and provided better tolerance in case of geometric anomalies. However, it had low load-carrying capacity. Therefore, a more improved design was required [1, 31, 33]. The static and dynamic performances of the GFBs are depended mainly on the properties of the underlying sub-structure. Therefore, several configurations such as bump type, leaf type etc. of the underlying sub-structure have been investigated. One of the foil bearings is the bump foil bearing, which had better performance and provided ease of manufacturing. The basic configuration of the bump-type foil bearing consists of metallic bump strips and a metallic top foil inside a rigid bearing housing [34]. The stress in the bump foil provides the load-carrying stiffness while the majority of the damping is provided due to the relative motion of the top foil and bump foil. In order to increase the load capacity, a different configuration of the bump foil bearing has been developed. Most of the variation in the foil bearing design is developed by MTI, AiResearch, and Hamilton Standard. In the Generation I type bump foil bearing the bump foil is symmetric in both axial and circumferential direction. In Fig 1.7a, the Generation I bump foil bearing has been shown. Generation II type bump foil bearings could modify the bump foil in axial as well as circumferential direction to alter the stiffness characteristics of the bearing. Further, the Generation III type bump

foil bearings, the bump foil was varied in axial and circumferential directions to improve the performance [17, 35]. Moreover, in Generation III type foil bearings often a third foil layer is added in between the top and bottom foil to provide additional stiffness to the top foil and more rigidity in between the peaks of the bump foil layer and also increases bearing damping due to the relative foil layer movements [1].

Heshmat et al. [36] suggested single-pad gas foil bearings configuration with sputtered copper elements for higher load carrying capacity and the three-pad gas foil bearings with variable stiffness gradient for whirl instability. The single pad foil bearing was modified by circumstantially splitting the bump foil along the axial length of the bearing, which provided enhanced alignment and axial compliance to the bearing.

Heshmat [7] introduced a multistage bump foil bearing to vary the stiffness gradient in both radial and circumferential directions. The convergence or lobing effect of segmented bump foil changes with load and becomes more prominent at higher speeds. It has been observed that for a better stabilizing effect, the convergence has to be more prominent. Therefore, at high speeds, improved stability is observed.

Further, gas bearings consisting of more than one segmented top foil without the bump foil, while overlapping the nearby segmented foil has been invented [1, 35, 37]. In general, three to six segmented foils are present, depending on the diameter of the bearing. In Fig 1.7b, a typical multi-leaf gas foil bearing has been shown. The multi-leaf foil bearings have high bending resiliency, which reduces the shaft vibration. However, due to low stiffness, the multi-leaf foil bearings have smaller load supporting capability [8]. The bump-type foil bearing has higher load carrying capacity due to high stiffness but has a limited resiliency. Heshmat and Heshmat [38] also incorporated a strip of backup springs beneath the foils in a multi-leaf foil bearing. Using the spacer keys, the compliant multi-leaf foils were attached to the bearing housing. The addition of the backup springs improved the load-carrying capacity of the conventional multi-leaf bearing.

In another advancement, a multideck gas foil bearing consisting of multiple layers of bumps has been developed [39,40]. In the protuberant foil bearing, the compliant structure is hemispherical dimples instead of the axial bumps [40]. The deformation of the top foil was increased in the protuberant foil, due to which minimum film thicknesses were higher, which in turn resulted in lower frictional torque. Hou et al. [41] used multi-decked protuberant foil as an elastic support structure for developing a new kind of GFB. The amplitude of vibration was minimized due to its multi-layered elastic sub-structure. The sub-synchronous vibration was also found to get reduced at high speed.

Further, a different approach for the compliance of the foil has been achieved using

wool-like metal mesh [42]. The damping capabilities of the metal mesh foil bearing was found to be higher when compared to the damping capabilities of the bump type foil bearing. Although the metal mesh bearing required higher frictional startup torque, lower lift off-speed was required. Moreover, it was also observed that the stiffness of the metal mesh bearing is less dependent on the frequency, unlike that of a bump-type foil bearing.

In another invention, the top foil was supported using a series of horizontal compression springs. The spring encased in a rigid shell followed the same orientation of the bump in the Generation I type foil bearings [43]. Therefore, as the spring contracts and expands due to pressure in top foil, the bearing structural stiffness is developed. An essential advantage of the compression is that each spring can be tailored made to vary the required stiffness around the circumference of the bearing. Moreover, as each spring is independent of each other in their individual shell, the influence of circumferential stiffness is absent, which is otherwise present in case of bump-type foil bearing. It was also demonstrated that the compression spring foil bearing had high nonlinear stiffness, while no increase in onset of instability was observed. However, the orbit of the rotor at the critical speed was within the limit to cause any damage to the rotor bearing system.

Kim et al. [44] developed a theoretical model for double bump foil bearings. The first layer is more elastic, while the second layer delivers higher stiffness. The top foil layer is activated at the initial stage of applying the load. The upper layer is deflected to discharge the load. If a heavier than designed load is applied, the second, stiffer layer is activated.

Feng et al. [45] developed a multi-cantilever gas foil bearing in which a series of foil cantilever supports the top foil. In the loading condition, the cantilever foil slides through the rigid backing shell and provides the required damping. The investigation revealed that in multi-cantilever bearing gas foil bearings, a large amount of nonlinear static stiffness is present, and the dynamic stiffness is mostly dependent on the frequency. It was observed that at low frequency the dynamic stiffness is small, but increases with the increase in frequency.

Lee et al. [46] combined multi-leaf foil bearing and bump foil bearing to develop a new hybrid foil journal bearing. The multi-leaf foil increased the resiliency of the hybrid bearing while bump foil acted as the stiffeners. Therefore, the hybrid bearing had high damping as well as high load capacity.

Further, Lee et al. [47] introduced piezoelectric actuators beneath the top foil for better stability and load-carrying capability. By the application of voltage to the piezoelectric actuators, the dynamic coefficient of the smart foil bearing could be increased whenever required. The working principle of a controllable gas foil bearing with piezoelectric

materials have been described by Park and Sim [48]. The clearance of the bearing is controlled using the piezo stacks. As a result, the fluid-film thickness and pressure get altered, which in turn have a great effect on the bearing dynamic coefficients.

Lee et al. [49] inserted a viscoelastic foil between the top foil and bump foil, which enhanced the dynamic coefficients of the bump foil. It was observed that the viscoelastic foil further improved the structural damping and reduced the bending critical speed.

Kim and Andrés [50] investigated the performance of GFB supported on piecewise linear elastic supports. A second bump strip or stop pin was inserted below a series of bump foil. The less stiff bump foil is placed on top while the more rigid bump foil constitutes the lower bump foil. This design provided tailor-made rotor dynamic coefficients as the second bump foil provided an additional source of energy dissipation. However, the cost of fabrication and complexity in assembly is increased.

Sim et al. [51] inserted three metal shims in between the bump strip layers and bearing housing. The shims acted as preloads and enhanced the generation of hydrodynamic pressure in the clearance. Moreover, the amplitude of sub-synchronous vibration was reduced significantly for the modified configuration.

Swanson and O'Meara [52] invented a new wing type foil bearing. The multidimensional array of multiple, formed, cantilever "wing foil" tabs formed the support element. The vibrational energy could be dissipated using the wing foil. The tabs can readily change their height and stiffness distribution. Moreover, the foil wings can be produced from a wide range of materials.

Recently, Sadri et al. [53] suggested an adaptive 3 pad air foil bearing, in which the bearing bore clearance could be changed depending on the operating conditions. Piezoelectric actuators are employed to change the compliant supports.

Recently, Feng et al. [54] proposed a novel gas foil journal bearing with taper-groove in the top foil. The results showed that the new arrangement helped in providing multi-extra local dynamic pressure and decrease the gas end leakage. Thus an improvement in static and dynamic properties could be observed. Moreover, the load capacity and direct stiffness were increased with the increment of groove depth

Most recently, Feng et al. [55] developed a GFB with shape memory alloy springs beneath the top foil. The stiffness of the shape memory alloy springs could be modified by controlling its temperature. The temperature could be monitored and controlled using a carefully designed electric heating and cooling system. The cooling method provided the circumferential and axial cooling flow to control the phase transformation temperature of the SMA springs. They demonstrated that substantial improvement in safety and

performance could be achieved with proper distribution of shape memory alloy springs.

1.4.3 Numerical Prediction Methods of GFB

The dynamics of a rotor system is significantly dependent on the characteristics of the bearing. Therefore, it is essential to understand and predict the behavior of the bearing under different operating conditions. A mathematical model thus helps in the numerical predicts of the rotor-bearing system. In this regard, in the case of hydrodynamic gas foil bearing, the first step is to determine an efficient method to solve nonlinear Reynolds equation for compressible flow. Then the foil deflection and deformation has to be incorporated and solved, to accurately predict the behavior of the gas foil bearing.

Ruscitto et al. [18] presented a model for Generation I foil bearing and validated it with the experimental results. The model showed good agreement in predicting the minimum film thickness. However, when the applied load was above 60N, the attitude angle showed lesser value. The stiffness and damping coefficients were predicted as functions of the excitation frequency.

Heshmat et al. [56] first used analytical equations in order to find the performance parameters of the foil bearings. He assumed the fluid film to be isothermal and perfect gas. The underlying sub-structure was considered to be linear without sagging between the top foil and bump foil. Moreover, the structural stiffness was assumed to be evenly distributed, while the deflection is solely dependent on the local forces. The non-dimensional Reynolds equation was coupled to film thickness and discretized using a finite difference equation. The boundary conditions were applied accordingly to capture the lift-off pressure of the top foil. Further, Ku and Heshmat [57] theoretically investigated the deformation of the bump foil under a given load distribution. Although the theoretical model considered the friction forces, variable load distributions, and the bump foil geometries, the top foil sag was neglected. Moreover, it was assumed that the concentrated load was applied to the top center of the bumps with no deflection of the foil segment between the bumps. The deformation was also considered constant and uniform in the circumferential direction. The results of stiffness and deflection of the bumps from the numerical followed similar trends with the experimental data. DellaCorte and Valco [35] introduced a simple empirical method in order to approximate the bearing loads for various types of foil bearings. They established that the bearing load capacity is dependent on the axial length and diameter of the bearing, as well as the speed of the rotor. DellaCorte et al. [3] further presented a performance map, an analogy of the Stribeck curve

for the foil bearing, based on the modified Sommerfeld number and the thermal power generation. Thus, in initial years, this map has been used as a reference or guidelines for designing foil bearings for safe operation. DellaCorte [58] calculated the stiffness and damping coefficients of the foil bearing using simple equations, which he derived from the empirical results. This estimation helped enormously in the design of the foil bearing.

Peng and Carpino [59] predicted the stiffness and damping coefficients assuming the gas to be perfect while ignoring the Coulomb friction between the foil and elastic support. The Reynolds equation was perturbed, and the finite difference method was used to discretized it, thus obtain the linearized dynamic coefficients of the elastically supported foil bearings. Further, Peng and Carpino [60] extended the theoretical model by incorporating the Coulomb damping in the foil structure model. This model demonstrated the significance of the Coulomb damping in the overall damping of the bearing. The Coulomb friction is mainly necessary when the speed, as well as the stiffness of the fluid film increases. Carpino and Talmage [61] developed a fully coupled finite element model for the top foil supported on radial springs. The model combined the structural deflections of the top and the bump foils with the fluid film pressure into a single finite element. Different physical models of the bump foil structure and the top foil can be implemented along with the fluid film model for the accurate prediction of the foil bearings. In this regard, Peng and Khonsari [62], developed a model that incorporated the compressibility of the air in the calculation of the pressure as well as the compliance of the underlying structure. The model predicted the load capacity, similar to the experimental results described by Heshmat [7].

Kim and San Andres [50,63,64] developed a simple physical model in order to predict the static and dynamic properties of the foil bearing. The Reynolds equation was coupled with the deflections of the top and bottom foil, assuming a simple elastic foundation model for the top and bottom foil. Further, using a finite element model to combine the elastic deformation of the top foil and the bump foil, the stiffness and damping coefficients for various parameters were predicted. A thermohydrodynamic model for predicting the performance of the gas foil bearing has also been developed [65]. Howard and San Andres [66] developed XLGFBTH, a foil bearing predictive tool at Texas A & M. The predictive tool allowed to separate the sub-structure stiffness distribution from the primary analysis in order to change to the geometry of the bearing.

Iordanoff et al. [67] presented coupled the simplified equation of the motion with the Reynolds equation and foil assembly model using a non-linear model. Their work showed that the dynamic behavior of the foil bearings could be increased by optimizing

the friction between the foils. Further, Knowels [68] used numerical algorithms to analyze the influence of foil thickness on the load capacity and power loss of the foil bearings.

Feng and Kaneko [69] developed an analytical model of bump type gas foil bearings that included the effects of local deflection of the top foil, friction forces of the various contact surfaces, the elasticity of the bump foil, and the interaction forces between the bumps. The top foil was modeled using shell elements, while the bump foil has been modeled as two rigid links with a radial spring between them.

Bensouilah et al. [70] included the dynamic deformations of the foil in their model. A simple elastic foundation model with uniform stiffness was used to model the bottom foil. The stiffness and damping coefficients for the given bearing properties and operating conditions were predicted using the perturbation method. The finite difference method was used to discretize the perturbed dynamic equation while Galerkin's finite element formulation was used to discretize the nonlinear stationary Reynolds equation. Further, the principle of superposition was implemented to combine the two solutions. It was demonstrated that the stiffness and damping coefficients get reduce due to the dynamic deformation.

Lee et al. [71] simulated an actual gas turbine configuration using a 3D thermohydrodynamic model of a preloaded three-pad foil bearing in a turbine simulator. The model applied transient energy equations in each component as well as the gas film. The temperature predicted by the model showed good agreement with the experimental results. Kim et al. [72] extended the 3D thermohydrodynamic model to include the thermal analyses of the surrounding structures of the bearing. The flow recirculation ratio for high axial cooling air pressures has been predicted using a computational fluid dynamics (CFD) model for the leading edge groove region. The model demonstrated the softening effect of the bump foil.

Feng and Kaneko [73] used a sparse matrix to provide a 3D thermohydrodynamic analysis of the bump foil, which was modeled as a link–spring structure earlier. The present model included the thermal expansion of the bearing components as well as the resulting variation of the stiffness of the bumps. Moreover, the heat convection into cooling air from the side of the bearing and flowing through the hollow journal, and temperature based material property variation was included in the model. Further, Moraru and Keith [74] increased the computational efficiency of the sparse mesh using the Lobatto point quadrature algorithm.

Feng and Guo [75] developed a model which included the dynamic friction. In order to include the static characteristics of friction as well as frictional lag, breakaway force,

and the Stribeck effect, the LuGre model was used to calculate the dynamic friction forces. The model showed a good correlation with the experimental data.

Grau et al. [76] [53] implemented an implicit finite difference method instead of an explicit method for the calculation of pressure at different time step in order to save time. The explicit scheme required a large number of steps to ensure numerical stability. This made the solution slow and rigorous. Bou-Said et al. [77] predicted the stability of gas foil bearing comparing linear and non-linear approach. The linear approach indicated inadequacy beyond a specific operating range and therefore emphasized on using non-linear methods to predict the dynamic performance of heavily loaded aerodynamic bearings. Lez et al. [78] solved the differential system of equations assuming the pressure variation between initial time and final time to be linear while updating the normal load at each iteration of the Reynolds equation. Further, Lee et al. [79] performed a transient analysis to predict the dynamic performance of airfoil bearings using the finite element method. The time derivative was discretized using iterative backward difference method. They pointed out that the time step has to be small in solving the time-dependent terms of the Reynolds equation using backward difference approximations in order to ensure an accurate solution. Wang et al. [80] used particle swarm optimization to compare different parallel computing schemes for an airfoil bearing design.

Recently, Bonello and Pham [81] presented an alternative dependent variable, which allowed the solution of time-domain implicit at each time step to assure numerical stability. The novel arbitrary-order Galerkin Reduction the simultaneous solution of all the state variables and ensured the true nature of the coupled solution. Harmonic Balance method has been used to solve the equations in the frequency domain in order to calculate the self-excited periodic response. A significant reduction in the computation time has been observed. Moreover, the structural damping could be incorporated in the analysis.

Along the same line, Larsen and Santos [82] developed a Newton-like method for solving the nonlinear compressible (Reynolds equation). The method showed faster convergence when compared to the standard iterative procedure based on successive under relaxation method. Following this, Larsen et al. [83], while examining the stability of GFB using the linearized method and the transient method, pointed out the inaccuracy of the frequency domain method for stability analysis for the GFBs. However, Osmanski et al. [84], demonstrated that the discrepancy between linearized method and non-linear transient method could be removed through the inclusion of the foil states and the governing equations of motion. They pointed out that the extended linearized perturbation method with the incorporation of foil states provide more realistic results. However, it

increases the computational effort due to a large number of first order equations. Therefore, they suggested solving the coupled system of equations using the time-integration method.

Recently, Pronobis and Liebich [85] compared the stability limits of GFBs obtained using time integration and the perturbation method. They confirmed the presence of discrepancies between both the two methods. This discrepancy further increases with the increase of foil compliance. Although, in order to reduce this discrepancy a new formulation for the dynamic compliance coefficient was developed, the disparity could not be eliminated entirely.

1.4.4 Hybrid Gas Foil Bearing

The top foil of the gas foil bearing and the journal has to suffer wear during the startup and the shutdown, which is prominent in the case of the heavily loaded machine [86, 87]. In order to overcome this demerit, a combination of hydrostatic and hydrodynamic bearing is developed. The bearings are fitted with ports for hydrostatic injection of the compressed air. At the startup, the ports are turned on till the bearing attains full hydrodynamic action, after which the ports can be turned off or kept open for additional cooling. Technological advancements make hybridization of the conventional bearings possible and extremely attractive. Researchers have already established the fact that a hybrid bearing is much more effective than the conventional one. A hybrid or non-conventional bearing can harness the strengths of each bearing and diminish each other's shortcomings. Several techniques have been attempted and suggested to minimize or avoid resonant response by applying suitable combinations of damping and stiffness coefficients of the bearing.

Barlow [88] first studied the effects of combined self-acting and external pressurization in a planer foil bearing. The foil was wrapped around support along the sources of axis-symmetrical line-pressure to provide the airflow. This configuration eliminated the circumferential flow effects. Further, Kim and Park [89] fabricated a prototype of a hybrid airfoil journal bearing where the air was supplied directly through the orifice holes in a flexible tube mounted on the back of top foil. The hybrid bearing protected the coating wear during start and stop. Moreover, the drag torque was reduced during start-up. Kim and Lee [90] fused hydrodynamic pressure with hydrostatic lift in a three pad hybrid foil bearing for a midsize turbomachine. Although the rotor was heavy, the hybrid bearing was successful in eliminating the wear during start-up and shut down. Recently, Feng et al. [91] built a prototype of hybrid bump and metal mesh foil bearings. The hybrid bearing acquired the advantages of both metal mesh and bump foil bearings, i.e. provided

better stability and could operate at high temperatures.

Morosi and Santos [92] developed a hybrid permanent magnet-gas bearing, with radially oriented magnetic rings. The permanent magnets removed the wear of top foil during start-up and at low speed, whereas at high speed, the dynamics characteristic of GFB was improved due to the offset of stator ring. Further, Morosi and Santos [93] demonstrated an active lubrication technique for gas journal bearing using piezoelectric actuators. The piezoelectric actuators are attached to the back of the bearing sleeve to control the lubricant, which in turn produced active forces and improved the dynamic coefficients of the GFB.

Polyakov et al. [94] introduced an actively adjustable radial gap in gas foil bearings. The hybrid bearing was designed combining the ball bearing and the GFB. The electromagnetic coils placed on the bearing housing (two for each foil) was capable of controlling the deformation of the foil, thus improving the dynamic characteristics of GFB.

A hybrid bearing exploiting the advantages of GFBs and AMBs is a possibility for application in high-speed turbomachinery. The AMB can support the load at zero and low speed while the foil bearing can support the load at high speed. The foil bearing can be housed inside or adjacent to the magnetic bearing. When the rotor is started or shutdown, the magnetic bearing supports the journal, which eliminates the low-speed wear of the top foil and journal surfaces. One added advantage of the hybrid bearing is that the GFBs provide better damping to the rotor drop than the rolling element backup bearing. The load of the journal can also be shared between the bearings and hence increase the overall load capacity [95]. In this context, a few developments have been made in combining GFBs and AMBs.

Scharrer [96] patented a magnetically active tape type foil bearing combining the tape type foil bearing with magnetic bearings. The levitation of the shaft was dependent on the magnetic field, while the foil bearings provided support to the shaft in case of failure in the magnetic field.

Heshmat et al. [97] introduced a hybrid bearing that combined the bump foil and the magnetic bearing. The load sharing mechanism was investigated on hybrid foil magnetic bearing arrangement. The mechanism to share the load depending on the rotor position without calculating the rotor trajectory corresponding to various rotor spin speeds. Swanson et al. [95] further investigated the capabilities of the control algorithm of load sharing in the hybrid bearing system during high-speed operation. Although the total bearing weight was reduced, the load-carrying capacity of the hybrid bearing system increased by three folds.

Further, Lee et al. [98] invented an airfoil magnetic hybrid bearing. The airfoil bearing was positioned in-between the bearing housing and the rotating shaft to form the dynamic pressure as the shaft rotated at high speed. The inner surface of the housing consisted of a magnetic core positioned radially. The coils wounded to the cores levitated the rotating shaft using an attractive magnetic force generated by the current. The airfoil bearings substituted the need for auxiliary bearing whereas the AMB provided the damping force whenever needed.

Looser et al. [99] implemented the concept of hybrid aerodynamic gas bearing in a small-sized self-sensing active magnetic damper for supporting the load. The hybrid bearing allowed a counteract in mitigating the instability caused because of the self-excited in the gas bearing, which in turn enabled high-speed operation. Although the complexity of the system got a nominal increment, the cost was reduced. The self-sensing electromagnetic damper acted directly on the rotor and enabled stable operation at high speed without lowering the gas bearing load capacity, or stiffness.

1.4.5 Control of Hybrid Gas Foil Magnetic Bearing

As the magnetic bearing in a hybrid foil-magnetic bearing is active, the control becomes an indispensable part. The journal should be operated at certain eccentricity and attitude angle in order to achieve proper sharing of the loads. The hydrodynamic force of Gas Foil Bearing does not act on a concentric rotor, whereas the magnetic bearing tries to move the journal to the reference position using a controller. Therefore, it is necessary to develop a control algorithm to overcome the disparity.

Tian et al. [100] suggested a control algorithm for the control of hybrid foil magnetic bearing in steady-state. The algorithm was successful in identifying the operating location for hybrid foil magnetic bearing irrespective of properties of foil bearings and operating speed. Pham et al. [101] proposed a PD controller for the hybrid foil magnetic bearing instead of PID, so that the synergy is not disrupted due to the integral control. The optimized tuning gains helped in achieving a 50% reduction of energy consumption in the driving motor along with a 26% improvement in the bending at a critical speed. Pierart and Santos [102] compared the simple proportional integral derivative controller and the optimal controller. The methodologies highlighted the importance of the control scheme in controlling a flexible rotor supported on the hybrid gas bearing. A significant increase in the system damping ratio was observed. Jeong and Lee [103] implemented a PD controller to investigate the optimum eccentricity of the hybrid bearing for proper

distribution of load. They recommended that for the proper distribution of load in the hybrid foil magnetic bearing the eccentricity has to be maintained in between 0.2 and 0.5. Further, Jeong et al. [104] controlled the rigid mode unstable vibration at 20,000 rpm, and also the asynchronous vibration due to aerodynamic instability using the hybrid foil magnetic bearing in a 225kW class turbo blower. The control of the rotor using the hybrid foil magnetic bearing showed better stability against unbalance and hydrodynamic instability in the range of 12,000–15,000 rpm. Recently, Tian et al. [105] implemented an adaptive control method for the hybrid foil magnetic bearing with the aim of simplifying the controller design and enhance the performance of the rotor-bearing system. The golden section controller was used to adapt the variation of the parameter of the GFB.The simulations showed that the new control method provides better performance results when compared to the conventional PD controller.

1.5 Research Gap

The review of the literature demonstrates the development of the GFB to meet the necessities of the industry. Various modifications of the underlying substructure have been considered to increase the load capacity and also to increase the damping. However, it has not been possible to increase its load capacity after a certain limit due to the presence of the sub-synchronous frequency. In the case of the GFBs, the sub-synchronous frequency has been found to be dependent on the stiffness of the bump foil and clearance. However, limited literature has been found with the aim of eliminating this sub-synchronous frequency.

It has been found in the literature that several attempts have been made to combine the hydrodynamic gas foil bearing with hydrostatic gas foil bearing. Further, attempts have also been made to develop a hybrid bearing combining a Gas Foil Bearing (GFB) with an Active Magnetic Bearing (AMB). Few researchers have successfully built the prototype of this hybrid GFB and investigated its behavior in various conditions. However, there is not much work done on the numerical modeling of the hybrid GFBs. Jeong et al. [106] and Yang et al. [107] investigated the dynamic coefficients of the combined bearing, considering the linearised stiffness and damping of the two bearings to be independent. This linearized stiffness and damping coefficients of the GFBs have been used to simulate the rotor response of the hybrid GFBs.

In view of the above, a coupled numerical model of a hybrid GFB, combining the dynamics of a GFB and an AMB, needs to be developed in the time domain

and investigated.

1.6 Motivation

In a Gas Foil Bearing (GFB), the development of the wedge effect producing the hydrodynamic force is relatively small due to the leakage. Moreover, higher speed is required for developing sufficient pressure to support the rotor. It has also been observed that a GFB encounters friction between the top foil and journal surfaces during start-up and shutdown and occasionally during overload situations. GFBs have low damping coefficients due to which the vibration control becomes imperative in rotors supported on GFBs. A possible solution to the above problems could be the introduction of an electromagnetic actuator (EMA) for the active control of the rotor-bearing system. This EMA is also referred as AMB in this thesis. The dynamic coefficients of the bearing can be modified by implementing actively controlled bearings to a rotor shaft system and thereby increasing the stability of the system. This bearing system will suppress the vibration of the rotating shaft and also mitigate any undesirable forces transmitted from the foundation. It is possible to install the existing GFBs and EMA separately.However, it requires additional spaces. The proposed bearing system can be useful if there is a limitation in space in installing the GFB and AMB separately.

Nonetheless, both GFBs and AMBs are oil-free technology, and therefore, environment-friendly. The operation of hybrid GFBs and AMBs will utilize the strength of each bearing and compensate for each other's weaknesses. It is cumbersome to build a prototype model every other time and optimize it for better results.

1.6.1 Scope and Objectives

A numerical approach would be helpful to study the behaviour of the hybrid bearing efficiently. Therefore, the present work is dedicated to develop a coupled numerical model for a hybrid gas foil bearing. The capabilities of hybrid bearing that synergies the GFBs and AMBs are investigated in this work. The main aim of this thesis is to develop a coupled numerical model of the hybrid GFB and provide a time domain analysis of hybrid gas foil bearing. It will be achieved by fulfilling the below-mentioned objectives:

1. Develop an efficient method to solve the nonlinear time domain Reynolds equation of a Gas Foil Bearing (GFB).
2. Investigate the stability of a rigid rotor supported on GFB with and without the

effect of an Electromagnetic Actuator (EMA).

3. Investigate the non-linear dynamics of a rigid rotor supported on Hybrid Gas Foil Bearing (HGFB) which combines a GFB and an AMB.
4. Investigate the bridge configured winding for the AMB also referred as electromagnetic actuator for a low-cost hybrid GFB.

1.7 Organisation of the thesis

Chapter 1 presents a brief introduction of GFB and AMB, along with their working principle. It also describes an exhaustive literature review involving the developments of GFB, and hybrid GFB. Further, the research gap and the aim of the present study have been described.
Chapter 2 describes the mathematical model of the rotor and GFB. The discretisation of the governing equations of GFB and its solution procedure is discussed in detail.
Chapter 3. The design procedure of an actuator for hybrid GFB has been discussed. The basic equations for the active magnetic bearing have also been derived.
Chapter 4 deals with the stability analysis of hybrid GFB. The stability of conventional GFB and hybrid GFB has been compared. Two cases (1) when the EMA of the hybrid bearing is switched ON from the start and (2) when the EMA is not switched ON from the start.
Chapter 5 presents the nonlinear dynamic analysis of hybrid GFB. The rotor response for sudden unbalance for both conventional GFB, and hybrid GFB has been investigated. FFT plots have been drawn for investigating the frequency components of both the bearings.
Chapter 6 describes the new winding scheme for the AMB. The electrical connections and electrical dynamics of the new winding scheme have been presented.
Chapter 7 concludes the present work with important observations and proposes the future scope of the work.

2

Modelling of Gas Foil Bearing

Contents

2.1 Introduction

In the previous chapter, an exhaustive literature review on Gas Foil Bearings (GFBs) has been described. Further, the details about the various types of hybrid gas bearings have been described. In this chapter, the governing equations of the GFBs have been provided. Two discretization procedures of the governing Reynolds equation have been presented. The methodology to solve the time dependent terms of the Reynolds has also been described. The method adopted to model the top foil has been presented. The effect of grid sizes on the results has been provided. Moreover, the mathematical formulation of the rotor supported on two bearings has been described. Further, the results from the numerical model have been compared with the published literature. The design and modelling of Active Magnetic Bearings (AMBs) have been provided in the next chapter.

2.2 Governing Equations of Gas Foil Bearings

In Fig 2.1, the schematic of a bump type gas foil bearing has been shown. The Reynolds equation for a Gas Foil Bearing with bump type foil with respect to the co-ordinate axis X and Y can be written as,

$$\frac{\partial}{\partial x}\left(\frac{\rho h^3}{12\mu}\frac{\partial p}{\partial x}\right)+\frac{\partial}{\partial z}\left(\frac{\rho h^3}{12\mu}\frac{\partial p}{\partial z}\right)-\frac{U}{2}\frac{\partial(\rho h)}{\partial x}=\frac{\partial(\rho h)}{\partial t} \tag{2.1}$$

where, x and z are the circumferential and axial coordinates on the plane of the bearing.

Substituting, $x=r\theta$, $Z={}^{z}/_{(L/2)}$, $\partial x=r\partial\theta$, $\partial \mathrm{z}=\left({}^{L}/_{2}\right)\partial \mathrm{Z}$ and $U=r\omega$ in Eqn.2.1 we get,

$$\frac{\partial}{r\partial\theta}\left(\frac{\rho h^3}{12\mu}\frac{\partial p}{r\partial\theta}\right)+\frac{\partial}{(L/2)\,\partial Z}\left(\frac{\rho h^3}{12\mu}\frac{\partial p}{(L/2)\,\partial Z}\right)-\frac{\omega}{2}\frac{\partial\rho h}{\partial\theta}=\frac{\partial ph}{\partial t} \tag{2.2}$$

In the case of gas bearings, the variation of density with pressure has to be considered. Therefore, considering the operating gas to be isothermal and perfect gas, the relationship between density and pressure can be written as,

$$p=\rho RT$$

where, R is the gas constant, and T is the absolute temperature. From the polytrophic

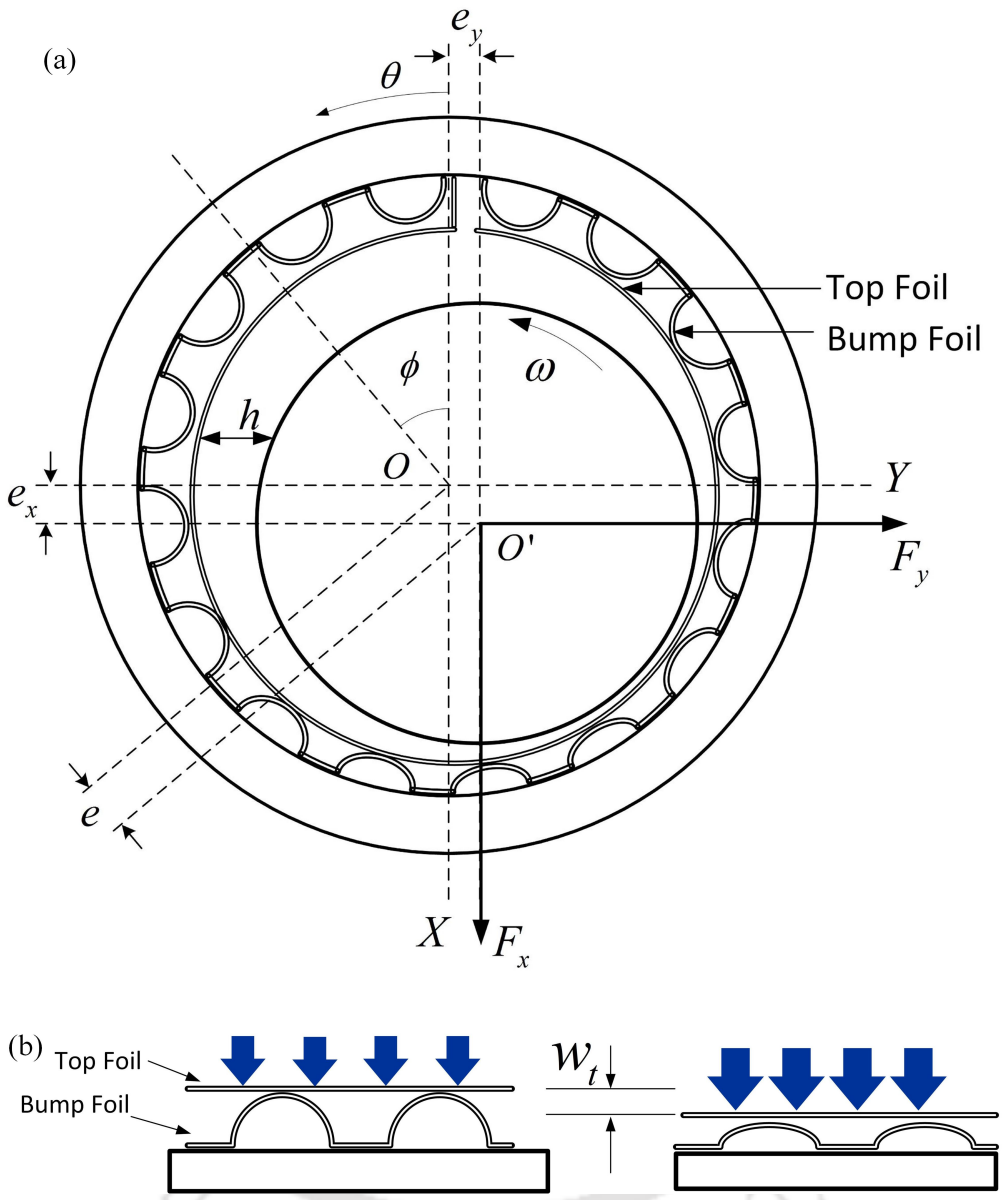

Figure 2.1: (a)Schematics of GFB (b) Bump foil deflection

relation $p\rho^{-\gamma} =$ constant where, $\gamma =$ polytropic gas expansion exponent, we get,

$$p = \frac{1}{\rho^{\gamma}}$$

$$\text{or, } \rho = \mathrm{p}^{\frac{1}{\gamma}}$$

Further for isothermal flow, $\gamma = 1$, therefore,

$$\rho = p \tag{2.3}$$

Therefore, using the relation of Eqn. 2.3, the Eqn. 2.2 can be written as,

$$\frac{1}{r^2}\frac{\partial}{\partial\theta}\left(\frac{ph^3}{12\mu}\frac{\partial p}{\partial\theta}\right)+\frac{1}{(L/2)^2}\frac{\partial}{\partial Z}\left(\frac{ph^3}{12\mu}\frac{\partial p}{\partial Z}\right)-\frac{\omega}{2}\frac{\partial ph}{\partial\theta}=\frac{\partial ph}{\partial t} \tag{2.4}$$

$$\frac{1}{12\mu r^2}\left[\frac{\partial}{\partial\theta}\left(ph^3\frac{\partial p}{\partial\theta}\right)+\frac{(2r)^2}{L^2}\frac{\partial}{\partial Z}\left(ph^3\frac{\partial p}{\partial Z}\right)\right]-\frac{\omega}{2}\frac{\partial ph}{\partial\theta}=\frac{\partial ph}{\partial t} \tag{2.5}$$

$$\frac{\partial}{\partial\theta}\left(ph^3\frac{\partial p}{\partial\theta}\right)+\frac{D^2}{L^2}\frac{\partial}{\partial Z}\left(ph^3\frac{\partial p}{\partial Z}\right)-6\mu\omega r^2\frac{\partial ph}{\partial\theta}=12\mu r^2\frac{\partial ph}{\partial t} \tag{2.6}$$

$$\begin{aligned}&ph^3\tfrac{\partial^2 p}{\partial\theta^2}+\left(\tfrac{\partial p}{\partial\theta}\right)\left(\tfrac{\partial ph^3}{\partial\theta}\right)+\left(\tfrac{D}{L}\right)^2\left[ph^3\tfrac{\partial^2 p}{\partial Z^2}+\left(\tfrac{\partial p}{\partial Z}\right)\left(\tfrac{\partial ph^3}{\partial Z}\right)\right]\\&-6\mu\omega r^2\tfrac{\partial(ph)}{\partial\theta}=12\mu r^2\tfrac{\partial(ph)}{\partial t}\end{aligned} \tag{2.7}$$

The film thickness equation for the given configuration can be written as [5],

$$h=C+e\cos(\theta-\phi)+w_t \tag{2.8}$$

or,

$$h=C+e\cos\theta cos\phi+e\sin\theta\sin\phi+w_t \tag{2.9}$$

or,

$$h=C+e_x\cos\theta+e_y\sin\theta+w_t \tag{2.10}$$

where, $e_x=e\cos\phi$ and $e_y=e\sin\phi$ and w_t is the deflection of the foil structure (Fig 2.1b). The modelling of the top foil has been described in the Section 2.4

Since, the bearing is open to air on both sides, therefore, the pressure takes the value of ambient pressure at the ends of the bearing. Moreover, the atmospheric pressure is present at the weld point, which joins the top foil and the bump foil to the bearing housing. Therefore, the boundary conditions for solving the Reynolds Equation can be mathematically represented as,

$$\left.\begin{aligned}&p=P_a\ \text{ at }\ \theta=0\ \text{ and }\ 2\pi\\&p=P_a\ \text{ at }\ z=0\ \text{ and }\ L\end{aligned}\right\} \tag{2.11}$$

The governing Reynolds equation can be discretized using various methods, to obtain a numerical solution for the pressure generated. Discretization implies creating a grid of $m\times n$ where m is the number of nodes in θ direction and n in z direction. Hence, a set of $m\times n$

state equations is formed, solving which the pressure field is obtained. The dimension of the pressure matrix p in the spatial domain in the matrix form will be $(m+1)\times(n+1)$. In general, Finite Difference Method or Finite Element Method is employed.

2.3 Discretization of Reynolds Equation

The derivatives of the differential equation and the boundary conditions are replaced by their finite-difference approximations and the resulting systems of equations are solved by any standard procedure. An exfoliated view of bearing is shown in Fig. 2.2. The area is divided into a number of mesh sizes $(\Delta\theta \times \Delta Z)$. A mesh of m nodes along circumferential direction and n nodes along the axial direction is created. Suppose, (i, j) is any arbitrary point in the matrix representation, its position in the vector representation can be written as $q = (j-1)(m+1)+i$. The four adjacent nodes associated with node (i, j) are $(i+1, j)$, $(i-1, j)$, $(i, j+1)$ and $(i, j-1)$ as shown in Fig. 2.2.

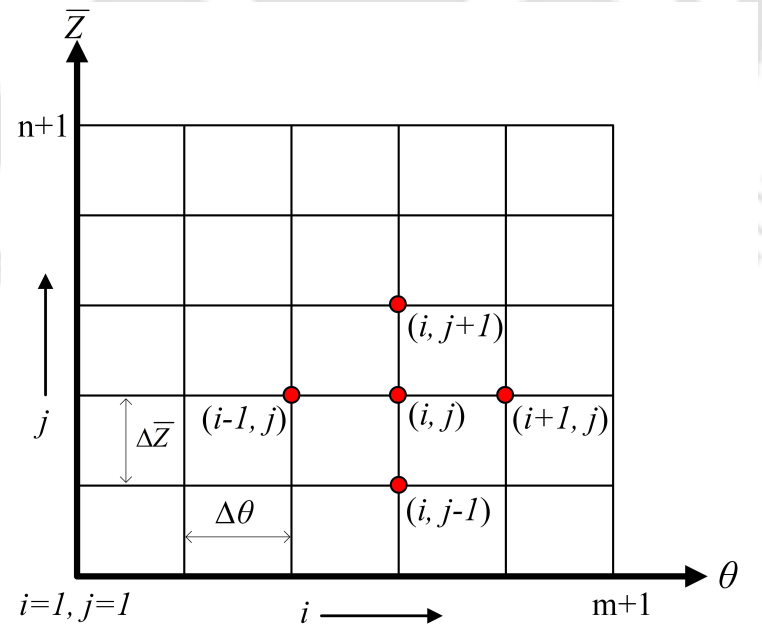

Figure 2.2: An exfoliated view of a bearing showing the mesh size and nodes

Hence, the $P_{i,j}$ is the pressure at any point (i, j). $H_{i,j}$ is the film thickness at any point (i, j) and $P_{i+1,j}, P_{i-1,j}, P_{i,j+1}, P_{i,j-1}$ are pressures at four adjacent points.

The finite difference approximations to the various derivatives can be described as:

$$\begin{aligned}
&\left(p_{(i,j)}h^3_{(i,j)}\right)\left(\frac{p_{(i+1,j)}+2p_{(i,j)}-p_{(i-1,j)}}{(\Delta\theta)^2}\right)+\left(\frac{p_{(i+1,j)}-p_{(i-1,j)}}{(2\Delta\theta)}\right)\left(\frac{p_{(i+1,j)}h^3_{(i+1,j)}-p_{(i-1,j)}h^3_{(i-1,j)}}{(2\Delta\theta)}\right)\\
&+\left(\frac{D}{L}\right)^2\left(p_{(i,j)}h^3_{(i,j)}\right)\left(\frac{p_{(i,j+1)}+2p_{(i,j)}-p_{(i,j-1)}}{(\Delta Z)^2}\right)+\left(\frac{D}{L}\right)^2\left(\frac{p_{(i,j+1)}-p_{(i,j-1)}}{(2\Delta Z)}\right)\left(\frac{p_{(i,j+1)}h^3_{(i,j+1)}-p_{(i,j-1)}h^3_{(i,j-1)}}{(2\Delta Z)}\right)\\
&-\Lambda\left(\frac{p_{(i+1,j)}h_{(i+1,j)}-p_{(i-1,j)}h_{(i-1,j)}}{(2\Delta\theta)}\right)=12\mu r^2\frac{\partial(ph)}{\partial t}
\end{aligned} \tag{2.12}$$

$$\begin{aligned}
&-\left[\left(\frac{2h^3_{(i,j)}}{(\Delta\theta)^2}\right)+\frac{r^2}{L^2}\left(\frac{2h^3_{(i,j)}}{(\Delta Z)^2}\right)\right]\left(p_{(i,j)}\right)^2\\
&+\left[h^3_{(i,j)}\left(\frac{p_{(i+1,j)}+p_{(i-1,j)}}{(\Delta\theta)^2}\right)+\frac{D^2}{L^2}h^3_{(i,j)}\left(\frac{p_{(i,j+1)}+p_{(i,j-1)}}{(\Delta Z)^2}\right)\right]\left(p_{(i,j)}\right)\\
&+\left(p_{(i+1,j)}-p_{(i-1,j)}\right)\left(\frac{p_{(i+1,j)}h^3_{(i+1,j)}-p_{(i-1,j)}h^3_{(i-1,j)}}{4(\Delta\theta)^2}\right)\\
&+\frac{D^2}{L^2}\left(p_{(i,j+1)}-p_{(i,j-1)}\right)\left(\frac{p_{(i,j+1)}h^3_{(i,j+1)}-p_{(i,j-1)}h^3_{(i,j-1)}}{4(\Delta Z)^2}\right)\\
&-6\mu\omega r^2\left(\frac{p_{(i+1,j)}h_{(i+1,j)}-p_{(i-1,j)}h_{(i-1,j)}}{2(\Delta\theta)}\right)=12\mu r^2\frac{\partial(ph)}{\partial t}
\end{aligned} \tag{2.13}$$

Therefore in matrix form it can be written as,

$$\begin{aligned}
&\begin{Bmatrix} p_{(i,j-1)}\\ p_{(i-1,j)}\\ p_{(i,j)}\\ p_{(i+1,j)}\\ p_{(i,j+1)}\end{Bmatrix}^T\begin{bmatrix} a_{11} & 0 & 0 & 0 & a_{15}\\ 0 & a_{22} & 0 & a_{24} & 0\\ a_{31} & a_{32} & a_{33} & a_{34} & a_{35}\\ 0 & a_{42} & 0 & a_{44} & 0\\ a_{51} & 0 & 0 & 0 & a_{55}\end{bmatrix}\begin{Bmatrix} p_{(i,j-1)}\\ p_{(i-1,j)}\\ p_{(i,j)}\\ p_{(i+1,j)}\\ p_{(i,j+1)}\end{Bmatrix}\\
&+\begin{bmatrix} 0 & \frac{6\mu\omega r^2h_{(i-1,j)}}{2(\Delta\theta)} & 0 & -\frac{6\mu\omega r^2h_{(i+1,j)}}{2(\Delta\theta)} & 0\end{bmatrix}\begin{Bmatrix} p_{(i,j-1)}\\ p_{(i-1,j)}\\ p_{(i,j)}\\ p_{(i+1,j)}\\ p_{(i,j+1)}\end{Bmatrix}=12\mu r^2\frac{\partial(ph)}{\partial t}
\end{aligned} \tag{2.14}$$

where,

$$a_{11} = \frac{D^2}{L^2}\frac{h^3_{(i,j-1)}}{4(\Delta Z)^2} \qquad a_{15} = -\frac{D^2}{L^2}\frac{h^3_{(i,j-1)}}{4(\Delta Z)^2} \qquad a_{22} = \frac{h^3_{(i-1,j)}}{4(\Delta\theta)^2}$$

$$a_{24} = -\frac{h^3_{(i-1,j)}}{4(\Delta\theta)^2} \qquad a_{31} = \frac{D^2}{L^2}\frac{h^3_{(i,j)}}{(\Delta Z)^2} \qquad a_{32} = \frac{h^3_{(i,j)}}{(\Delta\theta)^2}$$

$$a_{33} = -\frac{2h^3_{(i,j)}}{(\Delta\theta)^2} - \frac{D^2}{L^2}\frac{2h^3_{(i,j)}}{(\Delta Z)^2} \qquad a_{34} = \frac{h^3_{(i,j)}}{(\Delta\theta)^2} \qquad a_{35} = \frac{D^2}{L^2}\frac{h^3_{(i,j)}}{(\Delta Z)^2}$$

$$a_{42} = -\frac{h^3_{(i+1,j)}}{4(\Delta\theta)^2} \qquad a_{44} = \frac{h^3_{(i+1,j)}}{4(\Delta\theta)^2} \qquad a_{51} = -\frac{D^2}{L^2}\frac{h^3_{(i,j+1)}}{4(\Delta Z)^2}$$

$$a_{55} = \frac{D^2}{L^2}\frac{h^3_{(i,j+1)}}{4(\Delta Z)^2}$$

Therefore Eqn.2.14 can be written as,

$$\left(p^e_q\right)^T \mathbf{A}^e_q p^e_q + \mathbf{b}^e_q p^e_q = 12\mu r^2 \frac{\partial ph}{\partial \tau} \tag{2.15}$$

where, $p^e_q = \left\{ \begin{array}{ccccc} p_{(i,j-1)} & p_{(i-1,j)} & p_{(i,j)} & p_{(i+1,j)} & p_{(i,j+1)} \end{array} \right\}^T$ and its size is 5×1;

$$A^e_q = \begin{bmatrix} \frac{D^2}{L^2}\frac{h^3_{(i,j-1)}}{4(\Delta Z)^2} & 0 & 0 & 0 & -\frac{D^2}{L^2}\frac{h^3_{(i,j-1)}}{4(\Delta Z)^2} \\ 0 & \frac{h^3_{(i-1,j)}}{4(\Delta\theta)^2} & 0 & -\frac{h^3_{(i-1,j)}}{4(\Delta\theta)^2} & 0 \\ \frac{D^2}{L^2}\frac{h^3_{(i,j)}}{(\Delta Z)^2} & \frac{h^3_{(i,j)}}{(\Delta\theta)^2} & -\frac{2h^3_{(i,j)}}{(\Delta\theta)^2} - \frac{D^2}{L^2}\frac{2h^3_{(i,j)}}{(\Delta Z)^2} & \frac{h^3_{(i,j)}}{(\Delta\theta)^2} & \frac{D^2}{L^2}\frac{h^3_{(i,j)}}{(\Delta Z)^2} \\ 0 & -\frac{h^3_{(i+1,j)}}{4(\Delta\theta)^2} & 0 & \frac{h^3_{(i+1,j)}}{4(\Delta\theta)^2} & 0 \\ -\frac{D^2}{L^2}\frac{h^3_{(i,j+1)}}{4(\Delta Z)^2} & 0 & 0 & 0 & \frac{D^2}{L^2}\frac{h^3_{(i,j+1)}}{4(\Delta Z)^2} \end{bmatrix}$$

A^e_q is a 5×5 non-symmetric matrix;

$b^e_q = \begin{bmatrix} 0 & \frac{6\mu\omega r^2 h_{(i-1,j)}}{2(\Delta\theta)} & 0 & -\frac{6\mu\omega r^2 h_{(i+1,j)}}{2(\Delta\theta)} & 0 \end{bmatrix}$ is a row vector of size 1×5

Therefore, the bearing forces,

$$F_x = -r^2 \int_{-L/D}^{L/D} \int_0^{2\pi} p\cos\theta\, d\theta\, dZ \tag{2.16}$$

$$F_y = -r^2 \int_{-L/D}^{L/D} \int_0^{2\pi} p\sin\theta\, d\theta\, dz \tag{2.17}$$

2.3.1 Non-Dimensional form of Equations

In Reynolds Equation given in Eqn. 2.7, can be further normalized by using the following substitutions as follows:

$$\bar{H} = {}^{h}/_{C} \quad \bar{P} = {}^{p}/_{P_a} \quad \tau = \omega t$$

$$\begin{aligned} &\bar{P}P_a(\bar{H}C)^3\frac{\partial^2\bar{P}P_a}{\partial\theta^2} + \left(\frac{\partial\bar{P}P_a}{\partial\theta}\right)\left(\frac{\partial}{\partial\theta}\bar{P}P_a(\bar{H}C)^3\right) + \\ &\left(\frac{D}{L}\right)^2\left[\bar{P}P_a(\bar{H}C)^3\frac{\partial^2\bar{P}P_a}{\partial Z^2} + \left(\frac{\partial\bar{P}P_a}{\partial Z}\right)\left(\frac{\partial}{\partial Z}\bar{P}P_a(\bar{H}C)^3\right)\right] \\ &-6\mu\omega r^2\frac{\partial}{\partial\theta}\left(\bar{P}P_a(\bar{H}C)\right) = 12\mu r^2\frac{\partial}{\partial t}\left(\bar{P}P_a(\bar{H}C)\right) \end{aligned} \tag{2.18}$$

$$\begin{aligned} &P_a^2C^3\left[\bar{P}\bar{H}^3\frac{\partial^2\bar{P}}{\partial\theta^2} + \left(\frac{\partial\bar{P}}{\partial\theta}\right)\left(\frac{\partial\bar{P}\bar{H}^3}{\partial\theta}\right) + \left(\frac{D}{L}\right)^2\left[\bar{P}\bar{H}^3\frac{\partial^2\bar{P}}{\partial Z^2} + \left(\frac{\partial\bar{P}}{\partial Z}\right)\left(\frac{\partial\bar{P}\bar{H}^3}{\partial Z}\right)\right]\right] \\ &-6\mu\omega r^2P_aC\frac{\partial\bar{P}\bar{H}}{\partial\theta} = 12\mu r^2P_aC\frac{\partial\bar{P}\bar{H}}{\partial t} \end{aligned} \tag{2.19}$$

$$\begin{aligned} &\bar{P}\bar{H}^3\frac{\partial^2\bar{P}}{\partial\theta^2} + \left(\frac{\partial\bar{P}}{\partial\theta}\right)\left(\frac{\partial\bar{P}\bar{H}^3}{\partial\theta}\right) + \left(\frac{D}{L}\right)^2\left[\bar{P}\bar{H}^3\frac{\partial^2\bar{P}}{\partial Z^2} + \left(\frac{\partial\bar{P}}{\partial Z}\right)\left(\frac{\partial\bar{P}\bar{H}^3}{\partial Z}\right)\right] \\ &-\frac{6\mu\omega r^2}{P_aC^2}\frac{\partial\bar{P}\bar{H}}{\partial\theta} = \frac{12\mu r^2}{P_aC^2}\frac{\partial\bar{P}\bar{H}}{\partial t} \end{aligned} \tag{2.20}$$

$$\begin{aligned} &\bar{P}\bar{H}^3\frac{\partial^2\bar{P}}{\partial\theta^2} + \left(\frac{\partial\bar{P}}{\partial\theta}\right)\left(\frac{\partial\bar{P}\bar{H}^3}{\partial\theta}\right) + \left(\frac{D}{L}\right)^2\left[\bar{P}\bar{H}^3\frac{\partial^2\bar{P}}{\partial Z^2} + \left(\frac{\partial\bar{P}}{\partial Z}\right)\left(\frac{\partial\bar{P}\bar{H}^3}{\partial Z}\right)\right] - \Lambda\frac{\partial\bar{P}\bar{H}}{\partial\theta} \\ &= 2\Lambda\frac{\partial\bar{P}\bar{H}}{\partial\tau} \end{aligned} \tag{2.21}$$

where $\Lambda = \frac{6\mu\omega r^2}{P_aC^2}$

$$\begin{aligned} &\left(\bar{P}_{(i,j)}\bar{H}^3_{(i,j)}\right)\left(\frac{\bar{P}_{(i+1,j)}+2\bar{P}_{(i,j)}-\bar{P}_{(i-1,j)}}{(\Delta\theta)^2}\right) + \left(\frac{\bar{P}_{(i+1,j)}-P_{(i-1,j)}}{(2\Delta\theta)}\right)\left(\frac{\bar{P}_{(i+1,j)}\bar{H}^3_{(i+1,j)}-\bar{P}_{(i-1,j)}\bar{H}^3_{(i-1,j)}}{(2\Delta\theta)}\right) \\ &+\left(\frac{D}{L}\right)^2\left(\bar{P}_{(i,j)}\bar{H}^3_{(i,j)}\right)\left(\frac{\bar{P}_{(i,j+1)}+2\bar{P}_{(i,j)}-\bar{P}_{(i,j-1)}}{(\Delta Z)^2}\right) \\ &+\left(\frac{D}{L}\right)^2\left(\frac{\bar{P}_{(i,j+1)}-\bar{P}_{(i,j-1)}}{(2\Delta Z)}\right)\left(\frac{\bar{P}_{(i,j+1)}\bar{H}^3_{(i,j+1)}-\bar{P}_{(i,j-1)}\bar{H}^3_{(i,j-1)}}{(2\Delta Z)}\right) \\ &= \Lambda\left(\frac{\bar{P}_{(i+1,j)}\bar{H}_{(i+1,j)}-\bar{P}_{(i-1,j)}\bar{H}_{(i-1,j)}}{(2\Delta\theta)}\right) + 2\Lambda\frac{\partial(\bar{P}\bar{H})}{\partial\tau} \end{aligned} \tag{2.22}$$

which can be rearranged as,

$$
\begin{aligned}
&-\left[\left(\frac{2\bar{H}^3_{(i,j)}}{(\Delta\theta)^2}\right)+\left(\frac{D}{L}\right)^2\left(\frac{2\bar{H}^3_{(i,j)}}{(\Delta Z)^2}\right)\right]\left(\bar{P}_{i,j}\right)^2\\
&+\left[\bar{H}^3_{(i,j)}\left(\frac{\bar{P}_{(i+1,j)}+\bar{P}_{(i-1,j)}}{(\Delta\theta)^2}\right)+\left(\frac{D}{L}\right)^2\bar{H}^3_{(i,j)}\left(\frac{\bar{P}_{(i,j+1)}+\bar{P}_{(i,j-1)}}{(\Delta Z)^2}\right)\right]\left(\bar{P}_{i,j}\right)\\
&+\left(\frac{D}{L}\right)^2\left(\bar{P}_{(i+1,j)}-\bar{P}_{(i-1,j)}\right)\left(\frac{\bar{P}_{(i+1,j)}\bar{H}^3_{(i+1,j)}-\bar{P}_{(i-1,j)}\bar{H}^3_{(i-1,j)}}{4(\Delta\theta)^2}\right)\\
&+\left(\frac{D}{L}\right)^2\left(\bar{P}_{(i,j+1)}-\bar{P}_{(i,j-1)}\right)\left(\frac{\bar{P}_{(i,j+1)}\bar{H}^3_{(i,j+1)}-\bar{P}_{(i,j-1)}\bar{H}^3_{(i,j-1)}}{4(\Delta Z)^2}\right)\\
&-\Lambda\left(\frac{\bar{P}_{(i+1,j)}\bar{H}_{(i+1,j)}-\bar{P}_{(i-1,j)}\bar{H}_{(i-1,j)}}{2(\Delta\theta)}\right)=2\Lambda\frac{\partial(\bar{P}\bar{H})}{\partial\tau}
\end{aligned}
\tag{2.23}
$$

In matrix form the Eqn. 2.23, can be written as,

$$
\begin{aligned}
&\begin{Bmatrix}\bar{P}_{(i,j-1)}\\ \bar{P}_{(i-1,j)}\\ \bar{P}_{(i,j)}\\ \bar{P}_{(i+1,j)}\\ \bar{P}_{(i,j+1)}\end{Bmatrix}^T
\begin{bmatrix}\bar{a}_{11} & 0 & 0 & 0 & \bar{a}_{15}\\ 0 & \bar{a}_{22} & 0 & \bar{a}_{24} & 0\\ \bar{a}_{31} & \bar{a}_{32} & \bar{a}_{33} & \bar{a}_{34} & \bar{a}_{35}\\ 0 & \bar{a}_{42} & 0 & \bar{a}_{44} & 0\\ \bar{a}_{51} & 0 & 0 & 0 & \bar{a}_{55}\end{bmatrix}
\begin{Bmatrix}\bar{P}_{(i,j-1)}\\ \bar{P}_{(i-1,j)}\\ \bar{P}_{(i,j)}\\ \bar{P}_{(i+1,j)}\\ \bar{P}_{(i,j+1)}\end{Bmatrix}\\
&+\begin{bmatrix}0 & \frac{\Lambda\bar{H}_{(i-1,j)}}{2(\Delta\theta)} & 0 & -\frac{\Lambda\bar{H}_{(i+1,j)}}{2(\Delta\theta)} & 0\end{bmatrix}
\begin{Bmatrix}\bar{P}_{(i,j-1)}\\ \bar{P}_{(i-1,j)}\\ \bar{P}_{(i,j)}\\ \bar{P}_{(i+1,j)}\\ \bar{P}_{(i,j+1)}\end{Bmatrix}=2\Lambda\frac{\partial(\bar{P}\bar{H})}{\partial\tau}
\end{aligned}
\tag{2.24}
$$

where,

$$\bar{a}_{11} = \frac{D^2}{L^2}\frac{\bar{H}^3_{(i,j-1)}}{4(\Delta Z)^2} \qquad \bar{a}_{15} = -\frac{D^2}{L^2}\frac{\bar{H}^3_{(i,j-1)}}{4(\Delta Z)^2} \qquad \bar{a}_{22} = \frac{\bar{H}^3_{(i-1,j)}}{4(\Delta\theta)^2}$$

$$\bar{a}_{24} = -\frac{\bar{H}^3_{(i-1,j)}}{4(\Delta\theta)^2} \qquad \bar{a}_{31} = \frac{D^2}{L^2}\frac{\bar{H}^3_{(i,j)}}{(\Delta Z)^2} \qquad \bar{a}_{32} = \frac{\bar{H}^3_{(i,j)}}{(\Delta\theta)^2}$$

$$\bar{a}_{33} = -\frac{2\bar{H}^3_{(i,j)}}{(\Delta\theta)^2} - \frac{D^2}{L^2}\frac{2\bar{H}^3_{(i,j)}}{(\Delta Z)^2} \qquad \bar{a}_{34} = \frac{\bar{H}^3_{(i,j)}}{(\Delta\theta)^2} \qquad \bar{a}_{35} = \frac{D^2}{L^2}\frac{\bar{H}^3_{(i,j)}}{(\Delta Z)^2}$$

$$\bar{a}_{42} = -\frac{\bar{H}^3_{(i+1,j)}}{4(\Delta\theta)^2} \qquad \bar{a}_{44} = \frac{\bar{H}^3_{(i+1,j)}}{4(\Delta\theta)^2} \qquad \bar{a}_{51} = -\frac{D^2}{L^2}\frac{\bar{H}^3_{(i,j+1)}}{4(\Delta Z)^2}$$

$$\bar{a}_{55} = \frac{D^2}{L^2}\frac{\bar{H}^3_{(i,j+1)}}{4(\Delta Z)^2}$$

Hence, Eqn. 2.24 in $(i,j)^{th}$ node or q^{th} node can be written in a quadratic form as,

$$\left(\bar{P}^e_q\right)^T \mathbf{A}^e_q \bar{P}^e_q + \mathbf{b}^e_q \bar{P}^e_q = 2\Lambda\frac{\partial \bar{P}\bar{H}}{\partial \tau} \tag{2.25}$$

Further, using, $\bar{H} = h/C$ and $\bar{P} = p/P_a$ in Eqn. 2.10 the non-dimensional film thickness is given as,

$$\bar{H} = 1 + \bar{e}_x \cos\theta + \bar{e}_x sin\theta + \bar{w}_t \tag{2.26}$$

where, $\bar{e}_x = \frac{e_x}{C}$, $\bar{e}_y = \frac{e_y}{C}$ and $\bar{w}_t = \frac{w_t}{C}$
The bearing forces in the non-dimensional form can be described as,

$$F_x = -P_a r^2 \int_{-L/D}^{L/D}\int_0^{2\pi} \bar{P}\cos\theta d\theta dZ \tag{2.27}$$

$$F_y = -P_a r^2 \int_{-L/D}^{L/D}\int_0^{2\pi} \bar{P} sin\theta d\theta dZ \tag{2.28}$$

or,

$$\bar{F}_x = -\int_{-L/D}^{L/D}\int_0^{2\pi} \bar{P}\cos\theta d\theta dZ \tag{2.29}$$

$$\bar{F}_y = -\int_{-L/D}^{L/D}\int_{0}^{2\pi} \bar{P} sin\theta d\theta dZ \tag{2.30}$$

where, $\bar{F}_x = \frac{F_x}{P_a r^2}$ and $\bar{F}_y = \frac{F_y}{P_a r^2}$

2.3.2 Alternative Formulation of the Reynolds Equation

The Eqn. 2.6 in non-dimensional form can also be written as,

$$\frac{\partial}{\partial\theta}\left(\bar{P}\bar{H}^3\frac{\partial\bar{P}}{\partial\theta}\right)+\frac{\partial}{\partial\bar{Z}}\left(\bar{P}\bar{H}^3\frac{\partial\bar{P}}{\partial\bar{Z}}\right)-\Lambda\frac{\partial\bar{P}\bar{H}}{\partial\theta}=2\Lambda\frac{\partial(\bar{P}\bar{H})}{\partial\tau} \tag{2.31}$$

$$\frac{\partial}{\partial\theta}\left[\bar{P}\bar{H}\left\{\bar{H}^2\frac{\partial\bar{P}}{\partial\theta}+\bar{P}\bar{H}\frac{\partial\bar{H}}{\partial\theta}-\bar{P}\bar{H}\frac{\partial\bar{H}}{\partial\theta}\right\}\right]+\frac{\partial}{\partial\bar{Z}}\left[\bar{P}\bar{H}\left\{\bar{H}^2\frac{\partial\bar{P}}{\partial\bar{Z}}+\bar{P}\bar{H}\frac{\partial\bar{H}}{\partial\bar{Z}}-\bar{P}\bar{H}\frac{\partial\bar{H}}{\partial\bar{Z}}\right\}\right]-\Lambda\frac{\partial\bar{P}\bar{H}}{\partial\theta}$$
$$=2\Lambda\frac{\partial(\bar{P}\bar{H})}{\partial\tau} \tag{2.32}$$

which can be rewritten as,

$$\frac{\partial}{\partial\theta}\left[(\bar{P}\bar{H})\left\{\bar{H}\frac{\partial(\bar{P}\bar{H})}{\partial\theta}-(\bar{P}\bar{H})\frac{\partial\bar{H}}{\partial\theta}\right\}\right]+\frac{\partial}{\partial\bar{Z}}\left[(\bar{P}\bar{H})\left\{\bar{H}\frac{\partial(\bar{P}\bar{H})}{\partial\bar{Z}}-(\bar{P}\bar{H})\frac{\partial\bar{H}}{\partial\bar{Z}}\right\}\right]-\Lambda\frac{\partial(\bar{P}\bar{H})}{\partial\theta}$$
$$=2\Lambda\frac{\partial(\bar{P}\bar{H})}{\partial\tau} \tag{2.33}$$

The above formulation has been referred to as P formulation hereafter. In another formulation, $\psi = \bar{P}\bar{H}$ has been substituted in Eqn. 2.33 and the effect has been investigated.

$$\frac{\partial}{\partial\theta}\left[\psi\left\{\bar{H}\frac{\partial\psi}{\partial\theta}-\psi\frac{\partial\bar{H}}{\partial\theta}\right\}\right]+\left(\frac{D}{L}\right)^2\frac{\partial}{\partial\bar{Z}}\left[\psi\left\{\bar{H}\frac{\partial\psi}{\partial\bar{Z}}-\psi\frac{\partial\bar{H}}{\partial\bar{Z}}\right\}\right]=\Lambda\frac{\partial\psi}{\partial\theta}+2\Lambda\frac{\partial(\psi)}{\partial\tau} \tag{2.34}$$

$$\begin{aligned}&\bar{H}\frac{\partial\psi}{\partial\theta}\frac{\partial\psi}{\partial\theta}+\bar{H}\psi\frac{\partial^2\psi}{\partial\theta^2}-\psi\frac{\partial\psi}{\partial\theta}\frac{\partial\bar{H}}{\partial\theta}-\psi^2\frac{\partial^2\bar{H}}{\partial\theta^2}+\left(\frac{D}{L}\right)^2\bar{H}\frac{\partial\psi}{\partial Z}\frac{\partial\psi}{\partial Z}\\&+\left(\frac{D}{L}\right)^2\bar{H}\psi\frac{\partial^2\psi}{\partial Z^2}-\left(\frac{D}{L}\right)^2\psi\frac{\partial\psi}{\partial Z}\frac{\partial\bar{H}}{\partial Z}-\left(\frac{D}{L}\right)^2\psi^2\frac{\partial^2\bar{H}}{\partial Z^2}=\Lambda\frac{\partial\psi}{\partial\theta}+2\Lambda\frac{\partial(\psi)}{\partial\tau}\end{aligned} \tag{2.35}$$

$$\begin{aligned}
&\bar{H}_{i,j}\left[\frac{\psi_{i+1,j}-\psi_{i-1,j}}{2\Delta\theta}\right]\left[\frac{\psi_{i+1,j}-\psi_{i-1,j}}{2\Delta\theta}\right]+\bar{H}_{i,j}\psi_{i,j}\left[\frac{\psi_{i+1,j}-2\psi_{i,j}+\psi_{i-1,j}}{\Delta\theta^2}\right]\\
&-\psi_{i,j}\left[\frac{\psi_{i+1,j}-\psi_{i-1,j}}{2\Delta\theta}\right]\left[\frac{\bar{H}_{i+1,j}-\bar{H}_{i-1,j}}{2\Delta\theta}\right]-\psi_{i,j}^2\left[\frac{\bar{H}_{i+1,j}-2\bar{H}_{i,j}+\bar{H}_{i-1,j}}{\Delta\theta^2}\right]\\
&+\left(\frac{D}{L}\right)^2\bar{H}_{i,j}\left[\frac{\psi_{i+1,j}-\psi_{i-1,j}}{2\Delta Z}\right]\left[\frac{\psi_{i+1,j}-\psi_{i-1,j}}{2\Delta Z}\right]+\left(\frac{D}{L}\right)^2\bar{H}_{i,j}\psi_{i,j}\left[\frac{\psi_{i+1,j}-2\psi_{i,j}+\psi_{i-1,j}}{\Delta Z^2}\right]\\
&-\left(\frac{D}{L}\right)^2\psi_{i,j}\left[\frac{\psi_{i+1,j}-\psi_{i-1,j}}{2\Delta Z}\right]\left[\frac{\bar{H}_{i+1,j}-\bar{H}_{i-1,j}}{2\Delta Z}\right]-\left(\frac{D}{L}\right)^2\psi_{i,j}^2\left[\frac{\bar{H}_{i+1,j}-2\bar{H}_{i,j}+\bar{H}_{i-1,j}}{\Delta Z^2}\right]\\
&=\Lambda\left[\frac{\psi_{i+1,j}-\psi_{i-1,j}}{2\Delta\theta}\right]+2\Lambda\frac{\partial(\psi)}{\partial\tau}
\end{aligned}\tag{2.36}$$

$$\begin{aligned}
&\left\{\frac{\bar{H}_{i,j}}{4\Delta\theta^2}\left(\psi_{i+1,j}\right)^2-\frac{2\bar{H}_{i,j}}{4\Delta\theta^2}\psi_{i+1,j}\psi_{i-1,j}+\frac{\bar{H}_{i,j}}{4\Delta\theta^2}\left(\psi_{i-1,j}\right)^2\right\}\\
&+\left(\frac{\bar{H}_{i,j}}{\Delta\theta^2}\psi_{i,j}\psi_{i+1,j}-\frac{2\bar{H}_{i,j}}{\Delta\theta^2}\psi_{i,j}\psi_{i,j}+\frac{\bar{H}_{i,j}}{\Delta\theta^2}\psi_{i,j}\psi_{i-1,j}\right)\\
&+\left(\frac{\left(-\bar{H}_{i+1,j}+\bar{H}_{i-1,j}\right)}{4\Delta\theta^2}\psi_{i,j}\psi_{i+1,j}+\frac{\left(\bar{H}_{i+1,j}-\bar{H}_{i-1,j}\right)}{4\Delta\theta^2}\psi_{i,j}\psi_{i-1,j}\right)-\psi_{i,j}^2\left[\frac{\bar{H}_{i+1,j}-2\bar{H}_{i,j}+\bar{H}_{i-1,j}}{\Delta\theta^2}\right]\\
&-\left(\frac{D}{L}\right)^2\psi_{i,j}^2\left[\frac{\bar{H}_{i,j+1}-2\bar{H}_{i,j}+\bar{H}_{i,j-1}}{\Delta Z^2}\right]+\\
&\left(\frac{D}{L}\right)^2\left\{\frac{\bar{H}_{i,j}}{4\Delta Z^2}\left(\psi_{i,j+1}\right)^2-\frac{2\bar{H}_{i,j}}{4\Delta Z^2}\psi_{i,j+1}\psi_{i,j-1}+\frac{\bar{H}_{i,j}}{4\Delta Z^2}\left(\psi_{i,j-1}\right)^2\right\}\\
&+\left(\frac{D}{L}\right)^2\left(\frac{\bar{H}_{i,j}}{\Delta Z^2}\psi_{i,j}\psi_{i,j+1}-\frac{2\bar{H}_{i,j}}{\Delta Z^2}\psi_{i,j}\psi_{i,j}+\frac{\bar{H}_{i,j}}{\Delta Z^2}\psi_{i,j}\psi_{i,j-1}\right)\\
&+\left(\frac{D}{L}\right)^2\left(\frac{\left(-\bar{H}_{i,j+1}+\bar{H}_{i,j-1}\right)}{4\Delta Z^2}\psi_{i,j}\psi_{i,j+1}+\frac{\left(\bar{H}_{i,j+1}-\bar{H}_{i,j-1}\right)}{4\Delta Z^2}\psi_{i,j}\psi_{i,j-1}\right)=\Lambda\left[\frac{\psi_{i+1,j}-\psi_{i-1,j}}{2\Delta\theta}\right]+2\Lambda\frac{\partial(\psi)}{\partial\tau}
\end{aligned}\tag{2.37}$$

$$\begin{Bmatrix} \psi_{i,j-1} \\ \psi_{i-1,j} \\ \psi_{i,j} \\ \psi_{i+1,j} \\ \psi_{i,j+1} \end{Bmatrix}^T \begin{bmatrix} A_{11} & 0 & 0 & 0 & A_{15} \\ 0 & A_{22} & 0 & A_{24} & 0 \\ A_{31} & A_{32} & A_{33} & A_{34} & A_{35} \\ 0 & A_{42} & 0 & A_{44} & 0 \\ A_{51} & 0 & 0 & 0 & A_{55} \end{bmatrix} \begin{Bmatrix} \psi_{i,j-1} \\ \psi_{i-1,j} \\ \psi_{i,j} \\ \psi_{i+1,j} \\ \psi_{i,j+1} \end{Bmatrix} + \tag{2.38}$$

$$\begin{bmatrix} 0 & \frac{\Lambda}{2\Delta\theta} & 0 & -\frac{\Lambda}{2\Delta\theta} & 0 \end{bmatrix} \begin{Bmatrix} \psi_{i,j-1} \\ \psi_{i-1,j} \\ \psi_{i,j} \\ \psi_{i+1,j} \\ \psi_{i,j+1} \end{Bmatrix} = 2\Lambda \frac{\partial(\psi)}{\partial\tau}$$

where,

$$A_{11} = \frac{D^2}{L^2}\frac{\bar{H}_{i,j}}{4(\Delta Z)^2} \qquad A_{34} = \frac{\bar{H}_{i,j}}{\Delta\theta^2} + \frac{\left(-\bar{H}_{i+1,j}+\bar{H}_{i-1,j}\right)}{4\Delta\theta^2}$$

$$A_{15} = -\frac{D^2}{L^2}\frac{\bar{H}_{i,j}}{4(\Delta Z)^2} \qquad A_{35} = \frac{D^2}{L^2}\frac{\bar{H}_{i,j}}{\Delta Z^2} + \frac{D^2}{L^2}\frac{\left(-\bar{H}_{i,j+1}+\bar{H}_{i,j-1}\right)}{4\Delta Z^2}$$

$$A_{22} = \frac{\bar{H}_{i,j}}{4(\Delta\theta)^2} \qquad A_{42} = -\frac{\bar{H}_{i,j}}{4(\Delta\theta)^2}$$

$$A_{24} = -\frac{\bar{H}_{i,j}}{4(\Delta\theta)^2} \qquad A_{44} = \frac{\bar{H}_{i,j}}{4(\Delta\theta)^2}$$

$$A_{31} = \frac{D^2}{L^2}\frac{\bar{H}_{i,j}}{\Delta Z^2} + \frac{D^2}{L^2}\frac{\left(\bar{H}_{i,j+1}-\bar{H}_{i,j-1}\right)}{4\Delta Z^2} \qquad A_{51} = -\frac{D^2}{L^2}\frac{\bar{H}_{i,j}}{4(\Delta Z)^2}$$

$$A_{32} = \frac{\left(\bar{H}_{i+1,j}-\bar{H}_{i-1,j}\right)}{4\Delta\theta^2} + \frac{\bar{H}_{i,j}}{\Delta\theta^2} \qquad A_{55} = \frac{D^2}{L^2}\frac{\bar{H}_{i,j}}{4(\Delta Z)^2}$$

$$A_{33} = -\frac{\bar{H}_{i+1,j}+\bar{H}_{i-1,j}}{\Delta\theta^2} - \left(\frac{D}{L}\right)^2\frac{\bar{H}_{i,j+1}+\bar{H}_{i,j-1}}{\Delta Z^2}$$

Hence, Eqn. 2.35 in $(i,j)^{th}$ node or q^{th} node can be written in a quadratic form as,

$$\left(\psi_q^e\right)^T \mathbf{A}_q^e\, \psi_q^e + \mathbf{b}_q^e\, \psi_q^e = 2\Lambda\frac{\partial\psi}{\partial\tau} \tag{2.39}$$

2.4 Modelling of the Top Foil

The top foil is supported by the bump foil as shown in Fig. 2.1. For the modelling of the top foil under loading condition, it can be represented by Fig. 2.3. The top foil structure has been modelled as a flat plate supported on axially and radially distributed linear springs located at every bump pitch as shown in Fig. 2.3. To calculate the elastic deformation of the foil structure the foil structure has been formulated based on Classical Plate Theory (CPT) using the methodology given in [108]. Thus neglecting the inertia effects, the governing equation for the deflection of the top foil is given as,

$$\frac{\partial^2}{\partial x^2}\left(D_{11}\frac{\partial^2 w_t}{\partial x^2}+D_{12}\frac{\partial^2 w_t}{\partial z^2}\right)+\frac{\partial^2}{\partial z^2}\left(D_{12}\frac{\partial^2 w_t}{\partial x^2}+D_{22}\frac{\partial^2 w_t}{\partial z^2}\right)+2\frac{\partial^2}{\partial x\partial z}\left(2D_{66}\frac{\partial^2 w_t}{\partial x\partial z}\right)+K_f w_t=(\bar{p}-p_a) \tag{2.40}$$

where, K_f is the bump foil stiffness and w_t is the deflection of the top foil.

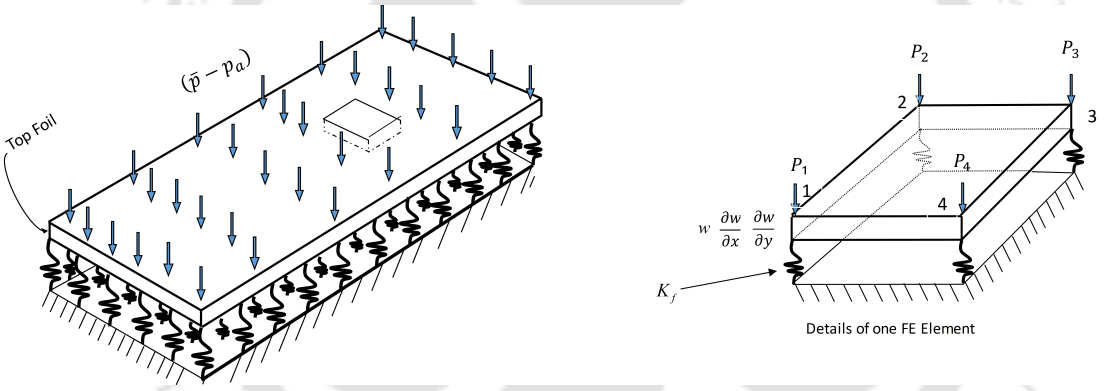

Figure 2.3: Configuration of top foil supported on bump strips and details of one element

Normalizing Eqn. 2.40 using, $S={}^{P_a}/_{K_f C}$, $\bar{w}_t={}^{w_t}/_{C}$ and other terms described above, we get,

$$\bar{w}_t=S(\bar{P}-1)-\left(\begin{array}{l}\frac{\partial^2}{\partial\theta^2}\left(D'_{11}\frac{\partial^2\bar{w}_t}{\partial\theta^2}+D'_{12}\frac{\partial^2\bar{w}_t}{\partial Z^2}\right)+\\ \frac{\partial^2}{\partial Z^2}\left(D'_{12}\frac{\partial^2\bar{w}_t}{\partial\theta^2}+D'_{22}\frac{\partial^2\bar{w}_t}{\partial Z^2}\right)+4\frac{\partial^2}{\partial\theta\partial Z}\left(D'_{66}\frac{\partial^2\bar{w}_t}{\partial\theta\partial Z}\right)\end{array}\right) \tag{2.41}$$

where, $D'_{11}=\frac{C}{P_aR^4}D_{11}$, $D'_{12}=\frac{C}{P_aR^2L^2}D_{12}$, $D'_{22}=\frac{C}{P_aL^4}D_{22}$, $D'_{66}=\frac{C}{P_aR^2L^2}D_{66}$ and $D_{11}=D_{22}=\frac{Et_t^3}{12(1-\upsilon^2)}$,$D_{12}=\frac{\upsilon Et_t^3}{12(1-\upsilon^2)}$, $D_{66}=\frac{Gt_t^3}{12}$ in which, υ is the Poisson's ratio, E is the Young's modulus of the top foil, t_t is the thickness of the top foil and G is the shear modulus.

The domain is discretized as $(m+1)\times(n+1)$ for solving the Reynolds equation, which in turn used for calculating the hydrodynamic gas pressure using finite difference

scheme. The same discretization of the domain is used for calculating the foil deflection using finite element method. The finite element equation for an element in matrix form can be written as [109],

$$[K^e_{CPT}]\{w^e_{CPT}\} = \{F^e_{CPT}\} \tag{2.42}$$

where, $[K^e_{CPT}]$ is the elemental stiffness matrix, $\{w^e_{CPT}\}$ is the vector of primary nodal variables or generalized displacements, and $\{F^e_{CPT}\}$ is the force vector. The elemental stiffness matrix $[K^e_{CPT}]$ can be written as,

$$\left[K^e_{CPT}\right] = \int_{\Omega_e} [B_2]^T [C] [B_2] \, d\mathbf{x} \tag{2.43}$$

where, $[B_2] = \begin{bmatrix} \frac{\partial^2 N_1}{\partial \theta^2} & \frac{\partial^2 N_2}{\partial \theta^2} & \cdots & \frac{\partial^2 N_{12}}{\partial \theta^2} \\ \frac{\partial^2 N_1}{\partial Z^2} & \frac{\partial^2 N_2}{\partial Z^2} & \cdots & \frac{\partial^2 N_{12}}{\partial Z^2} \\ 2\frac{\partial^2 N_1}{\partial \theta \partial Z} & 2\frac{\partial^2 N_2}{\partial \theta \partial Z} & \cdots & 2\frac{\partial^2 N_{12}}{\partial \theta \partial Z} \end{bmatrix}_{3\times 12}$ and, $[C] = \begin{bmatrix} D'_{11} & D'_{12} & 0 \\ D'_{12} & D'_{22} & 0 \\ 0 & 0 & D'_{66} \end{bmatrix}_{3\times 3}$

in which $\{N\}^T = \begin{Bmatrix} N_1 & N_2 & \cdots & N_{12} \end{Bmatrix}^T$ and $N_1, N_2, N_3, \cdots, N_{12}$ are the shape functions.

The force vector $\{F^e_{CPT}\}$ is calculated as,

$$\{F^e_{CPT}\} = \int_{\Psi} \mathbf{P}\{\mathbf{N}\} d\Psi \tag{2.44}$$

where, the pressure at a point on the domain is calculated as,

$$\mathbf{P} = N'_1 P_{i,j} + N'_2 P_{i,j+1} + N'_3 P_{i+1,j+1} + N'_4 P_{i+1,j} \tag{2.45}$$

and, $\{\mathbf{N}\} = \begin{Bmatrix} N_1 & N_2 & N_3 & \ldots & N_{10} & N_{11} & N_{12} \end{Bmatrix}$ are the interpolation functions.

The shape functions for the nodes $(i,j)^{th}$, $(i,j+1)^{th}$, $(i+1,j+1)^{th}$ and $(i+1,j)^{th}$ nodes are denoted as N'_1, N'_2, N'_3, N'_4 respectively thus constituting four-noded quadrilateral elements.

The size of the global matrix for a particular 2D CPT will be $[3(m+1)(n+1)] \times [3(m+1)(n+1)]$ considering three degrees of freedom per node. Therefore, the assem-

bled equation for the entire domain can be written as,

$$[K_{CPT}]\{w_{CPT}\} = \{F_{CPT}\} \tag{2.46}$$

where, $[K_{CPT}]$ is the assembled stiffness matrix, $\{w_{CPT}\}$is the nodal deflections and slopes and $\{F_{CPT}\}$ is the force vector.

Thus the nodal foil deflection is calculated using the finite element method and incorporated in Eqn. 2.26 to calculate the non-dimensional film thickness. This non-dimensional film thickness in turn is used in Eqn. 2.25 to compute the hydrodynamic pressure.

2.5 Crank Nicholson Method

In the explicit scheme the time dependent terms of the Partial Difference Equations (PDEs) are lagging in time in the integration of rotor Ordinary Differential Equations (ODEs), hence does not preserve the true simultaneously coupled nature of the state variables. The Crank Nicholson Method is an implicit method for time dependent problems, which implies solving an equation involving both the current state of the system and the later one [110]. It is a second-order finite difference method and is unconditionally stable. Thus, the time derivative on right hand side of Eqn. 2.15, Eqn. 2.25 and Eqn. 2.39 is approximated using Crank Nicholson Method.

Therefore, $\{\psi\}^{k-1} = \left\{\psi\left(t^{k-1}\right)\right\}$ has been solved at time t^{k-1} and $\{\psi\}^{k} = \left\{\psi\left(t^{k}\right)\right\}$ to be solved at time $t^{k} = t^{k-1} + \Delta t$. Then, from Crank-Nicolson Method, the nodal values of the next time step as,

$$\{\psi\}^{k} = \{\psi\}^{k-1} + \frac{\Delta t}{2}\left[\left(\frac{\partial \psi}{\partial \tau}\right)^{k} + \left(\frac{\partial \psi}{\partial \tau}\right)^{k-1}\right] \tag{2.47}$$

Where, $\psi = ph$ for Eqn. 2.15 and $\psi = \bar{P}\bar{H}$ for Eqn. 2.25 and Eqn. 2.39.
Therefore,

$$\frac{2}{\Delta t}\left[\{\psi\}^{k} - \{\psi\}^{k-1}\right] = \left[\left(\frac{\partial \psi}{\partial \tau}\right)^{k} + \left(\frac{\partial \psi}{\partial \tau}\right)^{k-1}\right] \tag{2.48}$$

Thus, Eqn. 2.15

$$\left[\left(p_q^e\right)^T\right]^k \left[\mathbf{A}_q^e\right]^k \left[p_q^e\right]^k + \left[\mathbf{b}_q^e\right]^k \left[p_q^e\right]^k = \left[12\mu r^2 \frac{\partial \psi}{\partial \tau}\right]^k \tag{2.49}$$

and,

$$\left[\left(p_q^e\right)^T\right]^{k-1}\left[\mathbf{A}_q^e\right]^{k-1}\left[p_q^e\right]^{k-1}+\left[\mathbf{b}_q^e\right]^{k-1}\left[p_q^e\right]^{k-1}=\left[12\mu r^2\frac{\partial\psi}{\partial\tau}\right]^{k-1} \tag{2.50}$$

Adding Eqn. 2.49 and 2.50, we get,

$$\begin{aligned}&\left[\left(p_q^e\right)^T\right]^{k}\left[\mathbf{A}_q^e\right]^{k}\left[p_q^e\right]^{k}+\left[\mathbf{b}_q^e\right]^{k}\left[p_q^e\right]^{k}-\tfrac{24\mu r^2}{\Delta t}\left[\{\psi\}^k\right]=\\&-\left\{\left[\left(p_q^e\right)^T\right]^{k-1}\left[\mathbf{A}_q^e\right]^{k-1}\left[p_q^e\right]^{k-1}+\left[\mathbf{b}_q^e\right]^{k-1}\left[p_q^e\right]^{k-1}+\tfrac{24\mu r^2}{\Delta t}\left[\{\psi\}^{k-1}\right]\right\}\end{aligned} \tag{2.51}$$

Therefore, Eqn. 2.25 can be written as,

$$\begin{aligned}&\left[\left(\bar{P}_q^e\right)^T\right]^{k}\left[\mathbf{A}_q^e\right]^{k}\left[\bar{P}_q^e\right]^{k}+\left[\mathbf{b}_q^e\right]^{k}\left[\bar{P}_q^e\right]^{k}-\tfrac{4\Lambda}{\Delta t}\left[\{\psi\}^k\right]=\\&-\left\{\left[\left(\bar{P}_q^e\right)^T\right]^{k-1}\left[\mathbf{A}_q^e\right]^{k-1}\left[\bar{P}_q^e\right]^{k-1}+\left[\mathbf{b}_q^e\right]^{k-1}\left[\bar{P}_q^e\right]^{k-1}+\tfrac{4\Lambda}{\Delta t}\left[\{\psi\}^{k-1}\right]\right\}\end{aligned} \tag{2.52}$$

and Eqn. 2.39 can be written as,

$$\begin{aligned}&\left[\left(\psi_q^e\right)^T\right]^{k}\left[\mathbf{A}_q^e\right]^{k}\left[\psi_q^e\right]^{k}+\left[\mathbf{b}_q^e\right]^{k}\left[\psi_q^e\right]^{k}-\tfrac{4\Lambda}{\Delta t}\left[\{\psi\}^k\right]=\\&-\left\{\left[\left(\psi_q^e\right)^T\right]^{k-1}\left[\mathbf{A}_q^e\right]^{k-1}\left[\psi_q^e\right]^{k-1}+\left[\mathbf{b}_q^e\right]^{k-1}\left[\psi_q^e\right]^{k-1}+\tfrac{4\Lambda}{\Delta t}\left[\{\psi\}^{k-1}\right]\right\}\end{aligned} \tag{2.53}$$

In Eqn. 2.51, Eqn. 2.52 and Eqn. 2.53 there are no more time derivatives. Furthermore, all the terms on the right hand side are either known from source terms or from the field solution at the previous time step.

2.6 Rotor Supported on GFBs

In Fig. 2.4, the schematics of the rotor bearing system has been shown. The system of equations describing the motion of the rigid rotor at the centre of gravity considering the shaft mass, transverse mass moment of inertia and the gyroscopic moment can be written as [83],

$$Mx'' = F_x \tag{2.54}$$

$$My'' = F_y \tag{2.55}$$

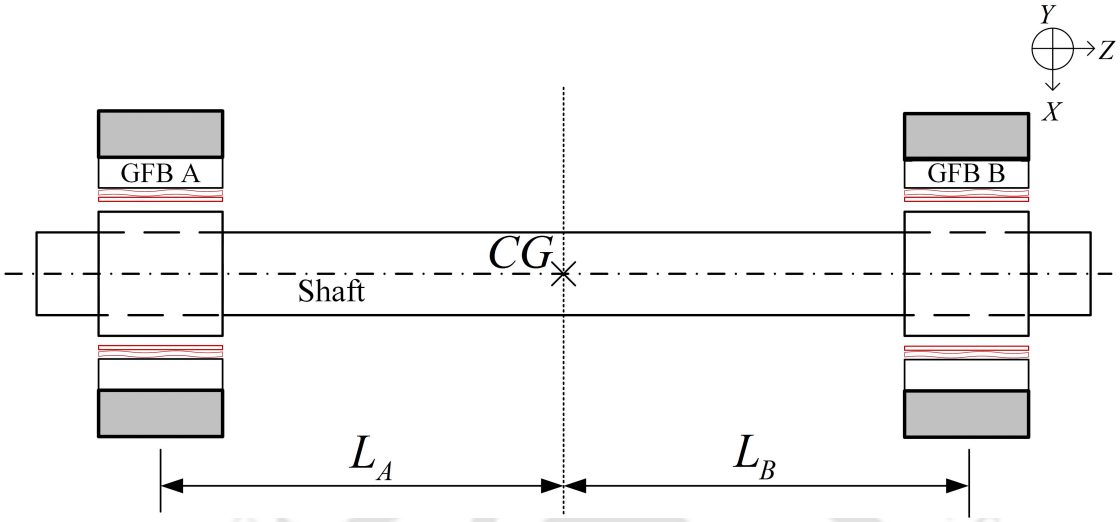

Figure 2.4: Schematic of rotor with GFB

$$I_{xx}\varphi'' - I_{zz}\omega\gamma' = M_x \tag{2.56}$$

$$I_{yy}\gamma'' + I_{zz}\omega\varphi' = M_y \tag{2.57}$$

In matrix form equation of motion at center of gravity can be written

$$[M_{CG}]\{q''_{CG}\} + [G_{CG}]\{q'_{CG}\} = \{F_{CG}\} + \{W_{CG}\} \tag{2.58}$$

where, $[M_{CG}] = \begin{bmatrix} M & 0 & 0 & 0 \\ 0 & M & 0 & 0 \\ 0 & 0 & I_{xx} & 0 \\ 0 & 0 & 0 & I_{yy} \end{bmatrix}$ $[G_{CG}] = \begin{bmatrix} 0 & 0 & 0 & 0 \\ 0 & 0 & 0 & 0 \\ 0 & 0 & 0 & -I_{zz}\omega \\ 0 & 0 & I_{zz}\omega & 0 \end{bmatrix}$

$\{q_{CG}\} = \begin{Bmatrix} x_{CG} \\ y_{CG} \\ \varphi \\ \gamma \end{Bmatrix}$ $\{F_{CG}\} = \begin{Bmatrix} F_x \\ F_y \\ M_x \\ M_y \end{Bmatrix}$

The equations of motion can be written in bearing location A and B using the following linear transformation,

$$[T_1] = \begin{bmatrix} 1 & 0 & 0 & L_A \\ 0 & 1 & -L_A & 0 \\ 1 & 0 & 0 & -L_B \\ 0 & 1 & L_B & 0 \end{bmatrix} \text{ and } [T_2] = \begin{bmatrix} 1 & 0 & 1 & 0 \\ 0 & 1 & 0 & 1 \\ 0 & -L_A & 0 & L_B \\ L_A & 0 & -L_B & 0 \end{bmatrix} \text{ So that, } \{q_{AB}\} =$$

$$[T_1] \begin{Bmatrix} x_{CG} \\ y_{CG} \\ \gamma \\ \varphi \end{Bmatrix} \text{ or } \{q_{AB}\} = [T_1]\{q_{CG}\}$$

$$\text{and } \{F_{AB}\} = [T_2]^{-1} \begin{Bmatrix} F_x \\ F_y \\ M_x \\ M_y \end{Bmatrix} \text{ or } \{F_{AB}\} = [T_2]^{-1}\{F_{CG}\}$$

Therefore, using the transformation matrix, $[T_1]$ and $[T_2]$ the equation of motion at the centre of gravity can transformed into the bearing location A and B as,

$$[M_{CG}][T_1]^{-1}\{q''_{AB}\} + (-\omega[G_{CG}])[T_1]^{-1}\{q'_{AB}\} = [T_2]\{F_{AB}\} + [T_2]\{W_{AB}\} \quad (2.59)$$

It can also be shown that, $[T_2]^{-1} = [T_1]^{-T}$

Therefore, the Eqn. 2.58 at the bearing location can be written as,

$$[M_{AB}]\{q''_{AB}\} + (-\omega[G_{AB}])\{q'_{AB}\} = \{F_{AB}\} + \{W_{AB}\} \quad (2.60)$$

where, $[M_{AB}] = [T_1]^{-T}[M_{CG}][T_1]^{-1}$, $[G_{AB}] = [T_1]^{-T}[G_{CG}][T_1]^{-1}$

In which,

$$[M_{AB}] = \frac{1}{L^2}\begin{bmatrix} L_B^2M + I_{yy} & 0 & L_AL_BM - I_{yy} & 0 \\ 0 & L_B^2M + I_{xx} & 0 & L_AL_BM - I_{xx} \\ L_AL_BM - I_{yy} & 0 & L_A^2M + I_{yy} & 0 \\ 0 & L_AL_BM - I_{xx} & 0 & L_A^2M + I_{xx} \end{bmatrix};$$

$$[G_{AB}] = \frac{1}{L^2}\begin{bmatrix} 0 & -I_{zz} & 0 & I_{zz} \\ I_{zz} & 0 & -I_{zz} & 0 \\ 0 & I_{zz} & 0 & -I_{zz} \\ -I_{zz} & 0 & I_{zz} & 0 \end{bmatrix};$$

$$\{q_{AB}\} = \begin{Bmatrix} x_A \\ y_A \\ x_B \\ y_B \end{Bmatrix}; \{F_{AB}\} = \begin{Bmatrix} F_{xA} \\ F_{yA} \\ F_{xB} \\ F_{yB} \end{Bmatrix}; \begin{Bmatrix} F_{xA} \\ F_{yA} \end{Bmatrix} = \int_{-L/D}^{L/D}\int_{0}^{2\pi} \begin{Bmatrix} p\cos\theta d\theta dz \\ psin\theta d\theta dz \end{Bmatrix}$$

In non-dimensional from the equations of motions can be written as, $\{\bar{q}_{AB}\} = \frac{\{q_{AB}\}}{C}$ and $\tau = \omega t$ hence,

$$\begin{Bmatrix} F_{xA} \\ F_{yA} \end{Bmatrix} = P_a r^2 \int_{-L/D}^{L/D}\int_{0}^{2\pi} \begin{Bmatrix} \bar{P}\cos\theta d\theta dZ \\ \bar{P}sin\theta d\theta dZ \end{Bmatrix} \tag{2.61}$$

therefore, $\begin{Bmatrix} \bar{F}_{xA} \\ \bar{F}_{yA} \end{Bmatrix} = \frac{1}{P_a r^2} \begin{Bmatrix} F_{xA} \\ F_{yA} \end{Bmatrix}$

Thus

$$\begin{Bmatrix} \bar{F}_{xA} \\ \bar{F}_{yA} \end{Bmatrix} = \int_{0}^{L}\int_{0}^{2\pi} \begin{Bmatrix} \bar{P}\cos\theta d\theta dZ \\ \bar{P}sin\theta d\theta dZ \end{Bmatrix} \tag{2.62}$$

$\{q'_{AB}\} = \frac{d}{dt}\{q_{AB}\} = \frac{d\{q'_{AB}\}}{d\tau}\frac{d\tau}{dt} = \omega\frac{d\{q'_{AB}\}}{d\tau} = \omega\{\ddot{q}_{AB}\}$

i.e., $\{q''_{AB}\} = \omega^2\{\ddot{q}_{AB}\}$

Therefore, Eqn. 2.60 can be non-dimensionalised as,

$$\frac{[M_{AB}]}{P_a r^2}\{q''_{AB}\} - \frac{\omega[G_{AB}]}{P_a r^2}\{q'_{AB}\} = \frac{\{F_{AB}\}}{P_a r^2} + \frac{\{W_{AB}\}}{P_a r^2} \tag{2.63}$$

$$\frac{[M_{AB}]}{P_a r^2} c\omega^2 \{\ddot{q}_{AB}\} - \frac{\omega[G_{AB}]}{P_a r^2} c\omega \{\dot{q}_{AB}\} = \{\bar{F}_{AB}\} + \{\bar{W}_{AB}\} \tag{2.64}$$

$$\frac{c\omega^2}{P_a r^2}[M_{AB}]\{\ddot{q}_{AB}\} - \frac{c\omega^2}{P_a r^2}[G_{AB}]\{\dot{q}_{AB}\} = \{\bar{F}_{AB}\} + \{\bar{W}_{AB}\} \tag{2.65}$$

$$[\bar{M}_{AB}]\{\ddot{q}_{AB}\} - [\bar{G}_{AB}]\{\dot{q}_{AB}\} = \{\bar{F}_{AB}\} + \{\bar{W}_{AB}\} \tag{2.66}$$

where, $[\bar{M}_{AB}] = \frac{c\omega^2}{P_a r^2}[M_{AB}]$, $[\bar{G}_{AB}] = \frac{c\omega^2}{P_a r^2}[G_{AB}]$, $\{\bar{F}_{AB}\} = \frac{1}{P_a r^2}\{F_{AB}\}$ and $\{\bar{W}_{AB}\} = \frac{1}{P_a r^2}\{W_{AB}\}$

2.7 Results and Discussion

The time step for the present simulation has been taken as 10^{-5}. Therefore, to simulate the rotor for a duration of 2 seconds, the number of time steps required is 200000. The code was written in MATLAB® on a standard desktop computer with Intel® Core™ i5 Processor.

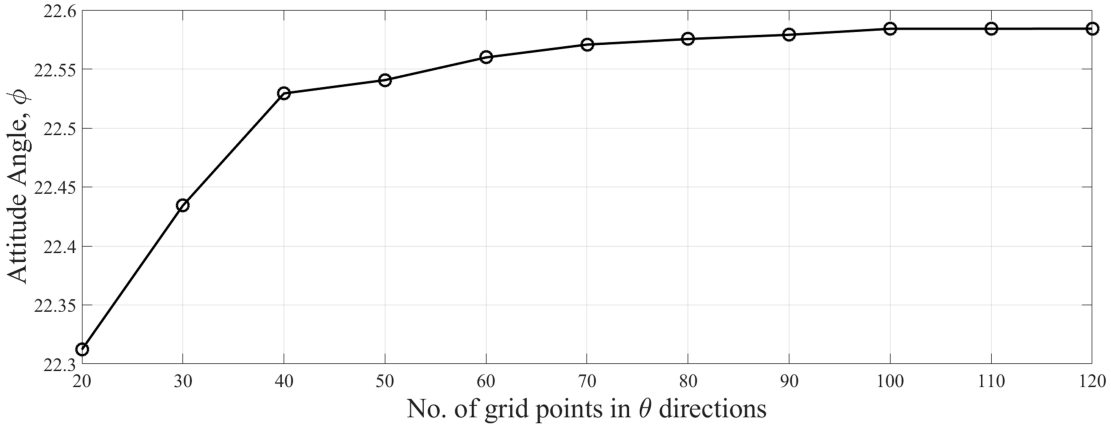

Figure 2.5: Variation of attitude angle due to grid size θ in direction

In the discretization process, the size of the grid influence the predicted results. Finer grid size provides better prediction. However, as the grid size increases, the computational time increases. Therefore, first a grid analysis has been done. The effect of grid size $(m \times n)$ on the attitude angle has been investigated. In Fig. 2.5 the variation of attitude angle due to variation in m with $n = 10$ has been shown. It has been observed that as the no of grid points are increased in θ direction, i.e. when m is increased the attitude

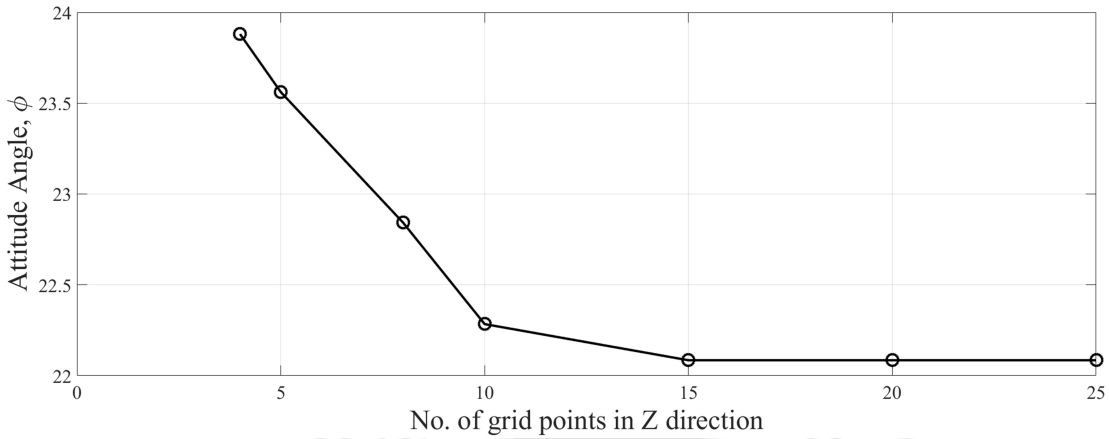

Figure 2.6: Variation of Attitude angle due to grid size Z in direction

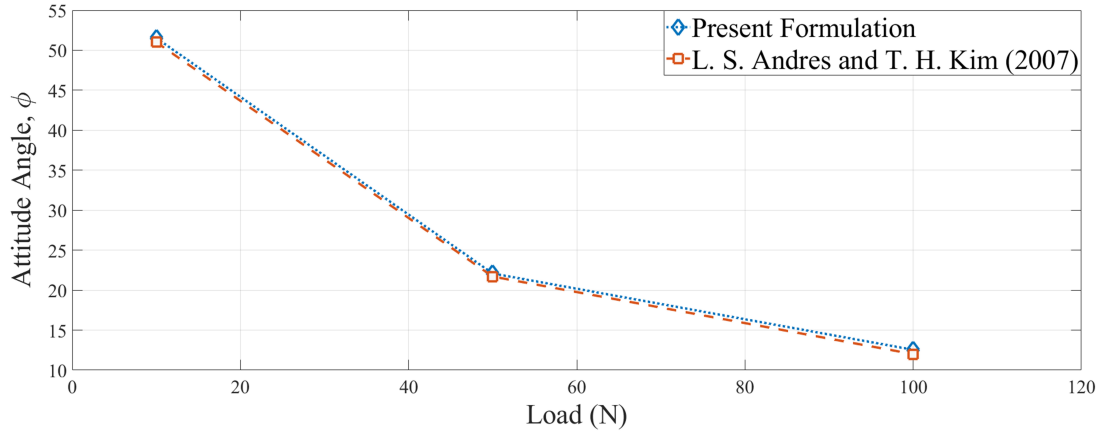

Figure 2.7: Validation of the attitude angle vs static load

angle increases. However, after $m = 100$, the attitude angle remains constant. Further, $m = 100$ is kept constant and n is varied. The variation of attitude angle due to variation of n has been shown in Fig. 2.6. It has been observed that as n is increased from 4 to 15, the attitude angle decreases. After $n = 15$ the attitude angle becomes constant, suggesting no effect on the attitude angle. Therefore the grid size of 100×15 has been choosen for the current work as finer grid has no effect on the results.

In order to validate the current formulation, the attitude angle of the journal versus the applied load at 30000 rpm has been depicted in Fig. 2.7. Figure 2.7 shows the predicted attitude angle using the current formulation and the attitude angle obtained by San Andrés and Kim [5]. Similar trend between the two results has been obtained with a small difference. The difference may be due to the different solution strategy used to solve the governing equation. Further, the simulation of the orbit has been validated with Larsen et al. [111]. The trajectory of the rotor, rotating at 12000 rpm using the

current formulation has been shown in Fig. 2.8. Although the trajectory simulated using the present formulation, and the trajectory simulated by Larsen et al. [111] has a little discrepancy, the trajectory converges to the same equilibrium point.

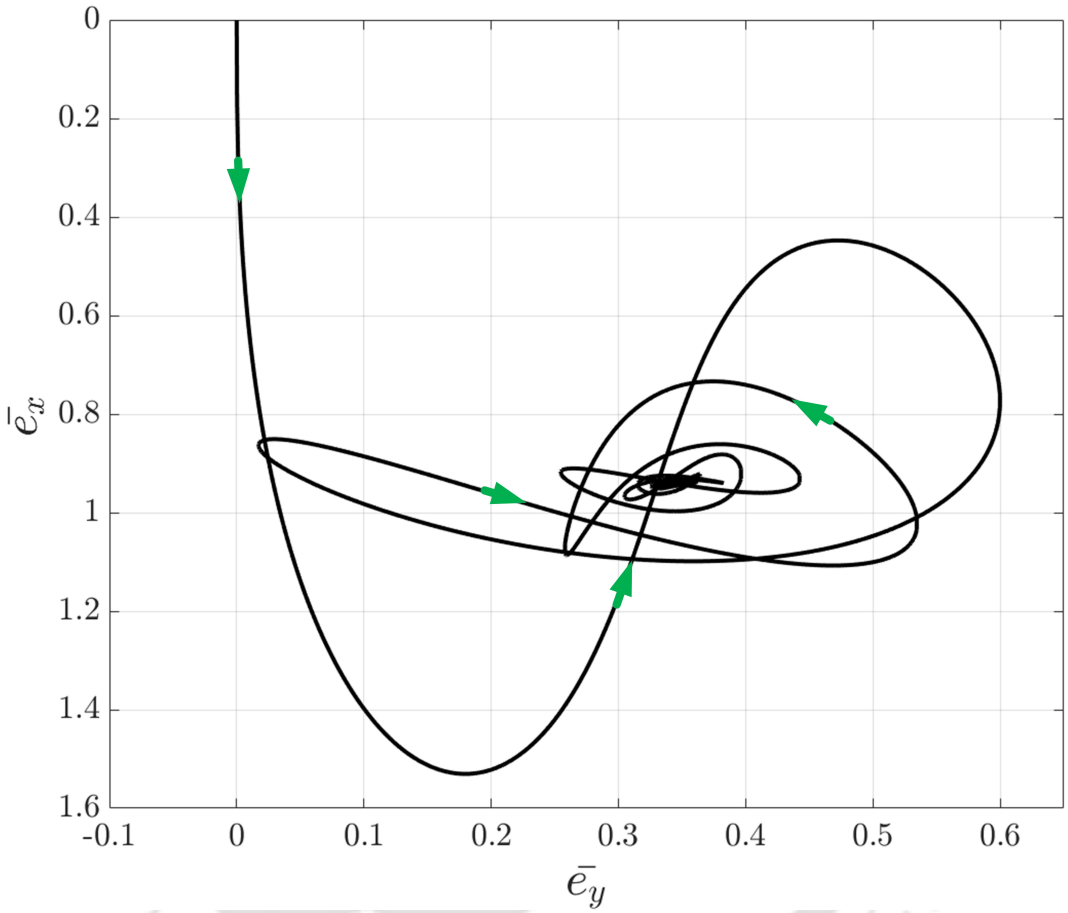

Figure 2.8: Validation of the rotor trajectory

In Table 2.2 the effect of grid sizes on the journal revolution has been presented. The time for computing the first 100 rev at 12000 rpm has been recorded. Further, the time for computing the next 100 rev has been recorded. It has been observed that the time required for computing the journal response of first 100 rev is always more than the time to compute the next 100 rev. Further, the computational time increases with the increase in grid size

In Fig. 2.9 the trajectory of the rotor rotating at 10000 rpm has been shown. The trajectory is somewhat different for both the cases, but the trajectory converges to the same equilibrium point. In Fig. 2.10 the trajectory of the rotor rotating at 16200 rpm simulated using the two simulation has been shown. It has been observed that with P formulation the rotor shows unstable operation (Fig. 2.10a), however with the ψ formulation the rotor shows stable operation. However the cause of the damped effect

Table 2.1: Parameters of the GFBs and the rotor system [83]

Parameter	Values
Bearing Radius, R	19.05 mm
Bearing Length, L	38.10 mm
Bearing Clearance, C	32 μm
Bump Foil Stiffness, K_f	9.26 GN/m^3
Ambient Pressure, P_a	1×10^5 Pa
Air Viscosity, μ	1.95×10^{-5} Pa.s

Table 2.2: Effect of grid size

Grid Size	Formulation	Time required for first 100 rev (s)	Time required for next 100 rev (s)
50×10	P Formulation	2930	2350
	ψ Formulation	2775	2175
50×15	P Formulation	2960	2378
	ψ Formulation	2791	2219
100×10	P Formulation	3412	2745
	ψ Formulation	3234	2650
100×15	P Formulation	3456	2811
	ψ Formulation	3523	2731

occurring due to the ψ formulation is not well understood. A further study is required to identify this cause. In view of the above, P formulation is considered to be reliable for carrying out further analysis in the latter chapters.

2.8 Inferences

In this chapter, the description of gas foil journal bearing and the solution strategy has been given. The discretization of the governing Reynolds equation using the central finite difference method has been shown. Moreover, an alternative formulation for the discretization of the Reynolds equation has been described. The time dependent terms of the Reynolds Equation have been discretized using the Crank Nicholson Method. The nonlinear system of equation obtained using the finite difference method has been solved using the Newton-Raphson method. The equation of motion of the rigid rotor in the bearing location has also been described. The validation of the current formulation

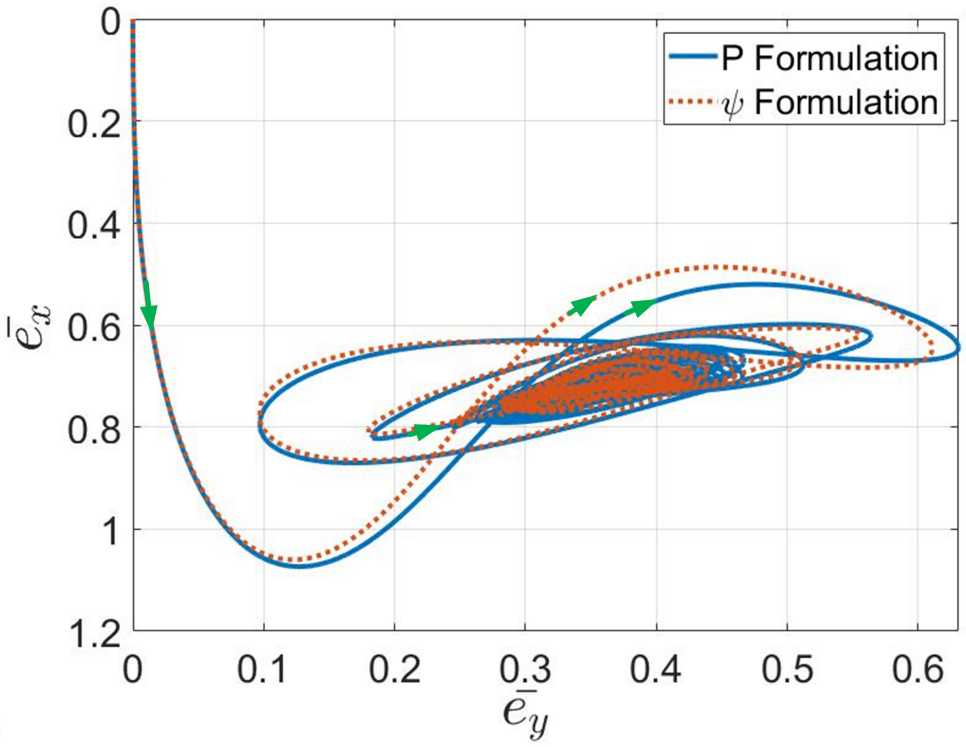

Figure 2.9: Trajectories of rotor at 10000 rpm

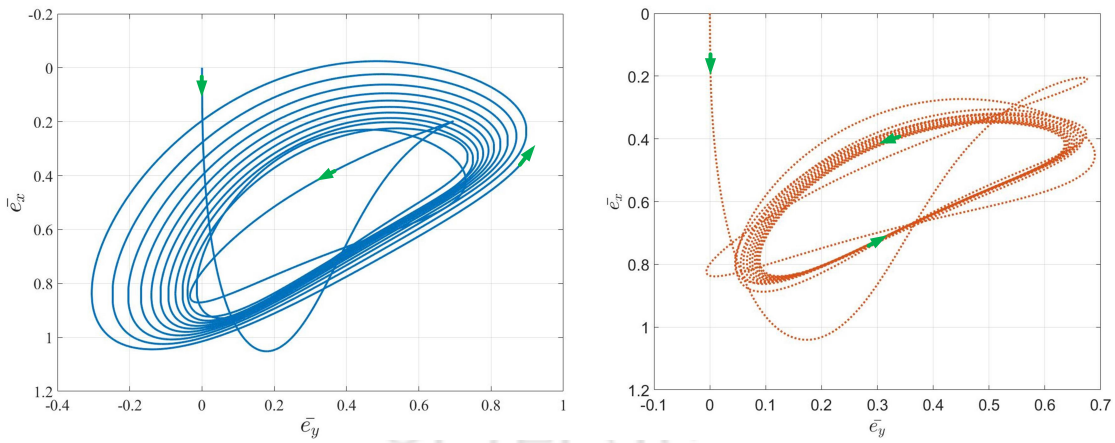

Figure 2.10: Trajectory of the rotor at 16200 rpm (a) with *P* formulation (b) with ψ formulation

has been provided. The effect of the two formulation on the stability analysis of the GFB has been discussed. The trajectories computed using the two formulation showed disparity although converged to the same equilibrium point. It is not clearly known how the damping effect is more prominent in ψ formulation compared to *P* formulation. Therefore, *P* formulation is used in latter chapters for future analysis.

In the next chapter the design and modelling of active magnetic bearing has been described.

3

Modelling of Active Magnetic Bearing

Contents

3.1 Introduction

In the previous chapter, the mathematical modelling of the Gas Foil Bearings (GFBs) has been presented. Since, the present is a combination of the GFBs and Active Magnetic Bearings (AMBs), the design and modelling of the AMBs are an indispensable part of the analysis of the hybrid GFBs. AMBs are electromagnetic actuators that work on the principle of electromagnetic suspension. The main objective of designing an AMB is the generation of magnetic forces that develop provides the required forces to support the rotor as well as to eliminate any externally applied forces. The design of AMBs is an iterative process as the design of each individual element of the AMB will have a strong influence on the design of other elements.

This chapter includes the design procedures adopted for conventional AMBs. Further, modelling of AMB using the Reluctance Network Method has been described in details. The active magnetic bearing has been considered as hetero-polar with eight poles and the generation of radial forces has been described.

3.2 Preliminary Design Procedure of AMB

In general, the required load capacity of the bearing has to be known while designing any active magnetic bearing. The load carrying capacity of the AMB is defined as the maximum force that the bearing can produce in any given direction. The load capacity of the bearing depends primarily on the type of the ferromagnetic material and the geometric design of the bearing magnet. The magnetic bearing's load capacity is limited due to the bearing coil current. Depending on the system, high coil current might only be maintained over a specific time period in order to prevent the power amplifier and the bearing coils from overheating. Therefore, the magnetic bearing has to be designed in such a way that the load capacity is well above the maximum expected external disturbance force. Hence, it can be understood that, unlike the conventional ball or fluid film bearings, the magnetic bearing does not provide any overload capability. Considering all the poles to be symmetric, the load carrying capacity along the vertical direction is given as [112],

$$F_{\max} = \sum_{j=1}^{n} \frac{B_j^2 A_p}{2\mu_0} \sin\theta_j \tag{3.1}$$

where, B_j is the magnetic flux density, A_p is the cross sectional area of the flux path and μ_0 is the permeability of free space.

Few other parameters which are to be pre-decided are tabulated below, along with its effect on the bearing design.

Table 3.1: Effects of free design parameters [113]

Parameter	Effect
Flux Splitting, β	• 0.5 for split flux and 1 for unsplit flux • Split flux uses the iron efficiently, hence smaller size bearings but high rotating losses and complicated current control • Unsplit flux has low rotating losses and simpler current control
Number of poles, n_p	• For larger shaft size the no. of poles should be increased • Lesser no. of poles yields smaller stator outside diameter for small journal radius
Iron Ratio, f_i	• The iron ratio is the ratio between the sum of the arc lengths of the pole faces to the available circumference • The lower limit is 0 while upper limit is based on leakage rules as $2\pi\left(r_j + S_0\right)\left(1 - f_i\right) > 3S_0$ • Large iron ratio reduces the area available for coils and can therefore, increase the stator outer diameter • Small iron ratio implies inadequate ferromagnetic material and leads to larger axial length
Saturation Flux, B_{sat}	• B_{sat} is the saturation of the ferromagnetic material, where the magnetic flux does not increase even though the current producing the magnetic field is increased. • Higher B_{sat} gives higher load capacity with lesser ferromagnetic material, however, bigger coils are required to take the advantage • Using Si-alloyed transformer sheets, the maximum flux density of 1.6 Tesla is recommended • Using Cobalt alloys, the maximum flux density of 2.4 Tesla is recommended
Biasing Ratio, α	• The biasing ratio is the ratio between the bias current and the current at which the stator iron begins to saturate • Higher α (up to 0.5) offers better slew rates and ensure linear operation. • Increase α increases the stiffness and the coil size

Few design constraints and design procedure to be considered while designing the geometry of the bearing actuator are listed below,

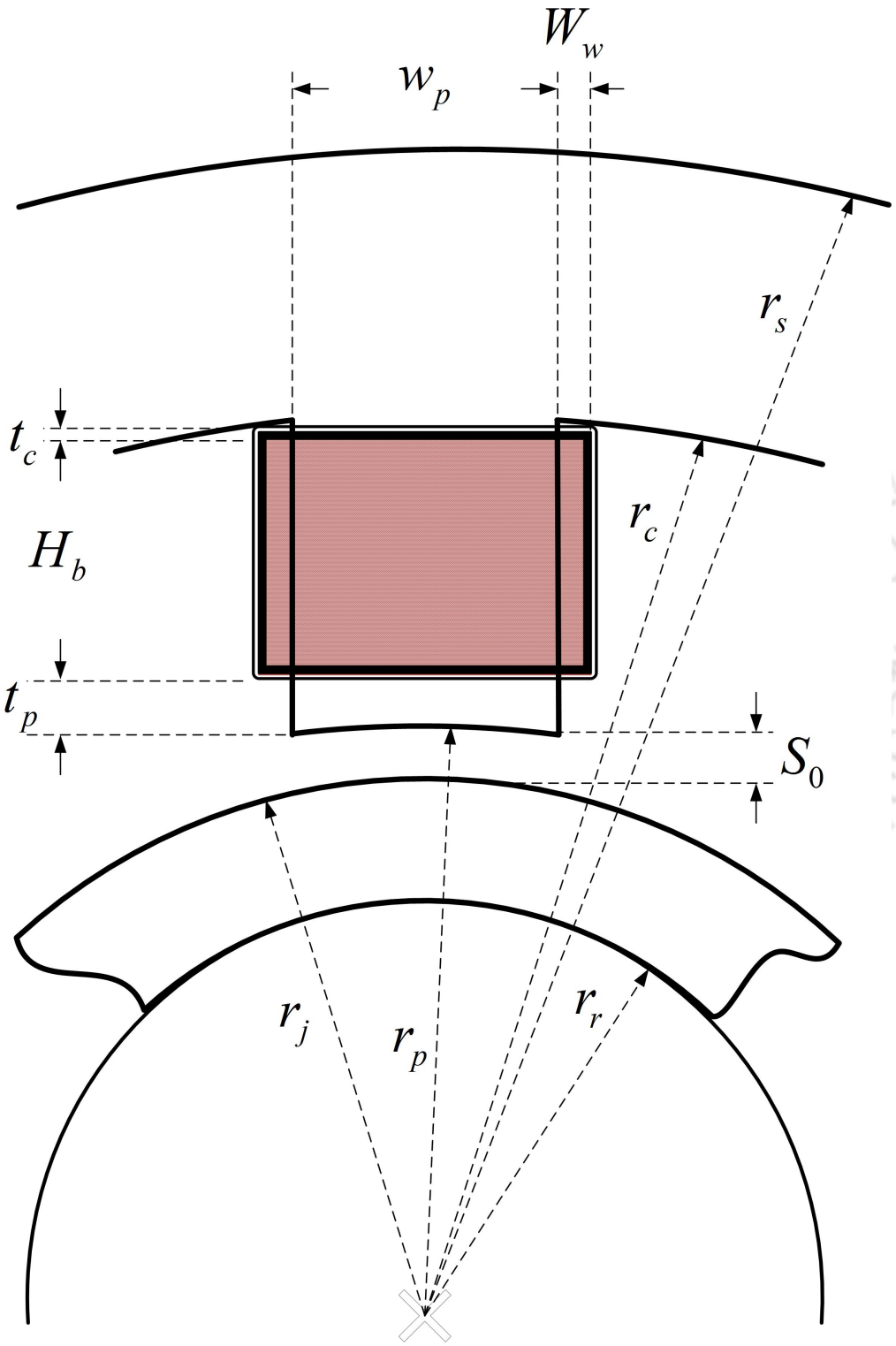

Figure 3.1: Geometry of the radial AMB

1. For a given specific design objective there is a best choice of iron ratio for each number of legs, which is sensitive to the required capacities and the iron saturation density. The iron ratio can be found as [113],

$$f_i = \frac{\delta_1 n_p}{2\pi} \tag{3.2}$$

2. Inorder to prevent the saturation of the back-iron or journal prior to saturation of the pole, the $r_j - r_r \geq \beta w_p$ has to be maintained. The radius of the journal can therefore be found from the relation [113],

$$r_j - r_r \geq 2\beta \left(r_j + S_0\right) \sin\left(\frac{\pi f_i}{n_p}\right) \tag{3.3}$$

or,

$$r_j - r_r \geq 2\beta \left(r_j + S_0\right) \sin\left(\frac{\delta_1}{2}\right) \tag{3.4}$$

3. The pole width allows flux lines from the back of the core to the journal to pass without saturation. The flux splitting parameter dictates the width of the pole. Once, the journal radius, r_j is known, the pole width can be found as [113],

$$w_p = 2\left(r_j + S_0\right) \sin\left(\frac{\delta_1}{2}\right) \tag{3.5}$$

4. The area of the actuator can be calculated from the load capacity. Therefore, once the width of the pole is known, the axial length of the actuator can be found as,

$$L_{AMB} = \frac{A_p}{w_p} \tag{3.6}$$

5. Therefore, the radius of the pole can be calculated as

$$r_p = r_j + S_0 \tag{3.7}$$

6. The winding width should be less than or equal to maximum winding width to avoid overlapping of adjacent electromagnets. The winding width of the coil is given by [114]

$$W_w \leq \beta_1 \left[\left\{\left(r_j + S_0\right) \cos\left(\frac{\delta_1}{2}\right) + t_p\right\} \tan\left(\frac{1}{2}\delta_1 + \delta_2\right) - \frac{1}{2} w_p\right] \tag{3.8}$$

where, $\delta_2 = \pi/8 - 1/2\delta_1$, $t_p = \beta_2 H_b$ and β_1,β_2 are constants less than unity.

Assembly ratio β_1 is used here to prevent W_b from reaching its maximum value even if both parts are equal. The assembly ratio β_2 is used to prevent assembling errors of AMBs in fabricating processes.

7. The height of the bobbin [114],

$$H_b = -\left(r_j + S_0\right)\cos\left(\frac{\theta_1}{2}\right) - t_p + \left[\left(r - w_p\right)^2 - \left(\frac{w_p}{2} + W_w\right)^2\right]^{1/2} \tag{3.9}$$

Since the inner area surrounded by the bobbin and the cross sectional area of the coil are identical, the number of turns per coil yields [114]

$$\frac{N\pi(r_w + t_{ins})^2}{WF} = (W_b - t_c)(H_b - 2t_c) \tag{3.10}$$

where, N is the number of turns, r_w is the radius of the wire, t_{ins} thickness of insulation on coil, t_c thickness of the coil casing

8. The area of wire cross section is determined depending on the limits of current and its density. The current density is limited to the maximum value in the wire, and the wire cross section is then expressed as [113]

$$a_{cond} = \frac{I_0}{J_0} \tag{3.11}$$

9. The required slot area, A_{slot} for these sections with an assumed filling factor, k_{fill} is given by [114]

$$A_{slot} = \frac{Na_{cond}}{k_{fill}} \tag{3.12}$$

where, k_{fill} is the fill factor $\left(0 < k_{fill} \leq 1\right)$

10. Stator outer diameter r_s can be calculated as [114]

$$r_s = 2\left(r_j + S_0 + t + H_b + w_p\right) \tag{3.13}$$

11. The coil space radius can also be calculated as [114],

$$r_c = r_s - \gamma w_p \tag{3.14}$$

It is also important to note that the available coil area A_v and the required coil area, A_c has to be matched, i.e. $A_v = \eta A_c$, where η is a factor more than 1 but less than 2. The required coil area depends on the selection of the coil size, number of turns

which are further dependent on the required magnetic flux density.

The available coil area for a full coil fill is given as [113],

$$A_v = \left(r_c^2 \frac{\pi}{n_p} - r_p^2 \tan \frac{\pi}{n_p} - (r_c - r_p) w_p \right) \Big/ 2 \tag{3.15}$$

while for removable coil, the available coil area is given as [113],

$$A_v = \left[r_p \tan \frac{\pi}{n_p} - \frac{w_p}{2} \right] (r_c - r_p) \tag{3.16}$$

Solving Eqn. 3.13 and 3.14, we can obtain the radius of the coil space

12. Winding Resistance [114]

$$W_r = \frac{\rho L_0}{a_{cond}} \tag{3.17}$$

13. The copper loss consumed by the winding is calculated as [2],

$$P_{cu} = R \left(i_{x+}^2 + i_{x-}^2 \right) + R \left(i_{x+}^2 + i_{x-}^2 \right) \tag{3.18}$$

$$P_{cu} = 2R \left(i_0^2 + i_x^2 \right) + 2R \left(i_0^2 + i_x^2 \right) \tag{3.19}$$

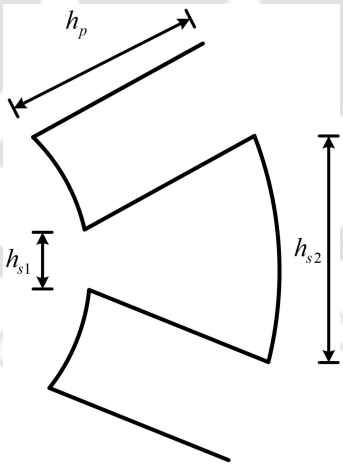

Figure 3.2: Schematic of slot area

In Fig. 3.2, the schematic of the slot area has been shown. Therefore, based on these dimensions, the dimensions of the slot for the winding can also be calculated as [115],

$$h_{s1} = \pi (D + 2g) \frac{45}{360} - \pi (r + S_0) \frac{\theta_t}{360} \tag{3.20}$$

The area of the slot is thus given as [115],

$$A_{slot} = h_p \frac{h_{s1} + h_{s2}}{2} \tag{3.21}$$

$$h_{s2} \approx h_{s1} + 2h_p \tan\left(\frac{\pi}{8}\right) \tag{3.22}$$

3.3 Analysis of Radial AMB

In the previous section, the steps and factors to be considered while designing the actuator of the Magnetic Bearing have been discussed. The design parameters influence the generation of magnetic forces. In analyzing the behavior of a magnetic actuator, the primary objective is to determine the forces generated by the actuator in response to voltages applied to its coils and motion of the actuated device. The generation of force is generally done using three methods i.e. analytically, reluctance method or finite element method. However, the basics of all the method is similar. The finite element method provides an accurate prediction of the AMB, however it is not very much attractive for dynamic simulations due to its high computational cost. The reluctance network method provides satisfactory results with less computational effort. In this section, the basic equations for finding the magneto motive force using the reluctance network method have been described.

3.3.1 Electrical Equivalent Circuit

The magnetic field in an actuator is generated by an electric current. The Ampere's current law gives the relation between the magnetic field, H_{mag} and the current enclosed by the closed integration path, l. If a current I excites the coil wounded around the actuator with N number of turns, the magneto motive force is given as [112],

$$\oint H_{mag}.dl = Ni = \text{MMF} \tag{3.23}$$

The magnetic flux density, B_j generated is dependent on the material properties. In case of diamagnetic material, the relative permeability μ_r is less than 1 while in case of paramagnetic materials μ_r is greater than 1. The magnetic flux density is related to the magnetic field as [112] ,

$$B_j = \mu_0 \mu_r H \tag{3.24}$$

where, μ_0 is the permeability of free space.

Figure 3.3(a) shows an electromagnet used to suspend a rotor with a magnetic force. Considering the actuator core has a width w_p with stack length l, the flux path in the core as l_1 and l_2 while flux path length in the rotor as l_3 , if the winding has N turns with the instantaneous current, I flowing the MMF produced will be NI.

The reluctance of the magnetic circuit is given as [112],

$$R_m = \frac{l_{fp}}{\mu_m A_p} \tag{3.25}$$

where, l_{fp} is the flux path length, μ_m is the permeability in the material $(\mu_m = \mu_0 \mu_r)$ and A_p is the cross sectional area of the flux path.

The inverse of the magnetic reluctance is permeance. Therefore, the permeance is given as [112],

$$P_m = \frac{\mu_m A_p}{l_{fp}} \tag{3.26}$$

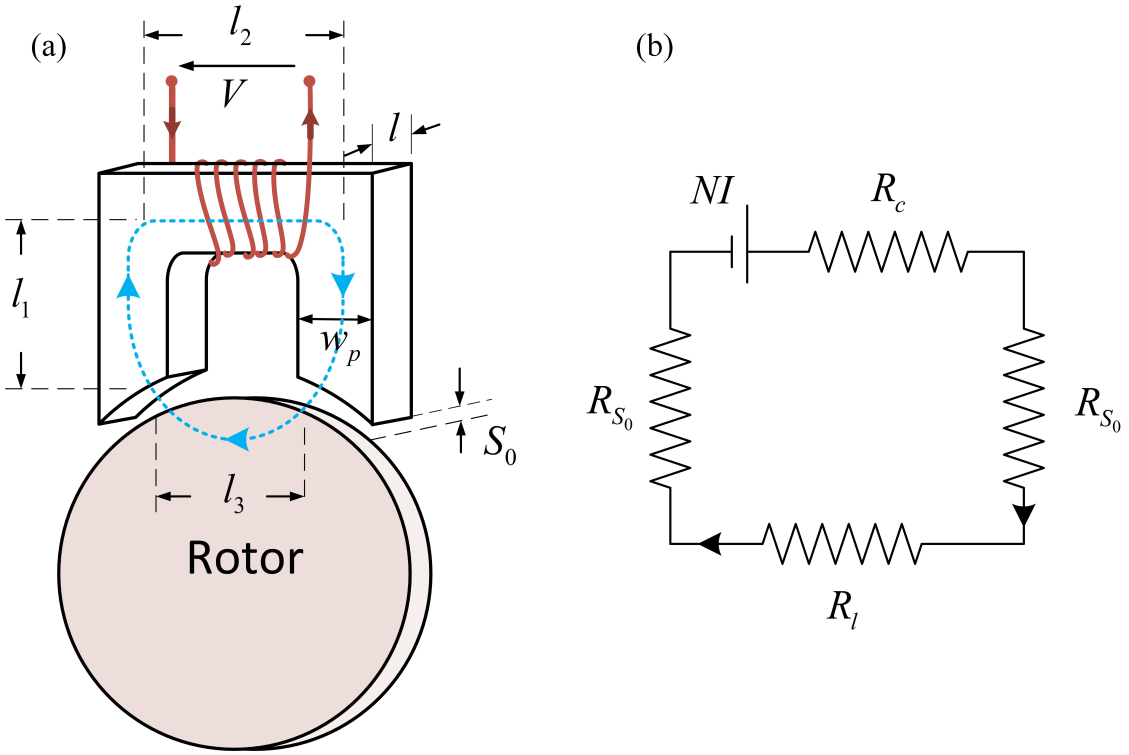

Figure 3.3: (a)Magnetic Force of Single Actuator (b) Equivalent Magnetic Circuit

The MMF, flux and reluctance of a magnetic circuit can be treated as the voltage, current and resistance in an electric circuit. The electrical equivalent circuit for the

magnetic circuit of the above electromagnet is shown in Fig. 3.3(b). The main difference between the magnetic circuit and the electrical circuit is that the magnetic reluctance is energy storage rather than a loss component. The MMF generated by the winding current is represented as NI resembling the DC voltage source. R_c represents the reluctance of the magnetic core, R_l represents the reluctance of the rotor and R_{S_0} represents the reluctance of the air gap. Thus the magnetic reluctances of the circuit can be written as [112],

$$R_{S_0} = \frac{S_0 - x_m}{\mu_0 w_p l} \tag{3.27}$$

where, x_m is the small displacement from the equilibrium position

$$R_c = \frac{2l_1 + l_2}{\mu_0 \mu_r w_p l} \tag{3.28}$$

$$R_j = \frac{l_3}{\mu_0 \mu_r w_p l} \tag{3.29}$$

where, μ_r is the relative permeability.

In general, the reluctance of the airgap is significantly larger than the reluctance of the iron, so that the magnetic reluctance in the iron can be neglected in the following calculation. Therefore the flux ϕ is given as,

$$\phi = \frac{NI}{2R_{S_0}} = \frac{NI}{2} \frac{\mu_0 w_p l}{S_0 - x_m} \tag{3.30}$$

The flux linkage Ψ of the coil, product of flux ϕ and the number of turns per coil N is given as [112],

$$\Psi = \frac{N^2 I w_p l}{2(S_0 - x_m)} \tag{3.31}$$

The inductance is defined as flux linkage divided by the current value $L_C = \frac{\Psi}{I}$, thus,

$$L_C = \frac{N^2 \mu_0 w_p l}{2(S_0 - x_m)} \tag{3.32}$$

3.3.2 Forces Generated within the Magnetic Bearings

In the present investigation, the active magnetic bearing has been considered as hetero-polar with eight poles as shown in Fig. 3.4. In Fig. 3.4, the poles 1 and 2 are at the right hand side of the bearing, pole 3 and pole 4 are at the top, poles 5 and 6 are at the

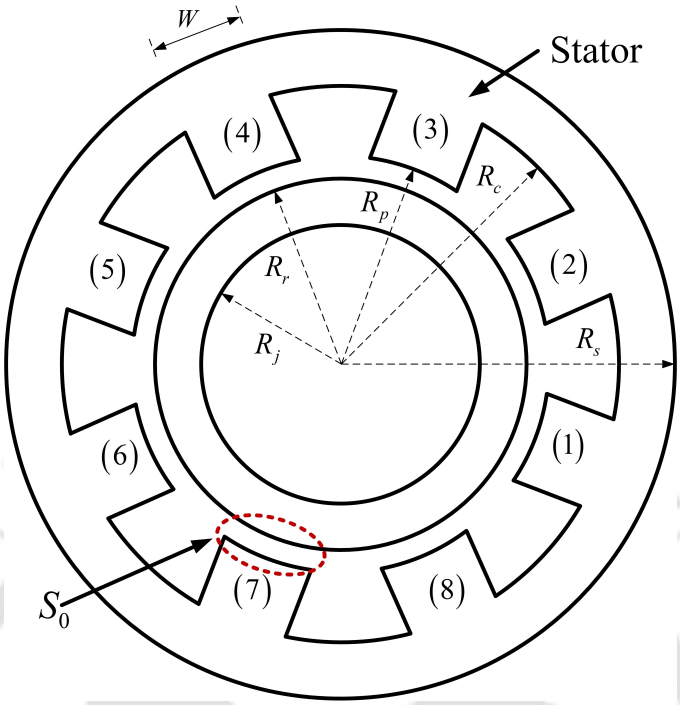

Figure 3.4: Schematic of the radial AMB

left hand side of the bearing, while poles 7 and 8 are at the bottom of the bearing. The reluctance network of the AMB has been shown in Fig. 3.5. The reluctance network shows 32 different reluctances.

$\{R_{S_01}, R_{S_02}, R_{S_03}, ...R_{S_08}\}$ denotes the reluctances in the airgap. This can be calculated as [112],

$$R_{S_0i} = \frac{S_0}{\mu_0 A_p} \tag{3.33}$$

where, the suffix i represents the pole number.

$\{R_{s1}, R_{s2}, R_{s3}, ...R_{s8}\}$ denotes the circumferential reluctances of the flux paths in the circumferential direction through the back of the core of the bearing. These are all identical and can be calculated as [112],

$$R_{si} = \frac{\pi (r_s + r_p)}{8\mu_0 \mu_r (r_s - r_p) l} \tag{3.34}$$

The other circumferential reluctances representing the flux paths of the bearing rotor is represented as $\{R_{j1}, R_{j2}, R_{j3}, ...R_{j8}\}$. These are also identical and calculated as,

$$R_{ji} = \frac{\pi (r_j + r_r)}{8\mu_0 \mu_r (r_j - r_r) l} \tag{3.35}$$

$\{R_{p1}, R_{p2}, R_{p3}, ...R_{p8}\}$ represents the radial reluctance of the flux path through the poles. In reality, these reluctances changes with the flux density, however their effect is considered to be very small that in the present work. Therefore it has been considered as constant and always equal. These are calculated as [112],

$$R_{pi} = \frac{(r_c - r_p)}{\mu_0 \mu_r w_p l} \tag{3.36}$$

Thus, the reluctance matrix can be written as,

$$R_{NET} = \begin{bmatrix} R_{11} & (-R_{j1}) & (-R_{j2}) & (-R_{j3}) & .. & (-R_{j7}) & (-R_{j8}) \\ (-R_{j1}) & R_{22} & -(R_{S_02}+R_{p2}) & 0 & .. & 0 & -(R_{S_01}+R_{p1}) \\ (-R_{j2}) & -(R_{S_02}+R_{p2}) & R_{33} & -(R_{S_03}+R_{p3}) & .. & 0 & 0 \\ (-R_{j3}) & : & -(R_{S_03}+R_{p3}) & R_{44} & .. & 0 & 0 \\ : & : & : & : & . & : & : \\ (-R_{j7}) & 0 & 0 & 0 & .. & R_{88} & -(R_{S_08}+R_{p8}) \\ (-R_{j8}) & -(R_{S_01}+R_{p1}) & 0 & 0 & .. & -(R_{S_08}+R_{p8}) & R_{99} \end{bmatrix} \tag{3.37}$$

where,

$$R_{11} = R_{j1}+R_{j2}+R_{j3}+R_{j4}+R_{j5}+R_{j6}+R_{j7}+R_{j8}$$

$$R_{22} = R_{S_01}+R_{p1}+R_{S_02}+R_{p2}+R_{j1}+R_{s1}$$

$$R_{33} = R_{S_02}+R_{p2}+R_{S_03}+R_{p3}+R_{j2}+R_{s2}$$

$$R_{44} = R_{S_03}+R_{p3}+R_{S_04}+R_{p4}+R_{j3}+R_{s3}$$

$$\ldots \quad \ldots \quad \ldots \quad \ldots \quad \ldots \quad \ldots \quad \ldots$$

$$R_{88} = R_{S_07}+R_{p7}+R_{S_08}+R_{p8}+R_{j7}+R_{s7}$$

$$R_{99} = R_{S_08}+R_{p8}+R_{S_01}+R_{p1}+R_{j8}+R_{s8}$$

The nine independent flux quantities of the reluctance network shown in Fig. 3.5 is denoted as $\{\phi_i, \phi_{12}, \phi_{23}, ..., \phi_{78}, \phi_{81}\}$. Therefore defining Φ as the vector of all magnetic flux quantities in the bearing,

$$\Phi = \begin{bmatrix} \phi_i & \phi_{12} & \phi_{23} & \phi_{34} & \phi_{45} & \phi_{56} & \phi_{67} & \phi_{78} & \phi_{81} \end{bmatrix}^T \tag{3.38}$$

Further, defining I_M as the particular vector of currents in the circuit as,

$$I_M = \begin{bmatrix} 0 & 2I_{12} & -(I_{12}+I_{34}) & 2I_{34} & -(I_{34}+I_{56}) & 2I_{56} & -(I_{56}+I_{78}) & 2I_{78} & -(I_{78}+I_{12}) \end{bmatrix}^T \tag{3.39}$$

Thus, the magnetic flux at any instant of time can be written as,

$$\Phi = (R_{NET})^{-1} \times NI_M \tag{3.40}$$

As all the currents in the bearings are known at any instant, Eqn. 3.40 can be used to determine the state of flux in the bearing. Assuming, that the flux is uniform over the area, the force acting each pole face can be calculated as [112],

$$F_i = \frac{\chi}{2A\mu_0}\left(\phi_{i,j+1} - \phi_{i-1,j}\right)^2 \tag{3.41}$$

where, χ is a factor slightly lower than 1, reflecting the fact that the pole-face is not flat and where $\phi_{8,9}$ and $\phi_{0,1}$ are to be interpreted as .

χ is defined as, $\chi = \left(\int_0^{\alpha} \cos\theta . d\theta\right) \Big/ \alpha = \frac{\sin\alpha}{\alpha}$

Therefore the net vertical force, F_{mag-x} and net horizontal force, F_{mag-y}, are calculated from the individual pole forces, $\{F_1, F_2, F_3, ..., F_8\}$ as,

$$\begin{aligned} F_{mag-x} &= \sum_{i=1}^{8} F_i \sin\left((2i-3)\pi/8\right) \\ F_{mag-y} &= \sum_{i=1}^{8} F_i \cos\left((2i-3)\pi/8\right) \end{aligned} \tag{3.42}$$

Assuming a linear system, the total magnetic energy stored in the bearing at any instant of time is given as [112],

$$E_{mag} = \frac{1}{2}\Phi^T R_{NET} \Phi \tag{3.43}$$

3.3.3 Electrical Connection in the Active Magnetic Bearing

The areas between the stator poles are the slots in which the windings arrangements are made. The currents are provided in this winding arrangements for the development of the magnetic flux. The winding current is the sum of the bias current and the feedback/control current (for radial positioning). In general, the bias current is DC, however, if the bias

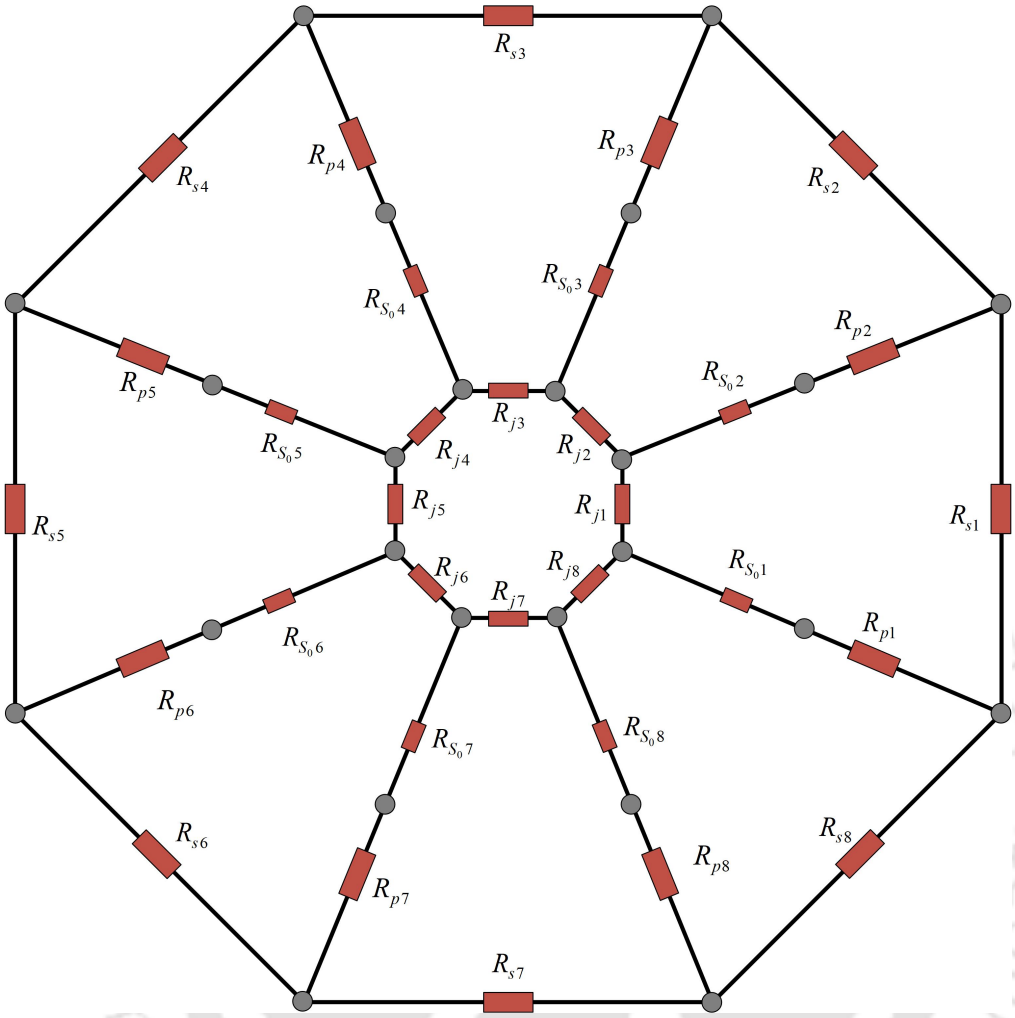

Figure 3.5: Reluctance network of the radial AMB

current has sinusoidal and co-sinusoidal variations in the $X-$ and $Y-$oriented windings then a revolving magnetic field is generated. The eight poles $(1,2,3,..7,8)$ are divided into four electromagnets, EMA-1, EMA-2, EMA-3 and EMA-4 as shown in Fig. 3.6. The normal winding arrangements for the electromagnets, EMA-2 and EMA-4 are shown in Fig. 3.6. In EMA-2, two short pitch coils are wound around two stator poles. These coils are connected in series so that only two terminals are required for one magnet. With a current i_y in a coil, MMF, flux and attractive radial force F_y are generated. EMA 2 generates radial force in the positive Y-axis direction whereas EMA 4 generates radial force in the negative Y-axis direction. Therefore, EMA-2 and EMA-4 are working in differential mode. Similarly, EMA-1 and EMA-3 produce X-axis radial force also in differential mode.

The winding arrangement mentioned above can also be realised using two half coils with N turns in each pole as shown in Fig. 3.7 . In this arrangement, the half coils HCP_{12A}

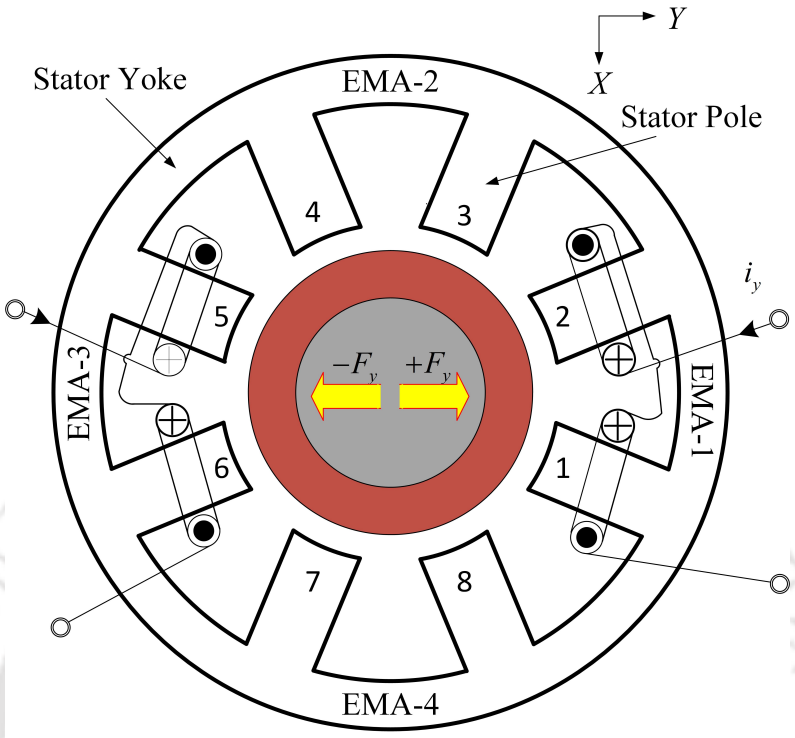

Figure 3.6: Electrical Configurations of the radial AMB

and HCP_{12B} are wounded in poles 1 and 2, and are connected in series. Similarly, HCP_{34A} and HCP_{34B} are wounded in poles 3 and 4, and so on. Thus, there are total of 16 half coils. A single independent drive provides the power in the half coils pairs. Therefore, four independent drives are required to power the half coil pairs. The half coil pairs $HCP_{12A}, HCP_{12B}, HCP_{56A}$ and HCP_{56B} controls the horizontal forces along Y-axis while $HCP_{34A}, HCP_{34B}, HCP_{78A}$ and HCP_{78B} controls the vertical forces along X- axis.

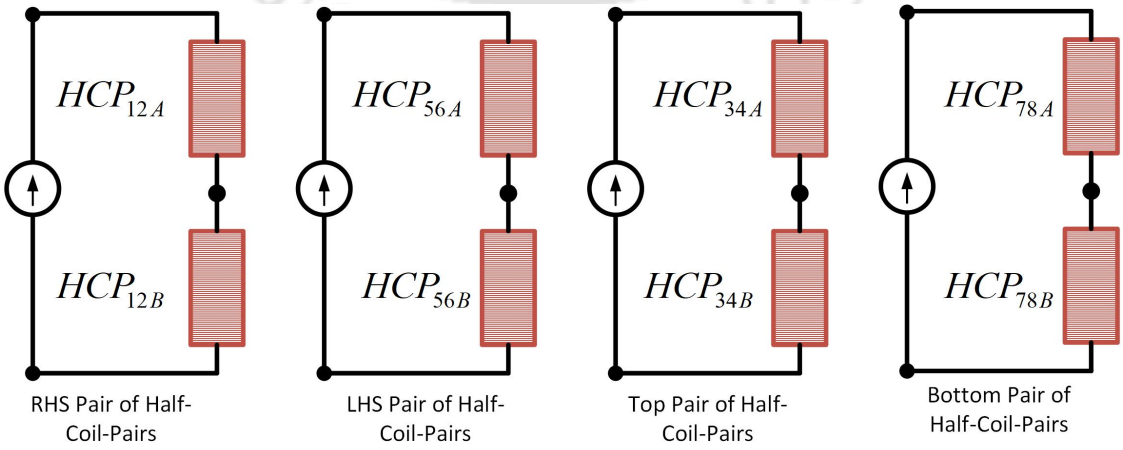

Figure 3.7: Half coil pairs of the radial AMB

The four independent currents in the circuit in vector can be represented in vector form as,

$$I_B := \begin{bmatrix} I_{12} & I_{34} & I_{56} & I_{78} \end{bmatrix}^T \tag{3.44}$$

A new current vector with all the half coil currents can be represented as,

$$I_A := \begin{bmatrix} I_{12A} & I_{12B} & I_{34A} & I_{34B} & I_{56A} & I_{56B} & I_{78B} & I_{78B} \end{bmatrix}^T \tag{3.45}$$

The vector of half coil current, I_A is transformed to the current vector, I_M using the implicit transformation matrix as,

$$I_M =: T_{MB} I_B =: T_{MB} T_{BA} I_A =: T_{MA} I_A \tag{3.46}$$

where, $T_{MB} = \begin{bmatrix} 0 & 0 & 0 & 0 \\ 2 & 0 & 0 & 0 \\ -1 & -1 & 0 & 0 \\ 0 & 2 & 0 & 0 \\ 0 & -1 & -1 & 0 \\ 0 & 0 & 2 & 0 \\ 0 & 0 & -1 & -1 \\ 0 & 0 & 0 & 2 \\ -1 & 0 & 0 & -1 \end{bmatrix}$, $T_{BA} = \begin{bmatrix} 1 & 1 & 0 & 0 & 0 & 0 & 0 & 0 \\ 0 & 0 & 1 & 1 & 0 & 0 & 0 & 0 \\ 0 & 0 & 0 & 0 & 1 & 1 & 0 & 0 \\ 0 & 0 & 0 & 0 & 0 & 0 & 1 & 1 \end{bmatrix}$ and

$T_{MA} = T_{MB} \times T_{BA}$

The four voltages corresponding to the four independent currents are represented in the vector form as,

$$V_B := \begin{bmatrix} V_{12} & V_{34} & V_{56} & V_{78} \end{bmatrix}^T \tag{3.47}$$

The resistance of the coils can be defined as,

$$R_{coil} = diag\left(\begin{bmatrix} 2R_{HCP} & 2R_{HCP} & 2R_{HCP} & 2R_{HCP} \end{bmatrix}\right) \tag{3.48}$$

where, R_{HCP} is the resistance of the single half coil.

The inductance of the circuit can be defined as,

$$L_C = N^2 {T_{MB}}^T (R_{NET})^{-1} T_{MB} \tag{3.49}$$

$$\dot{L}_C = N^2 {T_{MB}}^T \left({R_{NET}}^{-1} \left(\dot{R}_{NET} \right) {R_{NET}}^{-1} \right) T_{MB} \tag{3.50}$$

where, $\dot{R}_{NET}$ is implicit from Eqns. 3.33 - 3.37

Therefore, the electrical dynamics of the winding arrangement can be represented as,

$$V_B = R_{coil} I_B + L_C \dot{I}_B + \dot{L}_C I_B \tag{3.51}$$

3.4 Control Strategy

In the previous sections, the magnetic bearing force F_{mag-x} and F_{mag-y} has been described as a linearized function of the coil currents and the reluctances of the bearing. The reluctances of the AMB's requires feedback inorder to have a proper control over the rotor. In general, PID control scheme is utilized for each bearing unit or separately for each bearing axis to control the rotor. However, it is to be noted that the bearings and sensors are non-collocated, i.e. that their axis differ by a certain distance, as shown in Fig. 3.8 Most of the industrial AMBs are of this non-collocation type. However, as the sensors are mostly of eddy current or inductive type, they can usually not be integrated into the bearing. Therefore, the location of the sensors has also to be taken in consideration. The displacements of the rotor at the location of sensor A and sensor B can be written as,

$$\begin{aligned} x_{senA} &= x_{CG} + S_A \gamma \\ x_{senB} &= x_{CG} - S_B \gamma \\ y_{senA} &= y_{CG} + S_A \varphi \\ y_{senB} &= y_{CG} - S_B \varphi \end{aligned} \tag{3.52}$$

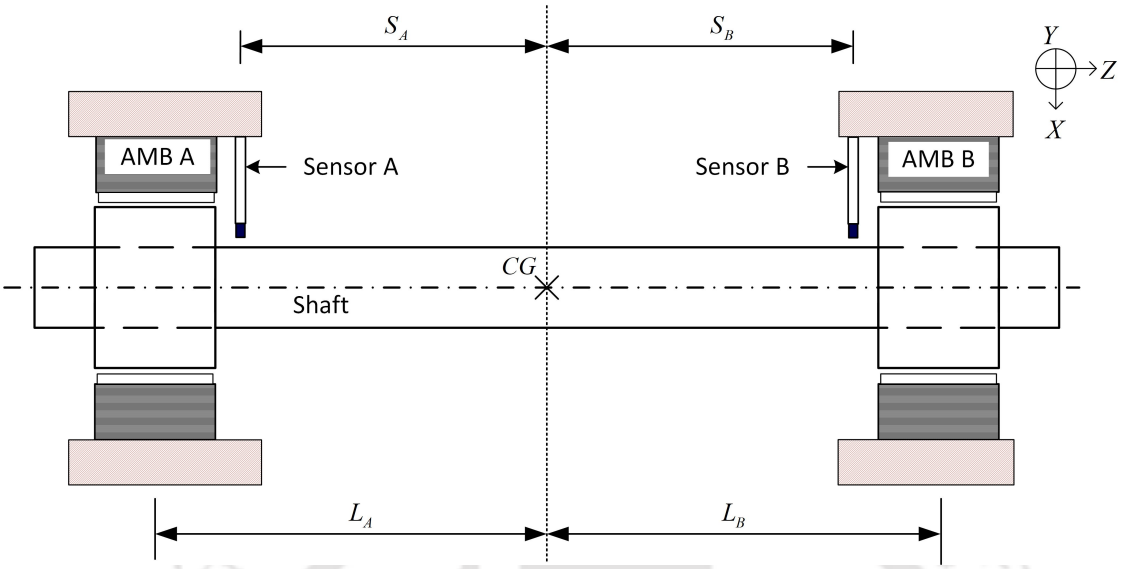

Figure 3.8: Schematic of rotor with AMB

Therefore 3.52 in matrix form, it can be describe as,

$$\begin{Bmatrix} x_{senA} \\ y_{senA} \\ x_{senB} \\ y_{senB} \end{Bmatrix} = \begin{bmatrix} 1 & 0 & 0 & S_A \\ 0 & 1 & -S_A & 0 \\ 1 & 0 & 0 & -S_B \\ 0 & 1 & S_B & 0 \end{bmatrix} \begin{Bmatrix} x_{CG} \\ y_{CG} \\ \varphi \\ \gamma \end{Bmatrix} \tag{3.53}$$

Therefore,

$$\{S_{AB}\} = [T_3]\{q_{CG}\} \tag{3.54}$$

where, $\{S_{AB}\} = \begin{Bmatrix} x_{senA} \\ y_{senA} \\ x_{senB} \\ y_{senB} \end{Bmatrix}$ $T_3 = \begin{bmatrix} 1 & 0 & 0 & S_A \\ 0 & 1 & -S_A & 0 \\ 1 & 0 & 0 & -S_B \\ 0 & 1 & S_B & 0 \end{bmatrix}$

The displacements of the rotor at the sensor location can be transformed to the

bearing locations as,

$$\begin{Bmatrix} x_{senA} \\ y_{senA} \\ x_{senB} \\ y_{senB} \end{Bmatrix} = \begin{bmatrix} 1 & 0 & 0 & S_A \\ 0 & 1 & -S_A & 0 \\ 1 & 0 & 0 & -S_B \\ 0 & 1 & S_B & 0 \end{bmatrix} [T_1]^{-1} \begin{Bmatrix} x_A \\ y_A \\ x_B \\ y_B \end{Bmatrix} \tag{3.55}$$

$$\begin{Bmatrix} x_{senA} \\ y_{senA} \\ x_{senB} \\ y_{senB} \end{Bmatrix} = \begin{bmatrix} 1 & 0 & 0 & S_A \\ 0 & 1 & -S_A & 0 \\ 1 & 0 & 0 & -S_B \\ 0 & 1 & S_B & 0 \end{bmatrix} \begin{bmatrix} \frac{L_B}{L_A+L_B} & 0 & \frac{L_A}{L_A+L_B} & 0 \\ 0 & \frac{L_B}{L_A+L_B} & 0 & \frac{L_A}{L_A+L_B} \\ 0 & -\frac{1}{L_A+L_B} & 0 & \frac{1}{L_A+L_B} \\ \frac{1}{L_A+L_B} & 0 & -\frac{1}{L_A+L_B} & 0 \end{bmatrix} \begin{Bmatrix} x_A \\ y_A \\ x_B \\ y_B \end{Bmatrix} \tag{3.56}$$

Therefore,

$$\begin{Bmatrix} x_{senA} \\ y_{senA} \\ x_{senB} \\ y_{senB} \end{Bmatrix} = \frac{1}{L} \begin{bmatrix} L_B+S_A & 0 & L_A-S_A & 0 \\ 0 & L_B+S_A & 0 & L_A-S_A \\ L_B-S_B & 0 & L_A+S_B & 0 \\ 0 & L_B-S_B & 0 & L_A+S_B \end{bmatrix} \begin{Bmatrix} x_A \\ y_A \\ x_B \\ y_B \end{Bmatrix} \tag{3.57}$$

In this work, a Proportional Derivative (PD) controller is used instead of Proportional Integral Derivative (PID) controller, since the integral control of the PID tries to maintain the rotor center at a predefined equilibrium position against the variation of the applied loads. However, in the hybrid bearing the equilibrium position is allowed to vary according to the equilibrium position of the GFBs. Therefore, the PD controller has been used.

Therefore the control current implemented at the bearing location is determined as,

$$\begin{Bmatrix} i_{xA} \\ i_{yA} \\ i_{xB} \\ i_{yB} \end{Bmatrix} = -\frac{1}{L}\begin{bmatrix} K_p & 0 & 0 & 0 \\ 0 & K_p & 0 & 0 \\ 0 & 0 & K_p & 0 \\ 0 & 0 & 0 & K_p \end{bmatrix}\begin{bmatrix} L_B+S_A & 0 & L_A-S_A & 0 \\ 0 & L_B+S_A & 0 & L_A-S_A \\ L_B-S_B & 0 & L_A+S_B & 0 \\ 0 & L_B-S_B & 0 & L_A+S_B \end{bmatrix}\begin{Bmatrix} x_A \\ y_A \\ x_B \\ y_B \end{Bmatrix}$$
$$-\frac{1}{L}\begin{bmatrix} K_d & 0 & 0 & 0 \\ 0 & K_d & 0 & 0 \\ 0 & 0 & K_d & 0 \\ 0 & 0 & 0 & K_d \end{bmatrix}\begin{bmatrix} L_B+S_A & 0 & L_A-S_A & 0 \\ 0 & L_B+S_A & 0 & L_A-S_A \\ L_B-S_B & 0 & L_A+S_B & 0 \\ 0 & L_B-S_B & 0 & L_A+S_B \end{bmatrix}\begin{Bmatrix} \dot{x}_A \\ \dot{y}_A \\ \dot{x}_B \\ \dot{y}_B \end{Bmatrix} \tag{3.58}$$

The control current i_{xA} is provided to I_{12} and I_{56} while i_{yA} is supplied to the I_{34} and I_{78} for bearing A. Similarly, for bearing B, i_{xB} is provided to I_{12} and I_{56} while i_{yB} is provided to I_{34} and I_{78}.

3.5 Inferences

In this chapter, the basic description of the AMBs has been provided. The preliminary design procedure of the AMB has been described. Further, the reluctance network method for calculating the magnetic forces has been outlined. The electrical winding scheme of the conventional AMB has also been illustrated.

4

Stability Analysis of Gas Foil Bearings integrated with Active Magnetic Bearings

Contents

4.1 Introduction

Rotors supported on Gas Foil Bearings (GFBs) have low damping and non-linear characteristics, which limits its application. A possible solution could be an integration of GFBs with Active Magnetic Bearings (AMBs). In the literature, it has been seen that the hybridization of conventional GFBs with AMBs has been increasingly popular and has led to many innovative improvements [93, 103]. However, the design of hybrid GFB is still sophisticated and mostly empirical. Hence a numerical investigation is required in order to understand the dynamics of a rotor supported on GFBs integrated with AMBs.

In the previous chapters, the two bearings were discussed independently. In this chapter, the coupled model of the GFB and the AMB has been described. The fluid film forces of the conventional GFB and the electromagnetic forces from the AMB are integrated into the equations of motion of the rotor. A time domain simulation using the coupled model has been carried out to compare the stability of the rotor supported on conventional GFBs (without the effect of EMA) and hybrid GFBs (with the effect of EMA). Further, the effect of application of EMA after an arbitrary time has also been discussed. Moreover, the control current required to control the rotor at different positions has been investigated.

4.2 Mathematical Model

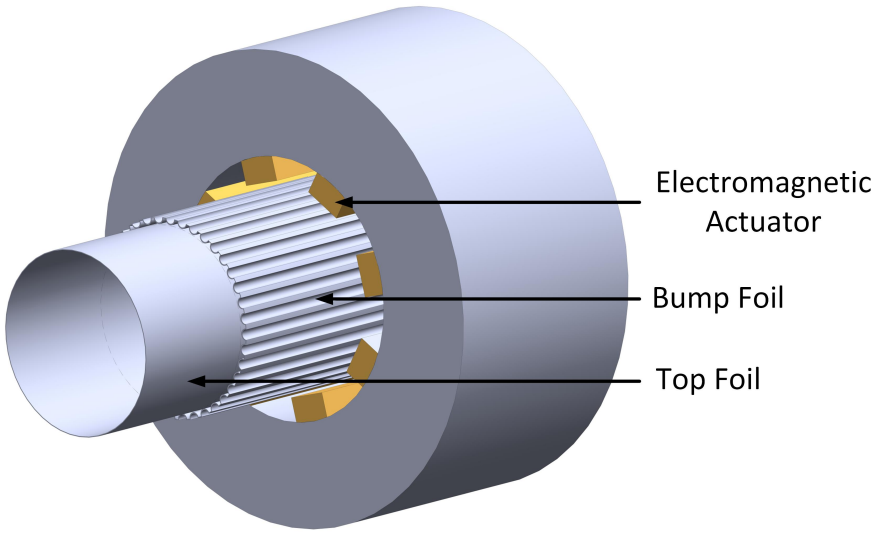

Figure 4.1: Hybrid Bearing Assembly

The assembly of a hybrid GFB for the present investigation is shown in Fig. 4.1. The

top foil and bump foil are placed in between the actuator and the rotor. The top foil and the bump foil has been assumed to be made of non-magnetic material like INCONEL X-750, such that it does not obstruct the path of the magnetic flux. However, the air gap increases due to the incorporation of the top foil and the bump foil. Higher air gap requires higher current to produce the required magnetic flux. In Fig. 4.2, the cross sectional view and the co-ordinate system of the hybrid GFB considered for the present study have been shown.

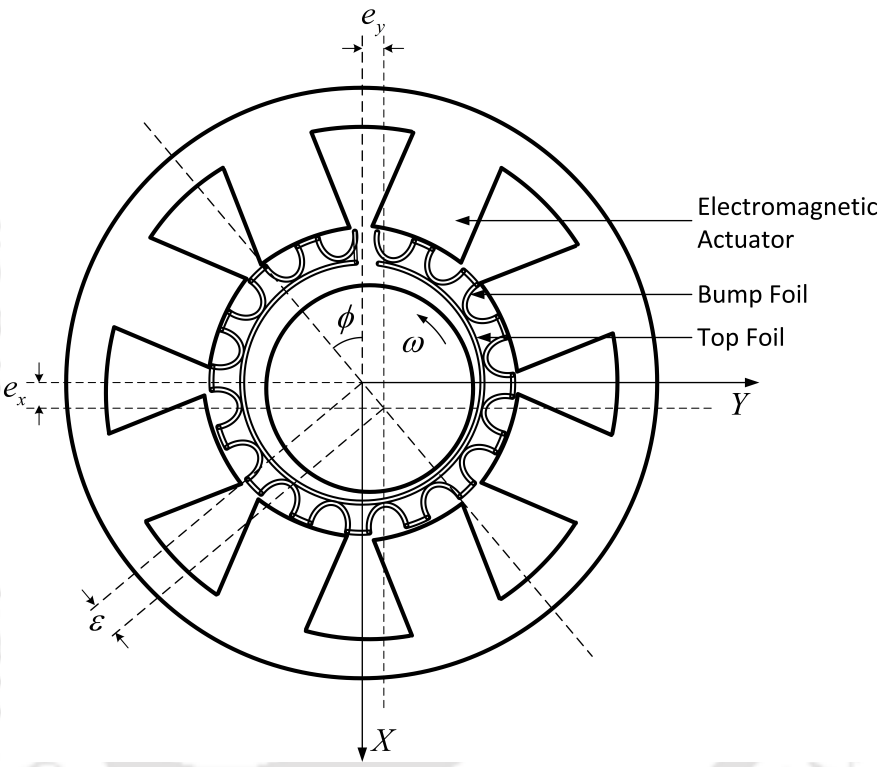

Figure 4.2: Cross section and co-ordinate system of the hybrid Bearing Assembly

A shaft supported on two hybrid GFBs, as shown in Fig. 4.3, has been considered for the study. The coupled equations of motion at the bearing location A and B as described in Chapter 2, can be written as,

$$[M_{AB}]\{q''_{AB}\} + [G_{AB}]\{q'_{AB}\} = \{F_{AB}\} + \{F_{mag-AB}\} + \{W_{AB}\} \tag{4.1}$$

where, $[M_{AB}] = \frac{1}{L^2}\begin{bmatrix} L_B^2M + I_{yy} & 0 & L_AL_BM - I_{yy} & 0 \\ 0 & L_B^2M + I_{xx} & 0 & L_AL_BM - I_{xx} \\ L_AL_BM - I_{yy} & 0 & L_A^2M + I_{yy} & 0 \\ 0 & L_AL_BM - I_{xx} & 0 & L_A^2M + I_{xx} \end{bmatrix}$,

$$[G_{AB}] = \frac{1}{L^2}\begin{bmatrix} 0 & -I_{zz} & 0 & I_{zz} \\ I_{zz} & 0 & -I_{zz} & 0 \\ 0 & I_{zz} & 0 & -I_{zz} \\ -I_{zz} & 0 & I_{zz} & 0 \end{bmatrix}, \{F_{AB}\} = \begin{Bmatrix} F_{xA} \\ F_{yA} \\ F_{xB} \\ F_{yB} \end{Bmatrix}, \{F_{mag-AB}\} = \begin{Bmatrix} F_{mag-xA} \\ F_{mag-yA} \\ F_{mag-xB} \\ F_{mag-yB} \end{Bmatrix}$$

$$\text{and } \{W_{AB}\} = \begin{Bmatrix} W \\ 0 \\ W \\ 0 \end{Bmatrix}$$

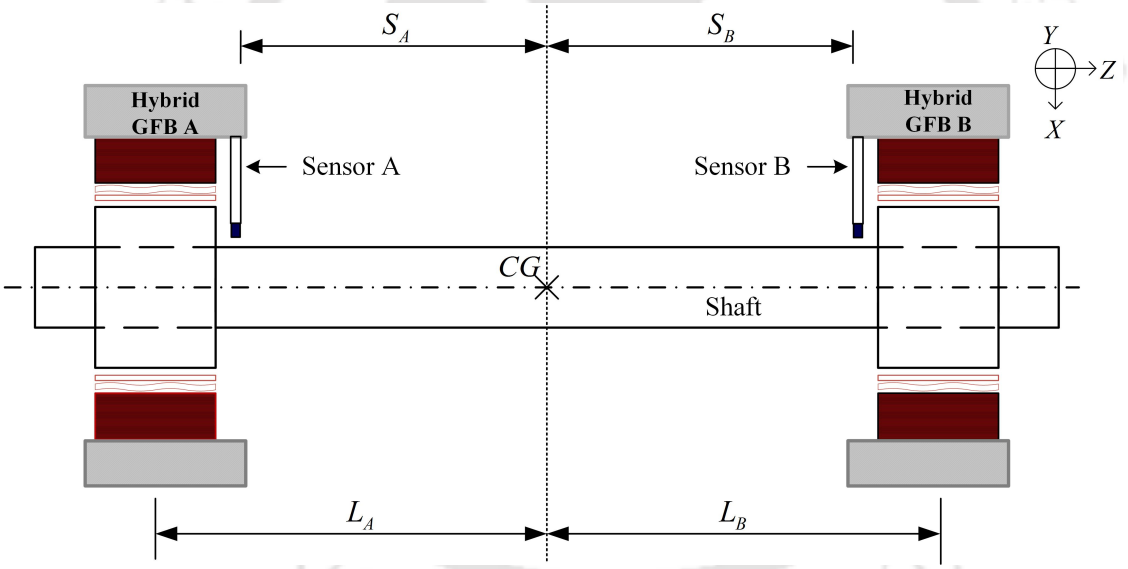

Figure 4.3: Schematic of rotor with hybrid GFB

The equations of motion of the journal are also non-dimensionalised in a similar procedure as followed for Reynolds equation so that both equations can be coupled in non-dimensional form. Therefore, Eqn. 4.1 can be written in non-dimensional form as,

$$[\bar{M}_{AB}]\{\ddot{\bar{q}}_{AB}\} + [\bar{G}_{AB}]\{\dot{\bar{q}}_{AB}\} = \{\bar{F}_{AB}\} + \{\bar{F}_{mag-AB}\} + \{\bar{W}_{AB}\} \tag{4.2}$$

The non-dimensional terms are defined as,
$[\bar{M}_{AB}] = \frac{C\omega^2}{P_a R^2}[M_{AB}]$, $[\bar{G}_{AB}] = \frac{C\omega^2}{P_a R^2}[G_{AB}]$, $\{\bar{F}_{AB}\} = \frac{1}{P_a R^2}\{F_{AB}\}$, $\{\bar{F}_{mag-AB}\} = \frac{1}{P_a R^2}\{F_{mag-AB}\}$
and $\{\bar{W}_{AB}\} = \frac{1}{P_a R^2}\{W_{AB}\}$

The bearing reaction force $\bar{F}_x$ and $\bar{F}_y$ has been found by integrating the fluid film

pressure as discussed in Chapter 2,

$$\bar{F}_x = -\int_0^{2\pi}\int_0^{L/R} \bar{P}(\theta,Z)\cos(\theta)dZd\theta \tag{4.3}$$

$$\bar{F}_y = -\int_0^{2\pi}\int_0^{L/R} \bar{P}(\theta,Z)\sin(\theta)dZd\theta \tag{4.4}$$

The magnetic force $\bar{F}_{mag-x}$ and $\bar{F}_{mag-y}$ are obtained using the reluctance method as described in Chapter 3, in which,

$$F_{mag-x} = \sum_{i=1}^{8} F_i \sin\left((2i-3)\,\pi/8\right) \tag{4.5}$$

$$F_{mag-y} = \sum_{i=1}^{8} F_i \cos\left((2i-3)\,\pi/8\right) \tag{4.6}$$

4.3 Results and Discussion

The purpose of the present work is to investigate a hybrid gas foil magnetic bearing combining GFB and AMB, which has been designed to enhance the performance characteristics of GFBs. Therefore, several parameters are already decided based on the dimension of GFB. Hereafter in this chapter, the AMB will be referred as EMA, as the AMB has been used along with GFB and not as an independent component. The specific parameters of GFB and the rotor system has been presented in Table 4.1 and are taken from [116]. Further, the parameters which are considered for designing the actuator is given in Table 4.2. Figure 4.4 represents different parameters of the bearing which have to be designed for the development of hybrid GFB.

The rotor is assumed to be perfectly balanced. All simulations have been performed by dropping the rotor from the bearing center while the rotor is rotating at constant speed. The dynamic forces of the hydrodynamic bearing are not possible if the rotor is concentric. The AMB, however, tries to align the rotor at the center of bearing, in case the center of the bearing is given as the reference position. Therefore, an offset position of the rotor has to be set to preserve the true nature of gas foil bearing. The equilibrium position of the rotor has been considered same as that of the GFB, thus the load is supported by both EMA and GFB. The equilibrium point for the convergence of the trajectory has been found to be as, $\bar{e}_x = 0.8$ and $\bar{e}_y = 0.35$ i.e. 3.2×10^{-5}m and 1.4×10^{-5}m.

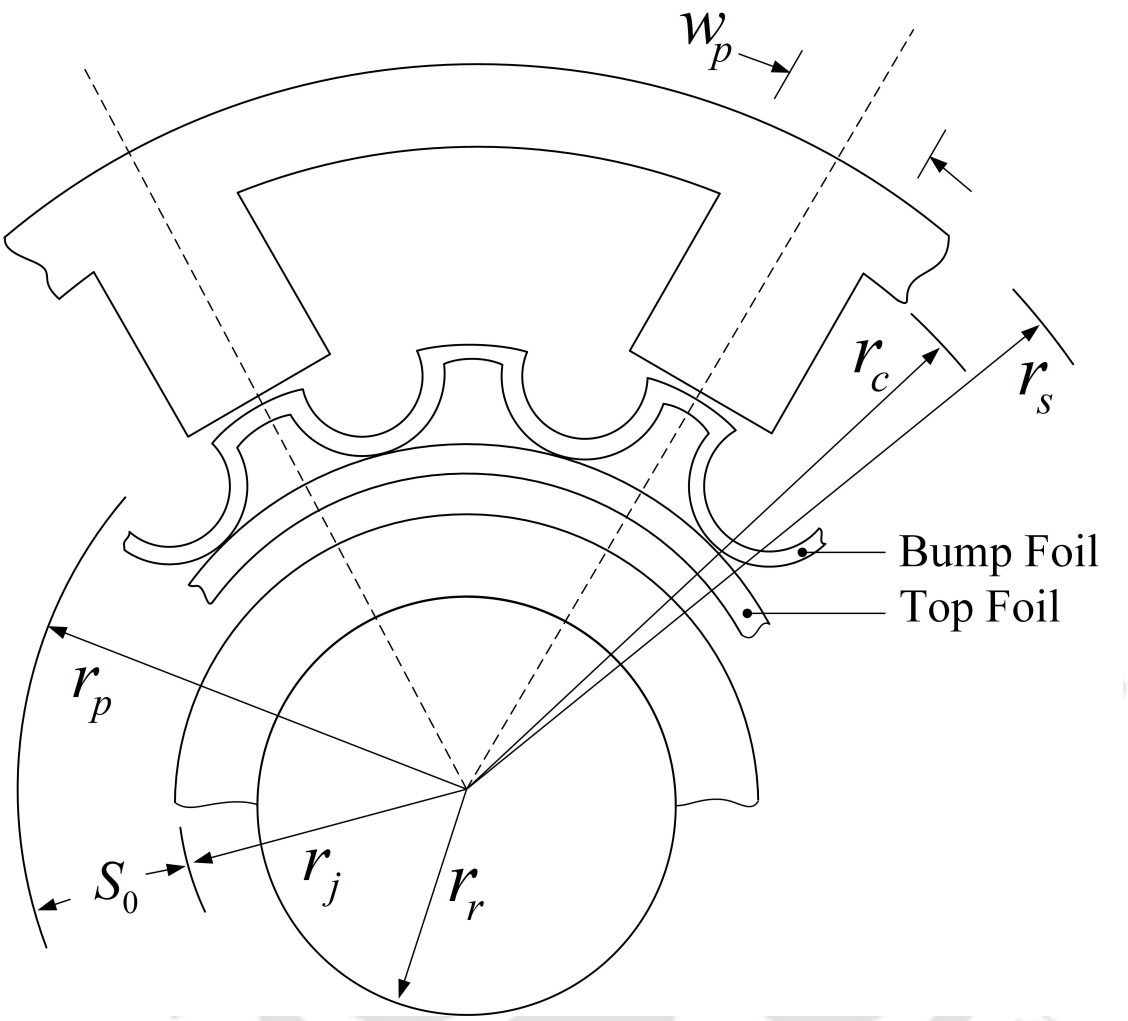

Figure 4.4: Schematic of the hybrid GFB

4.3.1 Case 1: The effect of EMA applied from start

Figure 4.5(a) and Fig. 4.5(b) show the rotor trajectories when the rotor is rotating at 20000 rpm for the conventional GFB (without EMA effect) and the hybrid GFB (with EMA effect) respectively. The effect of the EMA is applied at the start of the simulation. The trajectories presented in Fig. 4.5(a) and Fig. 4.5(b) are different, however, both the orbits show stable operations. The corresponding full spectrum FFT plots of rotor response is shown in Fig. 4.5(c). The FFT plot of the conventional GFB shows the presence of a spike at the sub-synchronous frequency of 116.1 Hz which is about one-third of the synchronous frequency. Another small peak at 238.3 Hz can also be observed. However, with the application of EMA the amplitude of sub-synchronous frequency reduces. The rotor has a forward sense of rotation as the magnitude of forward whirl component is

Table 4.1: Parameters of the GFBs and the rotor bearing system [116]

Parameter	Values
Bearing Radius, R	33.5 mm
Bearing Length, L	53.00 mm
Bearing Clearance, C	40 μm
Bump Foil Stiffness, K_f	8.8 GN/m^3
Ambient Pressure, P_a	1×10^5 Pa
Air Viscosity, μ	1.95×10^{-5} Pa.s
L_A	202.1 mm
L_B	197.9 mm
S_A	163.1 mm
S_B	158.4 mm
Mass, M	21.1166 kg
$I_{xx} = I_{yy}$	525.166×10^{-3} kgm^2
I_{zz}	30.079×10^{-3} kgm^2

more than the backward whirl component as observed in Fig. 4.5(c). Moreover, all other frequency components are eliminated. Figure 4.6(a) and Fig. 4.6(b) show the trajectories when the rotor is rotating at 25600 rpm supported on the conventional GFB and the hybrid GFB. It has been found that the rotor with the conventional GFB becomes unstable as depicted in Fig. 4.6(a). However, the trajectory of the rotor when the effect of EMA is applied, is stable as seen in Fig. 4.6(b). The corresponding FFT plots is shown in Fig. 4.6(c). The FFT plot of the conventional GFB show the presence of the sub-synchronous frequency at 152.6 Hz. It can be observed that in case of conventional GFBs the amplitude of the sub-synchronous vibration when the rotor speed is 25600 rpm is much higher than the amplitude of the sub-synchronous vibration when the rotor speed is 20000 rpm. This is perhaps is the probable cause of instability in the system. The presence of sub-synchronous at one third of the synchronous frequency has also been reported by [77, 78, 117]. In GFBs, the sub-synchronous frequency is very much dependent on the bump foil stiffness, nominal clearance and bump foil loss factor [118]. Therefore, it is important to reduce this sub-synchronous vibration in GFB. The PD gains of the EMA provides an additional stiffness to the system thus increasing the stability

Table 4.2: Parameters of the EMA

Parameter	**Values**
Rotor Radius, r_r	0.0288 m
Journal Radius, r_j	0.04 m
Radius of the pole faces, r_p	0.0411 m
Radius of depth of coils, r_c	0.066 m
Stator Outer Radius, r_s	0.0772 m
Width of the pole, w_p	0.0223 m^2
No. of turns per half coil, N	160
Bias current in each half coil, i_0	5A
Mean air gap, S_0	0.0011352 m
Per pole coverage of circumference, α	0.7
Pole face area, A	0.0012 m^2
Resistance of the circuit, R_x	0.3 Ω
Inductance of the circuit, L_x	0.005 H

of the rotor thus increasing the stability of the rotor. The increase in stiffness due to EMA is closely associated with the proportional gain while the damping of the system is associated with the derivative gain. It has been observed that the amplitude of the response of the sub-synchronous frequency is reduced by about 87%. Therefore, the sub-synchronous vibrations can be reduced implementing the EMA in GFB and the rotor can be operated over a wide range of speed. In Fig. 4.7 the forces generated due to fluid film and electromagnetic actuator when the rotor is rotating at 20000 rpm has been shown. It has been observed that the hydrodynamic forces generated is more in case of conventional GFB. However, due to the incorporation of EMA, the hydrodynamic forces gets reduced. Thus the load is shared between the GFB and EMA. Figure 4.8 shows the forces generated due to fluid film and electromagnetic actuator when the rotor is rotating at 25600 rpm.The hydrodynamic force increases with the increase of speed. This increment in hydrodynamic force can lead to instability. However, due to the implementation of EMA, the forces gets reduced. It has also been observed that with the application of little magnetic force, the unstable rotor becomes stable. The hydrodynamic force and magnetic force follow similar trend under different operating conditions hence, it has not been shown.

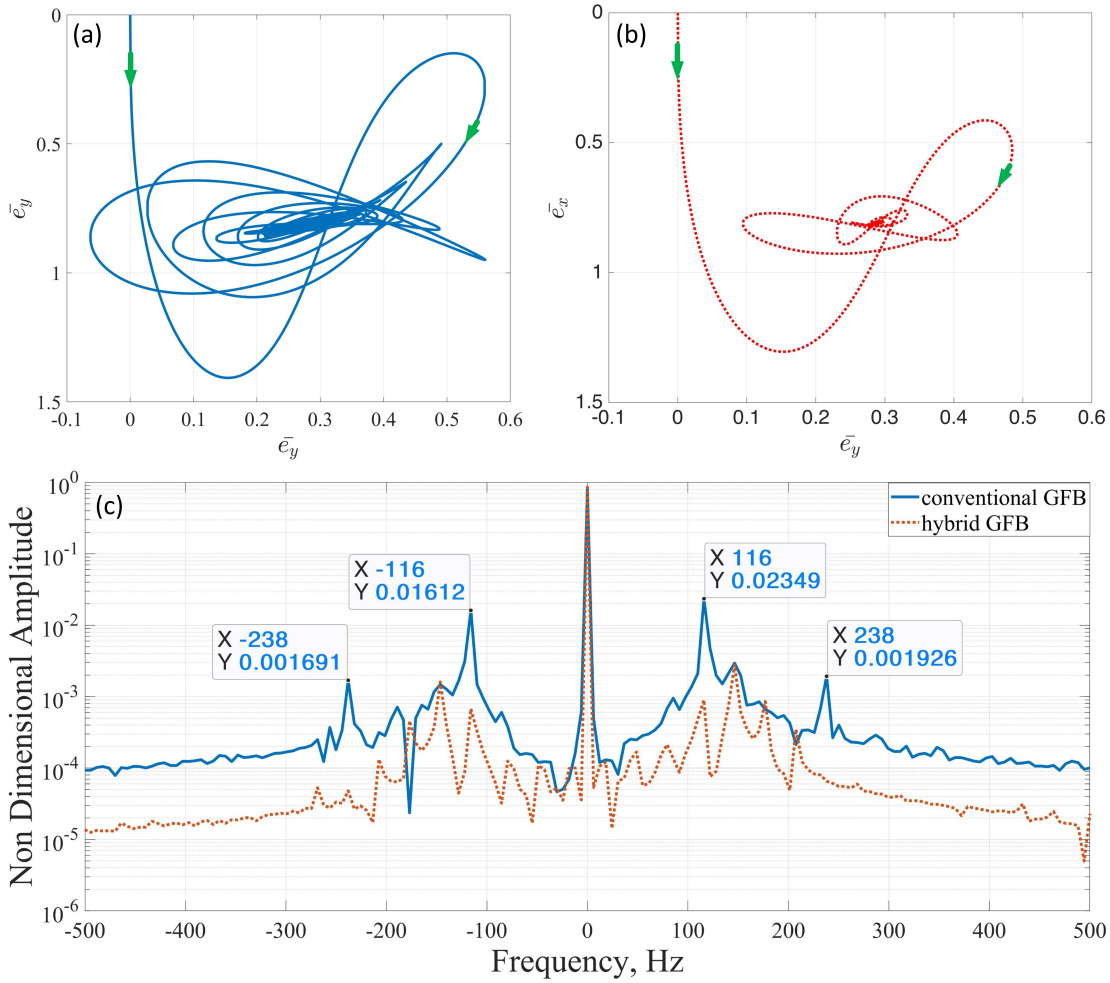

Figure 4.5: (a) Rotor trajectory conventional GFB (b) Rotor trajectory hybrid GFB (c)Full spectrum FFT when the rotor is rotating at 20000 rpm

4.3.2 Case 2: The effect of EMA applied at an arbitrary time

In the previous section, the results obtained from the simulation when the effect of the EMA is applied at the beginning have been discussed. It is proposed to investigate when the effect of EMA is applied at a later time. This helps in understanding the utility of the effect of EMA so as to switch on the EMA whenever needed.

In Fig. 4.9, the time history plot of the displacement along X-axis and Y-axis when the rotor is rotating at 20000 rpm is shown. The effect of EMA is applied after 0.7 sec. It has been observed that the amplitude of the vibration is diminished as the effect of EMA is applied. The time history of the displacement along X-axis and Y-axis when the rotor is rotating at 25600 rpm are shown in Fig. 4.10 and the amplitudes of the vibration increases as the time progresses. The effect of EMA is applied when the amplitudes

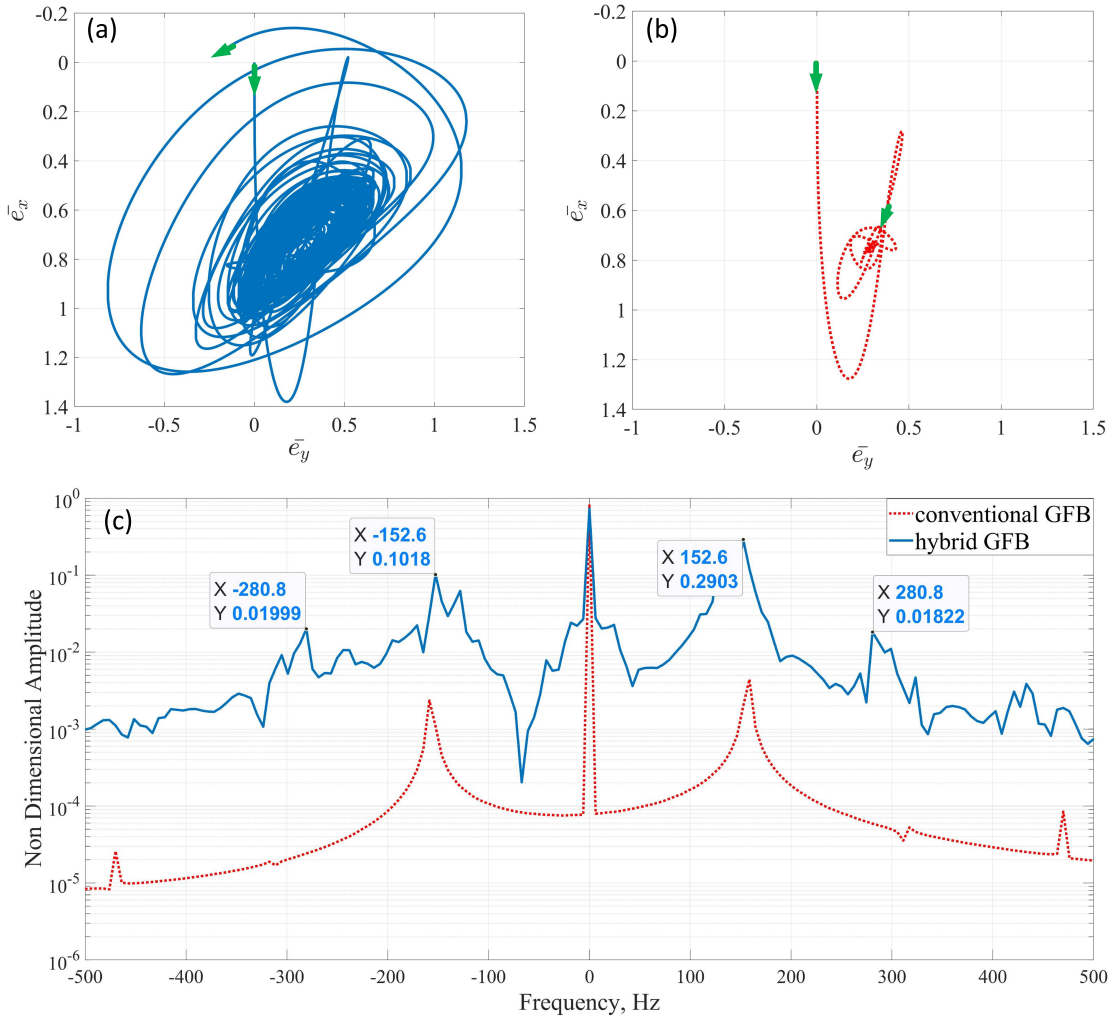

Figure 4.6: (a) Rotor trajectory conventional GFB (b) Rotor trajectory hybrid GFB (c)Full spectrum FFT when the rotor is rotating at 25600 rpm

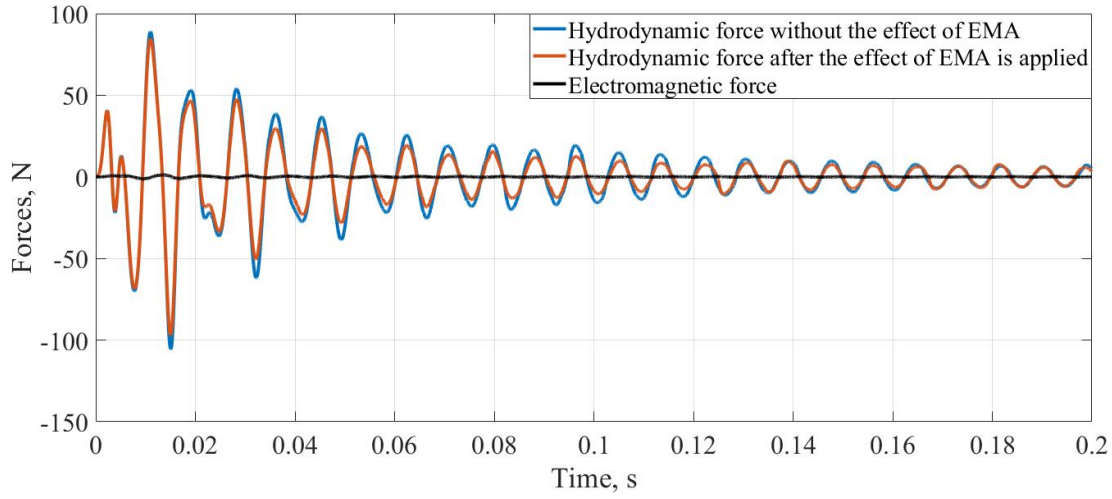

Figure 4.7: Forces generated when the rotor is rotating at 20000 rpm

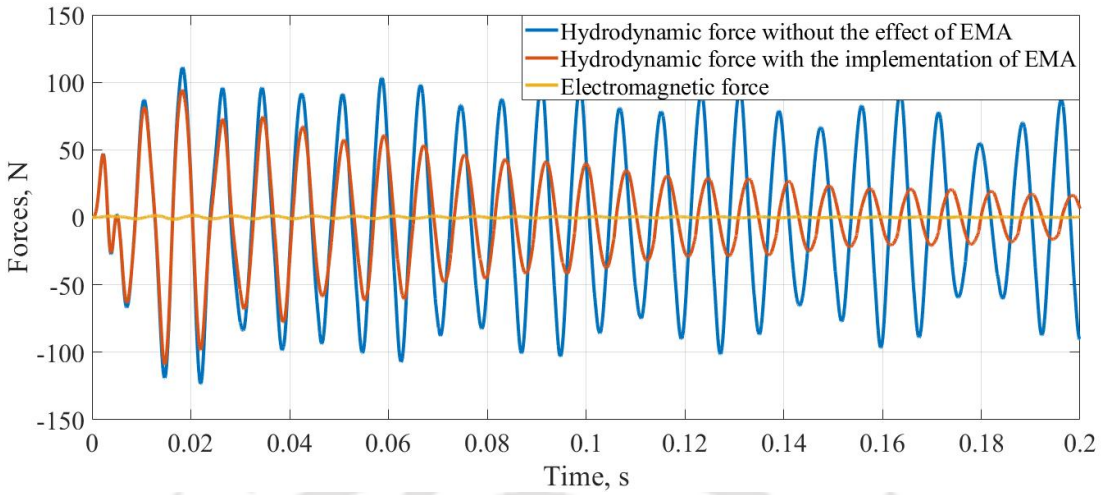

Figure 4.8: Forces generated when the rotor is rotating at 25600 rpm

of the vibration increase beyond a threshold value at a certain time say 0.7 sec in this case. It can be observed that the amplitudes of the vibration reduces as the effect of the EMA is applied. Therefore, the EMA can be switched "ON" whenever required and suppress the amplitude of the vibration.

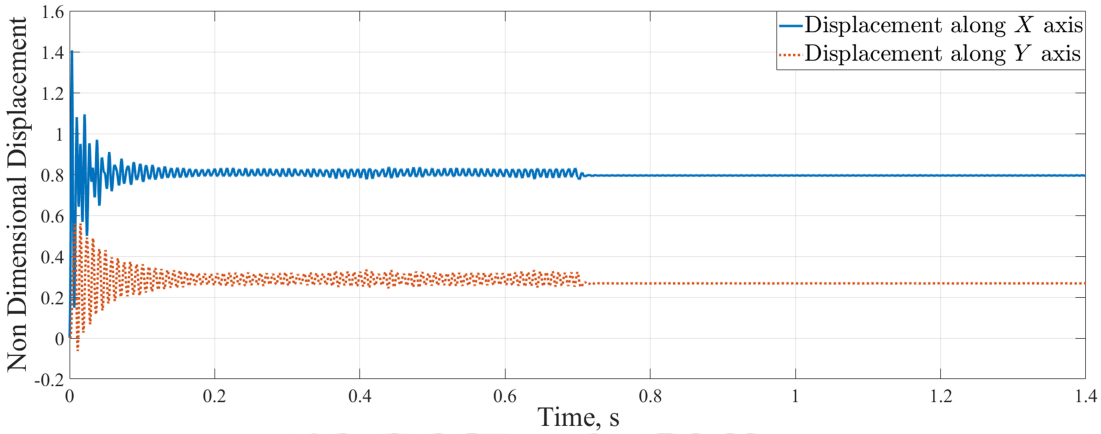

Figure 4.9: Non-dimensional displacements when the rotor speed is 20000 rpm.

In Fig 4.11 the full spectrum FFT of the response when the rotor is rotating at 20000 rpm before and after the application of EMA is shown respectively. It has been observed that before the application of EMA, the sub-synchronous vibrations are present at 116.9 Hz. However, after the application of EMA, the high amplitude of the response of sub-synchronous vibrations which was previously observed at 116.9 Hz gets reduced. Similar observation has been made in case of rotor rotating at 25600 rpm (Fig 4.12). The amplitude of sub-synchronous frequency has been reduced due to the effect of EMA and improve the stability of the rotor system.

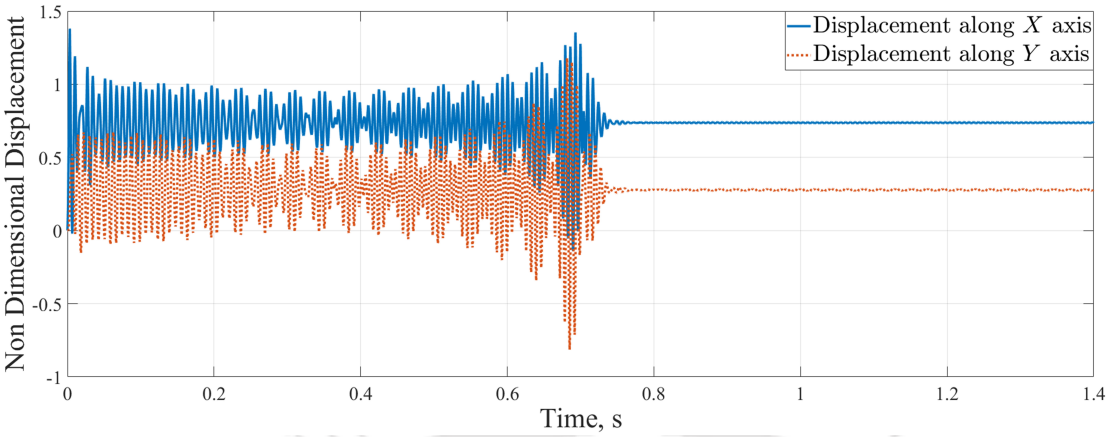

Figure 4.10: Non-dimensional displacements when the rotor speed is 25600 rpm.

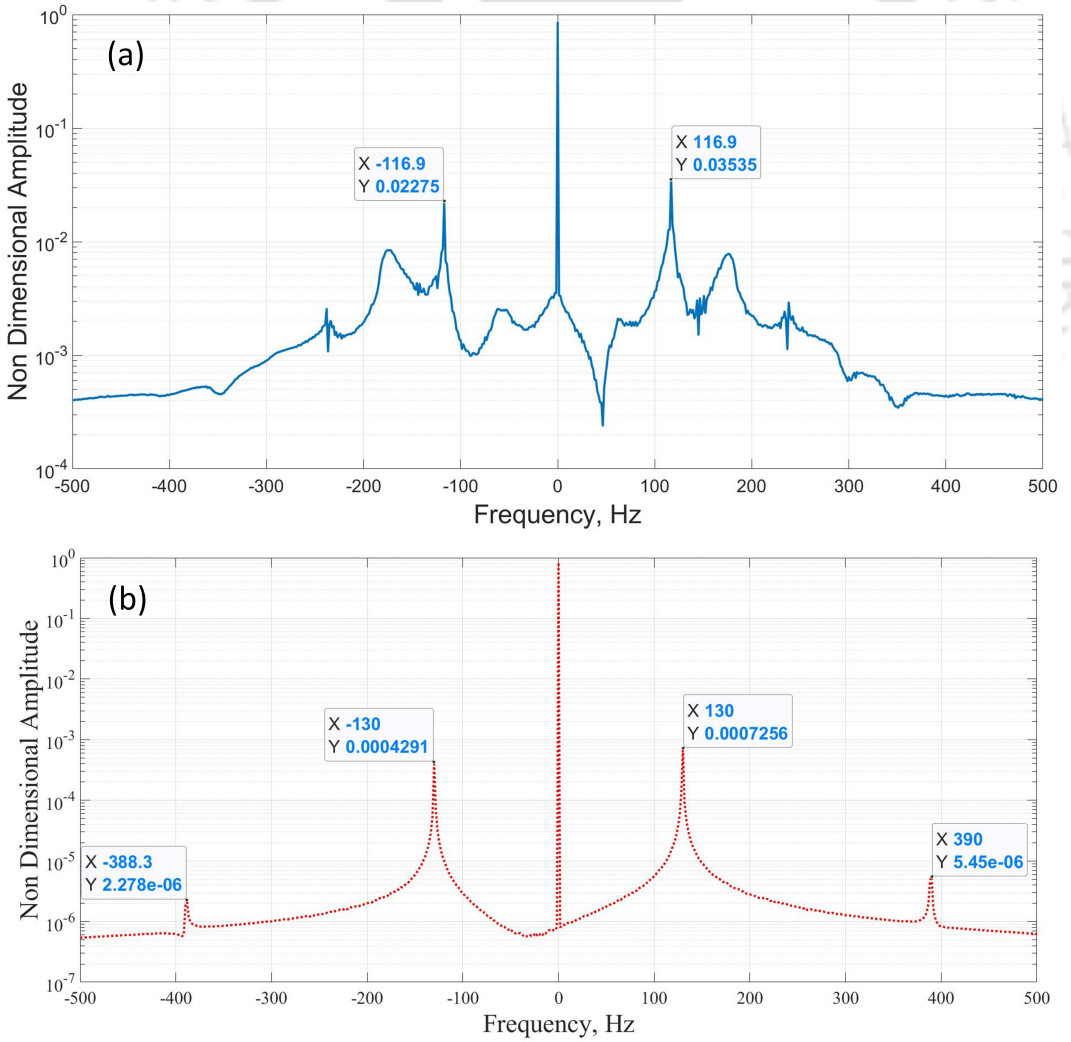

Figure 4.11: Full spectrum fast Fourier transform of the response when the rotor speed is 20000 rpm: (a) before electromagnetic actuator (EMA) applied and (b) after EMA applied.

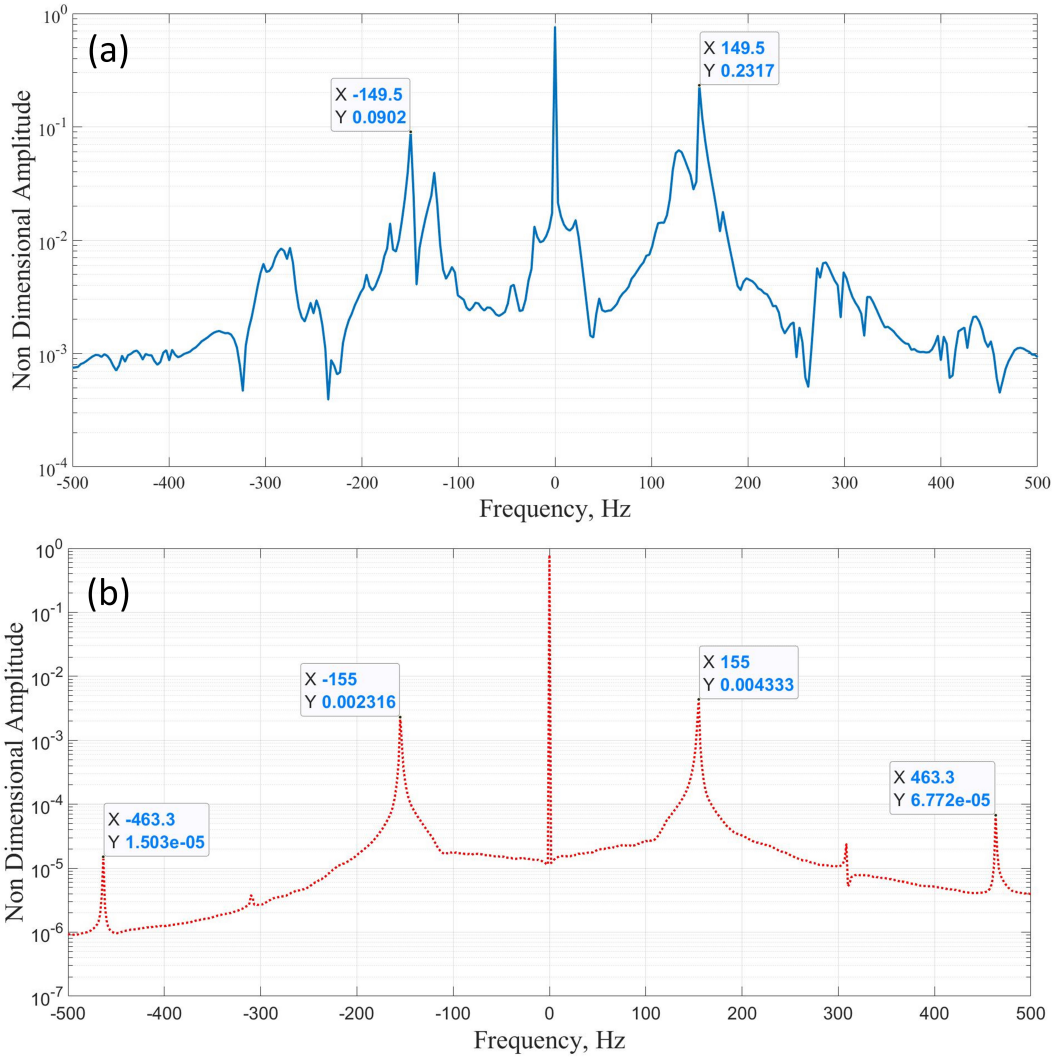

Figure 4.12: Full spectrum fast Fourier transform of the response when the rotor speed is 25600 rpm: (a) before electromagnetic actuator (EMA) applied and (b) after EMA applied.

4.3.3 Control Effort

The effect of the EMA has been discussed while explaining Case 1 and Case 2 in the previous section. It has been observed that the control effort plays a major role in controlling the rotor. In this section, the currents for controlling the rotor at 20000 rpm and 25600 rpm for both the cases, i.e. Case 1 and Case 2 mentioned in the previous section are investigated. The control effort also depends on the gains. In the present investigation, the proportional gain is taken as 500 A/m and the derivative gain is considered as 25 As/m.

In Fig. 4.13 the total current required to control the rotor along the X-axis neglecting the first 0.1s is shown. It has been observed that higher currents are required to control the rotor at 25600 rpm than the rotor rotating at 20000 rpm. As the rotor is unstable at

25600 rpm, higher control current is required to control the unstable rotor. It has also been noticed that the current required is less when the effect of EMA is not applied from the start. When the effect of EMA is not applied from start the current required is similar for both the speeds.

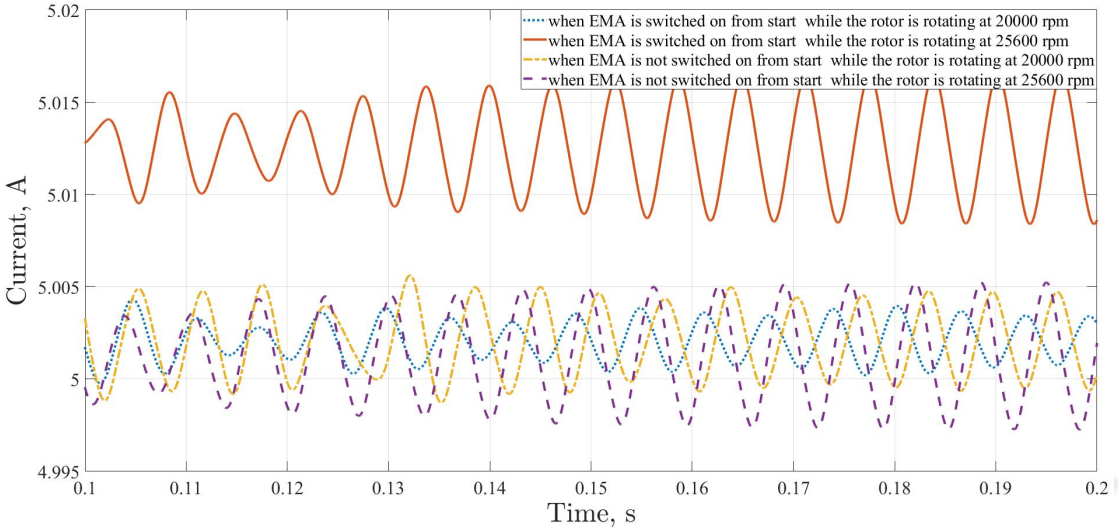

Figure 4.13: Total current required.

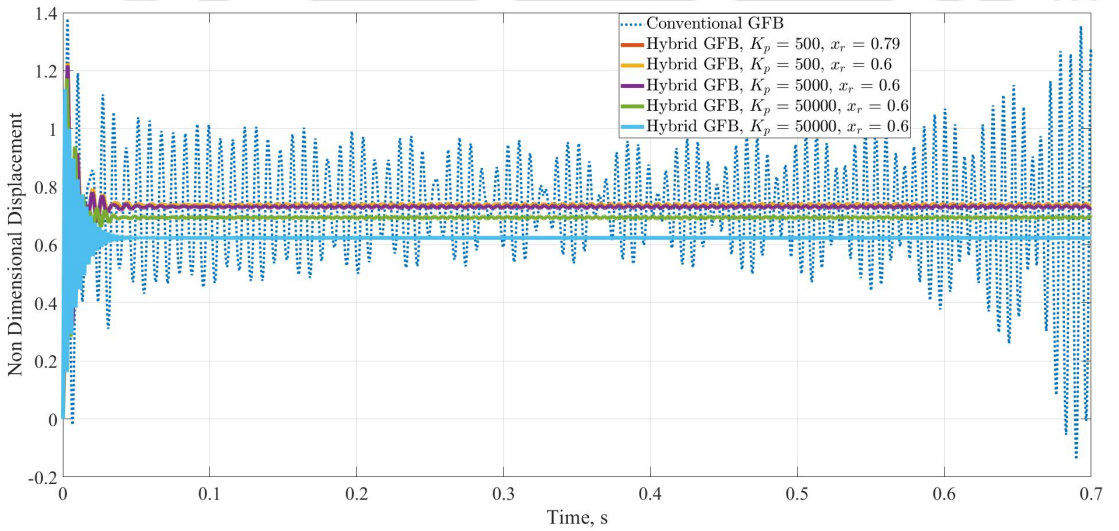

Figure 4.14: Non-dimensional displacement of rotor along X axis when the rotor speed is 25600 rpm for reference $x_r = 0.6$.

Further, a different reference value other than the natural steady state equilibrium position of GFB has been set and investigated. The new reference value has been choosen as $x_r = 0.6$ and $x_r = 0.9$ along X axis while it is kept constant along Y axis i.e. $y_r = 0.35$ in non-dimensional form. In Fig. 4.14, the effect of EMA on the displacement along X

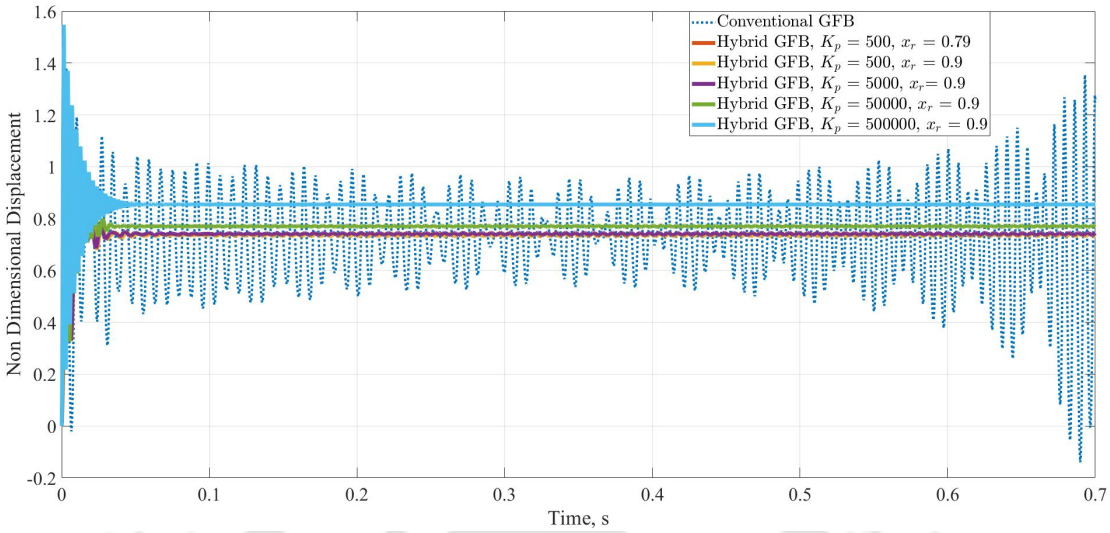

Figure 4.15: Non-dimensional displacement of rotor along X axis when the rotor speed is 25600 rpm for reference $x_r = 0.9$.

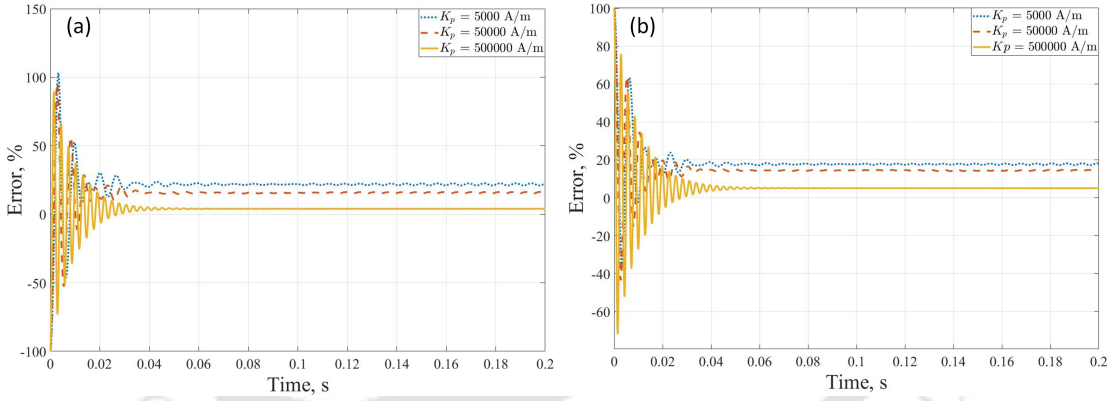

Figure 4.16: Error in displacement of rotor along X axis when the rotor speed is 25600 rpm for reference (a) $x_r = 0.6$ and (b) $x_r = 0.9$.

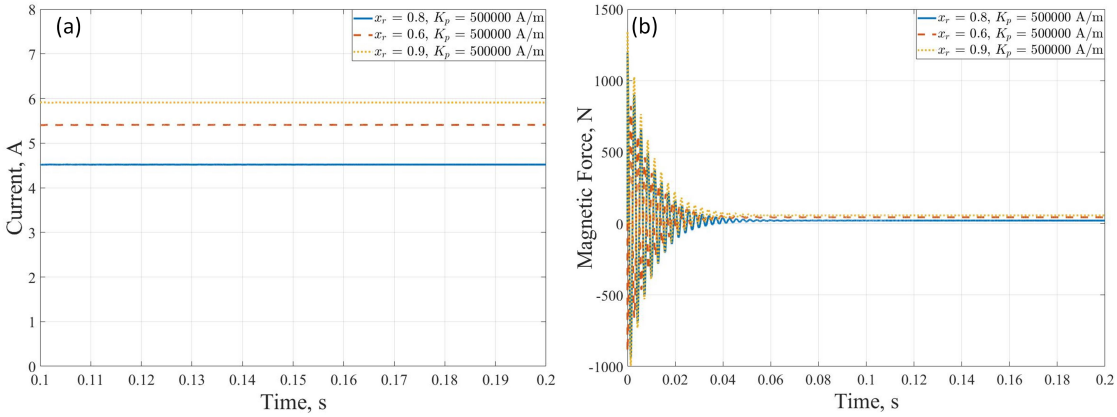

Figure 4.17: (a) Current along X axis when the rotor speed is 25600 rpm for different reference (b) Magnetic force along X axis when the rotor speed is 25600 rpm for different reference.

axis for different values of K_p for the reference point x_r = 0.6 when the rotor is rotating at 25600 rpm is shown. In Fig. 4.15, the effect of EMA on the displacement along X axis for different values of K_p for the reference point x_r = 0.9 when the rotor is rotating at 25600 rpm is shown. It has been observed that without the effect of EMA the amplitude of displacement is increasing. With the application of low magnetic force, the rotor became stable when the reference value is same as the natural steady state equilibrium position i.e. $x_r = 0.8$ along X axis and $y_r = 0.35$ along Y axis in non-dimensional form. The error in positioning the rotor in a set reference point and original displacement is more when the K_p is low as shown in Fig. 4.16. However as the K_p is value is increased the error becomes less. As such the response showed 30% of error from the set reference point to the actual steady state displacement when the K_p is 500 A/m. As the K_p is increased to 500000 A/m, the rotor moves to the set reference point and the error is reduced to 4.01% in case when the reference point is set as $x_r = 0.6$ while the error is reduced to 5.04 % in case of $x_r = 0.9$. The low K_p value produces low magnetic force, which is not sufficient to displace the rotor to the desired reference value. The reason for the requirement of high magnitude of the magnetic force is that the magnetic force has to act for supporting the rotor and move it to a desired reference value besides overcoming the hydrodynamic force. In any fluid film bearing, the hydrodynamic force generated due to the fluid film pressure supports the rotor weight. However, in hybrid Gas Foil Bearing the load has to be shared between the GFB and the EMA. The hydrodynamic force without the effect of EMA increases at 25600 rpm which causes the instability. The current required to control the rotor at the required position has been shown in Fig. 4.17(a). It has been observed that when the equilibrium position of the rotor is set other than the natural steady state of GFB, high current is required. It is also important to note that when the reference point is changed from the natural steady state of GFB, the hydrodynamic force decreases as the rotor is solely supported by the EMA. As a result, high magnetic force is required to maintain the rotor in the desired position. This has been shown in Fig. 4.17(b). Thus, it has been shown that with the incorporation of EMA, an unstable rotor can be made stable with very little effort.

4.4 Inferences

In the present chapter, a coupled model of GFB with and without the effect of EMA has been developed. The developed model has been used to investigate the effect of EMA on stability of the fully balanced rotor supported on GFB. In this regard, the following

two cases have been investigated: Case 1, i.e. when the effect of EMA is applied from start and Case 2 i.e. when the effect of EMA is applied at an arbitrary time. It has been demonstrated that using the EMA with a very small control current an unstable rotor can be made stable. The implementation of an electromagnetic actuator with a GFB reduces the amplitude of the response of the sub-synchronous frequency component for both the cases. As such 87% reduction in the amplitude of sub-synchronous vibration has been observed. The control current required to control the rotor in Case 2 i. e. when the effect of the EMA is not applied from the start, is less when compared to the control current in Case 1 i.e. when the effect of the EMA is applied from the start. Moreover, higher control current is required when the speed of the rotor increases. It has been observed that high magnetic force is required to control the rotor for a set reference value other than the natural steady state value of the response of the rotor supported by GFB without the effect of EMA. At low magnetic force the error between the set reference point and the natural reference point is about 30 %. Therefore, in order to reduce the power consumption, the reference value has to be set as the natural steady state value.

5

Unbalance response of rotor supported on Gas Foil Bearing integrated with Active Magnetic Bearing

Contents

5.1 Introduction

In the previous chapter, the stability of the rotor supported on hybrid Gas Foil Bearings has been discussed without considering the effect of mass unbalance. However, modern-day rotating machinery is exposed to severe kind of mechanical and environmental conditions. Controlling these vibrations and improving the dynamic behavior of the rotor are very important for the efficient and safe running of the machines. These vibrations can be reduced by applying some damping at the rotor supports. In this regard, the performance of a hybrid gas foil bearing (HGFB) adjoining conventional Gas Foil Bearing (GFB) along with Active Magnetic Bearing (AMB) as an electromagnetic actuator (EMA), to withstand unbalance has been investigated in the present chapter. Moreover, the ability to sustain sudden unbalance occurring in the rotor-bearing system has been investigated.

5.2 Mathematical Model

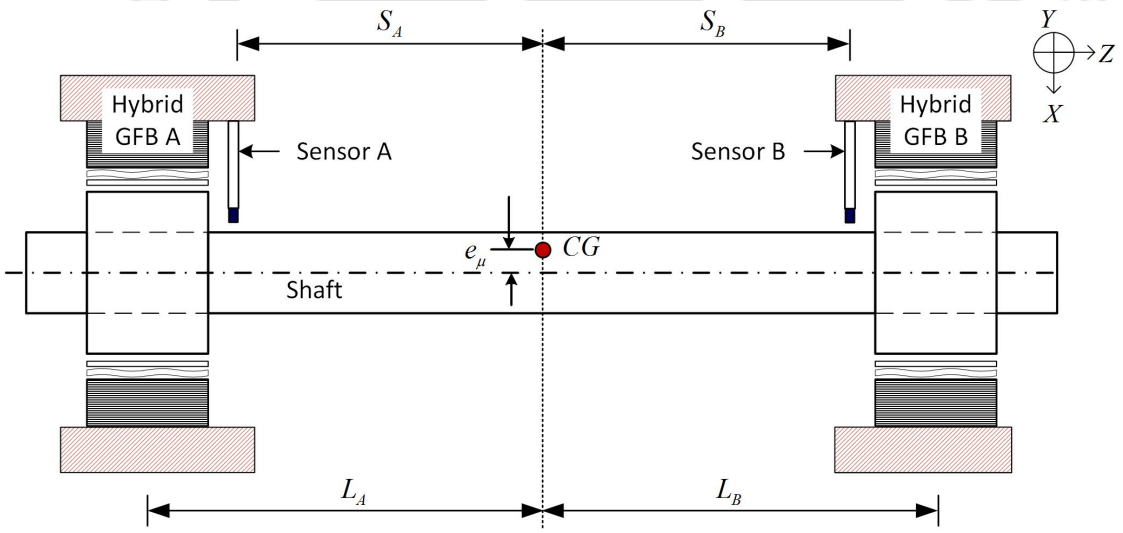

Figure 5.1: Schematic of rotor bearing assembly

The system of equations with unbalance at the bearing location A and B can be written as,

$$[M_{AB}]\{q''_{AB}\} + [G_{AB}]\{q'_{AB}\} = \{F_{AB}\} + \{F_{mag-AB}\} + \{F_{ub}\} + \{W_{AB}\} \tag{5.1}$$

$$\text{where, } [M_{AB}] = \frac{1}{L^2}\begin{bmatrix} L_B^2M + I_{yy} & 0 & L_AL_BM - I_{yy} & 0 \\ 0 & L_B^2M + I_{xx} & 0 & L_AL_BM - I_{xx} \\ L_AL_BM - I_{yy} & 0 & L_A^2M + I_{yy} & 0 \\ 0 & L_AL_BM - I_{xx} & 0 & L_A^2M + I_{xx} \end{bmatrix},$$

$$[G_{AB}] = \frac{1}{L^2}\begin{bmatrix} 0 & -I_{zz} & 0 & I_{zz} \\ I_{zz} & 0 & -I_{zz} & 0 \\ 0 & I_{zz} & 0 & -I_{zz} \\ -I_{zz} & 0 & I_{zz} & 0 \end{bmatrix}, \{F_{AB}\} = \begin{Bmatrix} F_{xA} \\ F_{yA} \\ F_{xB} \\ F_{yB} \end{Bmatrix}, \{F_{mag-AB}\} = \begin{Bmatrix} F_{mag-xA} \\ F_{mag-yA} \\ F_{mag-xB} \\ F_{mag-yB} \end{Bmatrix},$$

$$\{W_{AB}\} = \begin{Bmatrix} W \\ 0 \\ W \\ 0 \end{Bmatrix} \text{ and } \{F_{ub}\} = [T_1]^{-T} \begin{Bmatrix} Me_\mu \omega^2 \cos \omega t \\ Me_\mu \omega^2 sin\omega t \\ Me_\mu \omega^2 \cos \omega t \\ Me_\mu \omega^2 sin\omega t \end{Bmatrix}$$

5.3 Results and Discussion

5.3.1 Effect of unbalance eccentricity

The rotor bearing parameters used in the present investigation is given in Table 4.1 and Table 4.2. The steady state part of the journal response has been analysed and hence, the time series data of the initial 500 revolutions of the rotor has not been considered. Further, the simulations are performed with the various amount of unbalance at 20000 rpm. It has been mentioned earlier that hydrodynamic fluid film forces of the GFB bearings does not get generated in a concentric rotor. However, in general the AMB, tries to force the rotor to the centre of the bearing. Therefore, in order to uphold the load sharing characteristic of the hybrid GFBs an equilibrium position other than the bearing centre has to be set. The equilibrium point of the steady state of the rotor response, has been chosen as 0.8 along X -axis and 0.35 along Y -axis which is the steady state response of the rotor without unbalance.

In Fig. 5.2, the trajectory, Poincaré plot and full spectrum of the non-dimensional

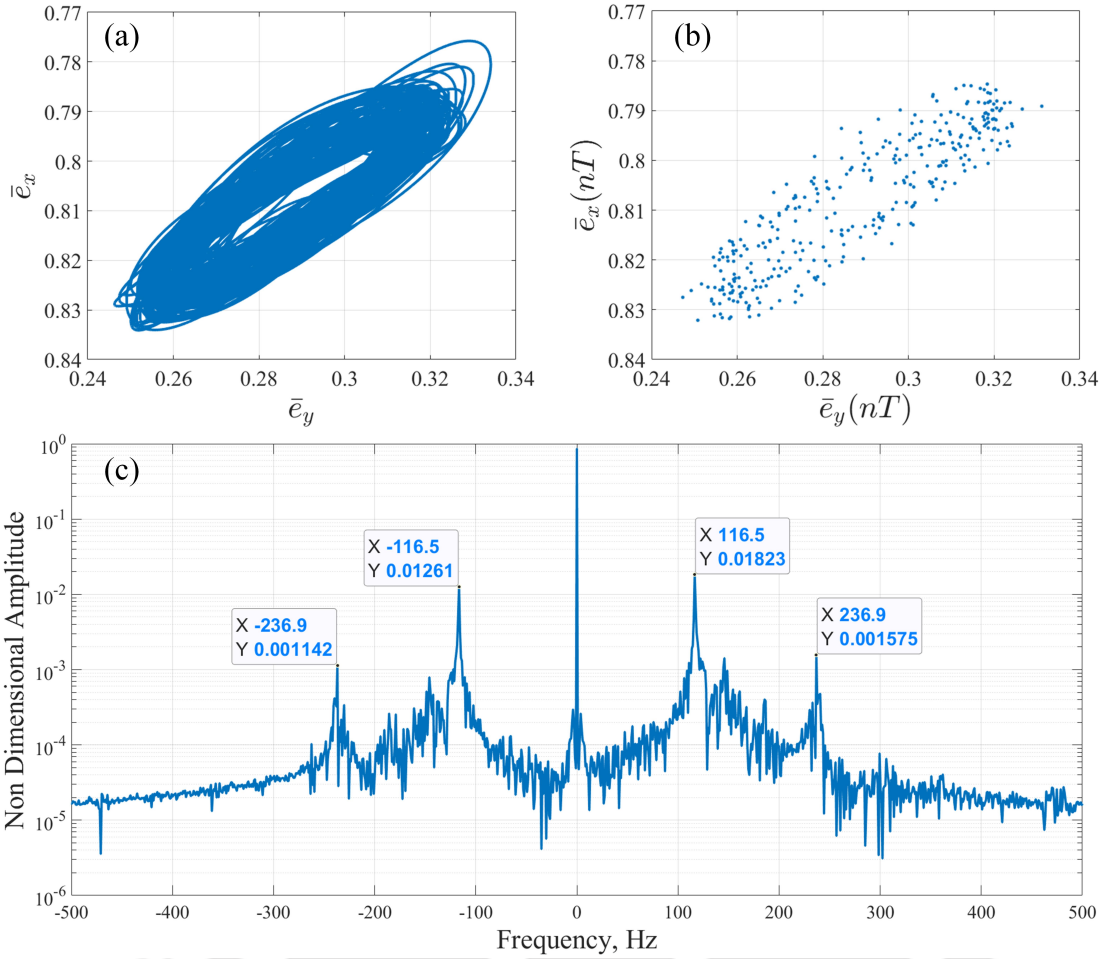

Figure 5.2: (a) Trajectory, (b) Poincaré plot and (c) FFT plot of the non-dimensional rotor response when the rotor supported on conventional GFB with an unbalance eccentricity of 1×10^{-10} m

displacements of the rotor when the rotor is supported on conventional GFBs with an unbalance eccentricity of 1×10^{-10} m is shown. It has been observed that the rotor traverses a quasi-periodic as seen in Fig. 5.2a and can be confirmed from the Poincaré plot (5.2b). In the full spectrum Fast Fourier Transform (FFT) plot, high amplitude of the sub-synchronous frequency at 116.5 Hz and 238.9 Hz has been observed. In Fig. 5.3, the trajectory, Poincaré plot and full spectrum of the non-dimensional displacements of the rotor when the rotor is supported on hybrid GFBs with an unbalance eccentricity of 1×10^{-10} m is shown. The rotor show different trajectory in case of hybrid although the unbalance eccentricity is same. It has been observed that the sub-synchronous frequency at 116.5 Hz is absent in case of hybrid GFB. However, another sub-synchronous frequency 146.1 Hz has been observed. This is probably because at low unbalance eccentricity the hydrodynamic force is more dominating rather than the unbalance force.

Figure 5.4 shows the trajectory, Poincaré plot and full spectrum of the non-dimensional

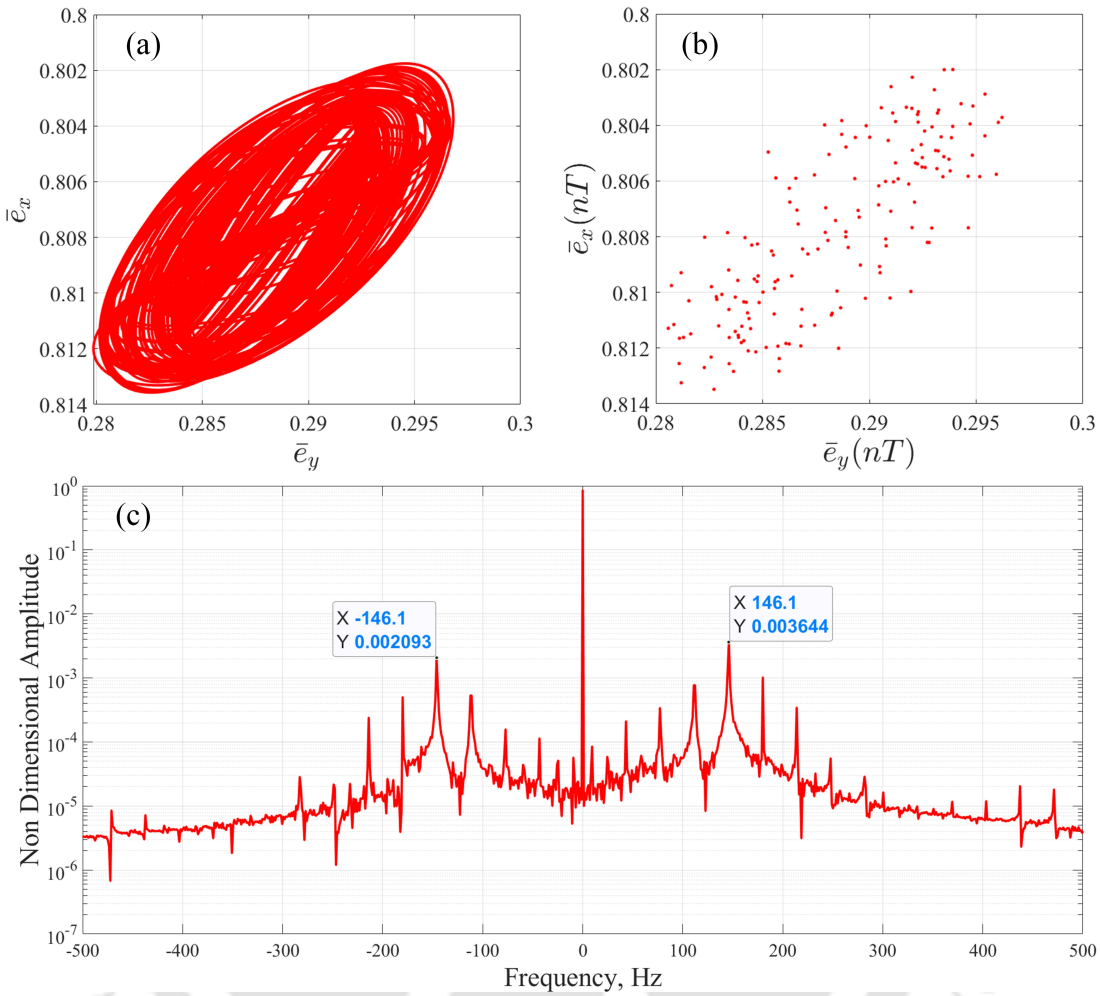

Figure 5.3: (a) Trajectory, (b) Poincaré plot and (c) FFT plot of the non-dimensional rotor response when the rotor supported on hybrid GFB with an unbalance eccentricity of 1×10^{-10} m

displacements of the rotor when the rotor is supported on conventional GFBs with an unbalance eccentricity of 1×10^{-8} m. At this unbalance eccentricity, a small peak of the synchronous frequency can be observed (Fig. 5.4c). The trajectory is quasi-periodic as observed in Fig. 5.4a and Fig. 5.4b. Nevertheless the sub-synchronous frequency at 116.5 is still the dominating frequency. In Fig. 5.5 the trajectory, Poincaré plot and full spectrum of the non-dimensional displacements of the rotor when the rotor is supported on hybrid GFBs with an unbalance eccentricity of 1×10^{-8} m is shown. The trajectory and Poincaré plot is also quasi-periodic. In the case of hybrid GFB, the FFT plot also show a small peak of synchronous frequency. It has been observed that the amplitude of the response of the synchronous frequency increases as the unbalance increases while the amplitude of the sub-synchronous frequency at 238.9 Hz decreases. At an unbalance eccentricity of 1×10^{-7} m, the sub-synchronous frequency at 238.9 Hz gets completely eliminated.

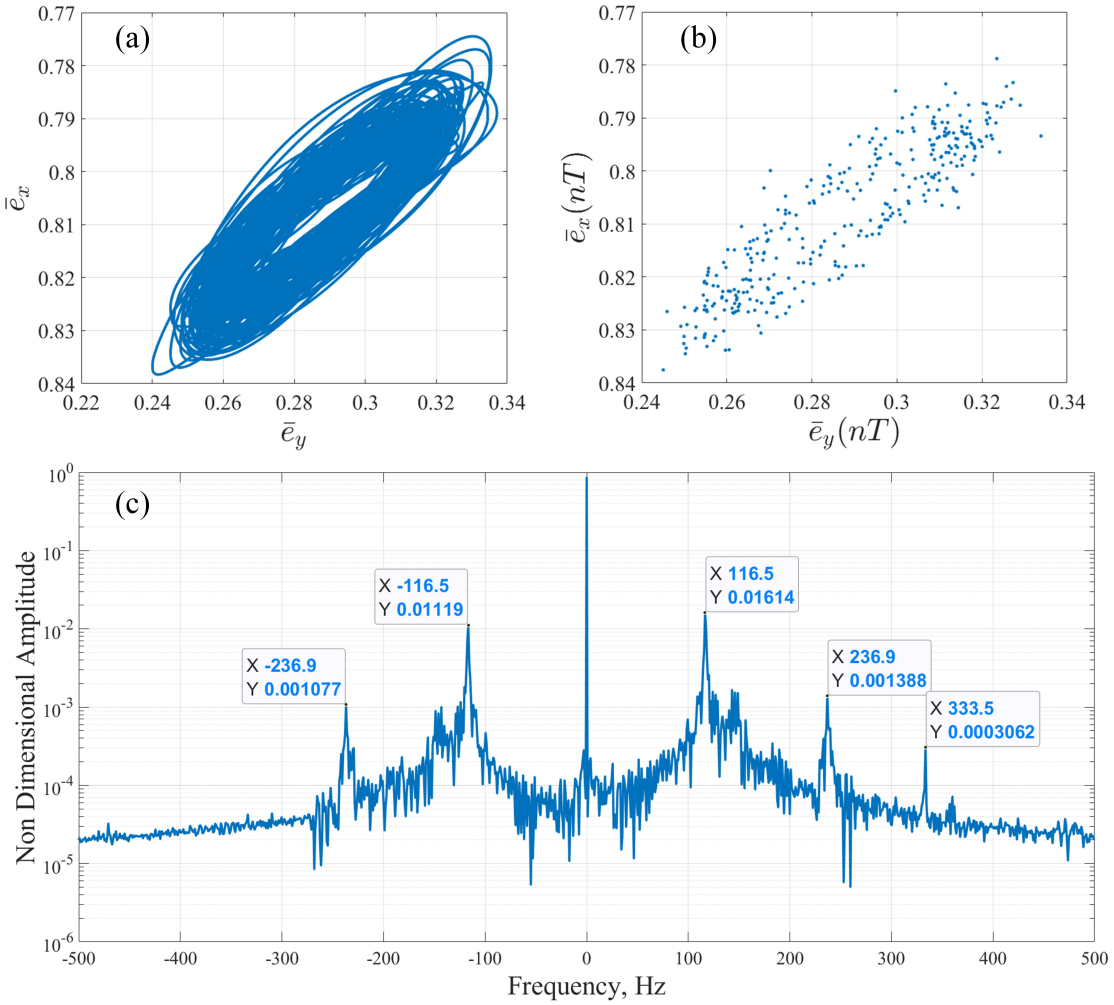

Figure 5.4: (a) Trajectory, (b) Poincaré plot and (c) FFT plot of the non-dimensional rotor response when the rotor supported on conventional GFB with an unbalance eccentricity of 1×10^{-8} m

However, the trajectory is still periodic and the sub-synchronous frequency at 116.5 Hz is still the dominating frequency. This has been shown in Fig. 5.6. Figure 5.7 shows the trajectory, Poincaré plot and full spectrum of the non-dimensional displacements of the rotor when the rotor is supported on hybrid GFBs with an unbalance eccentricity of 1×10^{-7} m. It has been observed that the amplitude of the response of the sub-synchronous is equal to the amplitude of the synchronous frequency in case of the hybrid GFB. In case of hybrid GFB, the sub-synchronous frequency occurs at is 145 Hz.

As the unbalance eccentricity is increased further, the amplitude of the response of the sub-synchronous frequency is further reduced and the synchronous frequency becomes the dominating frequency. In Fig. 5.8 the trajectory, Poincaré plot and full spectrum of the non-dimensional displacements of the rotor when the rotor is supported on conventional GFBs with an unbalance eccentricity of 1.5×10^{-7} m has been shown.

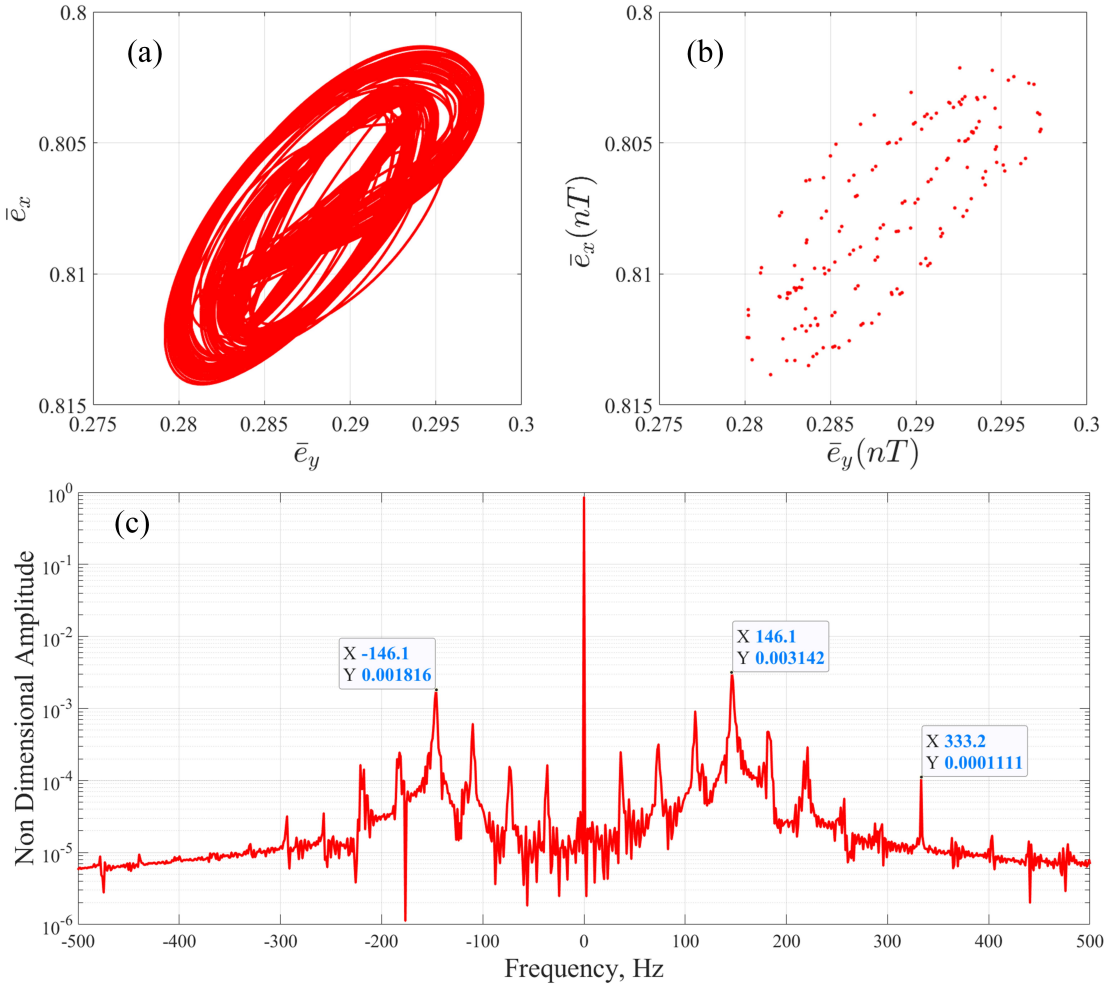

Figure 5.5: (a) Trajectory, (b) Poincaré plot and (c) FFT plot of the non-dimensional rotor response when the rotor supported on hybrid GFB with a unbalance eccentricity of 1×10^{-8} m

The trajectory plot show the rotor traversing a periodic motion. Moreover, in the FFT plot, high amplitude of synchronous frequency can be observed. In the case of hybrid GFB, the rotor trajectory is also periodic as observed in Fig. 5.9. In the FFT plot, it can be observed that, the sub-synchronous frequency is absent (Fig. 5.9c). As the unbalance eccentricity is further increased in case of conventional GFB, the amplitude of the response of the sub-synchronous frequency at about 116 Hz is reduced further. At an unbalance eccentricity of 2×10^{-6}, the amplitude of the response of the sub-synchronous frequency is almost eliminated in case of the conventional GFB (Fig. 5.10c). The rotor motion is still periodic as observed from trajectory plot and Poincaré plot shown in Fig. 5.10a and 5.10b respectively. In the case of hybrid GFB, the rotor motion is periodic and the sub-synchronous frequency is absent as shown in Fig. 5.11.

In Fig. 5.12, the trajectory, Poincaré plot and full spectrum of the non-dimensional

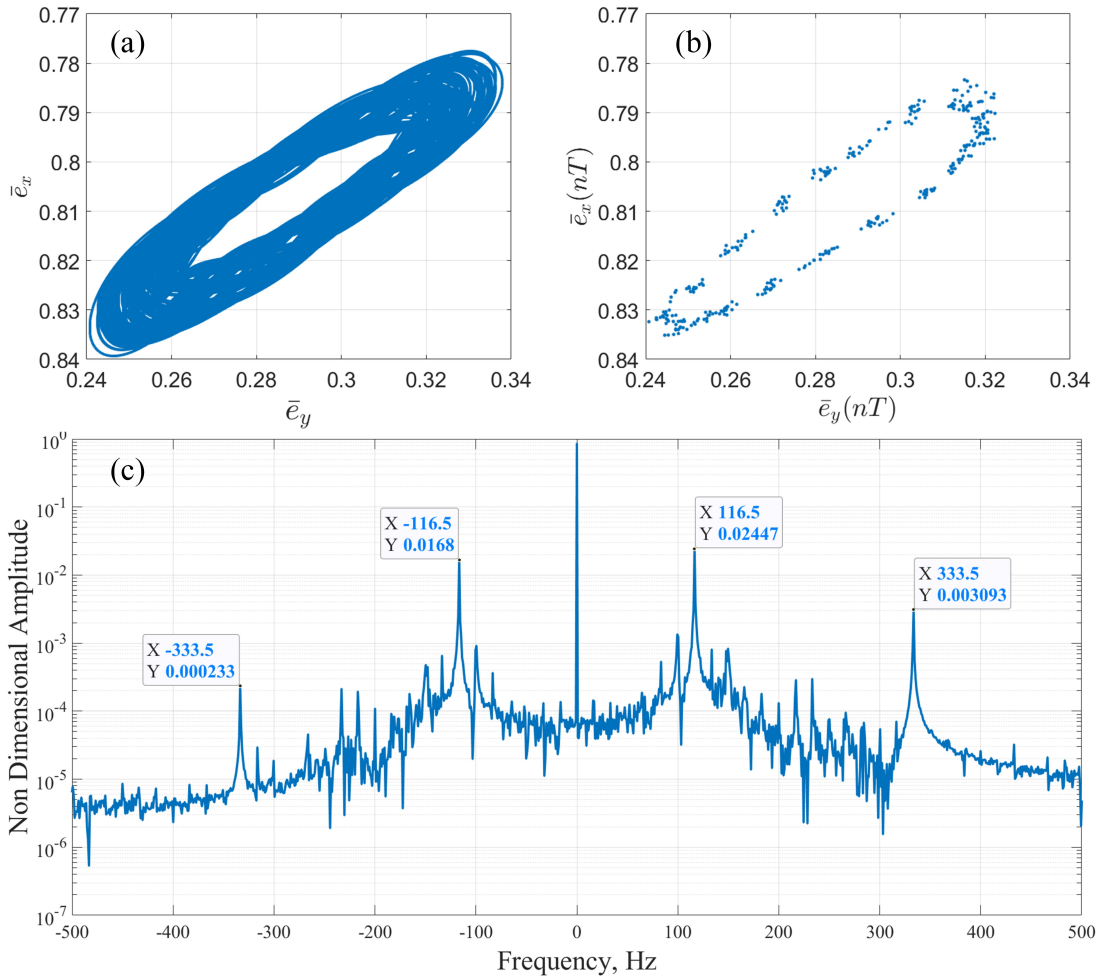

Figure 5.6: (a) Trajectory, (b) Poincaré plot and (c) FFT plot of the non-dimensional rotor response when the rotor supported on conventional GFB with an unbalance eccentricity of 1×10^{-7} m

displacements of the rotor when the rotor is supported on conventional GFBs with an unbalance eccentricity of 3×10^{-6} m is shown. The trajectory and Poincaré plot shows periodic motion of the rotor. However, it has been observed that the sub-synchronous frequency again start to reappear at 143.1 Hz. In Fig. 5.13, the trajectory, Poincaré plot and full spectrum of the non-dimensional displacements of the rotor when the rotor is supported on the hybrid GFBs with an unbalance eccentricity of 3×10^{-6} m is shown. The rotor motion is still periodic as observed from trajectory plot and Poincaré plot in case of hybrid GFB. The FFT plot show one single peak of the synchronous frequency. Further, it has been observed that at an unbalance eccentricity of 4.14×10^{-6} m, the rotor traverses period two motion as observed in Fig. 5.14a. The Poincaré plot show two distinct points confirming the period two motion. Moreover, the amplitude of response of the sub-synchronous frequency is higher than the amplitude of response of the synchronous

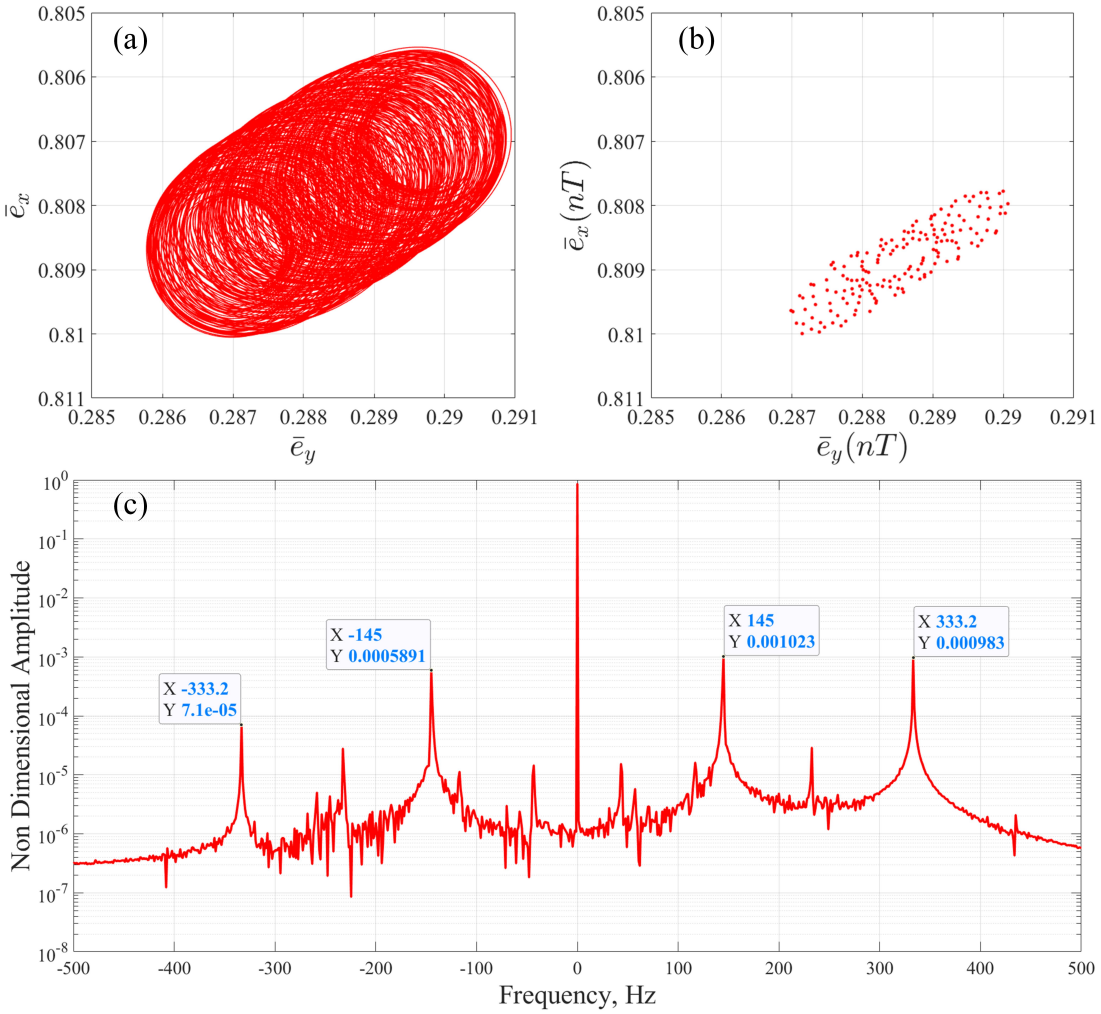

Figure 5.7: (a) Trajectory, (b) Poincaré plot and (c) FFT plot of the non-dimensional rotor response when the rotor supported on hybrid GFB with an unbalance eccentricity of 1×10^{-7} m

frequency. In case of the hybrid GFB, as the unbalance eccentricity is increased, the radius of the rotor orbit increases. However, the rotor motion is still periodic. The trajectory, Poincaré plot and full spectrum of the non-dimensional displacements of the rotor when the rotor is supported on hybrid GFBs with an unbalance eccentricity of 4.1×10^{-6} m is shown in Fig. 5.15. The FFT plot show presence of only synchronous frequency.

As the unbalance eccentricity is further increased to 5×10^{-6} m the rotor shows a peculiar trajectory in case of conventional GFB as shown in Fig. 5.16 .Moreover, multiple frequency components has been observed (Fig. 5.16c). The amplitude of the response of the sub-synchronous frequency at 145 Hz, is higher than the amplitude of the response of the synchronous frequency. In case of hybrid GFB, the rotor motion is periodic with only a synchronous peak at 333.2 Hz as shown in Fig. 5.17. Further, at an

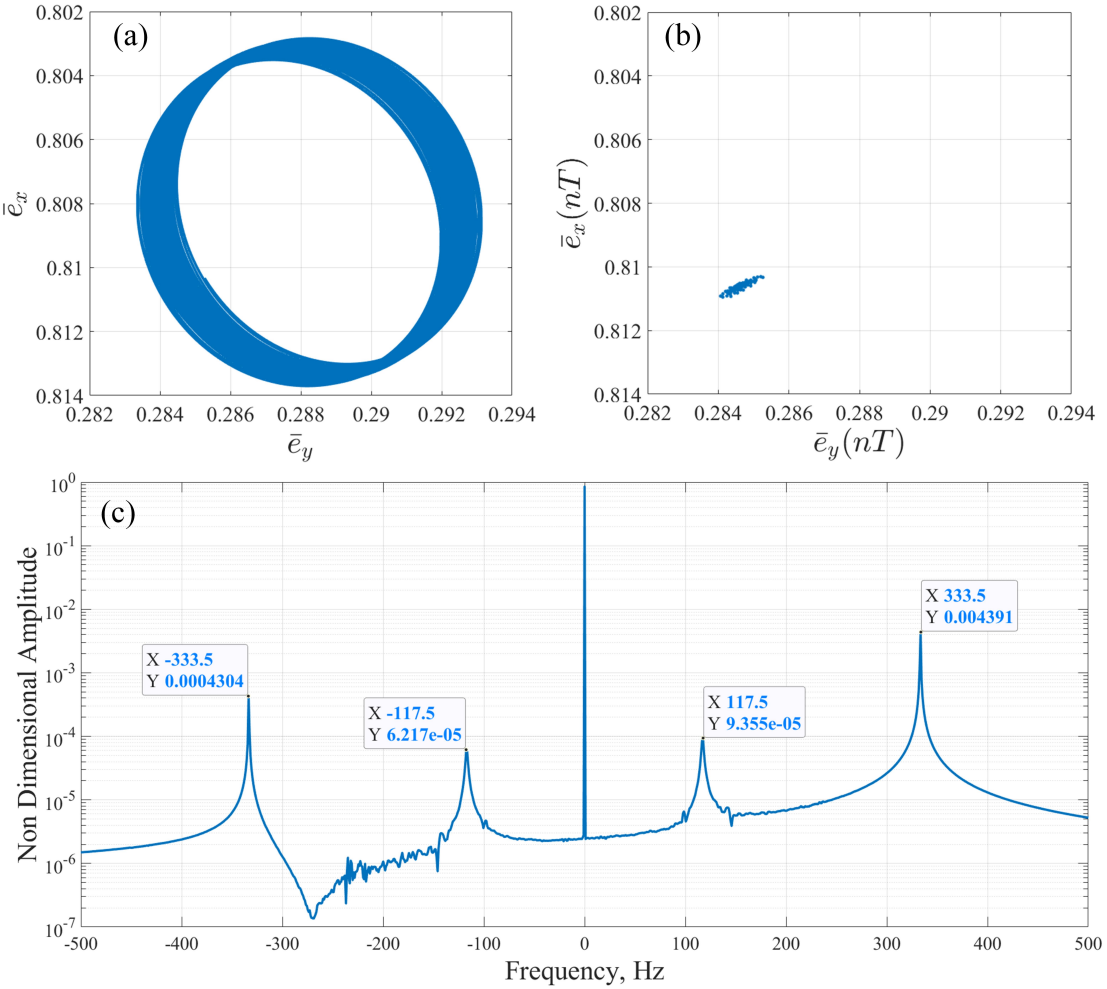

Figure 5.8: (a) Trajectory, (b) Poincaré plot and (c) FFT plot of the non-dimensional rotor response when the rotor supported on conventional GFB with an unbalance eccentricity of 1.5×10^{-7} m

unbalance eccentricity is increased to 6.5×10^{-6} m, the trajectory of the rotor supported on conventional GFB becomes random as observed in Fig. 5.18a and Fig. 5.18b. The FFT plot show high amplitude of the response of the positive component of the sub-synchronous and synchronous frequency at 148.8 Hz and 333.5 Hz respectively. However, the negative component of the synchronous frequency is absent. Figure 5.19 shows the trajectory, Poincaré plot and full spectrum of the non-dimensional displacements of the rotor when the rotor is supported on hybrid GFBs with an unbalance eccentricity of 6.5×10^{-6} m. The rotor trajectory is periodic and the dominating frequency is the synchronous frequency as anticipated. It has been observed that further simulation in case of conventional GFB has not been possible with higher eccentricity as the rotor trajectory becomes more unstable and the Reynolds equation fails to converge. However, the trajectory has been periodic with lower amplitude of the response of the synchronous

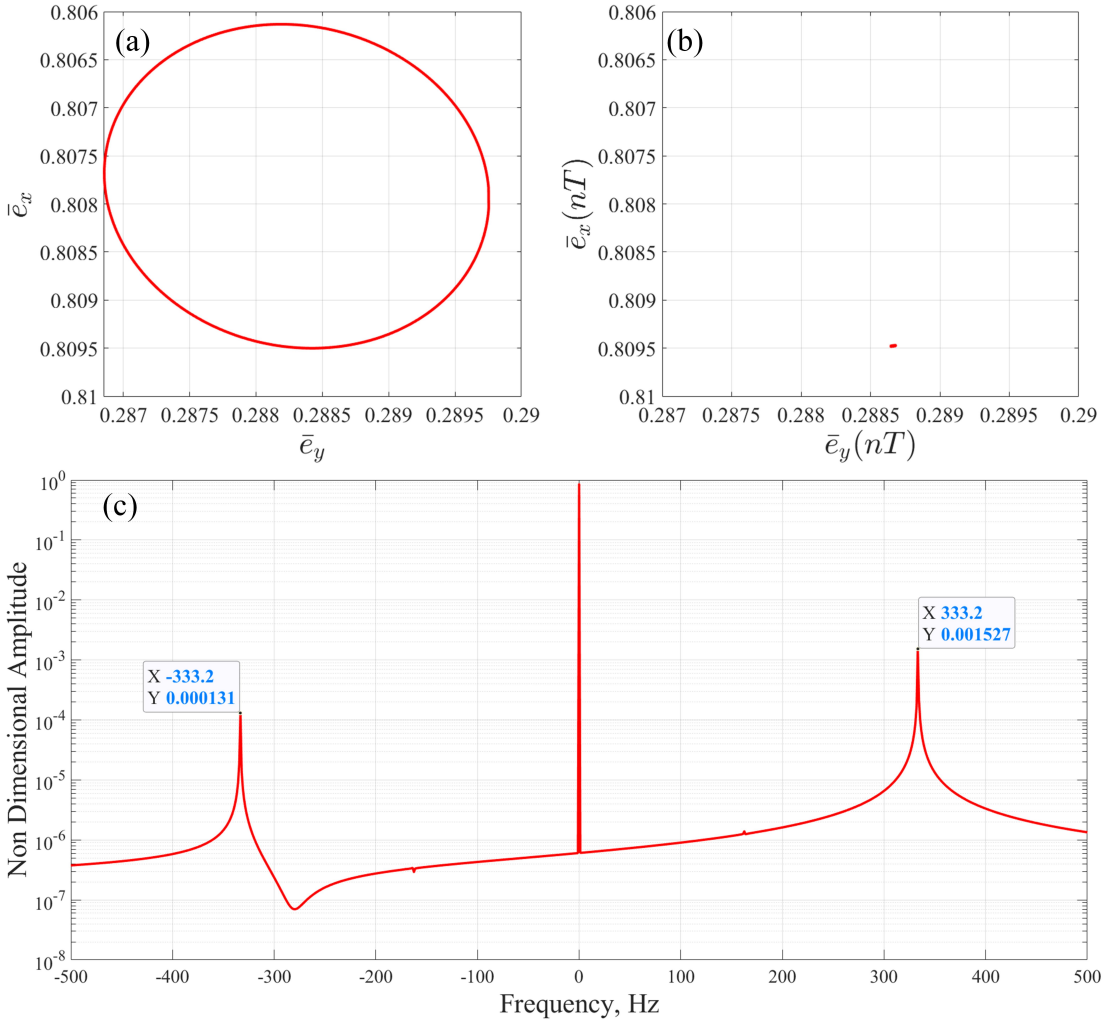

Figure 5.9: (a) Trajectory, (b) Poincaré plot and (c) FFT plot of the non-dimensional rotor response when the rotor supported on hybrid GFB with a unbalance eccentricity of 1.5×10^{-7} m

frequency in case of hybrid GFB suggesting the rotor could sustain higher unbalance.

Further, in order to investigate the limit of the hybrid GFB only the response of the hybrid GFB has been simulated for higher unbalance eccentricity. At an unbalance eccentricity of 3×10^{-5} m the rotor supported on hybrid GFB show period 2 motion as shown in Fig. 5.20a. Two distinct points could be observed in the Poincaré plot (Fig.5.20b). In the FFT plot a small peak of the sub-synchronous peak can be observed at 166.7 Hz as shown in Fig. 5.20c. In Fig. 5.21 the trajectory, Poincaré plot and full spectrum of the non-dimensional displacements of the rotor when the rotor is supported on hybrid GFBs with an unbalance eccentricity of 4.2×10^{-5} m has been shown. At this unbalance, the trajectory becomes multi-periodic. In the FFT plot multiple peaks of sub-synchronous frequency has been observed. It has been found that further increment in the

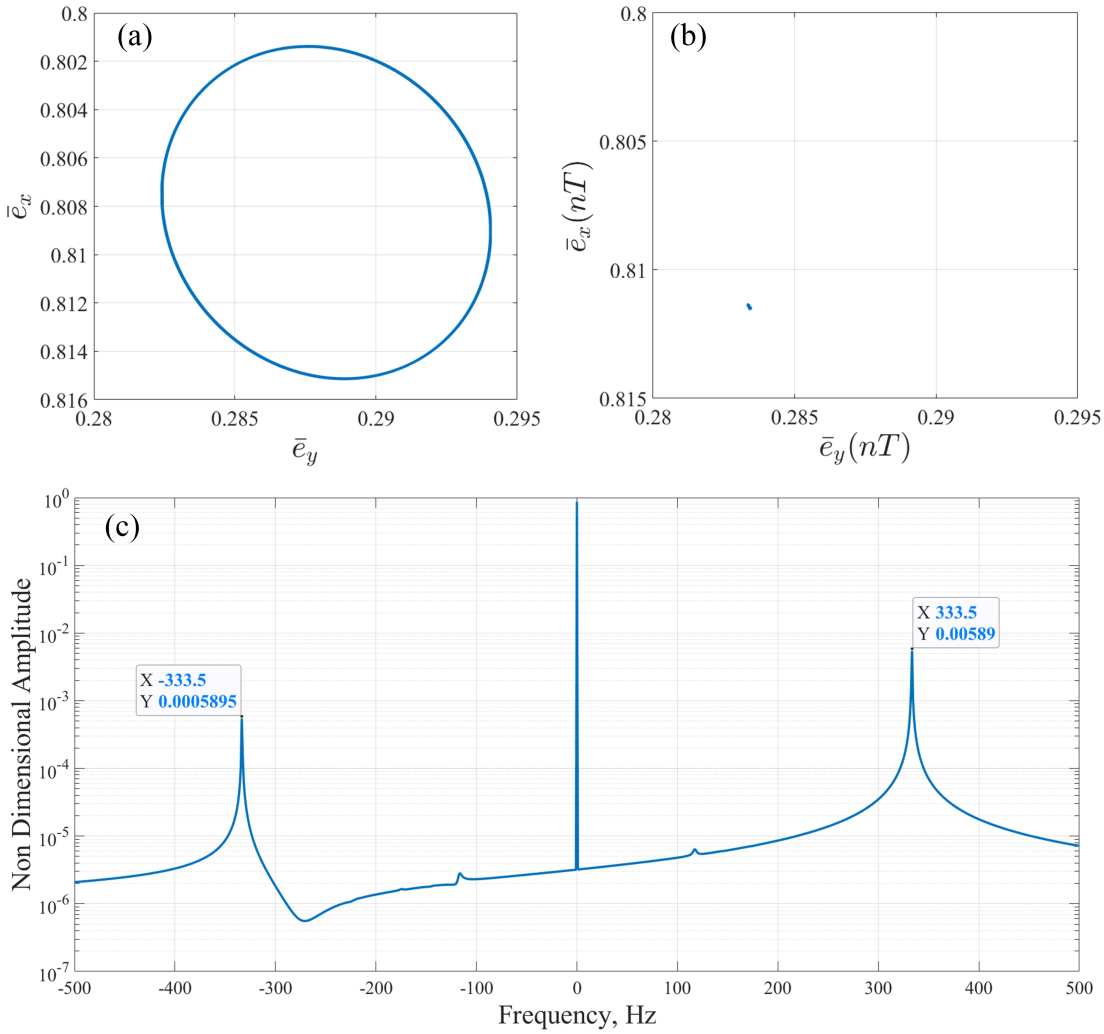

Figure 5.10: (a) Trajectory, (b) Poincaré plot and (c) FFT plot of the non-dimensional rotor response when the rotor supported on conventional GFB with an unbalance eccentricity of 2×10^{-6} m

unbalance lead to instability. Therefore, for the current AMB configuration, the limit of the unbalance can be increased from 6.5×10^{-6} m to 4.2×10^{-5} m. However, by tuning the Proportional and Derivative gains, the stability of the rotor can be further increased.

Effect on control current

The control current is an important factor in controlling the displacement of the rotor to keep it in the required position. The variation of the control currents have to be kept minimum in order to have a linearized magnetic force. Therefore, the total current has to be estimated. In general, for a linearized magnetic force the control current has to be of smaller magnitude compared to the applied bias current. Therefore, to consider the

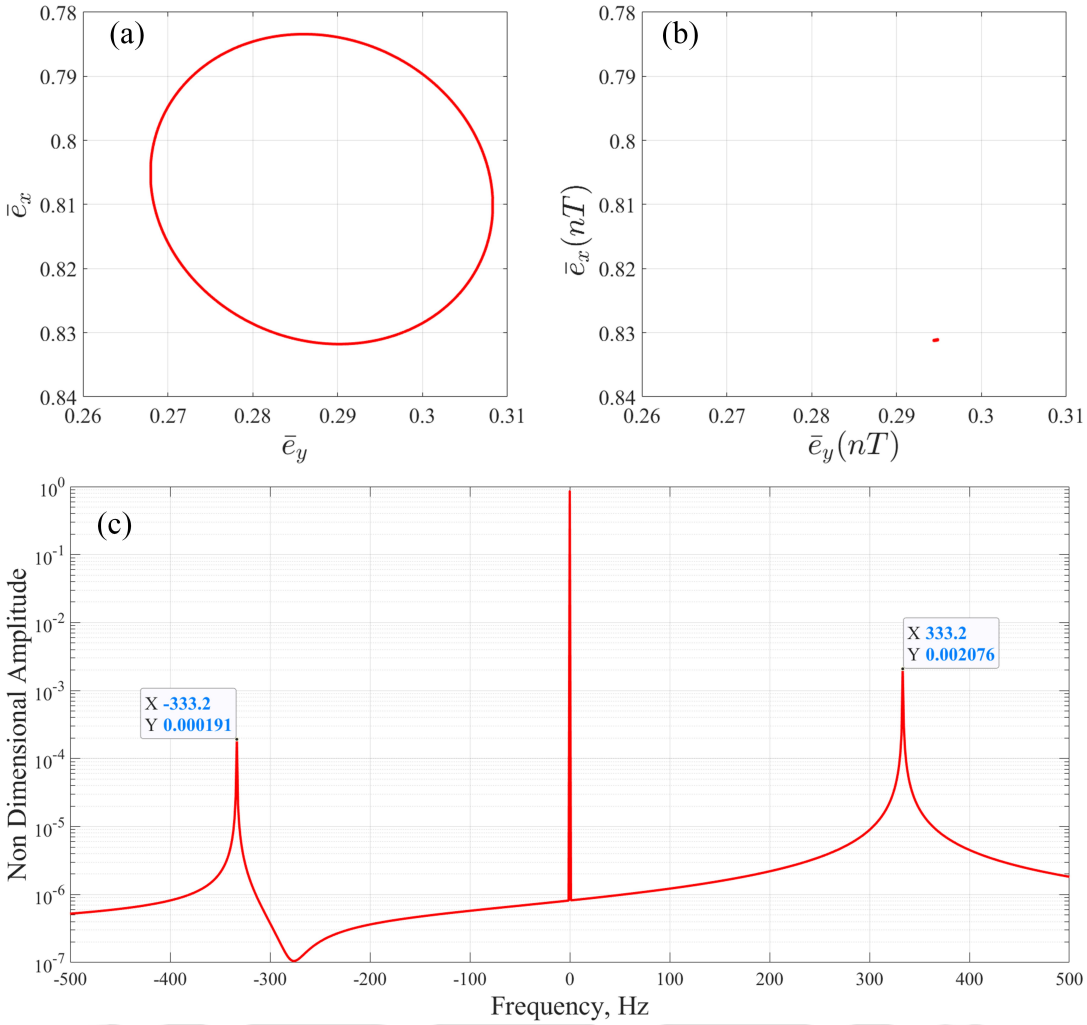

Figure 5.11: (a) Trajectory, (b) Poincaré plot and (c) FFT plot of the non-dimensional rotor response when the rotor supported on hybrid GFB with an unbalance eccentricity of 2×10^{-6} m

linearized magnetic force the variation of control current is allowed to be a variation of ±0.5A of the bias current. The total current necessary in order to control the rotor for various mass unbalance for the first 0.48 s to 0.5 s has been shown in Fig. 5.22 . Figure 5.22a show the effect of mass unbalance on the current along X axis for bearing A while, Fig. 5.22b show the variation of current along Y axis for bearing A. The current required to control the rotor is higher when the unbalance eccentricity is higher. It has been observed that at 4.2×10^{-5} mm the maximum current required is about 6A implying the limit of linearized magnetic force. Therefore, to avoid magnetic saturation of the actuator the unbalance has to be kept within certain limit. When the unbalance eccentricity is 2×10^{-5} the maximum current is about 5.5 A. Therefore, inorder to have a linearised magnetic force, the unbalance eccentricity has to be limited to 2×10^{-5}.

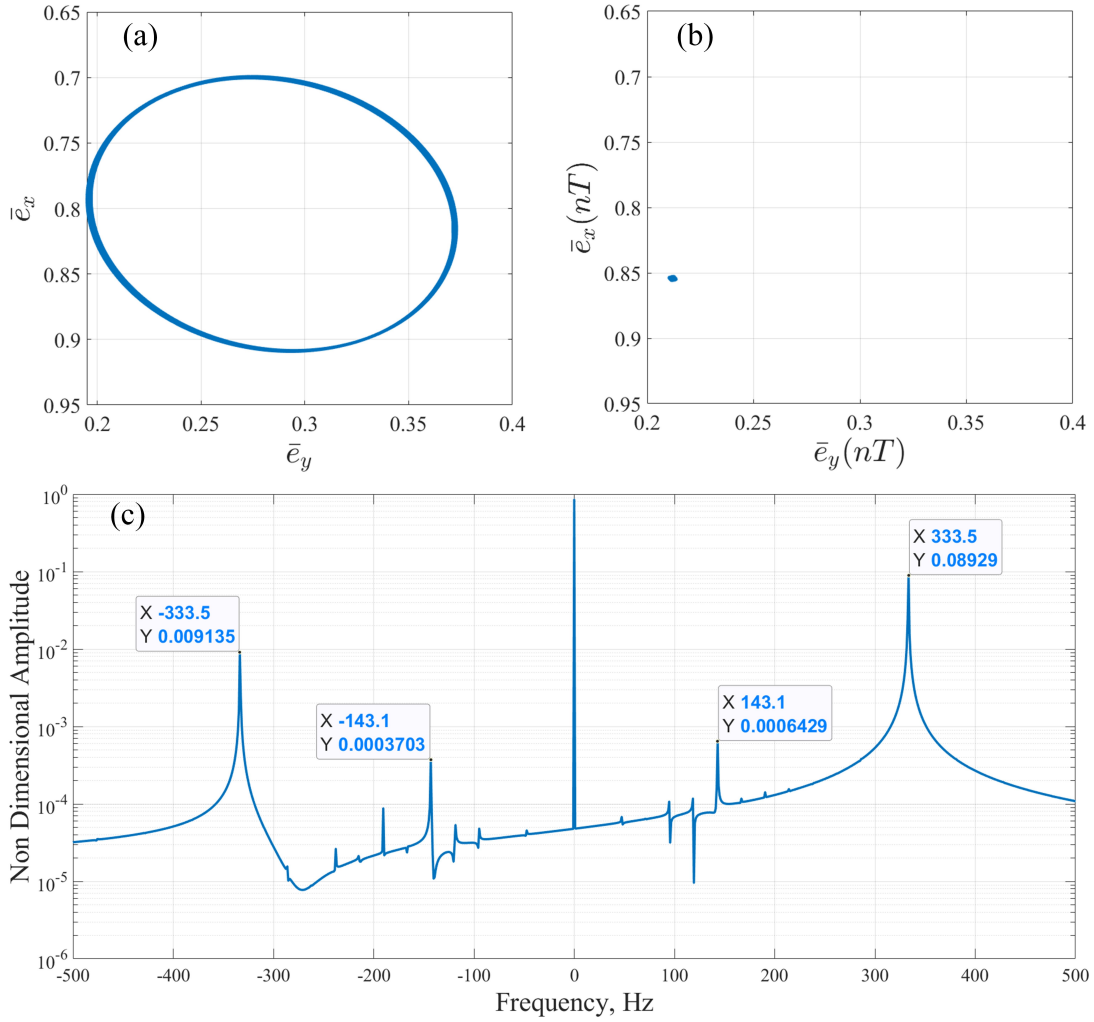

Figure 5.12: (a) Trajectory, (b) Poincaré plot and (c) FFT plot of the non-dimensional rotor response when the rotor supported on conventional GFB with an unbalance eccentricity of 3×10^{-6} m

Effect on Fluid Film Thickness

In a hydrodynamic bearing the fluid film plays an important role in developing the hydrodynamic pressure and avoid contact of the bearing inner surface with the journal. In Fig. 5.23, the variation of the minimum film thickness for an unbalance eccentricity of 1×10^{-6} m is shown. In the conventional GFB, high oscillations of the minimum film thickness can be observed, however, in case of the hybrid GFB, the oscillations of the minimum film thickness is reduced. When the unbalance eccentricity is increased to 4.6×10^{-6} m, the fluctuation of the minimum film thickness is further increased and becomes negative indicating a contact between the journal and bearing surface as shown in Fig.5.24. In case of hybrid GFB, the fluctuation of the minimum film thickness is

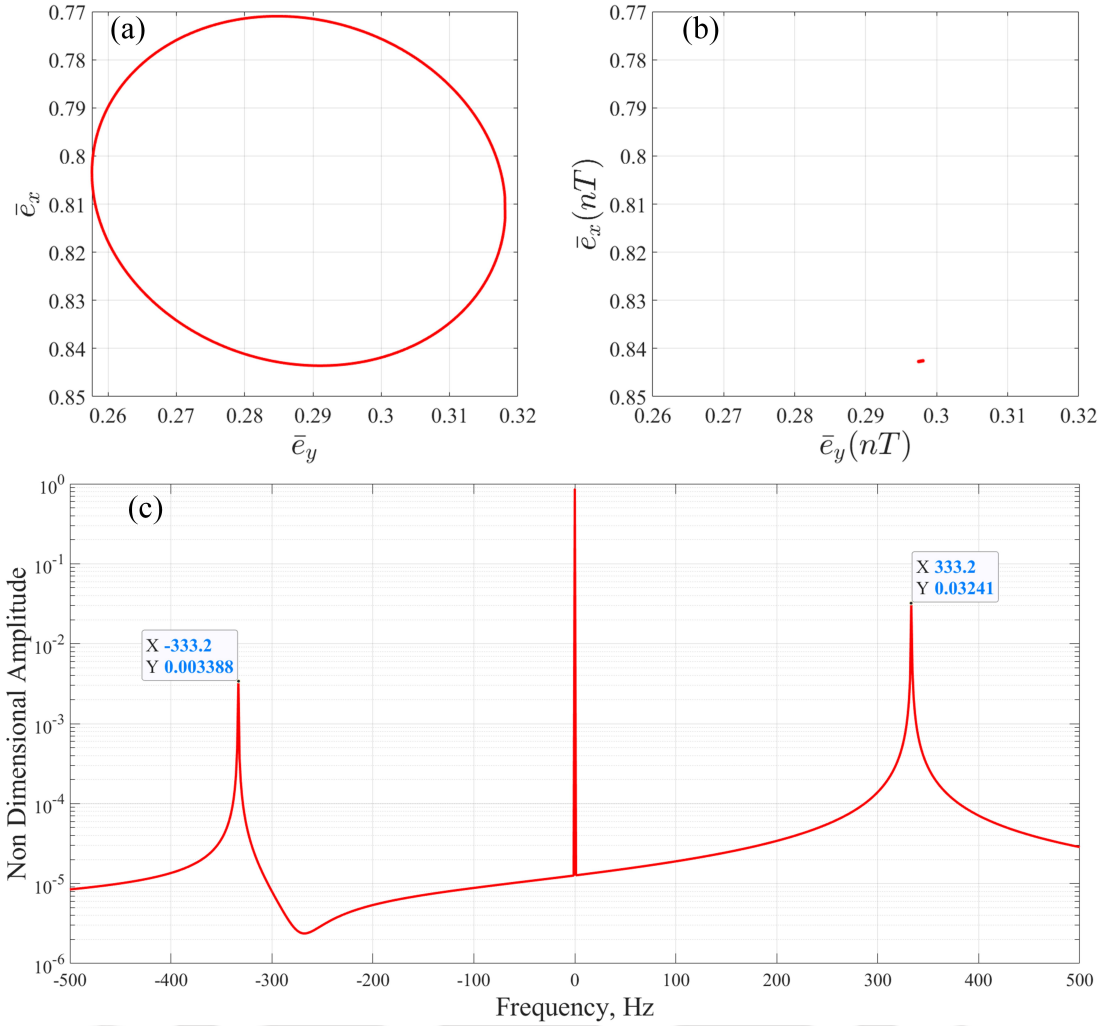

Figure 5.13: (a) Trajectory, (b) Poincaré plot and (c) FFT plot of the non-dimensional rotor response when the rotor supported on hybrid GFB with an unbalance eccentricity of 3×10^{-6} m

reduced but the smallest value of the minimum film thickness is nearly zero indicating the journal almost touches the bearing surface. However, when the mass unbalance is increased to 2×10^{-5} m, the minimum film thickness value decreases further and becomes negative (Fig. 5.25). Therefore, the rotor supported on hybrid GFB is able to withstand higher amount of unbalance.

5.3.2 Effect of sudden unbalance

A rotor has to withstand different kinds of aberrations during operations. A sudden unbalance may be triggered in the rotor system due to blade loss or loose nut that may come out during operation. Therefore, an investigation has been made to study the effect of sudden unbalance on the rotors supported on hybrid GFBs. Hence, mass unbalance

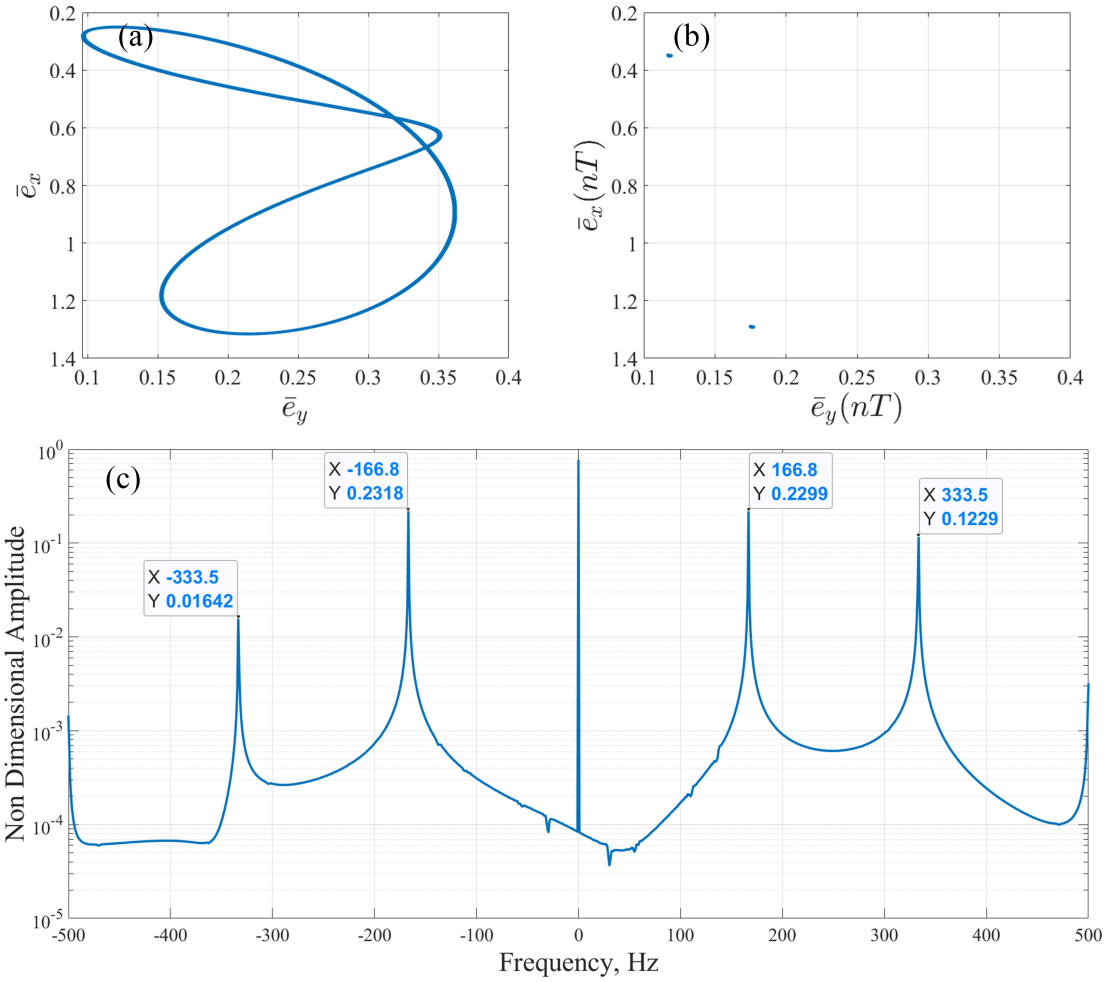

Figure 5.14: (a) Trajectory, (b) Poincaré plot and (c) FFT plot of the non-dimensional rotor response when the rotor supported on conventional GFB with an unbalance eccentricity of 4.14×10^{-6} m

has been introduced into the system after the rotor has been allowed to run up to a certain time. In the current investigation the unbalance has been introduced after 0.5 s. The speed of the rotor has been kept constant at 20000 rpm. Other parameters used in the present investigation is given in Table 4.1 and Table 4.2. The reference point of the AMB is set as the natural equilibrium position of the GFB i.e. 0.8 along X-axis and 0.35 along Y-axis.

In Fig. 5.26a, the time history of the non-dimensional response of the rotor supported on convention GFBs rotating at 20000 rpm is shown while a sudden mass unbalance of 10 g mm applied exactly at 0.5 s. It has been observed that at a mass unbalance of 10 g mm, the amplitude of the non-dimensional rotor response along the X-axis has been increased due to the application of mass unbalance. Similar response has been observed in the amplitude of the rotor response along the Y-axis. In case of hybrid

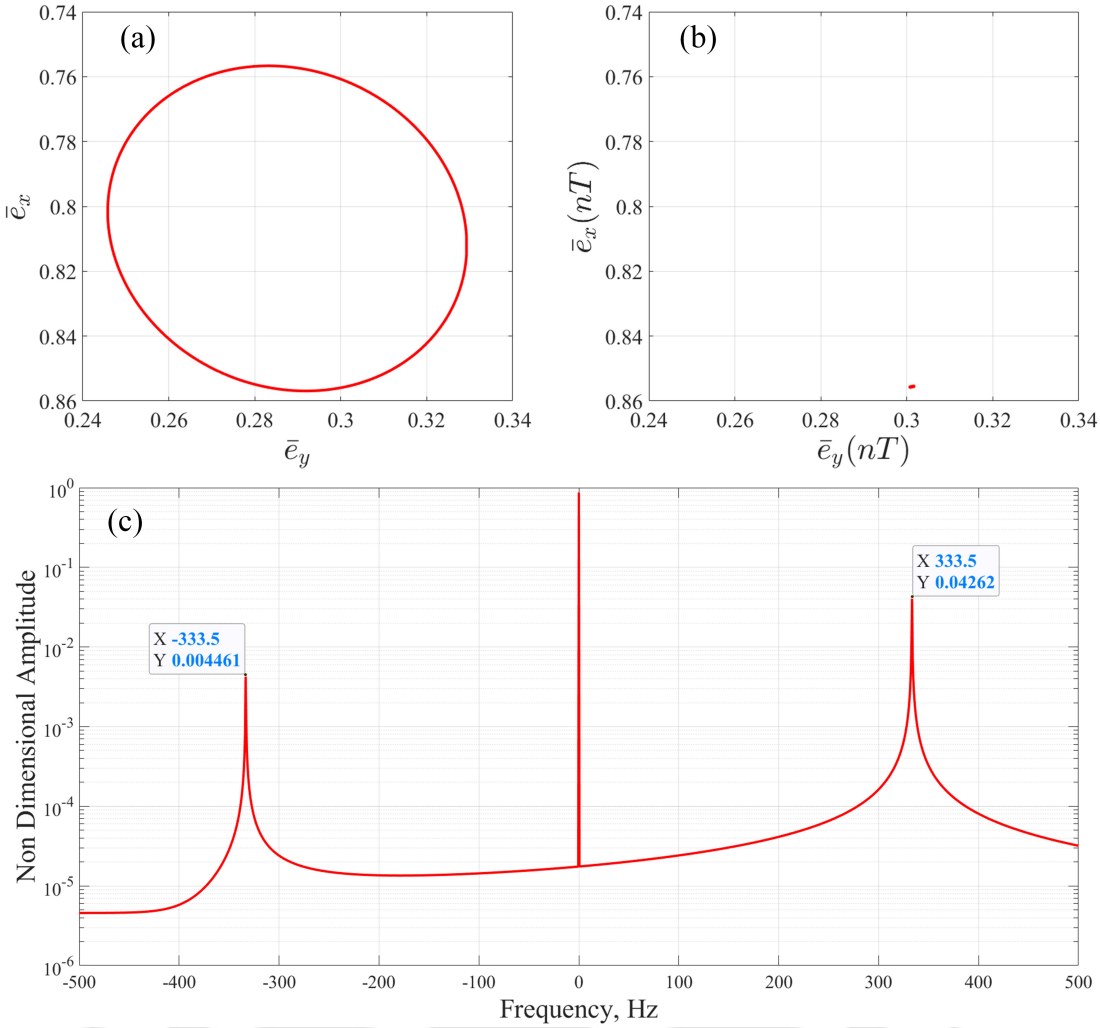

Figure 5.15: (a) Trajectory, (b) Poincaré plot and (c) FFT plot of the non dimensional rotor response when the rotor supported on hybrid GFB with an unbalance eccentricity of 4.14×10^{-6} m

GFBs, the amplitude of the non-dimensional response is much smaller compared to the conventional GFBs as observed in Fig. 5.26b . Figure 5.27 shows the trajectory of the rotor supported on conventional GFB before and after the application of sudden unbalance of 10 g mm. The trajectory changes from quasi-periodic to periodic due to the application of sudden unbalance. This has also been observed in case of hybrid GFB as shown in Fig. 5.28. In Fig. 5.29 the full spectrum FFT of the non-dimensional response of the rotor supported on conventional GFBs before and after the application of the mass unbalance of 10 g mm has been shown. Before the application of unbalance, only the sub-synchronous frequency has been observed at 116.2 Hz. However, both sub-synchronous peak and the synchronous peak have been observed after the application of mass unbalance at 116.2 Hz and 333.5 Hz respectively. Figure 5.30 shows the full

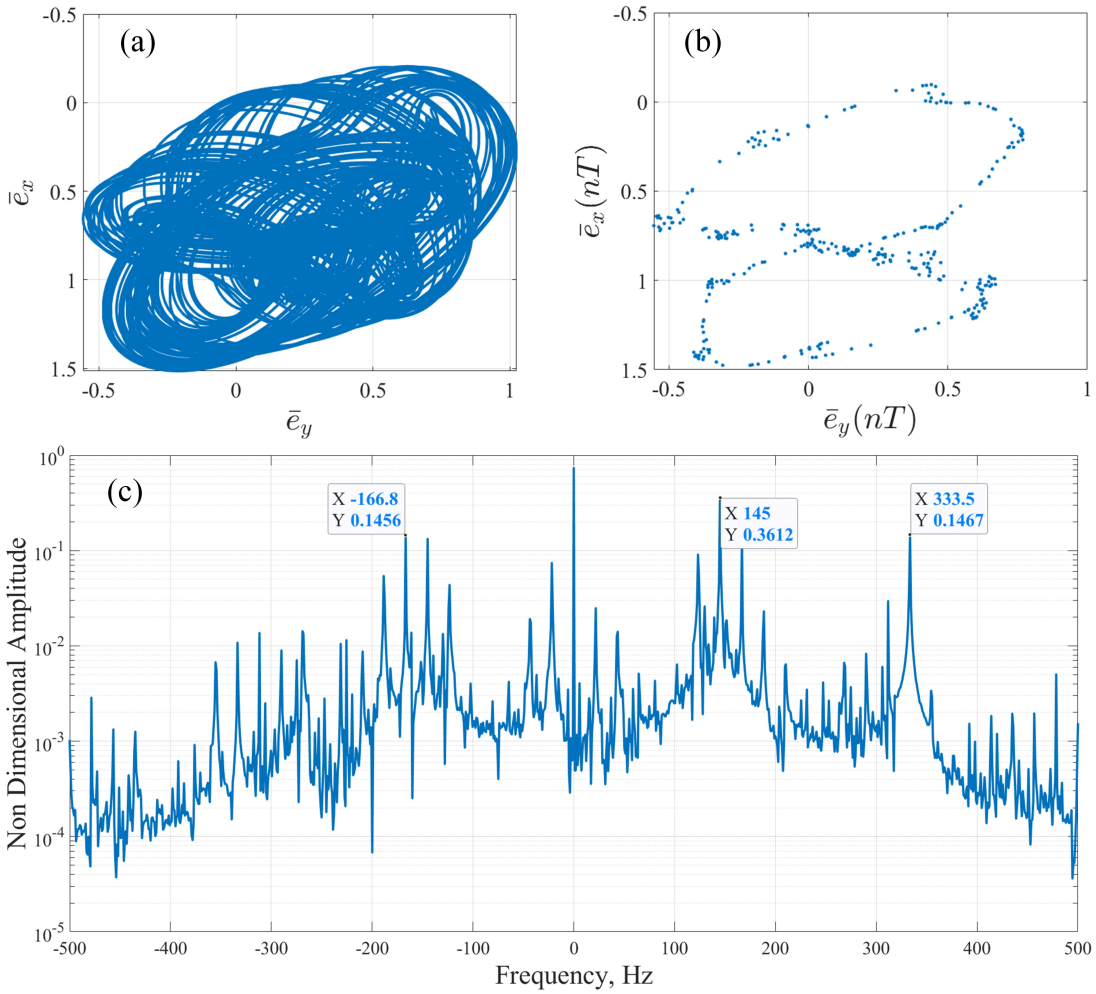

Figure 5.16: (a) Trajectory, (b) Poincaré plot and (c) FFT plot of the non-dimensional rotor response when the rotor supported on conventional GFB with an unbalance eccentricity of 5×10^{-6} m

spectrum FFT of the non-dimensional response of the rotor supported on hybrid GFBs before and after the application of the mass unbalance of 10 g mm. Before the application of mass unbalance, no significant peaks have been observed. The low amplitude of the response of the sub-synchronous frequency has been observed at 116.2 Hz and 145.3 Hz. After the application of mass unbalance, the synchronous frequency at 333.5 Hz appears and dominates the other frequency components.

The mass unbalance is then increased gradually in order to investigate the limit of sudden unbalance in the rotors supported on conventional GFBs and hybrid GFBs. The amplitude of the rotor displacement increases as the unbalance is increased. The non-dimensional response of rotor supported on conventional GFB due to the application of sudden unbalance of 63 g mm has been shown in Fig. 5.31a. At the mass unbalance

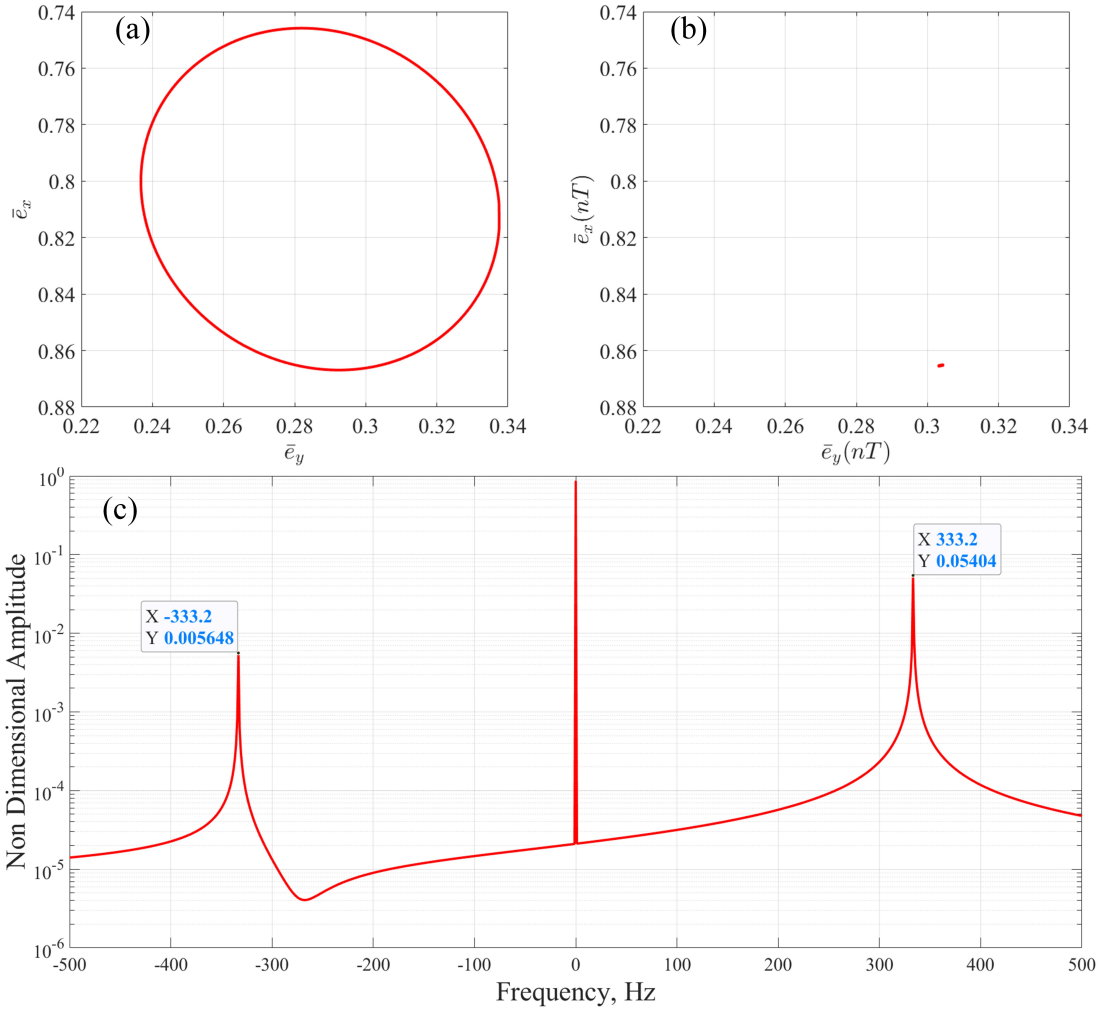

Figure 5.17: (a) Trajectory, (b) Poincaré plot and (c) FFT plot of the non-dimensional rotor response when the rotor supported on hybrid GFB with an unbalance eccentricity of 5×10^{-6} m

of 63 g mm the rotor displacement becomes high suggesting contact between the top foil and journal. However, in case of the hybrid GFBs, even though the amplitude of vibration increases it has been well within the limit (Fig. 5.31b). The trajectory of the rotor supported on conventional GFBs and hybrid GFBs after the application of mass unbalance has been shown in Fig. 5.32. The trajectory of the rotor supported on conventional GFB show chaotic behaviour while the rotor supported on hybrid GFB show periodic behaviour with small obrit radius. The comparison of the non-dimensional rotor response supported on conventional GFB and hybrid GFB after the application of 63 g mm mass unbalance has been shown in Fig. 5.33. It has been observed that a peak of high amplitude at sub-synchronous frequency and synchronous frequency occurs in case of conventional GFBs. However, the sub-synchronous frequency is suppressed in case

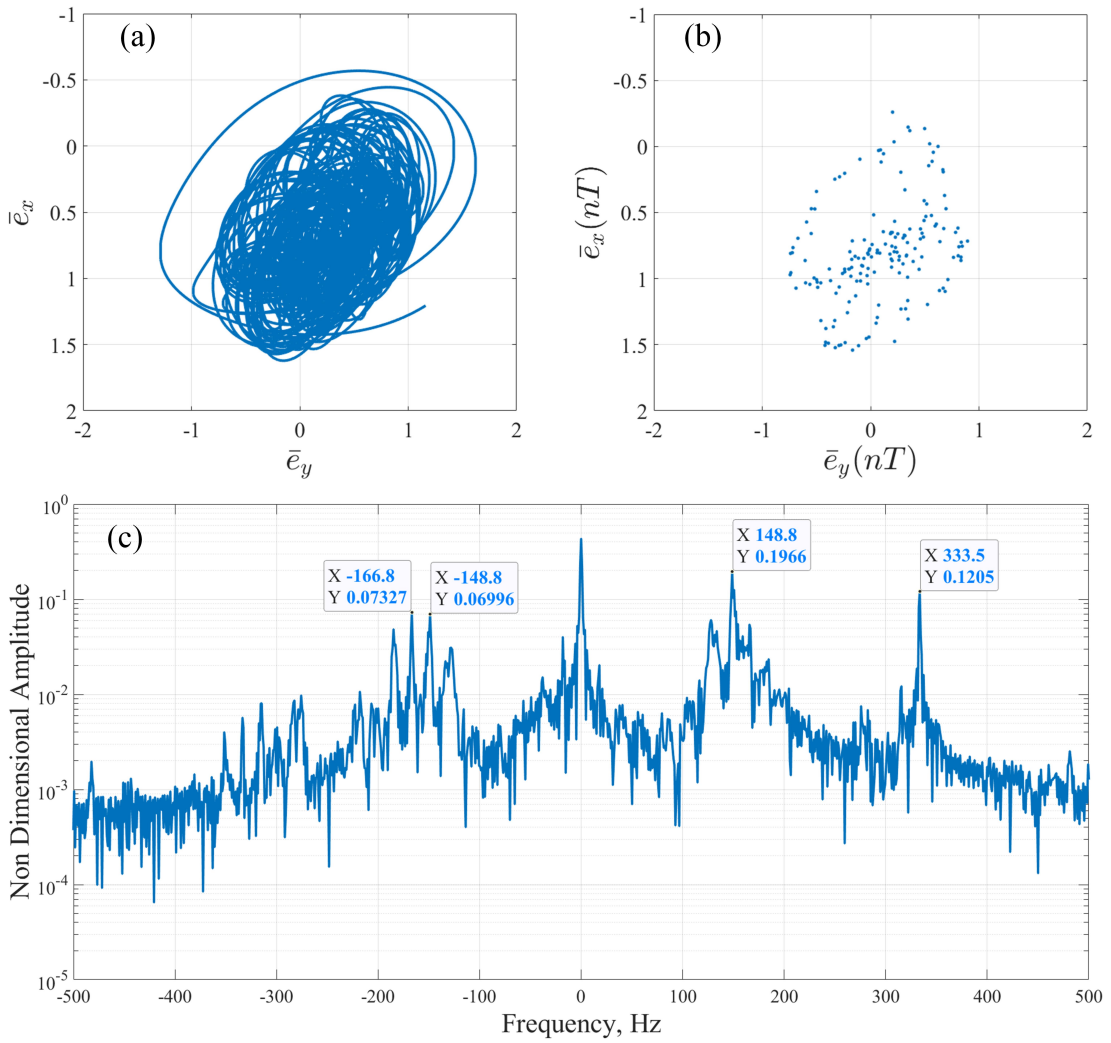

Figure 5.18: (a) Trajectory, (b) Poincaré plot and (c) FFT plot of the non-dimensional rotor response when the rotor supported on conventional GFB with an unbalance eccentricity of 6.5×10^{-6} m

of hybrid GFB. The synchronous frequency peak is observed at 332.8 Hz. It has been found that further application of mass unbalance into the rotor supported on conventional GFB lead to further increment in the rotor displacement and instability.

The mass unbalance has been further increased to investigate the limit of hybrid GFB. In Fig. 5.34a the non-dimensional response of the rotor supported on hybrid GFB due the application of the mass unbalance of 86 g mm has been shown. The rotor response show high amplitude of displacement. This probably show the limit of hybrid GFBs with the present configuration. The rotor trajectory after the application of the mass unbalance of 86 g mm is shown in Fig. 5.34b. The trajectory shows multi periodic motion with high orbit radius. The corresponding FFT plot is shown in Fig. 5.34c. High amplitude

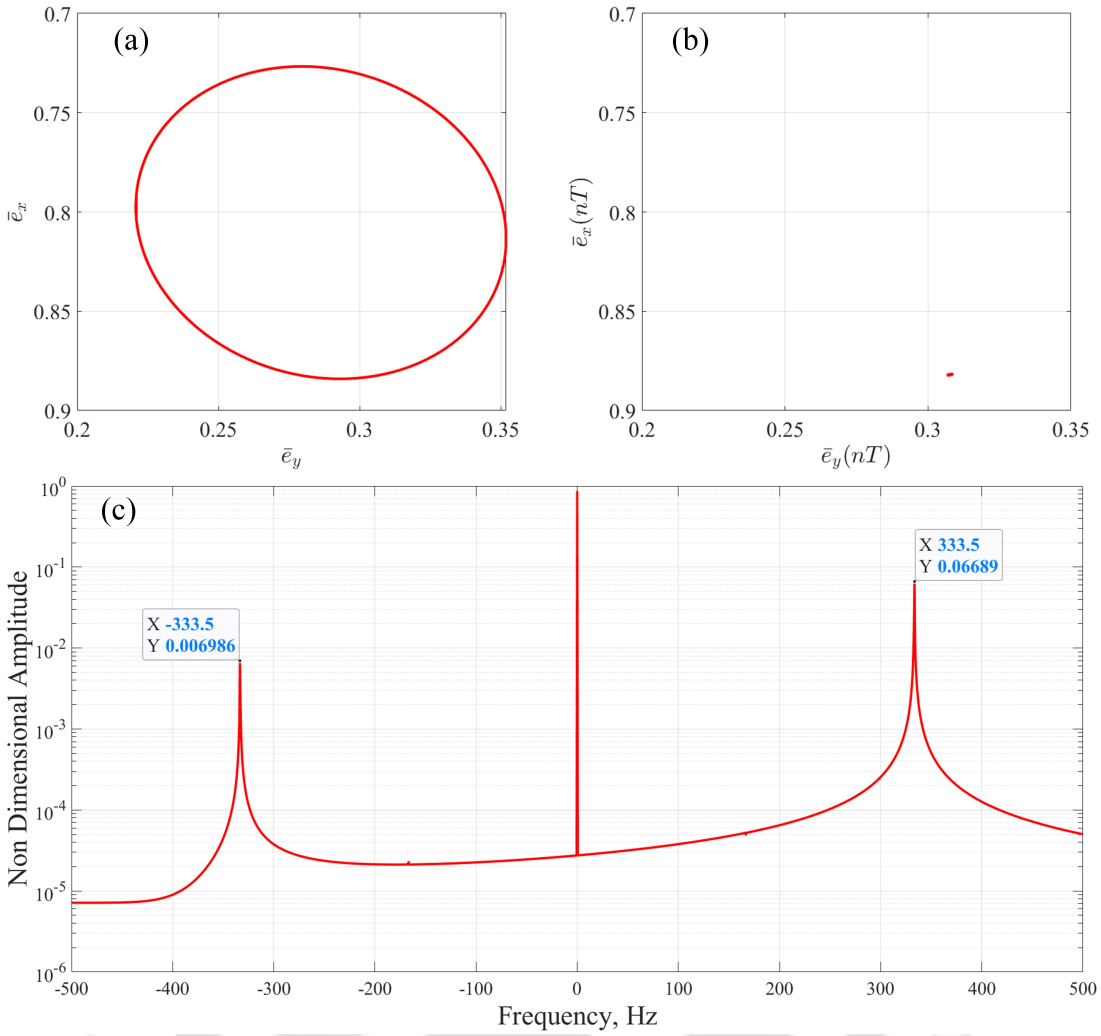

Figure 5.19: (a) Trajectory, (b) Poincaré plot and (c) FFT plot of the non-dimensional rotor response when the rotor supported on hybrid GFB with an unbalance eccentricity of 6.5×10^{-6} m

of the response of the rotor has been observed at 166.7 Hz and 333.4 Hz.

Therefore, it can be concluded that the hybrid bearing is capable of withstanding sudden unbalance and also capable of suppressing the sub-synchronous vibrations. The limit of the sudden unbalance has been increased from 63 g mm to 86 g mm due to the implementation of hybrid GFB.

5.4 Inferences

In this chapter, the unbalance response of the rotor supported on hybrid gas foil bearings (hybrid GFBs) combining a gas foil bearing (GFB) and active magnetic bearing (AMB) has been investigated and compared with the conventional GFB.

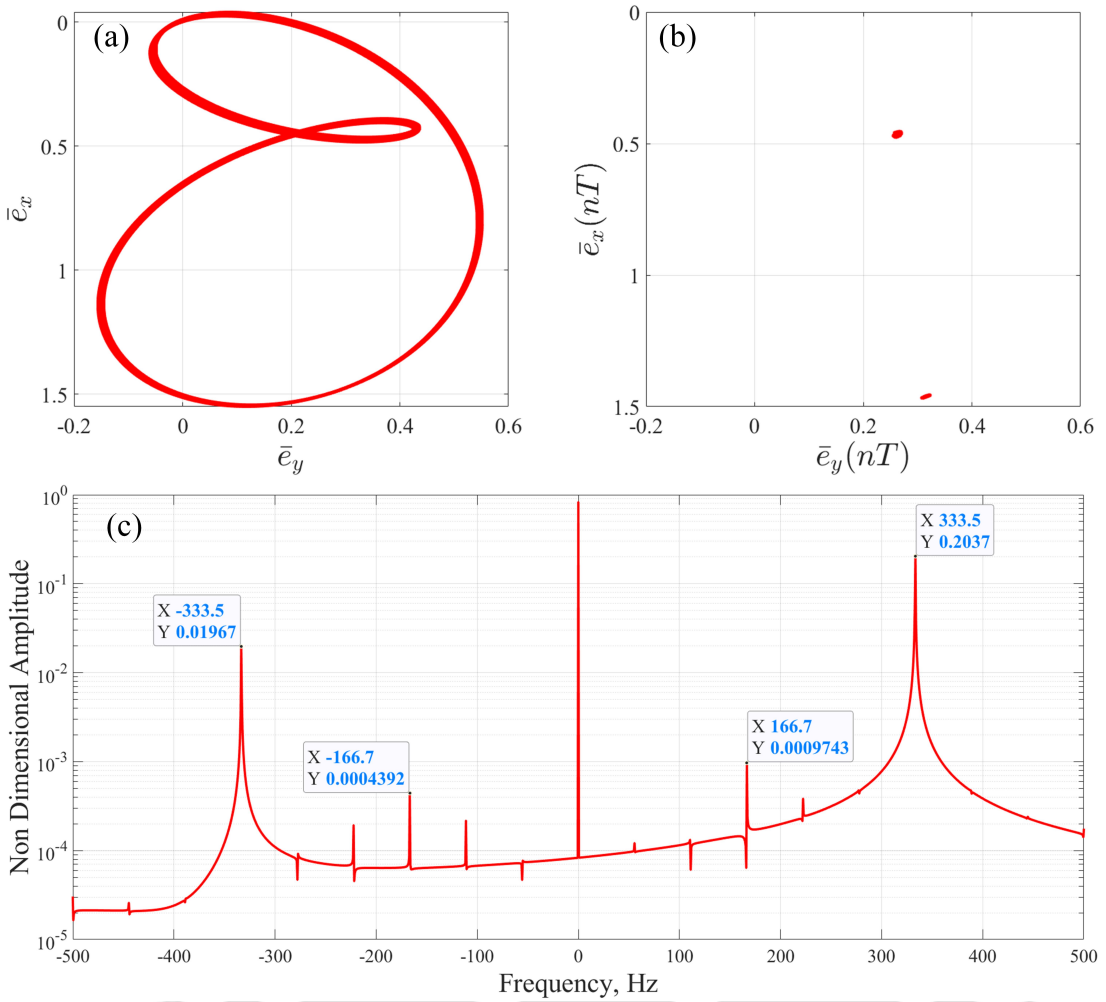

Figure 5.20: (a) Trajectory, (b) Poincaré plot and (c) FFT plot of the non-dimensional rotor response when the rotor supported on hybrid GFB with an unbalance eccentricity of 3×10^{-5} m

At low unbalance, the sub-synchronous is the dominating frequency in case of the conventional GFB. As the unbalance is increased in the case of conventional GFB, the synchronous frequency becomes dominant. However, at high unbalance the rotor supported on conventional GFBs shows the presence of high amplitude of the response of the sub-synchronous frequency as well as synchronous frequency which causes the instability. The sub-synchronous vibrations are eliminated due to the implementation of the hybrid GFBs. It has been demonstrated that the limit to withstand unbalance has also been increased due to the implementation of the hybrid GFB. The trajectory of the rotor supported on hybrid GFBs show periodic motion. However, the radius of the orbit of the rotor increases with the increase of unbalance eccentricity. The unbalance eccentricity limit has been increased from 6.5×10^{-6} m to 2×10^{-5} m due to the implementation of hybrid GFBs. It has been observed that in order to keep the rotor within the permissible

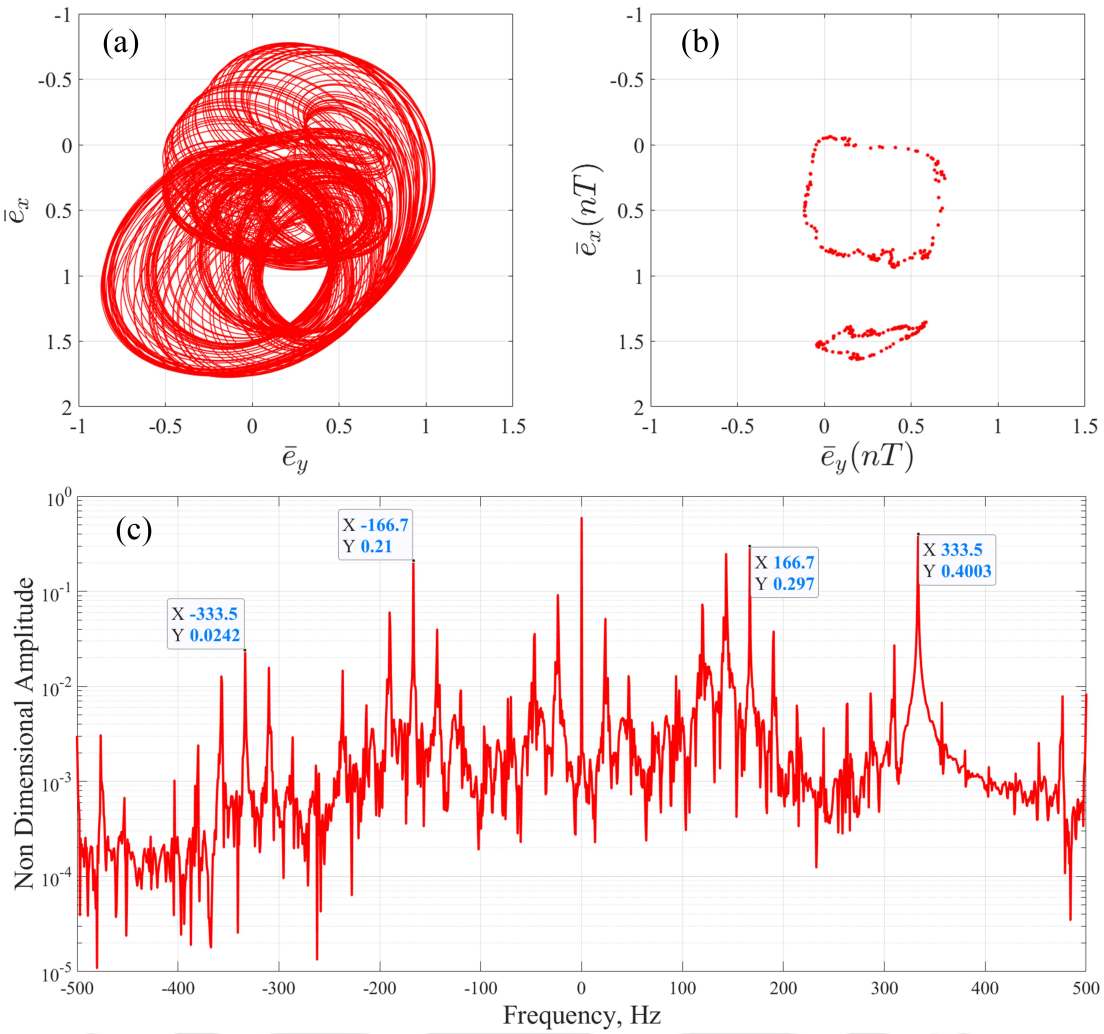

Figure 5.21: (a) Trajectory, (b) Poincaré plot and (c) FFT plot of the non-dimensional rotor response when the rotor supported on hybrid GFB with an unbalance eccentricity of 4.2×10^{-5} m

level higher control current is required for higher unbalance eccentricity. The value of minimum film thickness is also high in case of hybrid GFBs which avoids the contact between the rotor and bearing surface. It has also been demonstrated that the hybrid GFBs are also capable of withstanding higher sudden mass unbalance.

In the next chapter, a new winding scheme has been proposed. The new winding scheme requires only two drives to control the rotor. This winding scheme will therefore have lesser cost. A comparison between the response of the rotor supported on hybrid bearing with conventional winding scheme and the new winding scheme has been provided in the next chapter.

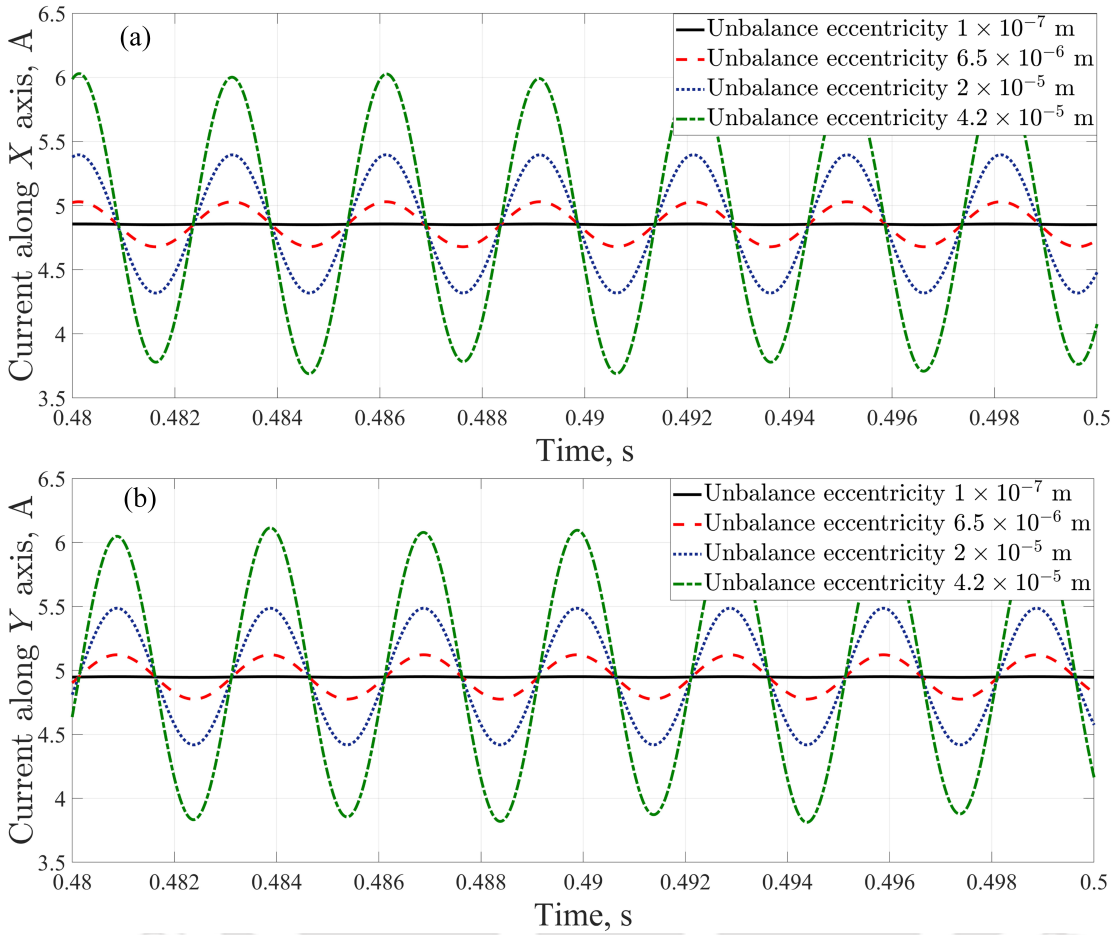

Figure 5.22: Control current required to control the rotor with various amount of unbalance eccentricity

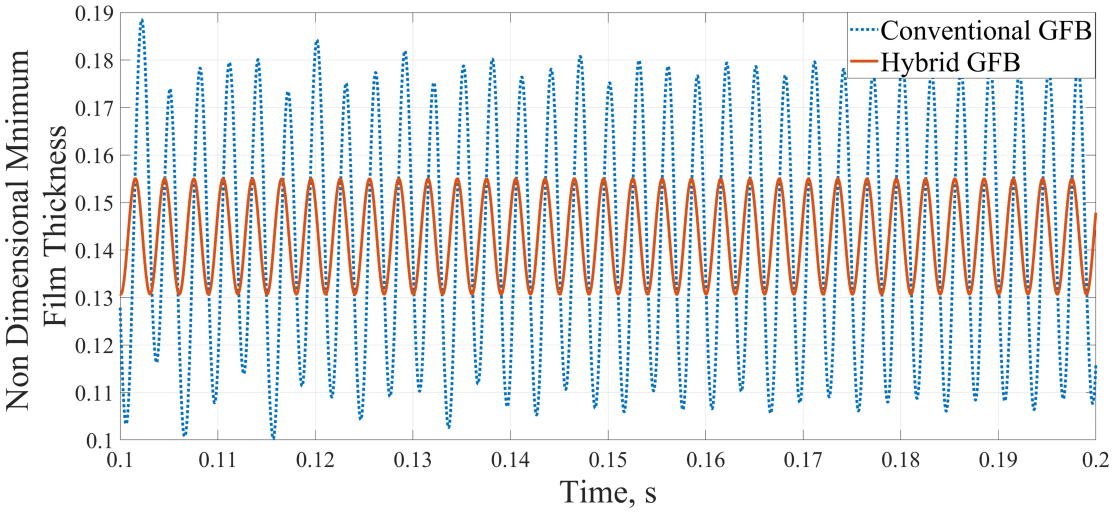

Figure 5.23: Minimum film thickness when the unbalance is 1×10^{-6} m

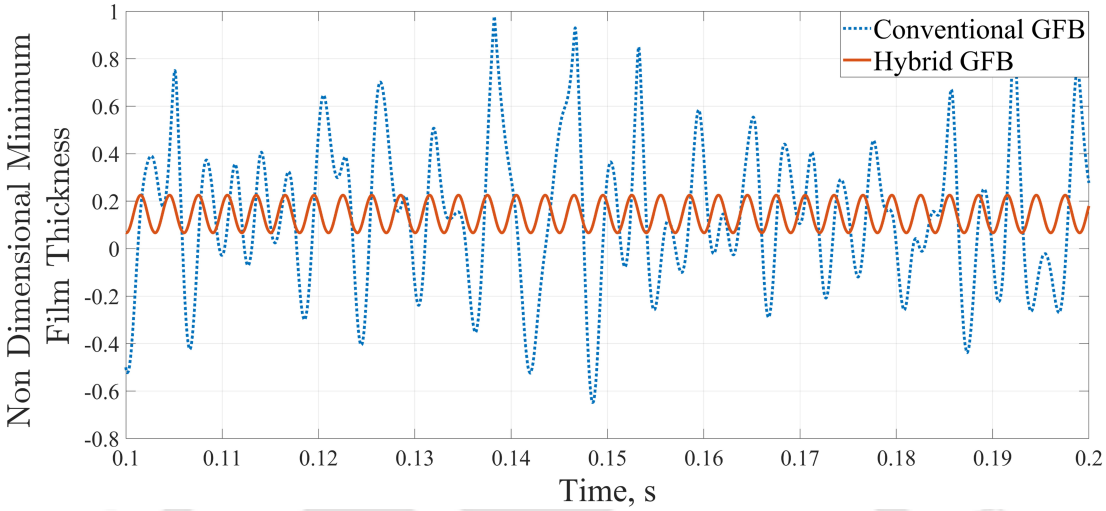

Figure 5.24: Minimum film thickness when the unbalance is 4.6×10^{-6} m

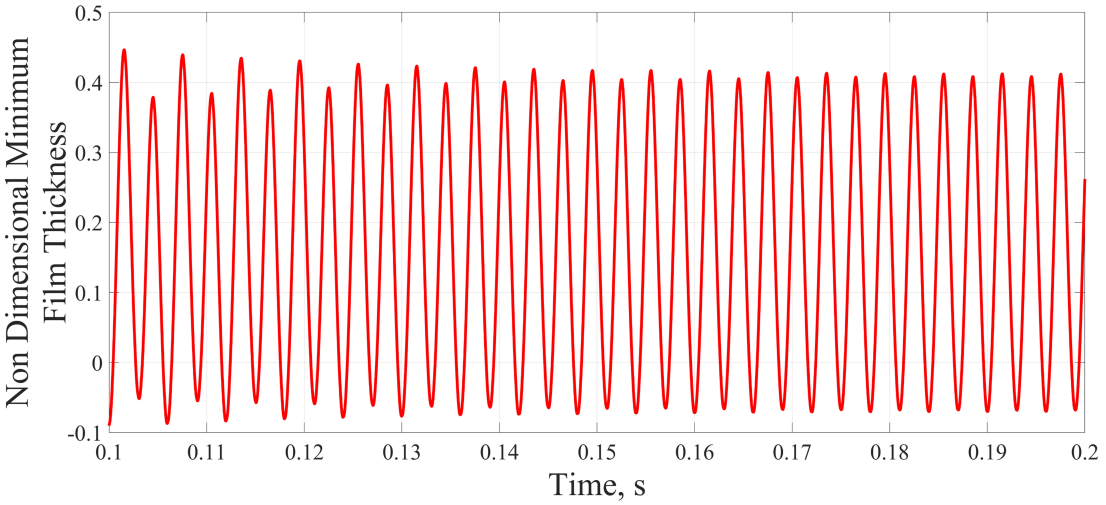

Figure 5.25: Minimum film thickness when the unbalance is 2×10^{-5} m

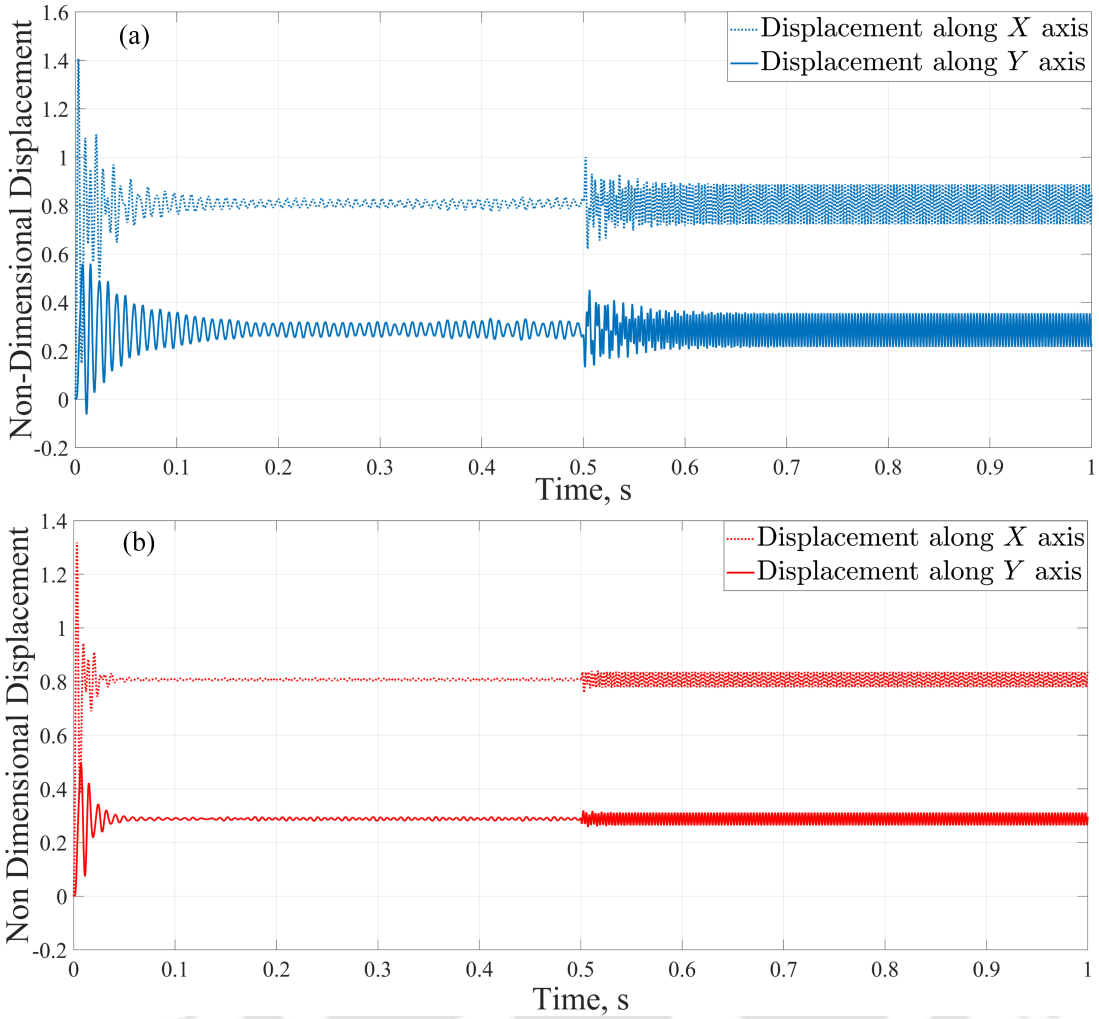

Figure 5.26: Non-dimensional response of rotor supported on (a) conventional GFBs (b) hybrid GFBs due to a sudden unbalance of 20 g mm

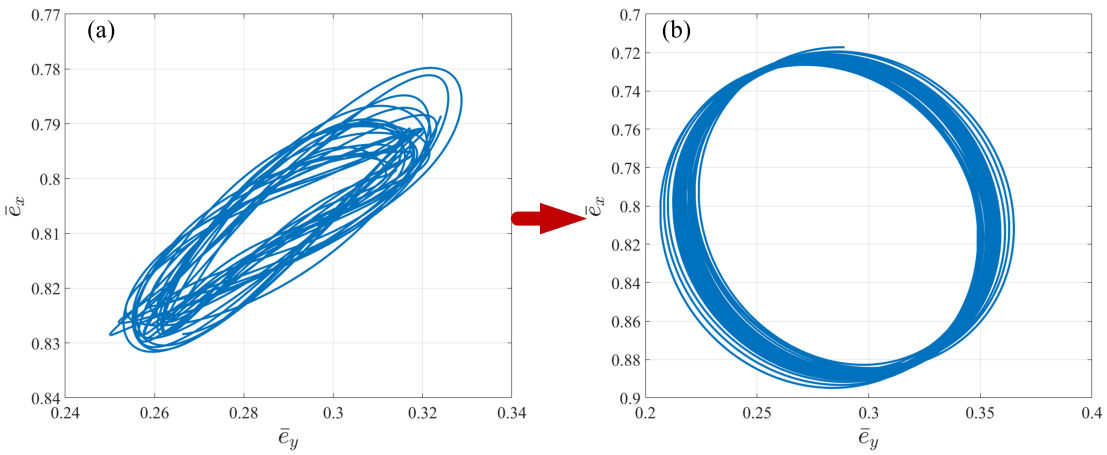

Figure 5.27: Trajectory of the rotor supported on conventional GFBs when (a) before the application of sudden unbalance of 20 g mm (b) after the application of sudden unbalance of 20 g mm

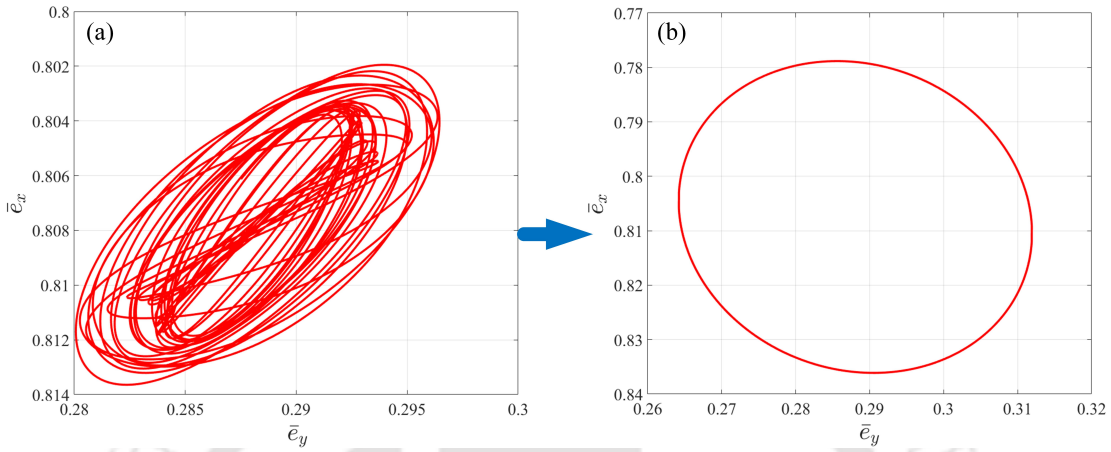

Figure 5.28: Trajectory of the rotor supported on hybrid GFBs when (a) before the application of sudden unbalance of 20 g mm (b) after the application of sudden unbalance of 20 g mm

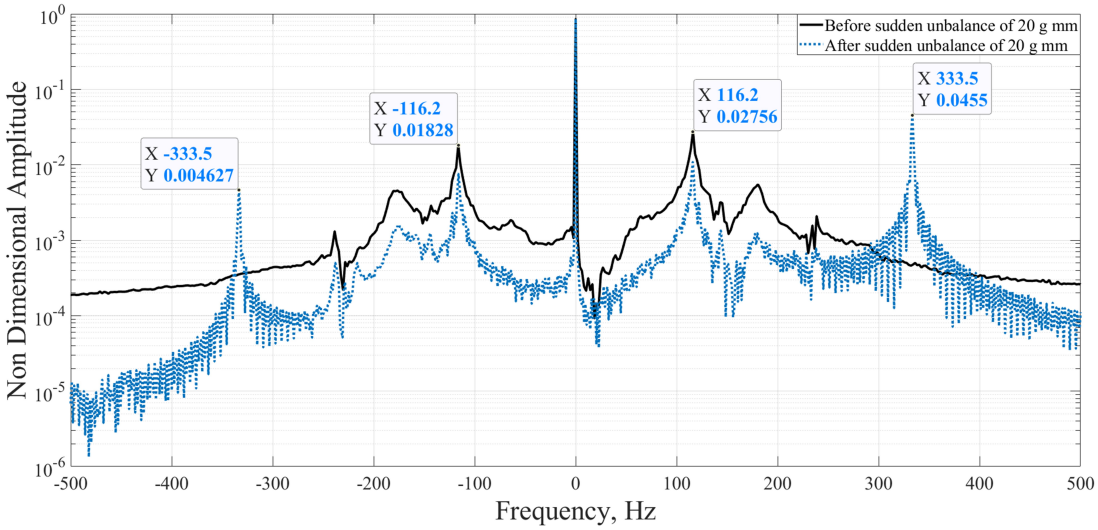

Figure 5.29: Full spectrum of the FFT of the non-dimensional response of the rotor supported on conventional GFBs before and after the application of 20 g mm mass unbalance

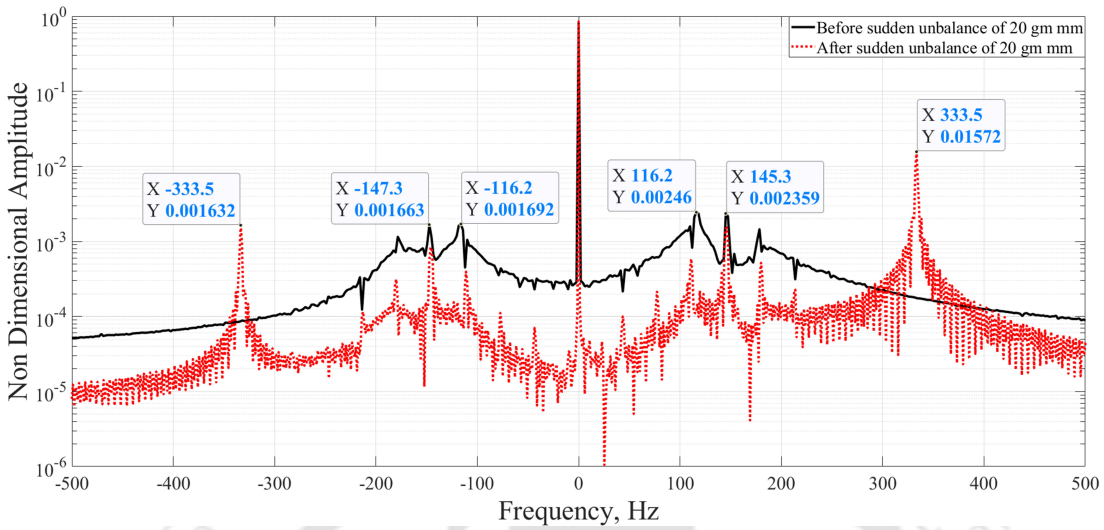

Figure 5.30: Full spectrum of the FFT of the non-dimensional response of the rotor supported on hybrid GFBs before and after the application of 20 g mm mass unbalance

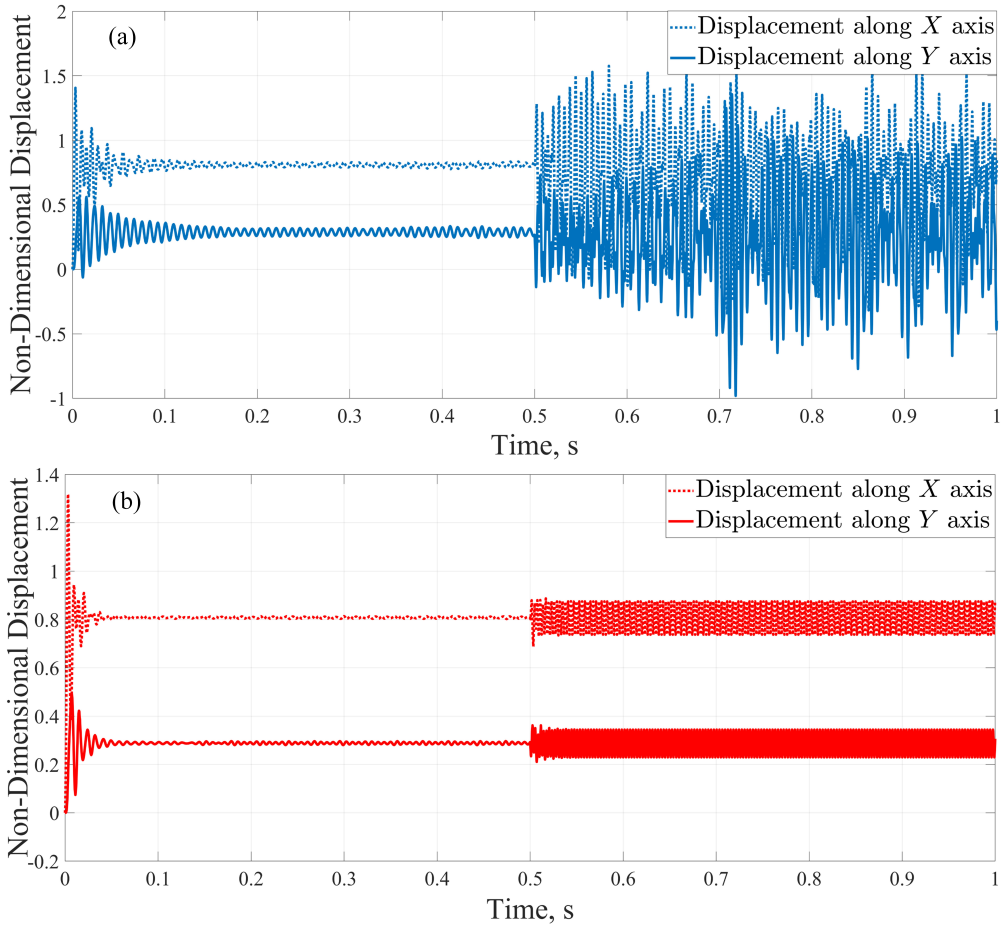

Figure 5.31: Non-dimensional response of rotor supported on (a) conventional GFBs (b) hybrid GFBs due to the application of sudden mass unbalance of 63 g mm

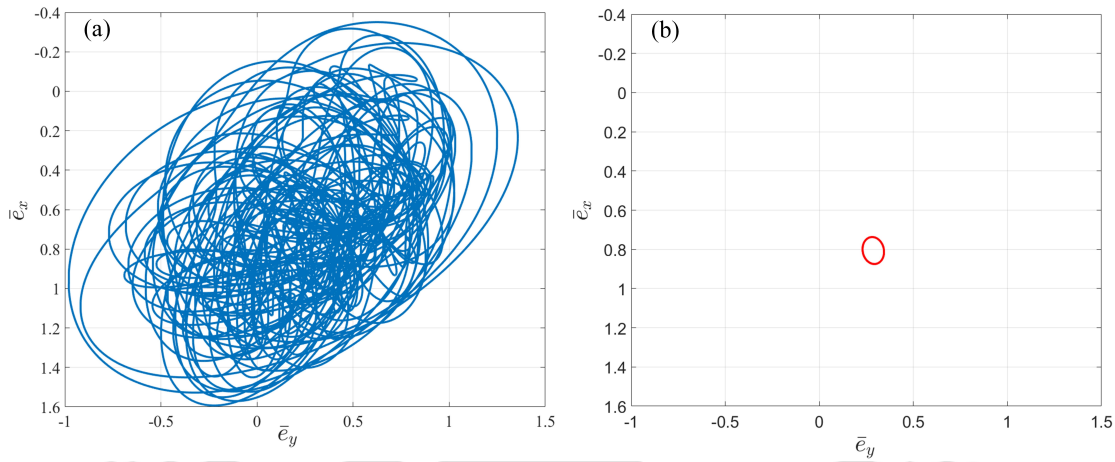

Figure 5.32: Trajectory of the rotor supported on (a) conventional GFBs (b) hybrid GFBs due to the application of sudden mass unbalance of 63 g mm

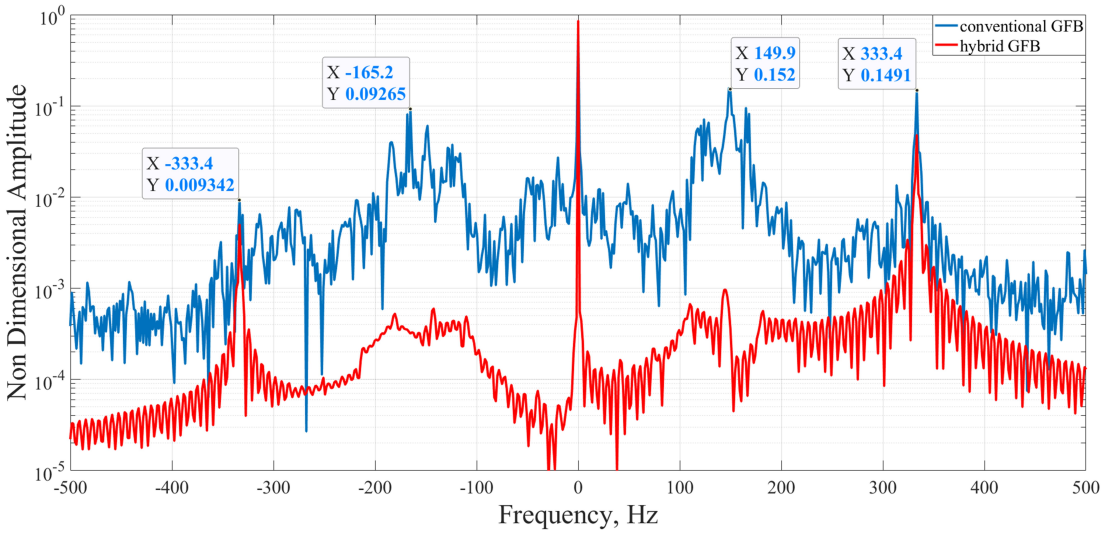

Figure 5.33: Full spectrum of the FFT of the non-dimensional response of the rotor supported on conventional GFBs and hybrid GFBs due to application of sudden mass unbalance of 63 g mm

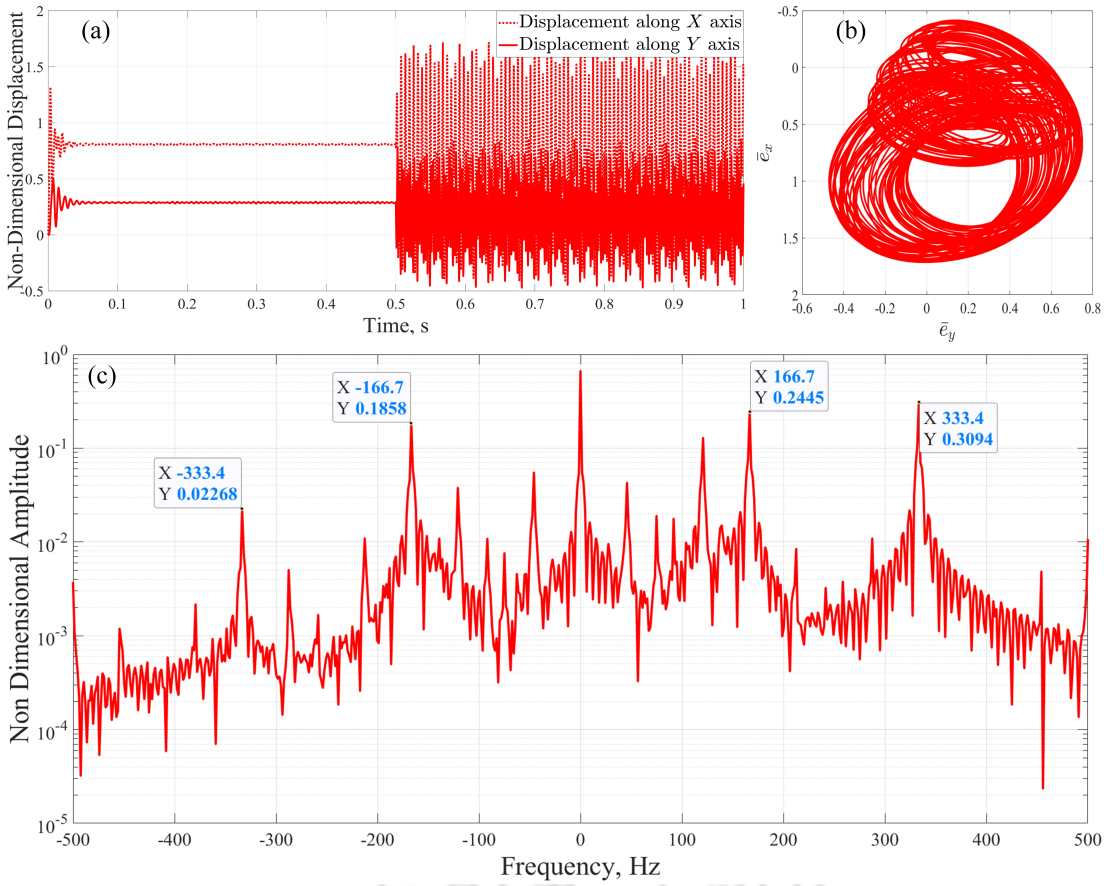

Figure 5.34: (a) Non-dimensional response (b) trajectory and (c) FFT of the rotor supported on hybrid GFBs due to the application of sudden mass unbalance of 86 g mm

6

Hybrid Gas Foil Bearing with Bridge Configured Winding

Contents

6.1 Introduction

In the previous chapters, the response of the rotor supported on hybrid GFBs has been investigated. The investigations showed the advantages of the implementation of the GFB. However, the cost of conventional Gas Foil Bearing increases due to its requirement of precise manufacturing method and the coating material for the top foil and bump foil. In case of Active Magnetic Bearing, the normal electrical arrangement includes a multiplicity of independently controlled current sources usually at least four drives per bearing which increases its cost. Therefore, the hybrid Gas Foil Bearing will have much higher cost.

An alternative way for minimizing the cost of hybrid GFBs can be by reducing the required number of drives. Therefore, a different winding approach for the AMBs where only two drives per bearing are required has been proposed for the hybrid GFBs that would bring down its cost. The winding arrangement of the active magnetic bearing follows a bridge-configured pattern, which is similar to the winding arrangements for self-bearing motors and induction machines [119–123]. The new winding arrangement requires a very different approach to the controller structure. The current-to-force model is directly applied in the fast loop, instead of translating a command force vector into a corresponding vector of required currents and then running a fast loop to achieve the control currents. Therefore, using this current-to-force model, the controller is continuously calculating the force exerted on the horizontal and vertical directions. Then compare it with the command force vector at any given time, driving the rates of change of currents in the two independent current-source drives accordingly. The revised controller strategy is based on the ability to utilize lower-cost components to power the magnetic bearing. In this chapter the implementation of the bridge configured winding connection for the electromagnetic actuator of the hybrid GFBs has been described. The dynamics of the rotor supported on hybrid GFBs comparing the conventional winding of the active magnetic bearing and bridge configured winding has been presented. Moreover, the advantages and disadvantages of the proposed winding scheme for the hybrid gas foil bearing have been discussed.

6.2 New Winding Connections

In Fig 3.7, the conventional arrangement of the active magnetic bearing has been shown. The half-coil-pairs $\{HCP_{12A}, HCP_{12B}, HCP_{56A}, HCP_{56B}\}$ controls the horizontal forces. The half-coil-pairs controls the vertical forces. In the conventional arrangement, the

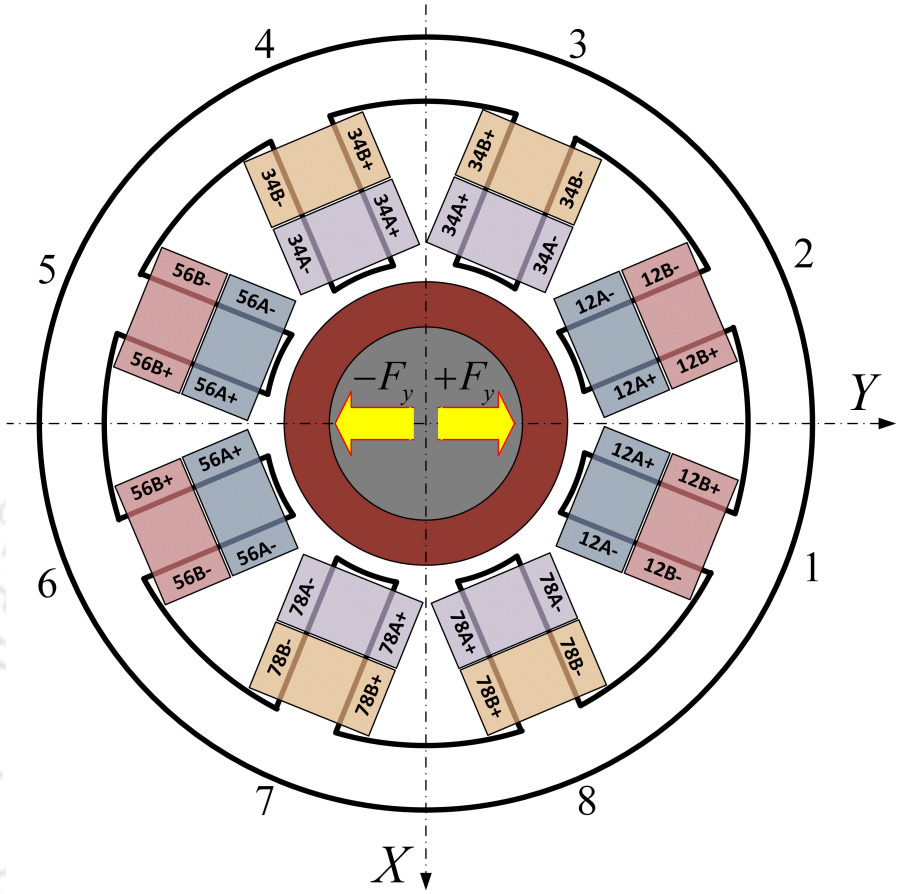

Figure 6.1: Bridge configured Winding arrangement of radial AMB

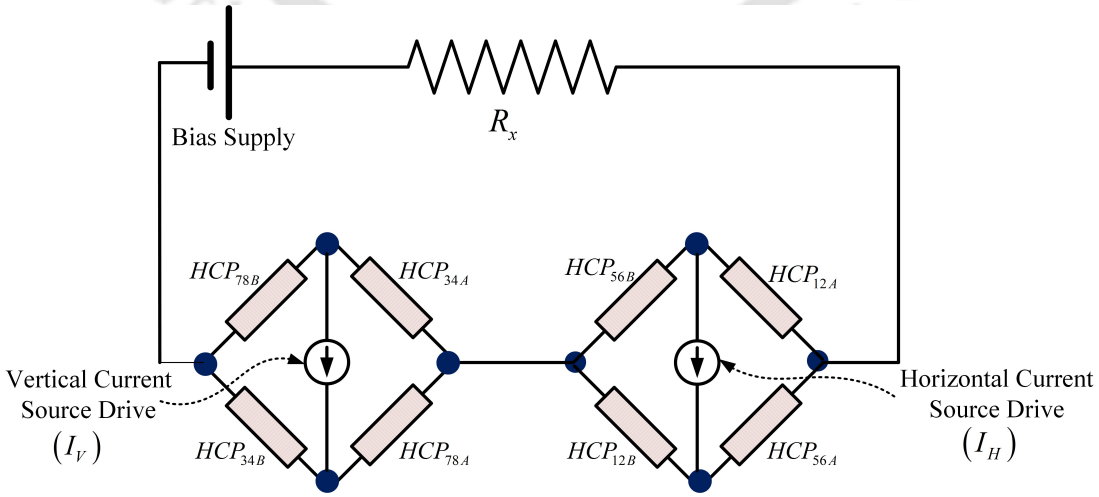

Figure 6.2: Bridge connections of the AMB

two half coils HCP_{12A} and HCP_{12B} are connected in series and are powered from a single independent drive. Similarly, the other half coils are connected in series and with an independent current drive. Therefore, four drives are required for controlling the rotor in the required position. In Fig 6.1, the half coil pairs of the proposed bridge configured circuit of the hybrid GFB has been shown. Two Wheatstone bridge type circuits, each consisting of four half coil pairs (HCP), are present with one common feed. The half-coil-pairs $\{HCP_{12A}, HCP_{12B}, HCP_{56A}, HCP_{56B}\}$ controlling the horizontal forces are connected, forming the Wheatstone bridge. Similarly, the half coils $\{HCP_{34A}, HCP_{34B}, HCP_{78A}, HCP_{78B}\}$ which controls the vertical force are connected, as shown in Fig 6.2. Each bridge utilizes a single drive capable of pushing current across it in either direction. The internal power circuitry, of the drive has the structure of a current source. Thus, only two independent drives are required rather than four in a conventional arrangement. However, each of the two drives must have its own DC link.

6.3 Magnetic Energy and the Electrical Dynamics

The total magnetic energy stored in the bearing at any instant of time under the assumption of magnetic linearity, is given as [112],

$$E_{mag} = \frac{1}{2}\Phi^T R_{NET}\Phi \tag{6.1}$$

The directions of current flow in the bridge configured winding has been shown in Fig. 6.3. Inorder to express the electrical dynamics of the new AMB winding configuration, a further current vector, I_C, associated voltage vector, V_C and the transformation matrix, T_MC has been defined. The vector I_C comprises of the three currents, I_{Bias} is the bias current, I_H is the current to control the horizontal force, I_V is the current to control the vertical force.

$$I_C = \begin{bmatrix} I_{Bias} & I_H & I_V \end{bmatrix} \tag{6.2}$$

The associated voltage vector can be represented as,

$$V_C = \begin{bmatrix} V_{Bias} & V_H & V_V \end{bmatrix} \tag{6.3}$$

where, V_{Bias} is the voltage corresponding to the bias current, V_H is the voltage corresponding to current controlling the horizontal force, V_V is the voltage corresponding to current controlling the vertical force. The current vector is I_c, is related to the

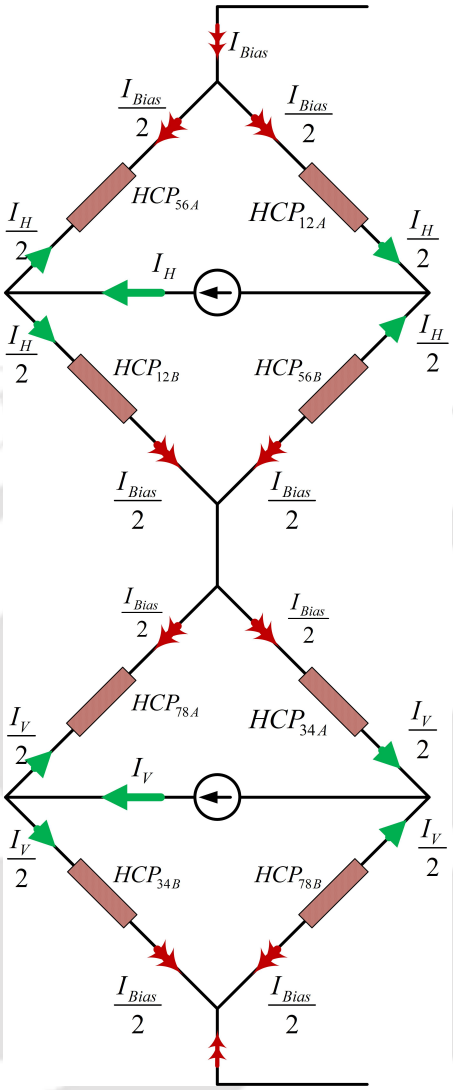

Figure 6.3: Current directions of the AMB with bridge configured winding

current in the half coils as,

$$I_A := T_A C \times I_C \tag{6.4}$$

where, I_A is the vector of 8 half coil currents $HCP_{12A}, HCP_{12B}, HCP_{34A}, ...HCP_{78A}, HCP_{78B}$ shown in Fig. 6.2 and given as,

$I_A := \begin{bmatrix} I_{12A} & I_{12B} & I_{34A} & I_{34B} & I_{56A} & I_{56B} & I_{78B} & I_{78B} \end{bmatrix}^T$ and,

$$T_{AC} = \frac{1}{2}\begin{bmatrix} 1 & 1 & 1 & 1 & 1 & 1 & 1 & 1 \\ 1 & 1 & 0 & 0 & -1 & -1 & 0 & 0 \\ 0 & 0 & 1 & 1 & 0 & 0 & -1 & -1 \end{bmatrix}^T$$

However the current in the current vector I_A are not independent. Current I_A is related to the current vector I_B as,

$$I_B := T_{BA} \times I_A \tag{6.5}$$

where, $I_B := \begin{bmatrix} I_{12} & I_{34} & I_{56} & I_{78} \end{bmatrix}^T$ and $T_{BA} = \begin{bmatrix} 1 & 1 & 0 & 0 & 0 & 0 & 0 & 0 \\ 0 & 0 & 1 & 1 & 0 & 0 & 0 & 0 \\ 0 & 0 & 0 & 0 & 1 & 1 & 0 & 0 \\ 0 & 0 & 0 & 0 & 0 & 0 & 1 & 1 \end{bmatrix}$

However, this current has to be transformed to the current in the reluctance network. Thus,

$$I_M := T_{MB} \times I_B \tag{6.6}$$

where, $I_M = \begin{bmatrix} 0 & 2I_{12} & -(I_{12}+I_{34}) & 2I_{34} & -(I_{34}+I_{56}) & 2I_{56} & -(I_{56}+I_{78}) & 2I_{78} & -(I_{78}+I_{12}) \end{bmatrix}^T$

and $T_{MB} = \begin{bmatrix} 0 & 0 & 0 & 0 \\ 2 & 0 & 0 & 0 \\ -1 & -1 & 0 & 0 \\ 0 & 2 & 0 & 0 \\ 0 & -1 & -1 & 0 \\ 0 & 0 & 2 & 0 \\ 0 & 0 & -1 & -1 \\ 0 & 0 & 0 & 2 \\ -1 & 0 & 0 & -1 \end{bmatrix}$

Thus the electrical dynamics of the new connection scheme are then given as,

$$V_C = R_C I_C + L_C \dot{I}_C + \dot{L}_C I_C \tag{6.7}$$

where, $R_C = diag\left(\begin{bmatrix} (R_X + 2R_{HCP}) & R_{HCP} & R_{HCP} \end{bmatrix}\right)$,

$L_C = N^2 {T_{MC}}^T (R_{NET})^{-1} T_{MC} + \begin{bmatrix} L_X & 0 & 0 \\ 0 & 0 & 0 \\ 0 & 0 & 0 \end{bmatrix}$, and

$\dot{L}_C = N^2 {T_{MC}}^T \left({R_{NET}}^{-1} \left(\dot{R}_{NET}\right) {R_{NET}}^{-1}\right) T_{MC}$

in which, R_X is the external resistance of the bias-current circuit and L_X is the inductance of the external circuit.

6.4 Results and Discussion

In this section, a comparison between the two winding scheme has been provided. The conventional winding scheme is described in section 3.3 The new winding winding arrangement as described in section 6.2 has been described.

The parameters of the gas foil bearing (GFB) and the rotor bearing system for the current simulation has been given in Table 4.1. In Table 4.2, the parameters of the Active Magnetic Bearing (AMB) are given. Although the current source drives are modelled as ideal components with no internal power losses but, in reality, these drives have losses that increase with both power and current. In the case of the conventional winding arrangement, to achieve the horizontal force, the sum $(I_{12} + I_{56})$ is kept constant at 10A while the difference $(I_{12} - I_{56})$ is adjusted. Similarly, the vertical force is achieved through maintaining the sum $(I_{34} + I_{78})$ at 10A while the difference $(I_{34} - I_{78})$ is adjusted to achieve the required vertical force. By contrast, in the case of the new connection, I_H and I_V are adjusted to control the bearing force while I_{Bias} is allowed to vary naturally around a value that returns to 10A if I_H and I_V stay constant at any value. Two cases of the rotor have been investigated. In the first case, the rotor has been assumed to be perfectly balanced, i.e. the unbalance eccentricity e_μ is assumed to be 0 while in the second case, the unbalance eccentricity is varied.

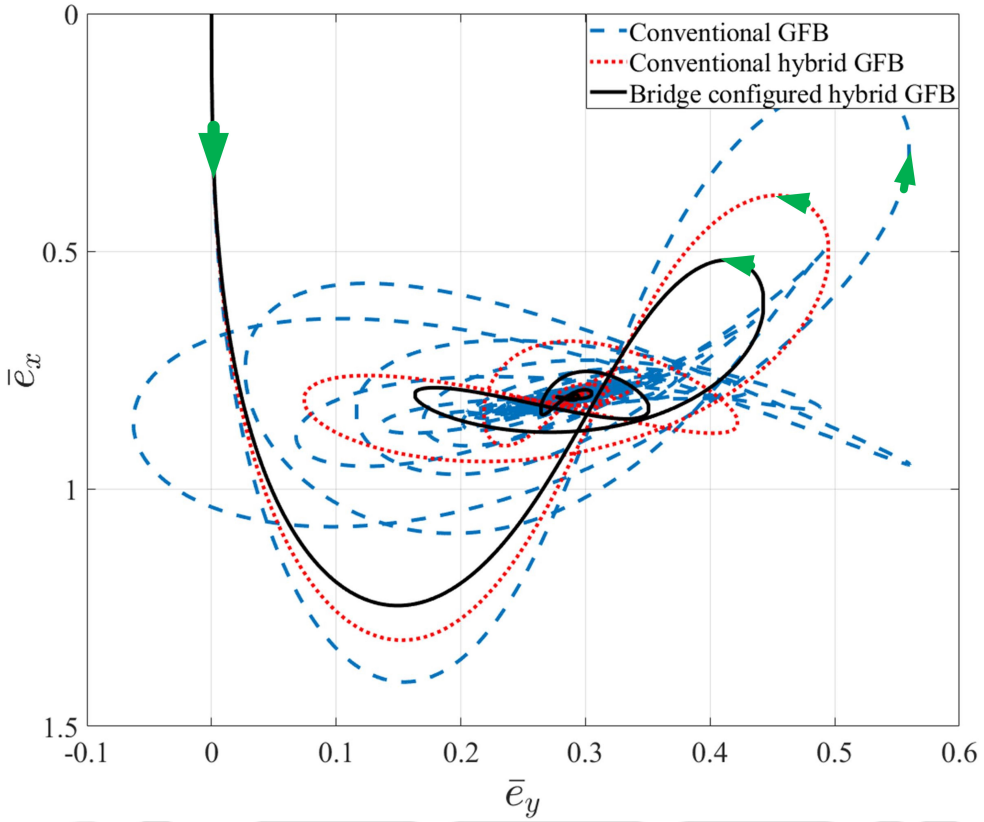

Figure 6.4: Trajectories of the rotor while rotating at 20000 rpm

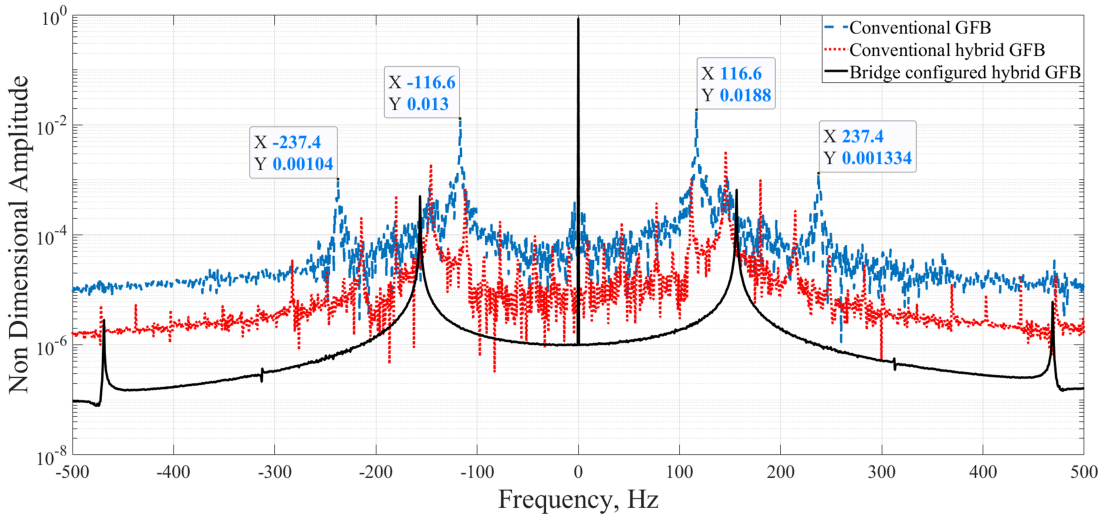

Figure 6.5: Full spectrum FFT of the rotor while rotating at 20000 rpm

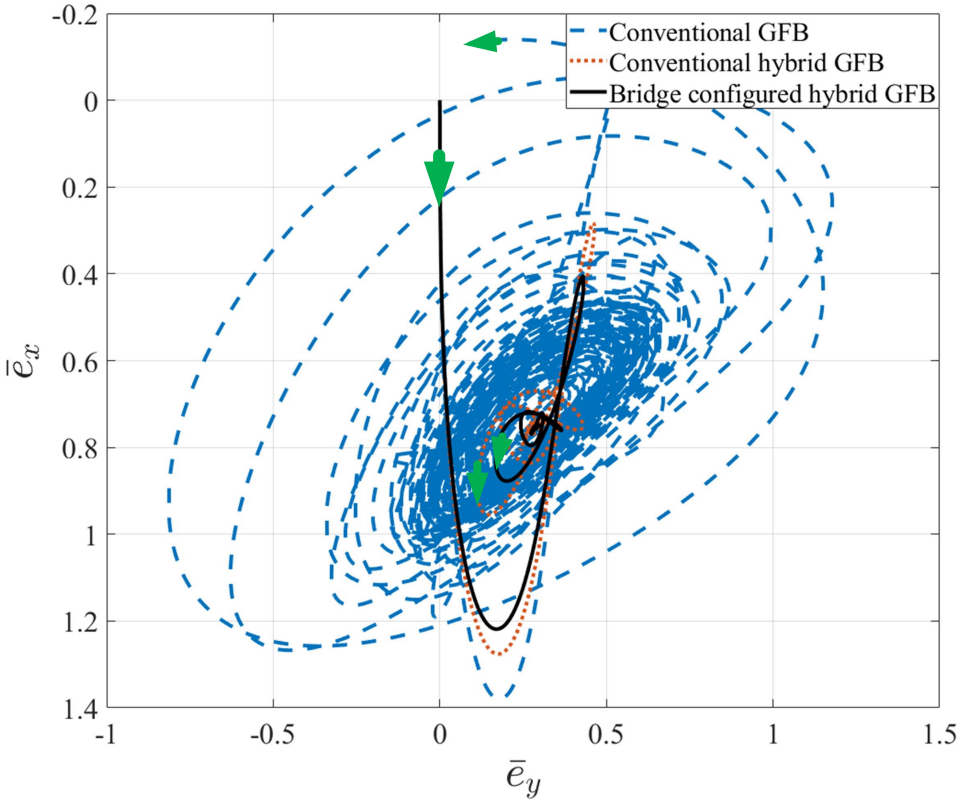

Figure 6.6: Trajectories of the rotor while rotating at 25600 rpm

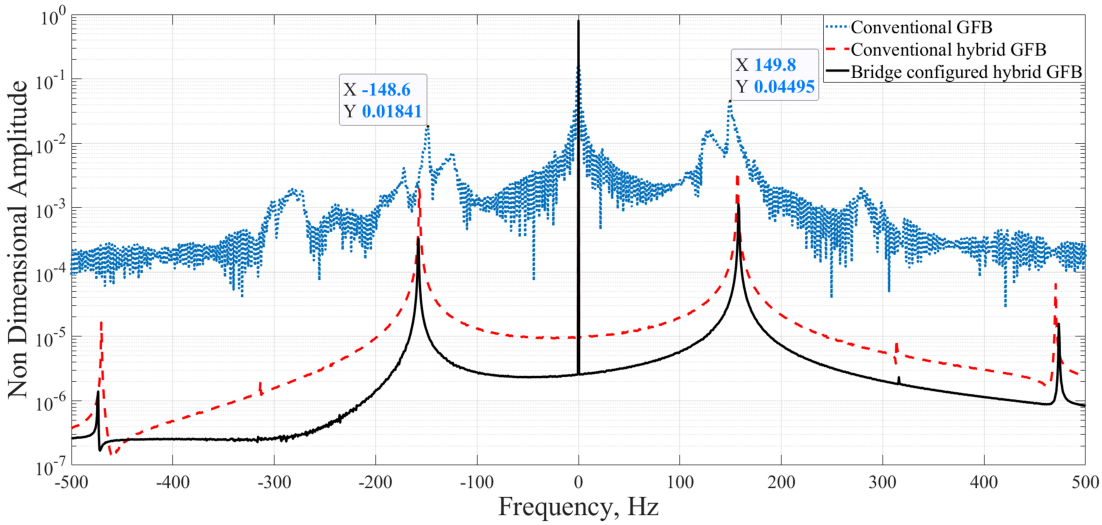

Figure 6.7: Full spectrum FFT of the rotor while rotating at 25600 rpm

Table 6.1: Results with Conventional Winding Scheme for different speed

	Conventional Winding Scheme								
	Speed (rpm)	Drive 1		Drive 2		Drive 3		Drive 4	
		Max	Min	Max	Min	Max	Min	Max	Min
Current(A)	20000	4.855	4.853	4.949	4.946	5.147	5.145	5.054	5.051
	25600	4.865	4.863	4.949	4.946	5.137	5.135	5.054	5.051
Voltage(V)	20000	7.203	7.061	7.369	7.188	7.895	7.217	7.898	6.978
	25600	7.197	7.097	7.342	7.213	8.007	7.076	8.053	6.819
Drive Power(W)	20000	34.966	34.270	36.465	35.558	40.625	37.141	39.901	35.255
	25600	35.014	34.513	36.336	35.680	41.123	36.445	40 .684	34.451

6.4.1 Effect on Stability

In Fig. 6.4, the trajectory of the rotor supported on the conventional GFB and hybrid GFB with conventional winding and bridge configured winding while rotating at 20000 rpm has been shown. The trajectory shows stable operation in all three cases. It has been observed that the rotor supported on the hybrid bearing becomes stable within a short span of time while compared to the conventional GFB. The rotor supported on hybrid GFB with conventional winding and bridge configured winding shows a similar trajectory. The corresponding full spectrum FFT is shown in Fig. 6.5 . It has been observed that both the winding scheme could successfully reduce the high amplitude of sub-synchronous frequency occurring in the case of conventional GFB. The amplitude of frequency due to both the winding scheme is similar, suggesting that equal magnetic forces have been generated using both the winding scheme.

Further, a case where the rotor supported on conventional GFB is unstable has been investigated. Figure 6.6 shows the comparison of the trajectories of the rotor supported on conventional GFB and the hybrid GFBs (conventional winding and bridge configured winding) while rotating at 25600 rpm. It has been observed that the rotor supported conventional GFB is unstable as the radius of the rotor trajectory is increasing. However, the rotor supported on hybrid bearings are stable. As expected, the trajectory of both the conventional winding and bridge configured winding is similar. In Fig. 6.7, the corresponding FFT plot has been shown. The response of conventional GFBs shows two high amplitude of sub-synchronous vibration. However, no significant peaks have been observed in case of both the hybrid bearings.

Table 6.1 and Table 6.2 reports the current, voltage and power in the drives for different rotor speeds with the conventional winding and bridge configured winding

Table 6.2: Results with Bridge Configured Winding Scheme for different speed

	Bridge Configured Winding						
	Speed (rpm)	Drive for Bias Current		Drive 1		Drive 2	
		Max	Min	Max	Min	Max	Min
Current(A)	20000	10.000	10.000	-0.291	-0.292	-0.104	-0.104
	25600	10.000	10.000	-0.271	-0.273	-0.104	-0.105
Voltage(V)	20000	14.715	14.715	-0.196	-0.233	-0.074	-0.080
	25600	14.715	14.715	-0.175	-0.225	-0.058	-0.059
Drive Power(W)	20000	147.154	147.154	0.068	0.057	0.008	0.008
	25600	147.154	147.154	0.061	0.048	0.010	0.006

respectively. As described earlier, in the case of the conventional connection arrangement, the sum of currents from drive 1 and drive 3 is maintained constant at 10A while the difference in currents of drive 1 and drive 3 is adjusted to achieve the required horizontal force. Similarly, the sum of currents from drive 2 and drive 4 is maintained constant at 10A while the difference in currents of drive 2 and drive 4 is adjusted to achieve the required vertical force. In the case of new winding arrangement, the current in drive 1 and drive 2 are adjusted to control the bearing force while the current from drive for bias current is allowed to vary naturally around a value that returns to 10A if current in drive 1 and drive 2 stay constant at any value. It has been observed that, the ranges of current and voltages encountered by the drives are almost identical in the two cases. However, a major difference can be observed in the ranges of power drawn from (or reinjected into) the drives in the two cases.

6.4.2 Effect on Unbalance Eccentricity

In order to compare the effect of the unbalance on the rotor supported on hybrid GFB with two winding scheme, the rotor speed is kept constant at 20000 rpm, while the unbalance eccentricity is varied. The time series data of the initial 500 revolutions of the rotor has not been considered in order to consider the steady state part of the journal response. In Fig. 6.8 the rotor orbit with an unbalance eccentricity of 1×10^{-7} m has been shown. The orbit of the rotor supported on conventional GFB is large. Both the winding scheme of the AMB is capable of controlling the rotor orbit as observed in Fig. 6.8. The trajectory of the rotor is quasi periodic in case of conventional GFB, while in case of both the hybrid GFBs the trajectory is periodic. In the FFT plot shown in Fig.

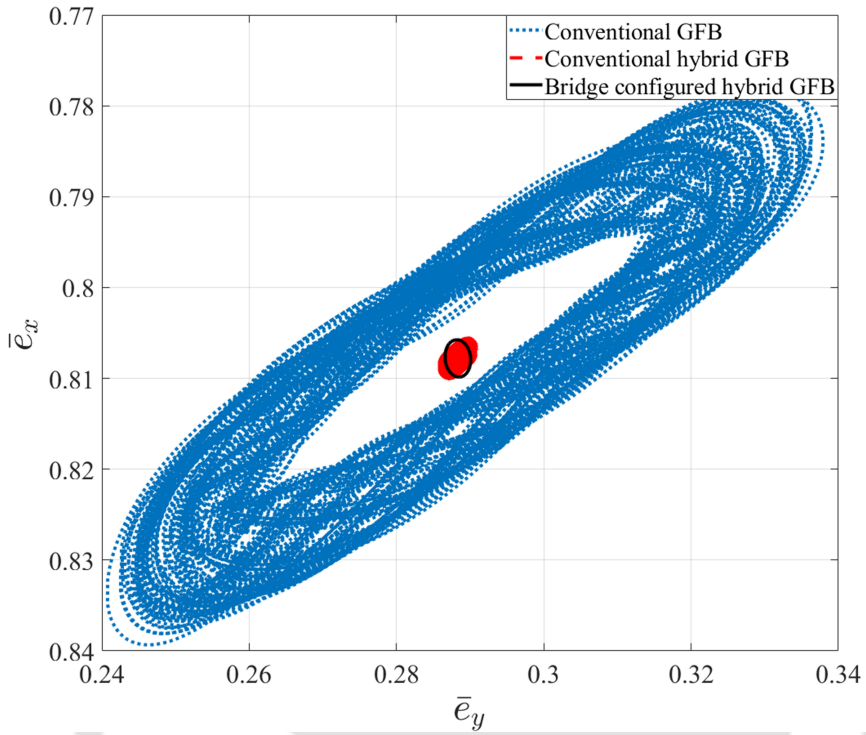

Figure 6.8: Trajectories of the rotor rotating at 20000 rpm with an unbalance eccentricity of 1×10^{-7} m

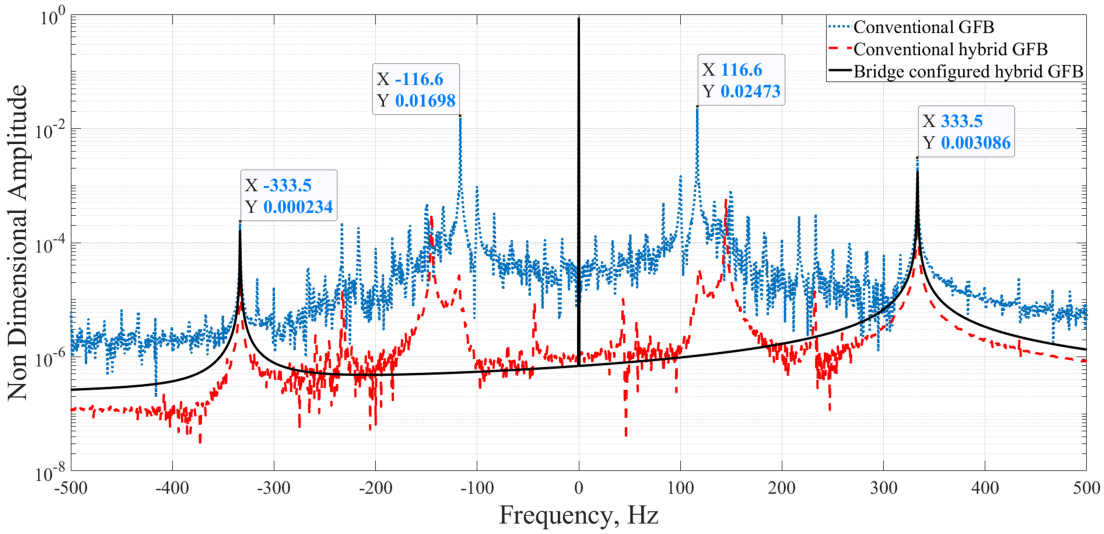

Figure 6.9: Full spectrum FFT of the rotor rotating at 20000 rpm with an unbalance eccentricity of 1×10^{-7} m

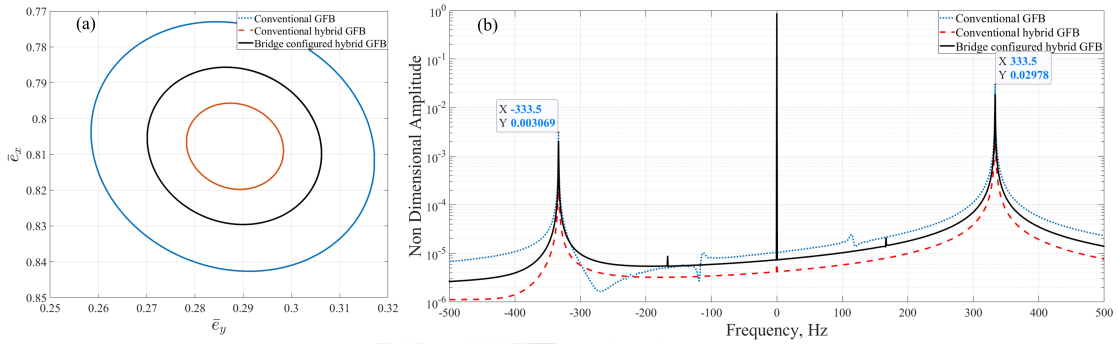

Figure 6.10: Trajectory and Full spectrum FFT of the rotor rotating at 20000 rpm with an unbalance eccentricity of 1×10^{-6} m

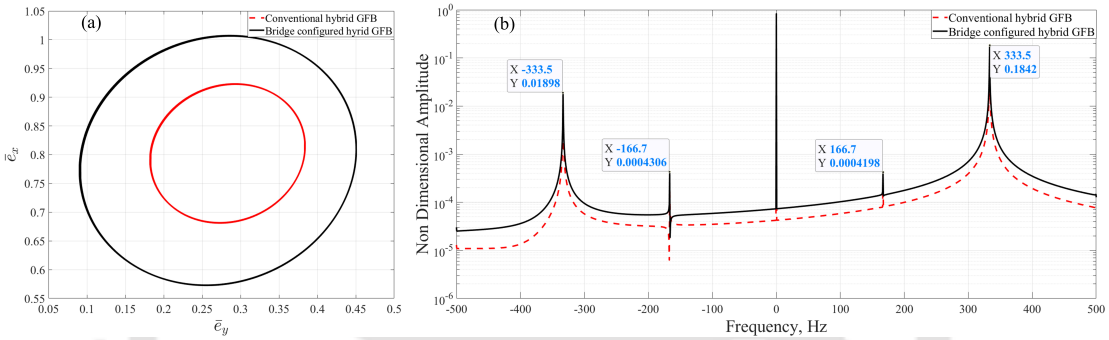

Figure 6.11: Trajectory and Full spectrum FFT of the rotor rotating at 20000 rpm with an unbalance eccentricity of 1×10^{-5} m

6.9, the rotor supported on conventional GFB shows high amplitude of sub-synchronous vibration along with the high amplitude of synchronous vibration. However, in the case of the hybrid bearings, only the synchronous frequency can be observed. The amplitude of the synchronous vibration is also lower than the amplitude of synchronous vibration in conventional GFB. As the unbalance eccentricity is further increased the rotor orbit size increases for all the three cases. The rotor orbits for an unbalance eccentricity of 1×10^{-6} m has been shown in Fig. 6.10a. The size of the orbit of the rotor supported on conventional GFB is the highest while the radius of the orbit with conventional winding scheme shows the lowest. The corresponding FFT plot is shown in Fig. 6.10b. It has been observed that the synchronous frequency is the dominating frequency at high unbalance eccentricity. The amplitude of synchronous frequency for the hybrid bearings are similar and lower than the conventional GFBs. Therefore it has been observed that both the winding scheme of the AMB can suppress the sub-synchronous vibration occurring in the rotor supported on conventional bearing and increase its stability range. The comparison of the rotor response at high unbalance eccentricity of 1×10^{-5} has been shown in Fig. 6.11. It has been observed that the orbit radius of the rotor supported on the hybrid

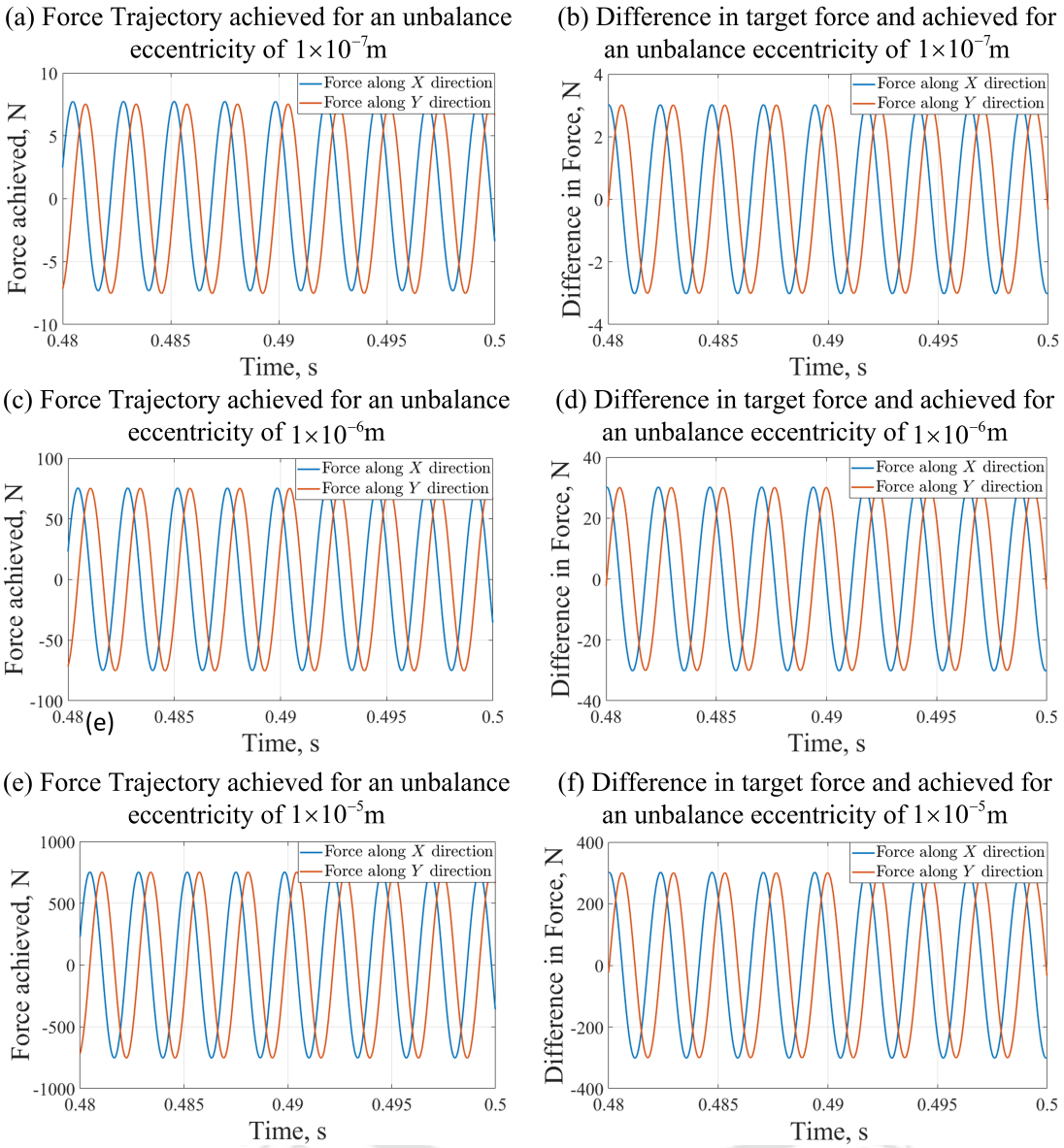

Figure 6.12: Force trajectory actually achieved and difference in forces for different unbalance eccentricity using hybrid GFB with conventional winding scheme

GFB with the conventional winding scheme is smaller compared to the hybrid GFB with bridge configured winding. In the FFT plot shown in Fig. 6.11b, a small peak of sub-synchronous frequency has been observed at 166.7 Hz. Therefore, it can be observed that the hybrid GFB with conventional winding shows better control over the rotor trajectory as well as the sub-synchronous vibration.

The achieved force and the difference between the targeted force and achieved force using the conventional winding scheme for an unbalance eccentricity of 1×10^{-7} m is shown in Fig. 6.12a and Fig. 6.12b respectively. At low unbalance the difference between

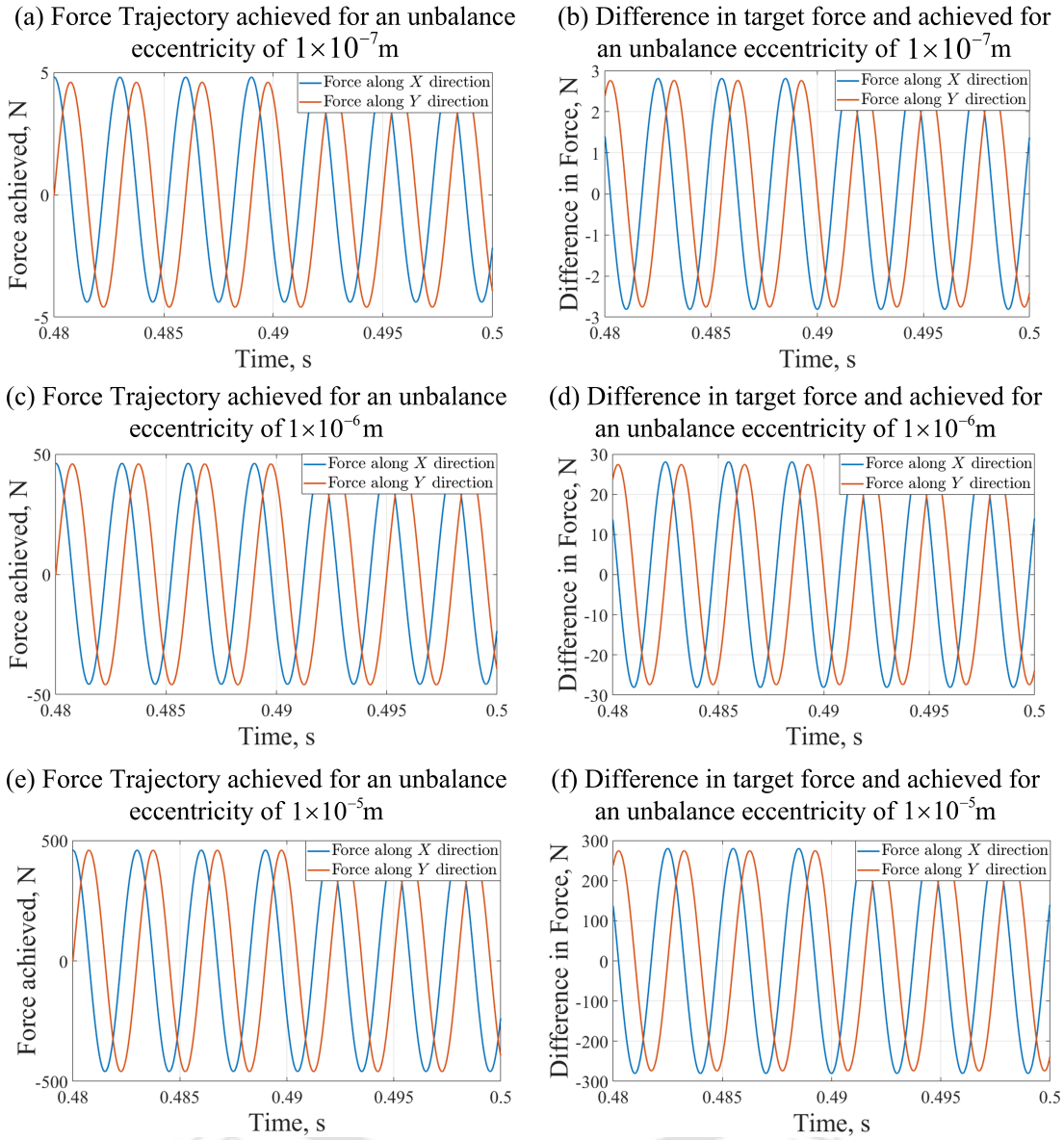

Figure 6.13: Force trajectory actually achieved and difference in forces for different unbalance eccentricity using hybrid GFB with bridge configured winding

the targeted force and achieved force has been observed to be about 3.022 N. As the unbalance eccentricity is increased, the difference gets further increased. The forces achieved using the conventional winding scheme for hybrid GFBs for the unbalance eccentricity of 1×10^{-6} m and 1×10^{-5} m has been shown in Fig.6.12c and Fig. 6.12e respectively. The corresponding difference in the targeted force and the achieved force is shown in Fig.6.12d and Fig. 6.12f. It has been observed that at high unbalance eccentricity of 1×10^{-5} m the difference becomes as large as 301.862 N.

Similar, observations have been made in case of hybrid GFB with bridge configured

Table 6.3: Results with Conventional Winding Scheme for different unbalance eccentricity

	Conventional Winding Scheme								
	Unbalance	Drive 1		Drive 2		Drive 3		Drive 4	
	Eccentricity (m)	Max	Min	Max	Min	Max	Min	Max	Min
Current(A)	1×10^{-7}	4.868	4.860	4.952	4.943	5.140	5.132	5.057	5.048
	1×10^{-6}	4.907	4.822	4.990	4.906	5.178	5.093	5.094	5.010
	1×10^{-5}	5.290	4.440	5.372	4.526	5.560	4.710	5.474	4.628
Voltage(V)	1×10^{-7}	9.500	4.814	9.586	4.973	9.888	5.273	9.795	5.056
	1×10^{-6}	30.531	-16.232	30.263	-15.719	29.858	-14.715	24.921	-15.026
	1×10^{-5}	240.264	-227.290	236.394	-223.324	231.360	-214.126	233.024	-216.286
Drive Power(W)	1×10^{-7}	46.212	23.411	47.434	24.602	50.787	26.981	49.487	25.540
	1×10^{-6}	148.632	-78.891	149.824	-77.741	153.374	-75.564	151.214	-75.888
	1×10^{-5}	1181.771	-1100.686	1180.221	-1103.607	1193.833	-1101.893	1185.274	-1092.456

Table 6.4: Results with Bridge Configured Winding Scheme for different unbalance eccentricity

	Bridge Configured Winding Scheme						
	Unbalance	Drive for Bias Current		Drive 1		Drive 2	
	Eccentricity (m)	Max	Min	Max	Min	Max	Min
Current(A)	1×10^{-7}	10.000	10.000	-0.287	-0.297	-0.99	-0.109
	1×10^{-6}	10.001	9.999	-0.243	-0.341	-0.056	-0.152
	1×10^{-5}	10.006	9.994	0.203	-0.774	0.381	-0.576
Voltage(V)	1×10^{-7}	14.716	14.715	0.836	-1.265	0.962	-1.115
	1×10^{-6}	14.722	14.709	10.343	-10.774	10.324	-10.478
	1×10^{-5}	14.773	14.647	105.227	-105.741	103.876	-104.095
Drive Power(W)	1×10^{-7}	147.161	147.148	0.370	-0.243	0.117	-0.100
	1×10^{-6}	147.219	147.088	3.256	-2.981	1.238	-1.118
	1×10^{-5}	147.737	146.466	54.616	-44.103	35.538	-28.955

hybrid GFB. In Fig. 6.13, the using the bridge configured winding scheme for an unbalance eccentricity of 1×10^{-7} m, 1×10^{-6} m and 1×10^{-5} m has been shown. The maximum difference observed in case of 1×10^{-5} m is 280.25 N. Hence, only a little variation can be observed between the two winding schemes in terms of the achieved forces .

Table 6.3 and Table 6.4 reports the current, voltage and power in the drives for different unbalance eccentricities with the conventional winding and bridge configured winding respectively. As the unbalance increases a substantial difference in voltage encountered by the drives has been observed in case of hybrid bearings with conventional winding. The voltages in the two drives of bridge configured winding schemes also increases with the increase in unbalance eccentricity. Further, in case of hybrid bearings

with conventional winding scheme, there is a large variation of power drawn from (or reinjected into) the drives. However, in case of hybrid bearings with bridge configured winding this variation of power is less.

6.5 Inferences

In this chapter, a Wheatstone-Bridge type connection pattern for the winding of the actuator has been implemented for the hybrid GFBs. It has been shown that, due to the implementing this winding scheme, the required force vector has been attained using only two current-source drives rather than four drives in case of conventional hybrid GFBs. Thus reducing the cost of hybrid GFBs. It is important to note that in the case of conventional winding scheme, the current always flows through the drive in the same direction . In the case of the bridge-configured arrangement, the current reverses its direction with no significant additional cost associated with the capability to pass the bi-directional current. Moreover, in the control approach the usual constraint of bias current has been removed in the new winding scheme. With the knowledge of the state of currents in the bearing and the bearing rotor position, the forces present in the bearing is calculated at any one instant and the controller is updated at high rates. The main disadvantage of the new connection arrangement is that the two drives do not share a common ground and must have its own DC link.

7

Conclusion and Future Work

Contents

7.1 Introduction

Gas Foil Bearings (GFBs) and Active Magnetic Bearings (AMBs) are novel oil-free bearings used in high speed rotating machines. The combination of GFB and AMB has been under rigorous investigation in recent years. In the first chapter, the basic introduction of the GFBs and AMBs has been described. Further, based on the literature review presented in Chapter 1, the aim and objectives of the present work has been stated. Earlier investigations indicated that the stability of the GFBs are reduced due to the presence of sub-synchronous frequency. Many researchers have attempted to eliminate or minimise this sub-synchronous frequency using different approaches. Widespread applications of the Gas foil bearings (GFBs) have been restricted due to its low load carrying capacity and low damping. Further, the wear of the top foil during start and stop generally reduces its lifespan. A probable solution for eliminating those demerits of GFBs is the incorporation of electromagnetic actuator along with the GFB. It is noteworthy that most of the numerical investigations carried out earlier considered the linearised stiffness and damping of the GFBs and AMBs to predict the response of hybrid GFBs. In view of this, a coupled numerical model in the time domain, combining the dynamics of the GFB and AMB has been developed. Further, a different winding scheme for the actuator with an aim of reducing the cost of the hybrid GFB has been suggested. In the second chapter, the modelling of GFBs has been described. The finite difference method has been used to discretise the spatial domain of the Reynolds equation. The time dependent term of the Reynolds Equation has been discretised using the Crank Nicholson Method. The numerical modelling of AMBs has been described in third chapter. The factors to be considered in order to design an AMB has also been described. The reluctance network method has been used to calculate the magnetic forces generated in the AMB. A coupled model combining the dynamics of GFB and AMB has been developed as presented in chapter four. The developed model has been used to investigate the effects of the electromagnetic actuator (EMA) on the stability of a fully balanced rotor. The control current required to control the rotor at the desired position has also been investigated. In the fifth chapter, the unbalance response of the rotor supported on the conventional GFB and hybrid GFB has been compared. Further, the effect of sudden unbalance on the dynamic behaviour of the rotor has been presented. Due to the requirement of precise manufacturing process, the cost of GFB increases. The cost of AMB increases due to the requirement of four independent drives. Therefore, the cost of the hybrid GFB further increases. A new winding scheme for the actuator with an aim of reducing the cost of

hybrid GFB has been presented in the sixth chapter. The new winding scheme follows a Wheatstone bridge type circuits. By implementing this approach, the required force vector has been achieved using only two current-source drives rather than four drives. The requirement of only two drives probably bring down the cost of the hybrid GFB.

7.2 Observations

This thesis exemplifies the combination of two oil-free bearings vis a vis GFBs and AMBs also referred to as hybrid GFBs. A coupled numerical model of a GFB and AMB also referred to as an electromagnetic actuator (EMA) has been developed. The fluid film forces and the magnetic forces are incorporated into the rotor equations of motion. The fluid film forces are obtained solving the Reynolds equation. The magnetic forces of the AMB are calculated using the reluctance network method. A rotor supported on two bearings has been considered for the simulating the rotor response. Based on the results obtained from the analysis, following observations are made:

7.2.1 Observation on stability analysis

In the stability analysis, the rotor has been considered to be perfectly balanced and the response of conventional GFB and hybrid GFB has been compared. The following observations were made:

1. Based on the rotor bearing parameters, the rotor supported on conventional GFBs showed instability at 25600 rpm. However, the rotor supported on hybrid GFBs showed stable operation at this speed. Therefore, the implementation of electromagnetic actuators with GFBs can increase the range of operating speed significantly. This increment in operating speed limit can be very high when rotor has no unbalance because the magnetic actuator can control the rotor position at the operating point.
2. The amplitude of the response of the sub-synchronous frequency has been reduced due to the implementation of the hybrid GFB. As such, 87% reduction in the amplitude of the response of the sub-synchronous frequency has been observed. This results in the improvement of the stability of the rotor supported by GFB.
3. It has been demonstrated that an unstable rotor can be made stable by using the EMA with a minimal control current. Higher control current is required when the speed of the rotor increases. The control current required to control the rotor when

the effect of the EMA is applied after observing the undulation of the response is less compared to when the effect of the EMA is applied from the start. Therefore the use of EMA at an instant when the rotor vibration increases can control the effect of unbalance with minimum control current.

4. It has been observed that a high magnetic force is required to control the rotor for a set reference value other than the natural steady-state value of the response of the rotor supported by GFB without the effect of EMA. An error of about 30% in the response has been observed when the reference point is changed from the natural steady-state value to another reference point.

7.2.2 Observation on unbalance analysis

Generally, due to manufacturing tolerances unbalance is inherently present in the system and can lead to instability in a GFB. The developed coupled model has been used to investigate the capability of the hybrid gas foil bearing to mitigate the effect of unbalance force and in turn, instability. Accordingly, the unbalance responses of a rotor supported on GFBs and hybrid GFBs are compared based on the amount of unbalance. The effects of unbalance on the control current and film thickness have also been investigated. Moreover, the impact of sudden unbalance has been investigated. The following are the observations made based on the unbalance response of the rotor:

1. The limit to withstand unbalance of the rotor has been found to have increased with the use of hybrid GFBs. The rotor supported only on conventional GFB could withstand only m of unbalance eccentricity while the hybrid GFB could withstand up to m of unbalance eccentricity.
2. At low unbalance eccentricity, the rotor supported on conventional GFBs showed quasi-periodic behaviour with high amplitude of the response of the sub-synchronous frequency. As the unbalance is increased in the case of conventional GFB, the amplitude of the response of the synchronous frequency becomes dominant.
3. At high unbalance eccentricity, the rotor trajectory supported on conventional GFBs becomes mutli-periodic. The FFT plot of the rotor response shows high amplitude of the sub-synchronous frequency and synchronous frequency.
4. The rotor supported on hybrid GFBs shows periodic motion. However, the radius of the orbit of the rotor increases with the increase in unbalance.
5. The FFT plot of the rotor response supported on hybrid GFBs shows only synchronous peak at low unbalance while at high unbalance the sub-synchronous peak

can also be observed along with the synchronous frequency.

6. Higher control current is required for higher unbalance in order to control the rotor.
7. The minimum film thickness goes below zero in conventional GFBs for higher unbalance cases, which implies contact taking place between the journal and the top foil surface. However, the value of minimum film thickness in the hybrid GFBs is higher than the conventional GFBs, for which the hybrid GFB can withstand higher unbalance without any contact of the journal and top foil. Therefore, the use of EMA with GFB to support a rotor ensures contactless operation of the journal and the top foil and thereby the rotor is enabled to withstand higher unbalance.
8. The hybrid GFBs are also capable of withstanding a higher amount of sudden unbalance. The rotor supported on hybrid GFBs could sustain an unbalance up to 86 g mm whereas the rotor supported on conventional GFBs could sustain 63 g mm of unbalance.

7.2.3 Observation on the new bridge configured winding

The cost of hybrid GFB would be much higher as the cost of both GFB and AMB are individually high. However, this cost could be brought down by utilizing only two drives. A different winding scheme is possible for the AMBs in which only two drives are utilised per bearing and bias current is provided (in the same set of windings) via a simple rectifier with a small series of choke and shunt capacitor. Implementing the new winding scheme, the required force vector can be attained using only two current-source drives rather than four drives in the case of hybrid GFBs with conventional winding scheme. Further, a new control strategy based on being able to utilise lower-cost components to power the magnetic bearing has been proposed. Applying the new control strategy, the limits on maximum force and maximum slew-rates can be changed from those of conventional bearing arrangement. The following observations were made based on the implementation of the new winding arrangement:

1. The magnetic forces achieved from the new winding scheme is similar to the magnetic forces produced with the conventional winding.
2. The current always flows through the drive in the same direction in case the conventional winding scheme. In the case of the bridge-configured arrangement, the current reverses its direction with no significant additional cost associated with the capability to pass the bi-directional current.
3. The new control approach removes the usual constraint of bias current. With the

knowledge of the state of the currents in the bearing and the bearing rotor position, the forces present in the bearing are calculated at any one instant, and the controller is updated at high rates.

7.3 Conclusion

The following conclusion can be drawn from the current work.

1. The effect of sub-synchronous whirling can be suppressed by using EMA with GFB. This results in the improvement of the stability of the rotor supported by GFB.
2. Use of EMA at an instant when the rotor vibration increases can control the effect of unbalance with minimum control current.
3. The use of only EMA without GFB to support a rotor-system requires high control current, and it enhances the maintenance cost. However, using GFB with EMA reduces the requirement of control current, thus reduces the maintenance cost.
4. Use of EMA with GFB to support a rotor ensures contactless operation of the journal and the top foil, and thereby the rotor is enabled to withstand higher unbalance.
5. The new winding scheme is economical and it does not deteriorate the characteristics of the hybrid bearing compared to conventional winding.
6. The use of new winding scheme also eliminates the constraint of constant bias current.

In view of the above, the new winding scheme is economical, and it does not deteriorate the characteristics of the hybrid bearing compared to conventional winding. Therefore recommended for use in hybrid GFB. However, there is a drawback of the new arrangement. In the conventional winding scheme, the four current-source drives can have a common single DC bus, since all four independent circuits share a common ground. However, it is not straightforward in case of the new winding arrangement. It is at least theoretical for the two source drives of the new winding arrangement to share energy between their respective “DC buses” using a system where a capacitor is charged-up to approximately twice the instantaneous voltage across one DC bus (using an inductor to provide the voltage overshoot) and then discharged to empty into the other DC bus.

7.4 Scope for Future Work

Based on the work presented in the thesis, some of the future works which may be undertaken are as follows,,

1. Since the current analysis is based on numerical modelling, therefore, it is pertinent to validate the results through an experiment.
2. Other types of GFBs, like wire mesh type, multi-leaf type, can be modelled with EMA.
3. A cylindrical shell model of the top foil can be modelled for more accurate results.
4. Further research is recommended to do away with the disadvantage of the new bridge configured winding scheme, i.e., to have common ground instead of two separate DC link.
5. In order to provide design guidelines, generalization of the different aspects for unbalance and stability can be been made.

References

[1] G. L. Agrawal, "Foil air/gas bearing technology—an overview," in *ASME 1997 International gas turbine and aeroengine congress and exhibition*. American Society of Mechanical Engineers, 1997, pp. V001T04A006–V001T04A006.

[2] G. Schweitzer and E. H. Maslen, *Magnetic bearings. Theory, design, and application to rotating machinery*. Springer, 2009.

[3] C. DellaCorte, K. C. Radil, R. J. Bruckner, and S. A. Howard, "A preliminary foil gas bearing performance map," NASA/TM—2006-214343, Tech. Rep., 2006.

[4] K. Nalepa, P. Pietkiewicz, and G. Żywica, "Development of the foil bearing technology," *Technical Sciences*, vol. 12, no. 1, pp. 229–240, 2009.

[5] L. San Andrés and T. H. Kim, "Computational analysis of gas foil bearings integrating 1d and 2d finite element models for top foil," *Turbomachinery Laboratory, Texas A&M University, Technical Report No. TRCB&C-1–06*, 2006.

[6] K. Shalash and J. Schiffmann, "On the manufacturing of compliant foil bearings," *Journal of Manufacturing Processes*, vol. 25, pp. 357–368, 2017.

[7] H. Heshmat, "Advancements in the performance of aerodynamic foil journal bearings: high speed and load capability," *Journal of Tribology*, vol. 116, no. 2, pp. 287–294, 1994.

[8] Y. Tian, Y. Sun, and L. Yu, "Structural stiffness and damping coefficients of a multileaf foil bearing with bump foils underneath," *Journal of Engineering for Gas Turbines and Power*, vol. 136, no. 4, p. 044501, 2014.

[9] D. Kim, M. S. Hossain, S.-J. Son, C.-J. Choi, and D. Krähenbühl, "Five millimeter air foil bearing operating at 350,000 rpm in a micro electric motor drive," in *ASME/STLE 2011 International Joint Tribology Conference*. American Society of Mechanical Engineers, 2011, pp. 163–166.

[10] Y.-B. Lee, S. B. Kwon, T. H. Kim, and K. Sim, "Feasibility study of an oil-free turbocharger supported on gas foil bearings via on-road tests of a two-liter class diesel vehicle," *Journal of Engineering for Gas Turbines and Power*, vol. 135, no. 5, p. 052701, 2013.

[11] L. San Andrés, K. Ryu, and T. H. Kim, "Thermal management and rotordynamic performance of a hot rotor-gas foil bearings system—part i: measurements," *Journal of Engineering for Gas Turbines and Power*, vol. 133, no. 6, p. 062501, 2011.

[12] T. H. Kim, A. W. Breedlove, and L. San Andrés, "Characterization of a foil bearing structure at increasing temperatures: static load and dynamic force performance," *Journal of Tribology*, vol. 131, no. 4, p. 041703, 2009.

[13] H.-J. Xu, Z.-S. Liu, G.-H. Zhang, and Y.-L. Wang, "Design and experiment of oil lubricated five-leaf foil bearing test-bed," *Journal of Engineering for Gas Turbines and Power*, vol. 131, no. 5, p. 054505, 2009.

[14] S. Kulkarni, S. D. Naik, K. S. Kumar, M. Radhakrishna, and S. Jana, "Development of foil bearings for small rotors," in *Proc. ASME 2013 Gas Turbine India Conference, American Society of Mechanical Engineers*, 2013, pp. V001T005A010–V001T005A010.

[15] T. Jamir and S. Kakoty, "Load capacity analysis of gas foil bearing (gfb) for different foil materials," in *Proceedings of International Conference on Advances in Tribology and Engineering Systems*. Springer, 2014, pp. 331–343.

[16] H. M. Chen, R. Howarth, G. Bernard, J. C. Theilacker, and W. M. Soyars, "Application of foil bearings to helium turbocompressor," Fermi National Accelerator Lab.(FNAL), Batavia, IL (United States), Tech. Rep., 2001.

[17] C. DellaCorte, K. C. Radil, R. J. Bruckner, and S. A. Howard, "Design, fabrication, and performance of open source generation i and ii compliant hydrodynamic gas foil bearings," *Tribology Transactions*, vol. 51, no. 3, pp. 254–264, 2008.

[18] D. Ruscitto, J. McCormick, S. Gray, and B. Bhushan, *Hydrodynamic air lubricated compliant surface bearing for an automotive gas turbine engine*. Department of Energy, Office of Conservation and Solar Applications . . . , 1978.

[19] M. K. Stanford and C. DellaCorte, "Friction and wear characteristics of cu-4al foil bearing coating at 25 and 650 c," NASA/TM-2004-212972, Tech. Rep., 2004.

[20] H. Heshmat, P. Hryniewicz, J. F. Walton Ii, J. P. Willis, S. Jahanmir, and C. DellaCorte, "Low-friction wear-resistant coatings for high-temperature foil bearings," *Tribology International*, vol. 38, no. 11-12, pp. 1059–1075, 2005.

[21] C. DellaCorte, A. R. Zaldana, and K. C. Radil, "A systems approach to the solid lubrication of foil air bearings for oil-free turbomachinery," *Journal of Tribology*, vol. 126, no. 1, pp. 200–207, 2004.

[22] H. Heshmat, S. Jahanmir, and J. F. Walton, "Coatings for high temperature foil bearings," in *ASME Turbo Expo 2007: Power for Land, Sea, and Air*. American Society of Mechanical Engineers, 2007, pp. 971–976.

[23] D. Lubell, C. DellaCorte, and M. Stanford, "Test evolution and oil-free engine experience of a high temperature foil air bearing coating," in *ASME Turbo Expo 2006: Power for Land, Sea, and Air*. American Society of Mechanical Engineers, 2006, pp. 1245–1249.

[24] R. Larsonneur, "Design and control of active magnetic bearing systems for high speed rotation," Ph.D. dissertation, ETH Zurich, 1990.

[25] A. J. Voigt, "Towards identification of rotordynamic properties for seals in multiphase flow using active magnetic bearings," *Design and Commissioning of a Novel Test Facility. Technical University of Denmark*, 2016.

[26] L. Burdet, "Active magnetic bearing design and characterization for high temperature applications," Ph.D. dissertation, Ecole Polytechnique Fédérale de Lausanne, 2006.

[27] Y. Kanemitsu, M. Ohsawa, E. Marui *et al.*, "Comparison of control laws for magnetic levitation," in *Proceedings of the Fourth International Symposium on Magnetic Bearings*, 1994.

[28] M. H. Rashid, *Power electronics handbook*. Butterworth-Heinemann, 2017.

[29] H. K. Baumeister, "Recording support devices," Dec. 2 1958, uS Patent 2,862,781.

[30] W. Gross, "Film lubrication-v. infinitely long incompressible lubricating films of various shapes," *IBM Research Laboratory, San Jose, CA, Report No. RJ*, pp. 117–5, 1958.

[31] L. Licht and M. Branger, "Design, fabrication, and performance of foil journal bearing for the brayton rotating unit," NASA-CR-2243, RR-72-25, Tech. Rep., 1973.

[32] J. Cherubim, "Hydrodynamic foil bearings," May 7 1974, uS Patent 3,809,443.

[33] C. DellaCorte and R. J. Bruckner, "Remaining technical challenges and future plans for oil-free turbomachinery," *Journal of Engineering for Gas Turbines and Power*, vol. 133, no. 4, p. 042502, 2011.

[34] H. Heshmat, J. F. Walton, C. Della Corte, and M. Valco, "Oil-free turbocharger demonstration paves way to gas turbine engine applications," in *ASME Turbo Expo 2000: Power for Land, Sea, and Air*. American Society of Mechanical Engineers, 2000, pp. V001T04A008–V001T04A008.

[35] C. DellaCorte and M. J. Valco, "Load capacity estimation of foil air journal bearings for oil-free turbomachinery applications," *Tribology Transactions*, vol. 43, no. 4, pp. 795–801, 2000.

[36] H. Heshmat, W. Shapiro, and S. Gray, "Development of foil journal bearings for high load capacity and high speed whirl stability," *Journal of Lubrication Technology*, vol. 104, no. 2, pp. 149–156, 1982.

[37] J. Du, J. Zhu, B. Li, and D. Liu, "Hydrodynamic analysis of multileaf gas foil bearing with backing springs," *Proceedings of the Institution of Mechanical Engineers, Part J: Journal of Engineering Tribology*, vol. 228, no. 5, pp. 529–547, 2014.

[38] C. Heshmat and H. Heshmat, "An analysis of gas-lubricated, multileaf foil journal bearings with backing springs," *Journal of Tribology*, vol. 117, no. 3, pp. 437–443, 1995.

[39] H. Yu, C. Shuangtao, C. Rugang, Z. Qiaoyu, and Z. Hongli, "Numerical study on foil journal bearings with protuberant foil structure," *Tribology International*, vol. 44, no. 9, pp. 1061–1070, 2011.

[40] T. Lai, S. Chen, B. Ma, Y. Zheng, and Y. Hou, "Effects of bearing clearance and supporting stiffness on performances of rotor-bearing system with multi-decked protuberant gas foil journal bearing," *Proceedings of the Institution of Mechanical Engineers, Part J: Journal of Engineering Tribology*, vol. 228, no. 7, pp. 780–788, 2014.

[41] Y. Hou, T. Lai, Y. ZHENG, S. CHEN *et al.*, "Experimental investigation on the multi-decked protuberant gas foil journal bearing," *Journal of Advanced Mechanical Design, Systems, and Manufacturing*, vol. 7, no. 4, pp. 791–799, 2013.

[42] L. San Andrés and T. A. Chirathadam, "A metal mesh foil bearing and a bump-type foil bearing: Comparison of performance for two similar size gas bearings," *Journal of Engineering for Gas Turbines and Power*, vol. 134, no. 10, p. 102501, 2012.

[43] J.-H. Song and D. Kim, "Foil gas bearing with compression springs: analyses and experiments," *Journal of Tribology*, vol. 129, no. 3, pp. 628–639, 2007.

[44] Y.-C. Kim, D.-H. Lee, and K.-W. Kim, "Performance analysis of double-bump air foil bearings," *Tribology Transactions*, vol. 51, no. 3, pp. 285–295, 2008.

[45] K. Feng, X. Zhao, and Z. Guo, "Design and structural performance measurements of a novel multi-cantilever foil bearing," *Proceedings of the Institution of Mechanical Engineers, Part C: Journal of Mechanical Engineering Science*, vol. 229, no. 10, pp. 1830–1838, 2015.

[46] Y. Lee, C. Kim, N. Lee, and T. Kim, "Hybrid air foil journal bearing and manufacturing method thereof," July 25 2002, uS Patent App. 09/912,965.

[47] Y. B. Lee, C. H. Kim, N. S. Lee, and T. H. Kim, "Smart foil journal bearing with piezoelectric actuators," June 24 2003, uS Patent 6,582,125.

[48] J. Park and K. Sim, "A feasibility study of controllable gas foil bearings with piezoelectric materials via rotordynamic model predictions," *Journal of Engineering for Gas Turbines and Power*, vol. 141, no. 2, p. 021027, 2019.

[49] Y.-B. Lee, T.-H. Kim, C.-H. Kim, N.-S. Lee, and D.-H. Choi, "Dynamic characteristics of a flexible rotor system supported by a viscoelastic foil bearing (vefb)," *Tribology International*, vol. 37, no. 9, pp. 679–687, 2004.

[50] T. H. Kim and L. San Andrés, "Analysis of advanced gas foil bearings with piecewise linear elastic supports," *Tribology International*, vol. 40, no. 8, pp. 1239–1245, 2007.

[51] K. Sim, L. Yong-Bok, T. H. Kim, and J. Lee, "Rotordynamic performance of shimmed gas foil bearings for oil-free turbochargers," *Journal of Tribology*, vol. 134, no. 3, p. 031102, 2012.

[52] E. E. Swanson and P. S. O'meara, "Wing foil bearings and methods of manufacturing same," Dec. 29 2015, uS Patent 9,222,509.

[53] H. Sadri, H. Schlums, and M. Sinapius, "Design characteristics of an aerodynamic foil bearing with adaptable bore clearance," in *ASME Turbo Expo 2018: Turbomachinery Technical Conference and Exposition*. American Society of Mechanical Engineers, 2018, pp. V07BT34A031–V07BT34A031.

[54] M. Feng, H. Hu, and T. Ren, "Performance potential of gas foil journal bearings enhanced with micro taper-grooves on top foil," *Industrial Lubrication and Tribology*, 2019.

[55] K. Feng, Y. Cao, K. Yu, H. Guan, Y. Wu, and Z. Guo, "Characterization of a controllable stiffness foil bearing with shape memory alloy springs," *Tribology International*, vol. 136, pp. 360–371, 2019.

[56] H. Heshmat, J. Walowit, and O. Pinkus, "Analysis of gas-lubricated foil journal bearings," *Journal of Lubrication Technology*, vol. 105, no. 4, pp. 647–655, 1983.

[57] C.-P. R. Ku and H. Heshmat, "Compliant foil bearing structural stiffness analysis: part i—theoretical model including strip and variable bump foil geometry," *Journal of Tribology*, vol. 114, no. 2, pp. 394–400, 1992.

[58] C. DellaCorte, "Stiffness and damping coefficient estimation of compliant surface gas bearings for oil-free turbomachinery," *Tribology Transactions*, vol. 54, no. 4, pp. 674–684, 2011.

[59] J. P. Peng and M. Carpino, "Calculation of stiffness and damping coefficients for elastically supported gas foil bearings," *Journal of Tribology*, vol. 115, no. 1, pp. 20–27, 1993.

[60] J.-P. Peng and M. Carpino, "Coulomb friction damping effects in elastically supported gas foil bearings," *Tribology Transactions*, vol. 37, no. 1, pp. 91–98, 1994.

[61] M. Carpino and G. Talmage, "A fully coupled finite element formulation for elastically supported foil journal bearings," *Tribology Transactions*, vol. 46, no. 4, pp. 560–565, 2003.

[62] Z.-C. Peng and M. Khonsari, "Hydrodynamic analysis of compliant foil bearings with compressible air flow," *Journal of Tribology*, vol. 126, no. 3, pp. 542–546, 2004.

[63] T. H. Kim and L. San Andrés, "Heavily loaded gas foil bearings: a model anchored to test data," *Journal of Engineering for Gas Turbines and Power*, vol. 130, no. 1, p. 012504, 2008.

[64] L. San Andrés and T. H. Kim, "Analysis of gas foil bearings integrating fe top foil models," *Tribology International*, vol. 42, no. 1, pp. 111–120, 2009.

[65] L. SanAndrés and T. H. Kim, "Thermohydrodynamic analysis of bump type gas foil bearings: a model anchored to test data," *Journal of Engineering for Gas Turbines and Power*, vol. 132, no. 4, p. 042504, 2010.

[66] S. A. Howard and L. San Andrés, "A new analysis tool assessment for rotordynamic modeling of gas foil bearings," *Journal of Engineering for Gas Turbines and Power*, vol. 133, no. 2, p. 022505, 2011.

[67] I. Iordanoff, B. B. Said, A. Mezianne, and Y. Berthier, "Effect of internal friction in the dynamic behavior of aerodynamic foil bearings," *Tribology International*, vol. 41, no. 5, pp. 387–395, 2008.

[68] S. W. Knowles, "An investigation of foil thickness on performance for oil–free bearings," Ph.D. dissertation, Case Western Reserve University, 2009.

[69] K. Feng and S. Kaneko, "Analytical model of bump-type foil bearings using a link-spring structure and a finite-element shell model," *Journal of Tribology*, vol. 132, no. 2, p. 021706, 2010.

[70] H. Bensouilah, M. Lahmar, and B. Bou-Saïd, "Elasto-aerodynamic lubrication analysis of a self-acting air foil journal bearing," *Lubrication Science*, vol. 24, no. 3, pp. 95–128, 2012.

[71] D. Lee, D. Kim, and R. P. Sadashiva, "Transient thermal behavior of preloaded three-pad foil bearings: modeling and experiments," *Journal of Tribology*, vol. 133, no. 2, p. 021703, 2011.

[72] D. Kim, J. Ki, Y. Kim, and K. Ahn, "Extended three-dimensional thermo-hydrodynamic model of radial foil bearing: case studies on thermal behaviors and dynamic characteristics in gas turbine simulator," *Journal of Engineering for Gas Turbines and Power*, vol. 134, no. 5, p. 052501, 2012.

[73] K. Feng and S. Kaneko, "A thermohydrodynamic sparse mesh model of bump-type foil bearings," *Journal of Engineering for Gas Turbines and Power*, vol. 135, no. 2, p. 022501, 2013.

[74] L. Moraru and T. Keith, "Lobatto point quadrature for thermal lubrication problems involving compressible lubricants," in *World Tribology Congress III*. American Society of Mechanical Engineers, 2005, pp. 171–172.

[75] K. Feng and Z. Guo, "Prediction of dynamic characteristics of a bump-type foil bearing structure with consideration of dynamic friction," *Tribology Transactions*, vol. 57, no. 2, pp. 230–241, 2014.

[76] G. Grau, I. Iordanoff, B. Bou Said, and Y. Berthier, "An original definition of the profile of compliant foil journal gas bearings: static and dynamic analysis," *Tribology Transactions*, vol. 47, no. 2, pp. 248–256, 2004.

[77] B. Bou-Said, G. Grau, and I. Iordanoff, "On nonlinear rotor dynamic effects of aerodynamic bearings with simple flexible rotors," *Journal of Engineering for Gas Turbines and Power*, vol. 130, no. 1, p. 012503, 2008.

[78] S. Le Lez, M. Arghir, and J. Frêne, "Nonlinear numerical prediction of gas foil bearing stability and unbalanced response," *Journal of Engineering for Gas Turbines and Power*, vol. 131, no. 1, p. 012503, 2009.

[79] D.-H. Lee, Y.-C. Kim, and K.-W. Kim, "The dynamic performance analysis of foil journal bearings considering coulomb friction: rotating unbalance response," *Tribology Transactions*, vol. 52, no. 2, pp. 146–156, 2009.

[80] N. Wang, H.-C. Huang, and C.-R. Hsu, "Parallel optimum design of foil bearing using particle swarm optimization method," *Tribology Transactions*, vol. 56, no. 3, pp. 453–460, 2013.

[81] P. Bonello and H. Pham, "The efficient computation of the nonlinear dynamic response of a foil–air bearing rotor system," *Journal of Sound and Vibration*, vol. 333, no. 15, pp. 3459–3478, 2014.

[82] J. S. Larsen and I. F. Santos, "Efficient solution of the non-linear reynolds equation for compressible fluid using the finite element method," *Journal of the Brazilian Society of Mechanical Sciences and Engineering*, vol. 37, no. 3, pp. 945–957, 2015.

[83] J. S. Larsen, I. F. Santos, and S. von Osmanski, "Stability of rigid rotors supported by air foil bearings: Comparison of two fundamental approaches," *Journal of Sound and Vibration*, vol. 381, pp. 179–191, 2016.

[84] S. von Osmanski, J. S. Larsen, and I. F. Santos, "Multi-domain stability and modal analysis applied to gas foil bearings: Three approaches," *Journal of Sound and Vibration*, vol. 472, p. 115174, 2020.

[85] T. Pronobis and R. Liebich, "Comparison of stability limits obtained by time integration and perturbation approach for gas foil bearings," *Journal of Sound and Vibration*, vol. 458, pp. 497–509, 2019.

[86] K. C. Radil and C. Dellacorte, "The effect of journal roughness and foil coatings on the performance of heavily loaded foil air bearings," *Tribology Transactions*, vol. 45, no. 2, pp. 199–204, 2002.

[87] D. Kim and G. Zimbru, "Start-stop characteristics and thermal behavior of a large hybrid airfoil bearing for aero-propulsion applications," *Journal of Engineering for Gas Turbines and Power*, vol. 134, no. 3, p. 032502, 2012.

[88] E. Barlow, "Externally pressurized foil gas bearings," *Journal of Basic Engineering*, vol. 87, no. 4, pp. 986–990, 1965.

[89] D. Kim and S. Park, "Hybrid air foil bearings with external pressurization," in *ASME 2006 International Mechanical Engineering Congress and Exposition*. American Society of Mechanical Engineers, 2006, pp. 63–69.

[90] D. Kim and D. Lee, "Design of three-pad hybrid air foil bearing and experimental investigation on static performance at zero running speed," *Journal of Engineering for Gas Turbines and Power*, vol. 132, no. 12, p. 122504, 2010.

[91] K. Feng, X. Zhao, C. Huo, and Z. Zhang, "Analysis of novel hybrid bump-metal mesh foil bearings," *Tribology International*, vol. 103, pp. 529–539, 2016.

[92] S. Morosi and I. F. Santos, "Stability analysis of flexible rotors supported by hybrid permanent magnet–gas bearings," in *PACAM XI–11th Pan-American Congress of Applied Mechanics, January*. Citeseer, 2010, pp. 4–8.

[93] S. Morosi and I. Santos, "Active lubrication applied to radial gas journal bearings. part 1: Modeling," *Tribology International*, vol. 44, no. 12, pp. 1949–1958, 2011.

[94] R. Polyakov, M. Bondarenko, and L. Savin, "Hybrid bearing with actively adjustable radial gap of gas foil bearing," *Procedia Engineering*, vol. 106, pp. 132–140, 2015.

[95] E. E. Swanson, H. Heshmat, and J. Walton, "Performance of a foil-magnetic hybrid bearing," *Journal of engineering for gas turbines and power*, vol. 124, no. 2, pp. 375–382, 2002.

[96] J. K. Scharrer, "Magnetically active foil bearing," May 21 1996, uS Patent 5,519,274.

[97] H. Heshmat, H. M. Chen, and F. W. I. James, "Hybrid foil-magnetic bearing," March 5 2002, uS Patent 6,353,273.

[98] Y. B. Lee, C. H. Kim, S. J. Kim, S. H. Lee, and H. S. Kim, "Airfoil-magnetic hybrid bearing and a control system thereof," July 8 2014, uS Patent 8,772,992.

[99] A. Looser and J. W. Kolar, "A hybrid bearing concept for high-speed applications employing aerodynamic gas-bearings and a self-sensing active magnetic damper," in *IECON 2011-37th Annual Conference on IEEE Industrial Electronics Society*. IEEE, 2011, pp. 1686–1691.

[100] Y. Tian, Y. Sun, and L. Yu, "Steady-state control of hybrid foil-magnetic bearings," in *ASME Turbo Expo 2012: Turbine Technical Conference and Exposition*. American Society of Mechanical Engineers, 2012, pp. 849–857.

[101] M. N. Pham and H.-J. Ahn, "Experimental optimization of a hybrid foil–magnetic bearing to support a flexible rotor," *Mechanical Systems and Signal Processing*, vol. 46, no. 2, pp. 361–372, 2014.

[102] F. G. Pierart and I. F. Santos, "Lateral vibration control of a flexible overcritical rotor via an active gas bearing–theoretical and experimental comparisons," *Journal of Sound and Vibration*, vol. 383, pp. 20–34, 2016.

[103] S. Jeong and Y. B. Lee, "Effects of eccentricity and vibration response on high-speed rigid rotor supported by hybrid foil-magnetic bearing," *Proceedings of the Institution of Mechanical Engineers, Part C: Journal of Mechanical Engineering Science*, vol. 230, no. 6, pp. 994–1006, 2016.

[104] S. Jeong, D. Jeon, and Y. B. Lee, "Rigid mode vibration control and dynamic behavior of hybrid foil–magnetic bearing turbo blower," *Journal of Engineering for Gas Turbines and Power*, vol. 139, no. 5, p. 052501, 2017.

[105] Z. Tian, Z. Wei, and Y. Sun, "Nonlinear adaptive control for hybrid foil-magnetic bearing," in *2017 IEEE International Conference on Mechatronics and Automation (ICMA)*. IEEE, 2017, pp. 81–86.

[106] S. Jeong, B. S. Choe, and Y. B. Lee, "Rotordynamic behavior and performance of controllable hybrid foil-magnetic bearing," in *Proceedings of the 9th IFToMM International Conference on Rotor Dynamics*. Springer, 2015, pp. 1465–1476.

[107] B. Yang, H. Geng, Y. Sun, and L. Yu, "Dynamic characteristics of hybrid foil-magnetic bearings (hfmbs) concerning eccentricity effect," *International Journal of Applied Electromagnetics and Mechanics*, vol. 52, no. 1-2, pp. 271–279, 2016.

[108] T. M. Jamir, "Gas foil bearing: effect of foil materials and stability analysis using different models for foil structure," Ph.D. dissertation, Indian Institute of Technology Guwahati, 2015.

[109] J. N. Reddy, "An introduction to the finite element method," *New York*, vol. 27, 1993.

[110] ——, *An Introduction to Nonlinear Finite Element Analysis: with applications to heat transfer, fluid mechanics, and solid mechanics*. OUP Oxford, 2014.

[111] J. S. Larsen, B. B. Nielsen, and I. F. Santos, "On the numerical simulation of nonlinear transient behavior of compliant air foil bearings," in *Proceedings of the 11th International Conference on Vibrations in Rotating Machines*, 2015, pp. 1–13.

[112] A. Chiba, T. Fukao, O. Ichikawa, M. Oshima, M. Takemoto, and D. G. Dorrell, *Magnetic bearings and bearingless drives*. Elsevier, 2005.

[113] E. Maslen, "Magnetic bearings," *University of Virginia, Charlottesville*, 2000.

[114] H. Chang and S.-C. Chung, "Integrated design of radial active magnetic bearing systems using genetic algorithms," *Mechatronics*, vol. 12, no. 1, pp. 19–36, 2002.

[115] M. I. Daoud, A. Abdel-Khalik, A. Massoud, S. Ahmed, and N. H. Abbasy, "A design example of an 8-pole radial amb for flywheel energy storage," in *2012 XXth International Conference on Electrical Machines*. IEEE, 2012, pp. 1153–1159.

[116] J. S. Larsen, A. J. Hansen, and I. F. Santos, "Experimental and theoretical analysis of a rigid rotor supported by air foil bearings," *Mechanics & Industry*, vol. 16, no. 1, p. 106, 2015.

[117] S. P. Bhore and A. K. Darpe, "Nonlinear dynamics of flexible rotor supported on the gas foil journal bearings," *Journal of Sound and Vibration*, vol. 332, no. 20, pp. 5135–5150, 2013.

[118] Z. Guo, K. Feng, T. Liu, P. Lyu, and T. Zhang, "Nonlinear dynamic analysis of rigid rotor supported by gas foil bearings: Effects of gas film and foil structure on subsynchronous vibrations," *Mechanical Systems and Signal Processing*, vol. 107, pp. 549–566, 2018.

[119] S. W. Khoo, R. L. Fittro, and S. D. Garvey, "Ac polyphase self-bearing motors with a bridge configured winding," in *Proc. 7th Int. Symp. Magn. Bearings*, 2002, pp. 47–52.

[120] W. Khoo, "Bridge configured winding for polyphase self-bearing machines," *IEEE Transactions on Magnetics*, vol. 41, no. 4, pp. 1289–1295, 2005.

[121] W. Khoo, K. Kalita, and S. Garvey, "Practical implementation of the bridge configured winding for producing controllable transverse forces in electrical machines," *IEEE Transactions on Magnetics*, vol. 47, no. 6, pp. 1712–1718, 2011.

[122] G. Kumar, K. Kalita, and K. Tammi, "Analysis of bridge currents and ump of an induction machine with bridge configured winding using coupled field and circuit modeling," *IEEE Transactions on Magnetics*, vol. 54, no. 9, pp. 1–16, 2018.

[123] S. D. Garvey, G. Johnson, S. Pearson, K. Kalita, G. Moore, and A. Kirk, "Control of rotors suspended on low-cost active magnetic bearings," in *2019 IEEE International Electric Machines & Drives Conference (IEMDC)*. IEEE, 2019, pp. 492–498.

भारतीय प्रौद्योगिकी संस्थान गुवाहाटी
Indian Institute of Technology Guwahati

List of Publications

Journals

1. Basumatary K. K., Kumar G., Kalita K., and Kakoty S. K., "Stability Analysis of Rigid Rotors Supported by Gas Foil Bearings Coupled with Electromagnetic Actuators", Proceedings of the Institution of Mechanical Engineers, Part C: Journal of Mechanical Engineering Science, https://doi.org/10.1177/0954406219877903.
2. Basumatary K. K., Kalita K., and Kakoty S. K., "Effect of Unbalance on the rotors supported on Gas Foil Bearing coupled with Electromagnetic Actuator", Journal of Mechanical Science and Technology (under review)
3. Basumatary K. K., Kalita K., Kakoty S. K., and Garvey S. D., "Comparative study of rotor response supported on hybrid gas foil bearing with conventional winding and bridge configured winding of magnetic bearings", (to be submitted)

Book Chapter

1. Basumatary K. K., Kakoty S. K., and Kalita K., "Stability Analysis of a Rigid Rotor supported on Gas Foil Bearings under Different Loading Conditions", Machines, Mechanism and Robotics. Lecture Notes in Mechanical Engineering. Springer, Singapore ISBN(Online) 978-981-10-8597-0, ISBN(Print) 978-981-10-8596-3, https://doi:10.1007/978-981-10-8597-0_6 .

International Conference

1. Basumatary K. K., Kalita K., Kakoty S. K., and Garvey S. D., "Vibration mitigation of rotors suspended on low-cost hybrid gas foil bearing" ASME Gas Turbine India Conference 2019, Chennai, India, 5th to 6th Dec, 2019, Paper No. GTINDIA2019-2539, V001T05A009; https://doi.org/10.1115/GTINDIA2019-2539
2. Basumatary K. K., Kumar G., Kalita K., and Kakoty S. K. "A Numerical study on Effect of Electromagnetic Actuator on Rigid Rotor Supported on Gas Foil Bearing" ASME Gas Turbine India Conference 2017, Bangalore, India, 7th to 8th Dec, 2017, Paper No. GTINDIA2017-4607, pp. V002T05A006; https://doi:10.1115/GTINDIA2017-4607

3. Basumatary K. K., Kalita K., and Kakoty S. K., "Sub-synchronous Vibration of Rotor Supported on Gas Foil Bearing", International Conference On Vibration Problems, IIT Guwahati 2017, 29th Nov to 2nd Dec, 2017, Paper ID-82.

National Conference

1. Basumatary K. K., Kalita K., and Kakoty S. K., "Effect of sinusoidal and non-sinusoidal periodic forces on the stability of Gas Foil Bearing" 6th National Symposium on Rotor Dynamics, CSIR-National Aerospace Laboratories, Bangalore, Paper Id- 25, 2nd July to 3rd July, 2019
2. Basumatary K. K., Kalita K., and Kakoty S. K., "Stability Analysis of Rigid Rotor Supported on Gas Foil Bearing", Recent Advances in Tribology and Maintenance, NIT Rourkela, 10th Feb to 11th Feb, 2017.